Passive-Scalar Transfer in Complex Turbulent Flows

Zur Erlangung des akademischen Grades eines
Doktors der Ingenieurwissenschaften (Dr.-Ing.)

von der KIT-Fakultät für Maschinenbau des
Karlsruher Instituts für Technologie (KIT)
angenommene

Dissertation

von

M.Sc. Francesco Secchi

Tag der mündlichen Prüfung:	01.08.2025

Hauptreferentin:	Prof. Dr.-Ing. Bettina Frohnapfel
Korreferent:	Prof. Ugo Piomelli

Acknowledgements

I would like to express my gratitude to my supervisor, Bettina Frohnapfel, for her continuous support and guidance throughout my PhD. Her expertise and insight have been invaluable to both my research and personal growth as a scientist.

I am also sincerely thankful to Davide Gatti, my co-supervisor, for his insightful advice, constructive feedback, and generous support throughout the course of this work.

I would like to thank Ugo Piomelli for hosting me during my research stay in Canada. His hospitality and the opportunity to collaborate in a stimulating academic environment greatly enriched my research experience.

I gratefully acknowledge the financial support provided by the Collaborative Research Centre SFB-TRR150. I also extend my thanks to the members of the project groups A06 and B03 for the fruitful collaboration and valuable discussions.

Special thanks go to the High-Performance Computing Center Stuttgart (HLRS) for providing the computational resources that made many parts of this work possible.

I am deeply grateful to all my colleagues at the institute for the stimulating discussions, their help along the way, and the friendships that made this journey more enjoyable.

Finally, I would like to thank my friends and family for their unwavering support, patience, and encouragement during these years. Their presence has been a constant source of strength and motivation.

Abstract

In many fluid systems, scalar quantities such as the fluid's temperature or the concentration of a chemical contaminant are transported by the flow and diffuse within it without significantly altering its dynamics. These quantities, named passive scalars, are governed by advection-diffusion equations and offer a seemingly simple framework to investigate scalar transport in complex flows. Despite their apparent simplicity, passive scalars exhibit rich behaviours, particularly in turbulent flows where scalar and momentum transfer often diverge, posing both theoretical and practical challenges.

This work focuses on the interaction between turbulent flows and solid boundaries, where momentum and scalar transfer become especially relevant for engineering applications, such as in the design of heat exchangers or combustion chambers, or in the study of environmental flows, in which case a scalar field can be used to model a passive contaminant in the atmosphere. Although analogies between scalar and momentum transfer exist, differences arise due to the distinct physical nature of scalar and velocity fields. Pressure, in particular, plays a central role in momentum dynamics but does not directly influence scalar transport, leading to significant deviations from similarity.

This research investigates mainly two wall-bounded flow configurations which patently exhibit non-analogous mean momentum and scalar transfer. These are rough wall fully-developed turbulent channel flows and turbulent impinging jets. To transition from fully-developed flows to spatially developing ones, the study considers also canonical turbulent boundary layers with and without surface roughness on the wall. In rough-wall flows, increased momentum transfer is primarily driven by the pressure drag of roughness elements, while an analogous mechanism does not exist for the mean scalar transfer enhancement. In impinging jets, pressure dominates the fluid's momentum change in the stagnation region of the flow, whereas the mean scalar is not equally affected.

In spite of the clear origin of non-analogous momentum and scalar transfer, their departure often fails to follow any currently available predictive law. This is especially true for flows in the fully rough regime, where mean momentum and scalar transfer tend to diverge in ways that remain difficult to quantify, highlighting the current lack of a mature understanding of the underlying mechanisms.

To address these challenges, the present investigation explores a novel framework that bypasses the direct influence of pressure by formulating the analogy in terms of the mean mechanical energy, given by the sum of kinetic and pressure energy, and one-half of the mean scalar concentration magnitude. Being scalar quantities, these are amenable for direct comparison and their mean distributions provide new grounds for understanding momentum and scalar transfer dissimilarities. This perspective enables the identification of flow regions in which scalar and momentum exchange deviate and links the local mean viscous dissipation mechanisms of mechanical energy and the squared scalar field to integral momentum and scalar transfer metrics. This fact is used to further evaluate the scalar transfer efficiency of the system, thus providing a means for addressing analogous momentum and scalar transfer from an energetic perspective.

The methodology is applied on direct numerical simulation data of the aforementioned flow configurations. For all the considered cases, the framework successfully highlights the energetic aspects of the momentum and scalar dissimilarities, offering new physical insights and a robust alternative to the classical Reynolds analogy approach.

Kurzfassung

In vielen Strömungen werden skalare Größen wie die Temperatur oder die Konzentration eines chemischen Stoffes durch die Strömung transportiert, ohne deren Dynamik wesentlich zu beeinflussen. Diese Größen, sogenannte passive Skalare, unterliegen Advektions-Diffusions-Gleichungen und bieten einen scheinbar einfachen Rahmen zur Untersuchung des Transport von Skalaren in komplexen Strömungen. Trotz ihrer augenscheinlichen Einfachheit zeigen passive Skalare ein reichhaltiges Verhalten, insbesondere in turbulenten Strömungen. Hier unterscheidet sich der Transport von Skalargrößen und Impuls häufig, was sowohl theoretische als auch praktische Herausforderungen mit sich bringt.

In dieser Arbeit steht die Interaktion turbulenter Strömungen mit festen Grenzflächen im Fokus. Impuls- und Skalartransport sind insbesondere für die Wärmeübertragung in Kühlsystemen, Verbrennungsprozesse in Brennkammern und die Modellierung von Kontaminanten in der Atmosphäre von entscheidender Bedeutung. Obwohl Analogien zwischen Skalar- und Impulstransport existieren, treten Unterschiede aufgrund der unterschiedlichen physikalischen Natur von Skalar- und Geschwindigkeitsfeldern auf. Besonders der Druck spielt eine zentrale Rolle in der Impulsdynamik, beeinflusst jedoch den Transport von Skalaren nicht direkt, was zu erheblichen Abweichungen von der Ähnlichkeit führt.

Die vorliegende Arbeit untersucht hauptsächlich zwei Strömungskonfigurationen, die deutlich nicht-analogen mittleren Impuls- und Skalartransport aufweisen: vollständig entwickelte turbulente Kanalströmungen über rauen Wänden sowie turbulente Prallstrahlen. Um den Übergang von vollständig entwickelten zu räumlich sich entwickelnden Strömungen zu erfassen, werden ergänzend auch kanonische turbulente Grenzschichten mit und ohne Wandrauheit betrachtet. In Strömungen über rauen Wänden wird der erhöhte Impulstransport primär durch den Druckwiderstand der Rauigkeitselemente getrieben, während ein entsprechender Mechanismus zur Erhöhung des mittleren Transports von Skalaren nicht existiert. In Prallstrahlen hingegen dominiert der Druck die Impulsänderung des Fluids im Stagnationsbereich, wohingegen der mittlere Skalartransport hiervon deutlich weniger beeinflusst wird.

Trotz des klar identifizierbaren Ursprungs der Unterschiede im Impuls- und Skalartransport folgt deren Abweichung häufig keiner derzeitig bekannten Vorhersage. Dies gilt insbesondere für Strömungen im vollständig rauen Regime, in denen sich mittlerer Impuls- und Skalartransport in einer Weise entkoppeln, die bislang nur schwer quantifizierbar ist; ein Indiz für das derzeit noch unvollständige physikalische Verständnis dieses Phänomens.

Zur adressierten Fragestellung wird in der vorliegenden Arbeit ein neuartiges theoretisches Konzept untersucht. Dieses umgeht den direkten Einfluss des Drucks, indem die Analogie zwischen Impuls- und Skalartransport über die mittlere mechanische Energie, definiert als Summe aus kinetischer und Druckenergie, sowie die Hälfte der mittleren Skalarkonzentration formuliert wird. Da es sich hierbei um skalare Größen handelt, lassen sie sich direkt miteinander vergleichen. Ihre mittleren Verteilungen bilden eine neue Grundlage zum Verständnis der physikalischen Mechanismen hinter den beobachteten Unterschieden. Der Ansatz ermöglicht die Identifikation von Strömungsregionen mit signifikanter Abweichung im Austausch von Impuls und Skalaren und stellt einen Zusammenhang her zwischen den lokalen mittleren viskose Dissipationsmechanismen der mechanischen Energie und des quadrierten Skalarfeldes einerseits und integralen Transportgrößen andererseits. Daraus ergibt sich eine Möglichkeit, die Effizienz des Skalartransports im System zu bewerten und den Vergleich zwischen Impuls- und Skalartransport aus energetischer Sicht vorzunehmen.

Die vorgeschlagene Methodik wird auf Datensätze direkter numerischer Simulationen der genannten Strömungskonfigurationen angewendet. In allen betrachteten Fällen hebt das Rahmenkonzept erfolgreich die energetischen Unterschiede zwischen Impuls- und Skalartransport hervor, liefert neue physikalische Einsichten und stellt eine robuste Alternative zur klassischen Reynolds-Analogie dar.

Contents

1 Introduction

A scalar field that convects and diffuses within a fluid flow may represent the fluid temperature, or the concentration of a chemical contaminant injected in the flow. Provided that the variations of the scalar concentration remain sufficiently small, their impact on the flow dynamics can be neglected and the scalar field is, in turn, named *passive*. Although disregarding altogether the feedback of the scalar field on the flow might be a crude assumption, the passive-scalar model plays a crucial role in the investigation of various natural and engineering systems, including atmospheric processes [61], combustion [101], heat exchange [44], and biological systems [6]. From an engineering perspective, it is of utmost importance to investigate the mechanisms of momentum and scalar transfer that occur through the interaction between the flow and a solid wall. The latter problem becomes particularly intriguing when the flow under consideration is turbulent; a ubiquitous circumstance in real-world flows.

1.1 Motivation

A fluid moving over a stationary wall loses its momentum to friction losses at the wall, which are proportional to the local velocity gradient through the molecular viscosity of the fluid. Turbulence emphasizes such momentum exchange by favouring, on average, the transport of high-speed fluid towards the wall vicinity, thus steepening the local velocity gradient. In turn, a higher wall-friction is experienced in comparison to an equivalent laminar flow. This phenomenon is the reflection of a mechanism through which near-wall turbulence sustains itself at the energetic expenses of the mean flow [35, 42]. This concise phenomenological explanation is the result of decades of investigations, which are yet extremely active. The reason behind such a research endeavour goes beyond the pure scientific amusement: friction constitutes the main contributor to the total drag force experienced by most of locomotion vehicles. Mastering the physics behind the turbulence-wall interaction can potentially inform more efficient designs, with enormous economical, environmental, and strategic benefits [12].

The inclusion of a passive scalar field into this scenario seems to be an effortless exercise: given the knowledge of the velocity, the passive-scalar distribution can be determined by solving an additional linear advection-diffusion equation. The latter representing either the conservation of the fluid internal energy, in case the scalar field is interpreted as the temperature field, or the mass conservation for the chemical species represented by the scalar concentration. This alleged simplicity, joint with the difficulties of measuring accurately scalar concentrations in turbulent flows [3], has perhaps hindered and delayed the research on scalar transfer, determining a significant lag in comparison with the state-of-the-art of our current understanding on momentum transfer. A gap that, in several contexts, is arduous to fill by simple extrapolation from the current knowledge of fluid motion. This, *per se*, represents a hurdle for scientists searching for a unifying theory of turbulence. In practical terms, the present immaturity of the subject leads to inefficient designs of cooling systems [9, 76] and chemical reactors [99], as well as an inability to understand and control the transport of contaminants in the atmospheric boundary layer [55].

1.2 Background

The similarity between the fluctuating scalar and the velocity fields becomes elusive at the smallest scales of turbulent motion, with the result that some statistical aspects of the scalar tend to deviate significantly from the statistics of the turbulent velocity field. In this respect, outstanding is the anomalous scaling of high-order scalar statistical moments, whose departure from the behaviour predicted by classical turbulence theories differs from that observed for turbulent velocity statistics [87, 100]. Yet, low-order statistics seem to be less affected by these discrepancies; for them, similarity arguments, deployed for the determination of velocity scaling laws, have been extended to scalar statistics with a good degree of success.

In wall-bounded flows, a major achievement in this respect is the logarithmic *law of the wall* for the mean scalar profile, whose theoretical existence can be predicted based on analogous assumptions as those used for the mean velocity profile [107], and whose occurrence has received vast support from a plethora of studies [5, 43, 46, 68, 70, 90]. At the origin of this success stand the similar physical processes involved in the transport of momentum and scalar concentration from the largest scales of motion, down to the smallest ones, where molecular diffusivity comes into play and sets the dissipation of velocity and scalar fluctuations. In particular, these similar mechanisms turn into perfectly analogous outcomes in case the fluid is characterized by similar momentum and thermal molecular diffusivities; whereby the dissipative velocity and scalar processes take place approximately at comparable scales of motion.

Even for a fluid characterized by similar heat and momentum diffusivities, a source of dissimilarity is intrinsic within the nature of the velocity and the scalar fields. The former being a three-dimensional vector field, whereas the latter a simple scalar quantity. The lack of a directional character, inherent in the scalar, can be ascertained through the evaluation of its gradient field, which provides information about the directionality of molecular energy transfer within the fluid. For instance, in case of a temperature field, its gradient informs about the molecular heat conduction. Therefore, by definition, the scalar is directly related to an irrotational vector field that expresses the directionality of energy transfer; a character that is not matched by a turbulent velocity field. In the common scenario of incompressible flow, however, the velocity field is constrained to be solenoidal, *i.e.* having zero divergence. This different nature of the velocity and scalar fields is not just a mathematical subtlety: the enforcement of the divergence-free constraint occurs through the action of the pressure gradient field, which intervenes in the momentum balance without directly affecting the balance of the scalar.

For a few simple flow configurations, such as smooth-wall channel flow and zero-pressure gradient boundary layers, the net effect of the pressure gradient on momentum transfer remains negligible, and an integral similarity is observed between velocity and scalar statistical quantities. This reflects, for instance, in similar mean scalar and velocity profiles and analogous momentum and scalar fluxes at the wall. Nevertheless, in many situations of engineering interest, the change in momentum due to the action of the pressure gradient becomes the dominant contribution to the overall momentum balance; an action that does not directly affect the scalar transfer. Correspondingly, a significant departure from perfectly analogous scalar and momentum transfer is observed. Although the source of this discrepancy is patent, predicting the particular fashion through which the scalar and momentum transfer differ is yet an open question of high practical and theoretical relevance. Two exemplary flows are instrumental for understanding the described scenario; these are turbulent flows over surface roughness, and impinging jet flows.

1.2.1 Turbulent flows over surface roughness

The surface of any solid exposed to a fluid flow is, up to a certain size, corrugated and irregular due to the action of the environment, or because of the machining processes used for the surface finishing. This characteristic of any real-world surface goes under the name of surface roughness. The flow starts perceiving the roughness when the smallest scales involved in its motion become comparable to the characteristic physical size of the roughness topography. In particular, the effects of roughness become ever more significant as the overlap between the roughness size and viscous length scale of the flow increases. Phenomenologically, there exist three different scenarios [13, 41]. When sufficient separation of flow and roughness length scales exists, the flow does not perceive the roughness and effectively behaves as if it were over a smooth surface. In these settings, the flow is said to be in the *hydrodynamically smooth* regime. As an overlap starts existing between the roughness and the flow length scales, the flow enters the *transitionally rough* regime. As an integral effect, the mean momentum and scalar exchange are enhanced, but with an important difference. Momentum exchange increases due to the combined action of viscous and pressure drag, whereas the augmentation of the mean scalar transfer can only be attributed to a magnification of molecular conduction. Therefore, even for similar molecular diffusivities of momentum and scalar, the net momentum transfer augmentation, induced by surface roughness, surpasses the corresponding increase in scalar transfer. The hiatus becomes even more prominent in the *fully rough* regime, where the pressure drag contribution dominates over the viscous contribution to the mean momentum exchange.

The phenomenological knowledge behind the dissimilar momentum and scalar transfer induced by surface roughness has yet failed to provide with a definitive predictive law capable of providing the scalar transfer augmentation for a given roughness topography and flow condition. While it is well established how the induced momentum transfer augmentation increases as a function of the flow regime, there is not yet consensous on the corresponding scalar exchange enhancement. In particular, evidences in the literature indicate that, for fully rough conditions, contrary to an ever increasing momentum deficit, the corresponding scalar transfer enhancement tends to saturate to a constant value [36, 44]. This behaviour requires further confirmation and, at the moment, lacks an agreed-upon physical explanation.

1.2.2 Impinging jet flow

Jet impingement is realized by directing a free jet flow towards a target plate and is a common means used in industrial applications for cooling, drying and abrading surfaces. In particular, crucial areas of application of impinging jets are the inner cooling of turbine blades, or the cooling of electric circuitry [9, 76]. Due to their practical relevance, impinging jets have been intensively studied in the past. Most of available works attempted at determining semi-empirical correlations capable of delivering the integral heat transfer coefficient for a given impinging jet configuration and functioning condition. These investigations readily revealed the difficulties in relating the wall-heat transfer to the flow.

Near the jet axis, the flow exhibits the *stagnation region* which is characterized by the flow deflection and its reorientation along the impingement plate parallel direction. This region features an apparent departure from an analogous momentum and scalar exchange: the flow deflection occurs through the action of an adverse pressure gradient that is experienced by the flow incoming from the free jet. Naturally this does not directly affect the scalar field with the result that the wall-momentum and scalar fluxes are highly dissimilar in the stagnation region [9]; the former, becomes vanishingly small near the jet axis, whereas the latter attains its global maximum in this region.

Downstream of the stagnation region, a wall jet develops along the impingement plate. In the *wall jet region*, an intriguing aspect of the mean scalar transfer is its local enhancement induced by the coherent structures that originate in the shear layer of the free jet. Their advection towards the wall determines the formation of secondary toroidal structures near the impingement plate. The interplay between these coherent vortices, jointly with the subsequent formation of smaller scale structures, leads to a local heat transfer enhancement which is known in the literature as the *secondary peak* in the mean heat transfer distribution. A substantial amount of literature is dedicated in understanding this phenomenon and the conditions under which it appears [14, 34, 58, 94, 97]. Interestingly, as shown by Dairay et al. [14], the net augmentation of mean scalar transfer occurs dissimilarly from the mean momentum transfer over the same region, where local unsteady flow separation, induced by large-scale coherent vortices, produces intermittent events of high scalar transfer.

As the flow develops downstream, the mean scalar and momentum transfer are also seen to decrease with the distance from the jet axis, but at different rates [103]. In particular, on average, the momentum flux has a faster rate of decay compared with the scalar flux at the wall due to the radial expansion of the flow [85].

1.3 Objectives

For the two introduced exemplary flows, pressure is responsible for a dissimilar momentum and scalar transfer. However, as argued by Gresho and Sani [32], pressure is somewhat an enigmatic entity in an incompressible flow: it is not attached to any thermodynamic equation of state, it is an instantaneous quantity that enforces the incompressibility constraint everywhere in the flow field and, yet, its gradient represents an actual force per unit volume with an intuitive physical meaning. Thanks to this latter property, understanding and interpreting the pressure contribution to the momentum balance is a seemingly viable exercise; conversely, quantifying and modelling its effects on the scalar transfer appears as a challenging task.

To circumvent this difficulty, the present work aims at finding an alternative path for the description of the momentum and scalar transfer dissimilarity which, eluding the pressure contribution, enables the identification and quantification of flow regions where the dissimilarity occurs. As starting point, the similarity is searched in terms of the kinetic energy (*i.e.* half of the squared momentum magnitude) and the half of the squared scalar magnitude. As argued by Secchi et al. [86] and Secchi et al. [85], these two quantities are much more amenable for comparison due to the fact that they are both scalar fields that are driven by momentum and scalar power inputs and that dissipate within the flow. Pressure appears into the kinetic energy balance through transport-diffusion terms, which enable to cast the kinetic energy equation in terms of the total mechanical energy, defined as the sum of the kinetic energy and pressure work.

An analogous form of the total mechanical energy and the squared-scalar field becomes apparent in the case of statistically stationary flows, whereby, on average, a dissimilar scalar and momentum transfer can be related to the different degree at which these quantities dissipate in the flow. This property is used to unveil flow regions where dissimilar scalar and momentum transfer occurs. The direct relationship between integral dissipation rates and power inputs to the system is further exploited to quantify the global effect that such regions have on the integral scalar and momentum transfer. For canonical forced convection problems, this readily reduces to a quantification of the integral momentum and scalar fluxes at the wall, hence offering an alternative perspective on the evaluation of the classical *Reynolds analogy*; the term used in the literature to describe the similarity between heat and momentum transfer, following the pioneering work of Reynolds [73]. For more complex flows, the proposed framework expands the assessment of the momentum and scalar analogy to the comparison of the scalar power transferred through the system and the consumed mechanical power required to drive the flow, hence linking the analogy to the evaluation of the thermal efficiency of the system.

The framework is first introduced formally, starting from the governing equations of incompressible flows. Then, its application to wall-bounded flows of increasing complexity is presented. The basic configuration consists in fully-developed channel flows, with particular attention to rough-wall channel flows; in this case it is shown how the method enables a novel interpretation of classical results on the departure from similar scalar and momentum transfer. Spatial development of the flow is introduced by considering zero-pressure gradient boundary layers. This application is helpful in addressing how the presented framework can be instrumental in interpreting the momentum and scalar analogy from an energetic perspective. This interpretation is further exploited to investigate the highly complex flow of an impinging jet, whereby the flow exhibits a stagnation region and a developing region affected by highly dissimilar scalar and momentum transfer. For each presented case, direct numerical simulation data is used to assess the proposed framework and to gain further physical insights into the investigated flows.

2 Theoretical formulation

2.1 Governing equations

2.1.1 Momentum

The incompressible motion of a fluid continuum is governed by the equations,

$$\frac{\partial u_i}{\partial x_i} = 0, \tag{2.1}$$

$$\frac{\partial u_j}{\partial t} + u_i \frac{\partial u_j}{\partial x_i} = f_j + \frac{1}{\rho}\frac{\partial \tau_{ij}}{\partial x_i}. \tag{2.2}$$

Fluid's properties are assumed to be constant throughout this work. In equations (2.1) and (2.2), u_i, with $i = 1, 2, 3$, represents the velocity component in the ith coordinate direction, x_i; ρ is the density of the fluid, f_j is an externally applied force per unit volume. The nature of the fluid is expressed through the stress tensor τ_{ij}; in the present study, only Newtonian fluids will be considered. Note that index summation is implied whenever two repeated indices appear in an equation, following Einstein's notation.

Equation (2.1) expresses the conservation of the volume of fluid elements during their motion. As such, it is a purely kinematic relationship and will be referred to as the *incompressibility constraint*. Equation (2.2) represents the balance of momentum; the acceleration of the fluid at a given point in space, represented by the unsteady and convection terms on the left-hand side of the equation, is balanced by the action of external forces, f_j, and of the resultant of the stresses that act on a fluid element surface. For a Newtonian fluid, subject to an incompressible motion, the relationship between stresses and deformation is given by $\tau_{ij} = -p\delta_{ij} + 2\mu s_{ij}$, where p is the pressure, δ_{ij} denotes the identity second-order isotropic tensor, μ is the dynamic viscosity of the fluid, and $s_{ij} = (u_{i,j} + u_{j,i})/2$ is the strain rate tensor. Throughout this work, partial differentiation of will be interchangeably denoted with either the standard notation, $\frac{\partial \cdot}{\partial x_i}$, or with the comma notation, $(\cdot)_{,i}$.

For Newtonian fluids, the incompressible $Navier$-$Stokes$ equations, (2.1) and (2.2), read:

$$\frac{\partial u_i}{\partial x_i} = 0, \tag{2.3}$$

$$\frac{\partial u_j}{\partial t} + u_i \frac{\partial u_j}{\partial x_i} = f_j - \frac{1}{\rho}\frac{\partial p}{\partial x_j} + \nu \frac{\partial^2 u_j}{\partial x_i \partial x_i}. \tag{2.4}$$

In equation (2.4), $\nu = \mu/\rho$ denotes the kinematic viscosity of the fluid. Pressure intervenes in the momentum balance (2.4) only through its gradient and, as such, adding any uniform-in-space pressure contribution to it is irrelevant in terms of fluid motion. Instantaneously, the pressure must satisfy the Poisson's equation obtained by applying the divergence operator to (2.4); namely [8],

$$-\frac{1}{\rho}\frac{\partial^2 p}{\partial x_j \partial x_j} = \frac{\partial}{\partial x_j}\left(u_i \frac{\partial u_j}{\partial x_i}\right) = s_{ij}s_{ij} - \frac{1}{2}\omega_i\omega_i, \tag{2.5}$$

where $\omega_i = \varepsilon_{ijk} u_{k,j}$ is the ith component of the vorticity vector (ε_{ijk} is the Levi-Civita permutation third-order tensor). As argued by Adrian [4], the decomposition of the pressure source term in the last equality of (2.5) is not unique and alternative decompositions in terms of rotational and irrotational sources can be found (where irrotational indicates a flow with $\omega_i = 0$, for $i = 1, 2, 3$). Yet, the form of (2.5) is particularly useful for the present formulation, as it will become evident in the following.

An equation for the kinetic energy, $\mathcal{K} = u_j u_j/2$, follows from (2.2) upon multiplication of both its sides by u_j and contraction of repeated indices of the resulting scalar expression. For a Newtonian fluid, the result reads:

$$\frac{\partial \mathcal{K}}{\partial t} = f_j u_j + \frac{\partial}{\partial x_j}\left(-\mathcal{K} u_j + \tau_{ij} u_j\right) - 2\nu s_{ij} s_{ij}. \tag{2.6}$$

Locally, the time rate of change of kinetic energy is dictated by the net contribution of the power exerted by external agencies, $f_j u_j$, the convected kinetic energy and the power exerted by surface stresses (respectively the first and second terms within the parentheses of the second term on the right-hand side of equation (2.6)), and the kinetic energy dissipation represented by the right-most term in (2.6).

2.1.2 Passive scalar

Energy conservation can be used to derive an evolutive equation for the fluid temperature [49]. The change in kinetic and internal energy of a fluid element occurs due to the work done by external forces and surface stresses and due to heat generation and exchange within and across the fluid element volume. Subtraction of equation (2.6) from this balance leads to an equation for the fluid internal energy $e = c_{\mathrm{P}} T$, where c_{P} and T are, respectively, the heat capacity at constant temperature and the fluid temperature. For constant properties, and assuming that only heat conduction through Fourier's law occurs across the fluid element boundary, such an equation reduces to:

$$\frac{\partial T}{\partial t} + u_i \frac{\partial T}{\partial x_i} = q_{\mathrm{T}} + \alpha_{\mathrm{T}} \frac{\partial^2 T}{\partial x_i \partial x_i} + 2\nu s_{ij} s_{ij}, \tag{2.7}$$

where q_{T} indicates an external source term per unit volume and α_{T} represents the molecular thermal diffusivity of the fluid, related to the fluid conductivity, λ, through $\alpha_{\mathrm{T}} = \lambda/(\rho c_{\mathrm{P}})$. The last term on the right-hand side of (2.7) represents the heat source resulting from the dissipation of kinetic energy, as can be readily observed from the comparison with equation (2.6).

In case the flow consists of multiple chemical species that mix at molecular level, the mass concentration, ρ_k, of the species k, contained in a fluid element, changes due to molecular flux at the fluid element volume boundary and, possibly, due to its production, or destruction, driven by chemical reactions. When the molecular flux is driven only by concentration gradients, *i.e.* when it is described by Fick's first law, the mass conservation for ρ_k reads:

$$\frac{\partial \rho_k}{\partial t} + u_i \frac{\partial \rho_k}{\partial x_i} = q_{\mathrm{R}k} + \alpha_{\mathrm{R}k} \frac{\partial^2 \rho_k}{\partial x_i \partial x_i}, \tag{2.8}$$

where $q_{\mathrm{R}k}$ and $\alpha_{\mathrm{R}k}$ represent, respectively, the production/destruction rate and the molecular concentration diffusivity of the kth chemical species. Naturally, for a mixture of M species, it must be verified that $\sum_{k=1}^{M} \rho_k = \rho$, and $\sum_{k=1}^{M} q_{\mathrm{R}k} = 0$.

In general, additional transport and source terms can be added to the equations (2.7) and (2.8), depending on the considered problem. For instance, temperature gradients can produce transport of chemical species, a phenomenon known as *Soret effect*. Analogously, concentration gradients do induce a heat flux, as observed through the *Dufour effect*. These effects can, or cannot, be disregarded depending on the specific application of interest; the verification of the validity of these assumptions goes beyond the scope of the present investigation and will not be pursued here.

From a fundamental perspective, it is of interest to study the evolution of a generic scalar field, ϑ, governed by an equation that shares the same structure as (2.7) and (2.8), *i.e.* an unsteady advection-diffusion equation subject to a velocity field satisfying (2.3) and (2.4). More precisely,

$$\frac{\partial \vartheta}{\partial t} + u_i \frac{\partial \vartheta}{\partial x_i} = q + \alpha \frac{\partial^2 \vartheta}{\partial x_i \partial x_i}, \tag{2.9}$$

where q indicates an external source term per unit volume and α represents the molecular diffusivity of the scalar field ϑ. The source term, representative of the heat source due to momentum dissipation in the temperature equation (2.7), has also been disregarded from the generic scalar equation (2.9). This assumption is the standard for low *Eckert number* flows, where the Eckert number is representative of the ratio between internal and kinetic energy variations characteristic of the considered flow. Further, it can be argued that, due to linearity, the knowledge of the solution to the homogenous equation (2.9) is always of interest, for its superposition with the particular solution to the forced equation gives the complete solution [78].

In any case, it must be stressed that the scalar ϑ does not exert any feedback on the momentum balance and, as such, it is named *passive-scalar* field. This assumption limits the applicability of equation (2.9) to model the heat transfer or the transport of chemical species when, respectively, temperature and concentration gradients do not induce fluid motion (*e.g.* buoyancy effects in heat transfer problems).

2.2 Mechanical energy and squared-scalar field equations

Analogous momentum and scalar transfer is typically inferred based on the observation that equations (2.4) and (2.9) are similar in form, disregarding the presence of the pressure gradient in the momentum balance (2.4). Yet, the vectorial nature of (2.4) makes the comparison with the scalar equation (2.4) rather cumbersome. A natural remedy to this issue is to seek analogy between two scalar quantities and, to this aim, the kinetic energy is a perfect candidate, as it represents the momentum magnitude and its evolution is governed by the scalar equation (2.6). With aid of (2.5), and using standard vector identities, it is possible to write (2.6) in a form that better highlights the structural similarities and differences with equation (2.9). Namely,

$$\frac{\partial \mathcal{K}}{\partial t} + u_i \frac{\partial \mathcal{B}}{\partial x_i} = f_j u_j + \nu \frac{\partial^2 \mathcal{B}}{\partial x_i \partial x_i} - \nu \omega_i \omega_i, \tag{2.10}$$

where $\mathcal{B} = \mathcal{K} + (p/\rho)$ denotes the *mechanical energy* [86]. Despite evident similarities in the form of (2.9) and (2.10), important differences appear; while the time rate of change of ϑ depends on its local convection, molecular diffusion and input from external source terms, that of $\mathcal{K}$ depends on the local convection and diffusion of the mechanical energy, $\mathcal{B}$, and on external power sources; further, an important difference is played by the fact that $\mathcal{K}$, unlike ϑ, is subject to viscous dissipation in the flow volume.

This remark encourages to further look for similarities in terms of $\mathcal{K}$ and the scalar quantity $\mathcal{G} = \vartheta^2/2$. As $\mathcal{K}$ represents one-half of the squared momentum magnitude, $\mathcal{G}$ is defined as one-half of the squared scalar magnitude. The governing equation for $\mathcal{G}$ is readily obtained upon multiplication of both sides of (2.9) by ϑ and the result is given by:

$$\frac{\partial \mathcal{G}}{\partial t} + u_i \frac{\partial \mathcal{G}}{\partial x_i} = q\vartheta + \alpha \frac{\partial^2 \mathcal{G}}{\partial x_i \partial x_i} - \alpha \vartheta_{,i}\, \vartheta_{,i}\, . \tag{2.11}$$

$\mathcal{K}$ and $\mathcal{G}$ share a very similar structure in their governing equations, with the remaining difference that the time rate of change of $\mathcal{K}$ depends locally on the convection and diffusion of mechanical energy $\mathcal{B}$, whereas that of $\mathcal{G}$ depends on the convection and diffusion of $\mathcal{G}$ itself.

Under statistically stationary conditions, time averaging causes the time rate of change terms on the left-hand side of equations (2.10) and (2.11) to vanish, resulting in two structurally analogous equations for $\mathcal{B}$ and $\mathcal{G}$. By denoting with an overline the time-averaging operator, these read:

$$0 = \overline{f_j u_j} + \frac{\partial}{\partial x_i}\left(-\overline{\mathcal{B} u_i} + \nu \frac{\partial \overline{\mathcal{B}}}{\partial x_i}\right) - \nu \overline{\omega_i \omega_i}, \tag{2.12}$$

$$0 = \overline{q\vartheta} \quad + \frac{\partial}{\partial x_i}\left(-\overline{\mathcal{G} u_i} + \alpha \frac{\partial \overline{\mathcal{G}}}{\partial x_i}\right) - \alpha \overline{\vartheta_{,i}\, \vartheta_{,i}}. \tag{2.13}$$

Hence, for statistically stationary flows, the mechanical energy and the squared-scalar field are expected to have similar distributions on average, provided that they are externally excited by similar input sources and boundary conditions and that they have similar molecular diffusivities, ν and α. In these settings, dissimilar momentum and scalar transfer can be related to different dissipation rates of mechanical energy and squared scalar field, respectively, $\nu\overline{\omega_i\omega_i}$ and $\alpha\overline{\vartheta_{,i}\,\vartheta_{,i}}$. Formally, $\nu\overline{\omega_i\omega_i}$ represents the time-averaged dissipation rate of kinetic energy. However, this also amounts to the mechanical energy dissipated on average when the time-averaged transport of $\mathcal{B}$ in equation (2.12) is considered. This consideration is valid since, as shown by equation (2.10), the pressure intervenes in the kinetic energy balance only through transport terms of convection and molecular diffusion, without contributing to the volumetric production or destruction of mechanical energy. On these grounds, $\nu\overline{\omega_i\omega_i}$ will be referred to as the time-averaged mechanical energy dissipation rate.

2.2.1 Equivalence of kinetic energy dissipation rates

According to equations (2.6) and (2.10), the local dissipation rate of kinetic energy can be defined, respectively, as $2\nu s_{ij}s_{ij}$ and $\nu\omega_i\omega_i$; given (2.5), these two expressions are not equivalent, and their difference is given by:

$$2\nu s_{ij}s_{ij} - \nu\omega_i\omega_i = -\frac{2\nu}{\rho}\frac{\partial^2 p}{\partial x_j \partial x_j} = 2\nu\frac{\partial}{\partial x_j}\left(u_i\frac{\partial u_j}{\partial x_i}\right). \tag{2.14}$$

Integration of the latter expression inside a volume $\mathcal{V}$ and application of Gauss' divergence theorem gives:

$$\int_{\mathcal{V}} 2\nu s_{ij}s_{ij}\,\mathrm{d}\mathcal{V} - \int_{\mathcal{V}} \nu\omega_i\omega_i\,\mathrm{d}\mathcal{V} = \oint_{\partial\mathcal{V}} 2\nu u_i \frac{\partial u_j}{\partial x_i} n_j\,\mathrm{d}\partial\mathcal{V}, \tag{2.15}$$

where $\partial\mathcal{V}$ denotes the boundary of $\mathcal{V}$, and n_j, with $j = 1, 2, 3$, the unit outward normal vector to $\partial\mathcal{V}$. The right-hand side of (2.15) vanishes whenever $u_i\frac{\partial u_j}{\partial x_i}n_j = 0$ on $\partial\mathcal{V}$, whereby the two dissipation rates are equivalent in an integral sense.

Even in case the right-hand side of (2.15) vanished, the integral equivalence of the kinetic energy dissipation rates does not imply their local equivalence. Hence, this raises the question of which expression is the most natural choice for assessing local kinetic energy dissipation rates. Wu et al. [105] argue that the local difference between the two dissipation rates equals the work done by viscous forces with the superficial strain rate tensor; the latter is defined by Dishington [17] as $b_{ij} = u_{m,m}\delta_{ij} - u_{i,j} = -u_{i,j}$, where the last equivalence applies, in the present case, due to the incompressibility constraint. As shown by Wu [104], this can be seen by splitting the stress tensor into $\tau_{ij} = -p\delta_{ij} + 2\mu r_{ji} - 2\mu b_{ij}$, where $r_{ji} = (u_{j,i} - u_{i,j})/2$ is the (transposed) rotation tensor. Note that this decomposition does not affect the momentum balance (2.4) since $(b_{i,j})_{,i} = 0$

and $2\mu(r_{ji})_{,i} = \mu u_{j,ii}$. Substituting this particular decomposition of τ_{ij} and $2\nu s_{ij}s_{ij} = \nu\omega_i\omega_i - 2\nu(u_j b_{ij})_{,i}$ into (2.6) gives:

$$\frac{\partial \mathcal{K}}{\partial t} = f_i u_i \underbrace{- \frac{\partial}{\partial x_i}\left(\mathcal{K}u_i + \frac{p}{\rho}u_i\right)}_{-\frac{\partial}{\partial x_i}(\mathcal{B}u_i)} + \underbrace{2\nu\frac{\partial}{\partial x_i}\left(r_{ji}u_j\right)}_{\nu\frac{\partial^2\mathcal{B}}{\partial x_i \partial x_i}} - 2\nu\frac{\partial}{\partial x_i}\left(b_{ij}u_j\right) \underbrace{- \nu\omega_i\omega_i + 2\nu\frac{\partial}{\partial x_i}\left(b_{ij}u_j\right)}_{-2\nu s_{ij}s_{ij}}, \tag{2.16}$$

which is fully equivalent to (2.10) and highlights that the viscous dissipation rate, $2\nu s_{ij}s_{ij}$, contains a contribution which gets simultaneously cancelled by the viscous work done by the superficial strain deformation. Nevertheless, Wu et al. [105] further argue that the latter, and hence the difference between the two dissipation rates, is practically always negligible and becomes relevant in the vicinity of free-surfaces.

2.2.2 Turbulent mixing

While the kinetic energy equation, (2.10), has a straightforward and physically sound interpretation, considering an equation for the squared magnitude of the scalar field may initially seem more arbitrary. However, beyond mere speculation about its analogies to the kinetic energy equation, further justification can be sought by exploring a physical interpretation of the equation for $\mathcal{G}$.

One property of turbulence is the enhancement of mixing of substances through the chaotic motion of the fluid. Lines of constant scalar concentration stretch and fold according to the local velocity field, thus creating patches of high concentration gradients, whose size progressively decreases (on average) until molecular diffusivity takes over and dissipates the scalar fluctuations. Accordingly, scalar mixing can be defined in terms of the dissipation rate of scalar variance fluctuations [87], tacitly establishing a link between the intuitive concepts of mixing and irreversibility. In fact, for a thermal problem, the molecular dissipation of temperature variance fluctuations can be related to the local entropy source term associated with heat conduction in the fluid. The same rational is followed here to show that the molecular dissipation rate of $\mathcal{G}$, namely $\alpha\vartheta_{,i}\vartheta_{,i}$, represents a volumetric source term for a *scalar entropy* function.

For a thermodynamic system the well-known Gibbs relationship for an isochoric (*i.e.* incompressible) transformation, $c_p \mathrm{d}T = T\mathrm{d}s$ (where s denotes the thermodynamic entropy). An analogous relationship can be written for the generic scalar field ϑ,

$$c\left(\frac{\partial\vartheta}{\partial t} + u_i\frac{\partial\vartheta}{\partial x_i}\right) = \vartheta\left(\frac{\partial\mathcal{S}}{\partial t} + u_i\frac{\partial\mathcal{S}}{\partial x_i}\right), \tag{2.17}$$

where the differentials have been expressed in Eulerian form [48], *i.e.* $\mathrm{d}(\cdot) = \frac{\partial(\cdot)}{\partial t} + u_i\frac{\partial(\cdot)}{\partial x_i}$, and $\mathcal{S}$ indicates the scalar entropy which, in case ϑ represented a temperature field, can be interpreted as the thermodynamic entropy, s. In (2.17), c is a constant coefficient that represents the analogous to the heat capacity at constant pressure for the thermal problem.

Multiplication of both sides of equation (2.17) by ϑ establishes a direct link between the evolution of $\mathcal{S}$ and $\mathcal{G}$,

$$c\left(\frac{\partial\mathcal{G}}{\partial t} + u_i\frac{\partial\mathcal{G}}{\partial x_i}\right) = 2\mathcal{G}\left(\frac{\partial\mathcal{S}}{\partial t} + u_i\frac{\partial\mathcal{S}}{\partial x_i}\right). \tag{2.18}$$

Finally, solving equation (2.17) for the material time rate of change of $\mathcal{S}$ and using (2.11) gives:

$$\frac{\partial\mathcal{S}}{\partial t} + u_i\frac{\partial\mathcal{S}}{\partial x_i} = c\alpha\frac{\partial}{\partial x_i}\left(\frac{1}{\vartheta}\frac{\partial\vartheta}{\partial x_i}\right) + \frac{c\alpha}{\vartheta^2}\frac{\partial\vartheta}{\partial x_i}\frac{\partial\vartheta}{\partial x_i}. \tag{2.19}$$

The first term on the right-hand side of (2.19) embodies the local entropy change (positive or negative) due to molecular scalar flux; the remaining term is positive-definite and thus represents the volumetric source of entropy attached to the dissipation of $\mathcal{G}$. For a thermal problem, this corresponds to the creation of thermodynamic entropy associated with molecular heat conduction [49].

Considering the derivation of equation (2.18), it is spontaneous to wonder whether an analogous equation holds for the kinetic energy $\mathcal{K}$. The starting point of such an analogy is the definition of a *mechanical entropy* function, $\mathcal{Z}$, such that,

$$\frac{\partial u_j}{\partial t} + u_i \frac{\partial u_j}{\partial x_i} = u_j \left(\frac{\partial \mathcal{Z}}{\partial t} + u_i \frac{\partial \mathcal{Z}}{\partial x_i} \right) . \tag{2.20}$$

The multiplication of both sides of (2.20) by u_j, followed by a contraction of the index j, reads:

$$\frac{\partial \mathcal{K}}{\partial t} + u_i \frac{\partial \mathcal{K}}{\partial x_i} = 2\mathcal{K} \left(\frac{\partial \mathcal{Z}}{\partial t} + u_i \frac{\partial \mathcal{Z}}{\partial x_i} \right) , \tag{2.21}$$

which is the formal equivalent of equation (2.18). Similar arguments led Yao et al. [109] to derive an alternative expression for the mechanical entropy balance at different scales of turbulent motion, suggesting possible connections with statistical mechanics and non-equilibrium thermodynamics.

The kinetic energy balance (2.10) can be substituted in (2.21) and the resulting expression can be solved for the material time rate of change of $\mathcal{Z}$; namely, this gives:

$$\frac{\partial \mathcal{Z}}{\partial t} + u_i \frac{\partial \mathcal{Z}}{\partial x_i} = \underbrace{\frac{1}{2} \frac{\partial}{\partial x_i} \left(\frac{1}{\mathcal{K}} \frac{\partial \mathcal{H}}{\partial x_i} \right)}_{\text{Local transport}} + \underbrace{\frac{1}{2\mathcal{K}^2} \frac{\partial \mathcal{H}}{\partial x_i} \frac{\partial \mathcal{K}}{\partial x_i} - \frac{\nu \omega_i \omega_i}{2\mathcal{K}}}_{\text{Production/sink}} , \tag{2.22}$$

where the gradient of $\mathcal{H}$ is defined as $\mathcal{H}_{,i} = \nu \mathcal{B}_{,i} - u_i \, (p/\rho)$. The first term on the right-hand side of (2.22) represents the local change of $\mathcal{Z}$ (positive or negative) induced by the mechanical energy flux and the pressure-related transport. On the other hand, the second term on the right-hand side of the equation is a production or sink term, which involves the product of the gradients of the local mechanical energy, the pressure and the velocity components. It is non-trivial to recover a simpler expression for this term and to prove, or to disprove, its positive definiteness. Although this matter can be of great relevance for the investigation of the energy cascade in turbulent flows (see for instance, [109]), it is out of the scope of the present work to further delve into this direction. Here, it is simply left as an observation that, starting from the quantities $\mathcal{K}$ and $\mathcal{G}$ it is possible to draw a link to the scalar and mechanical entropy functions, $\mathcal{S}$ and $\mathcal{Z}$; however, the source term of the former is directly related to the dissipation rate of $\mathcal{G}$, whereas an analogous link to the dissipation of mechanical energy is not yet clear.

2.2.3 Scalar transfer efficiency

Equations (2.9) and (2.10) represent an energetic balance for the scalar field and the kinetic energy of the system. It is reasonable to expect that, for analogous scalar and momentum transfer, the mechanical energy required to drive the flow through a system approximately equals the amount of scalar flux transferred through it. Conversely, a dissimilar momentum and scalar transfer should reflect in two sensibly different amounts of these quantities. The analogy between momentum and scalar transfer can then be measured in terms of a scalar transfer efficiency. The latter can be defined as the ratio between the net scalar flux across the boundary of the control volume and the total mechanical energy consumed within it. Denoting the control volume with $\mathcal{V}$ and its boundary with $\partial\mathcal{V}$, the scalar transfer efficiency, η, is

$$\eta = \frac{\pi_\vartheta}{\pi_M} = \left| \oint_{\partial\mathcal{V}} c\alpha \overline{\vartheta_{,i}} n_i \, \mathrm{d}\partial\mathcal{V} \right| \times \left(\int_{\mathcal{V}} \nu \overline{\omega_i \omega_i} \, \mathrm{d}\mathcal{V} \right)^{-1} , \tag{2.23}$$

where the π_ϑ and π_M are, respectively, the net scalar flux and the net mechanical power per unit density. More precisely, these are:

$$\pi_\vartheta = \left| \frac{1}{\mathcal{V}} \oint_{\partial\mathcal{V}} c\alpha \overline{\vartheta_{,i}} n_i \, \mathrm{d}\partial\mathcal{V} \right|, \tag{2.24}$$

$$\pi_M = \frac{1}{\mathcal{V}} \int_{\mathcal{V}} \nu \overline{\omega_i \omega_i} \, \mathrm{d}\mathcal{V}. \tag{2.25}$$

Note that the absolute value is used in the definition of π_ϑ to ensure positive-definite quantities in the definition of the scalar transfer efficiency (2.23).

The scalar transfer efficiency (2.23) is straightforward to interpret in case the scalar field, ϑ, represents the temperature of the fluid; in this case, the efficiency η measures the amount of thermal power exchanged at the boundaries of the control volume with respect to the total mechanical power required to drive the flow across the control volume. The actual value of the scalar transfer efficiency depends on the system under consideration and on its conditions at the boundary. For instance, in case of a scalar transfer problem, it is easy to see that, for a given amount of mechanical energy, η can be increased by increasing the temperature difference over which the heat transfer takes place. The non-dimensional form of flow variables in (2.23) clarifies this point. Assuming that the characteristic variation in the scalar energy of a system is $c\Delta\Theta_c$, and that in kinetic energy is U_c^2, the scalar transfer efficiency, (2.23), can be expressed as:

$$\eta = \frac{c\Delta\Theta_c}{U_c^2} \left| \oint_{\partial\mathcal{V}^\star} \overline{\vartheta_{,i}^\star} n_i \, \mathrm{d}\partial\mathcal{V}^\star \right| \times \left(\int_{\mathcal{V}^\star} \overline{\omega_i^\star \omega_i^\star} \, \mathrm{d}\mathcal{V}^\star \right)^{-1}, \tag{2.26}$$

where the $\star$ superscript is used to denote the normalization with the generic characteristic quantities $\Delta\Theta_c$, U_c, and L_c (the latter being a meaningful length scale of the system). From (2.26), it is evident that for a given flow, the scalar transfer efficiency value depends on the characteristic scalar and velocity changes of a specific system. However, the two terms in the parentheses in (2.26) are dimensionless and their comparison should provide information about the scalar transfer efficiency regardless of the specific boundary conditions of the problem. Hence, the ratio between these two terms is an ideal candidate to assess the momentum and scalar transfer similarities from an energetic perspective. It is convenient to define the *Reynolds analogy efficiency factor*, RA_π, as:

$$RA_\pi = \left| \oint_{\partial\mathcal{V}^\star} \overline{\vartheta_{,i}^\star} n_i \, \mathrm{d}\partial\mathcal{V}^\star \right| \times \left(\int_{\mathcal{V}^\star} \overline{\omega_i^\star \omega_i^\star} \, \mathrm{d}\mathcal{V}^\star \right)^{-1}. \tag{2.27}$$

From the knowledge of RA_π of a given flow, and of the specific operating conditions, the scalar transfer efficiency can be recovered from:

$$\eta = \frac{c\Delta\Theta_c}{U_c^2} RA_\pi. \tag{2.28}$$

The knowledge of the Reynolds analogy efficiency factor for a specific flow contains the relevant information about the structural similarity between momentum and scalar transfer. This argument is tested on channel flows and spatially developing flows in chapter 3 of the present work. In particular, a connection between RA_π and the classical Reynolds analogy factor, RA, measuring the ratio between the non-dimensional momentum and scalar wall fluxes, can be established for canonical wall bounded flows. Further, the joint analysis of RA_π with an integral balance of equation (2.13) is used to draw links between the boundary scalar fluxes and the mean bulk dissipation rate of the squared magnitude of the scalar field.

3 Theoretical applications: from wall-parallel flows to impinging jets

The vast majority of flows of practical interest are confined by one or more walls. These can be either internal flows, such as the flow inside pipes and ducts and confined impinging jets, or external flows, as the boundary layer flows that develop around the surfaces of cars, aircraft and ship hulls. In this chapter, the theoretical framework developed in chapter 2 is applied to the analysis of momentum and scalar transfer of several wall-bounded flow configurations of increasing complexity. The simplest is the case of fully developed channel flows, where flow statistics can be considered invariant in the wall-parallel directions. The presence of spatial development of the flow increases the flow complexity with significant impacts on the momentum and scalar transfer analogies. This is showcased by applying the theoretical framework to the analysis of canonical boundary layer flows, where the flow is made to develop along the streamwise direction. As last application, the analysis is applied to semi-confined impinging jets. In this case, the impingement of a circular jet determines the formation of a complex flow that is constituted by markedly different regions where momentum and scalar transfer exhibit dissimilar behaviours.

3.1 Channel flow

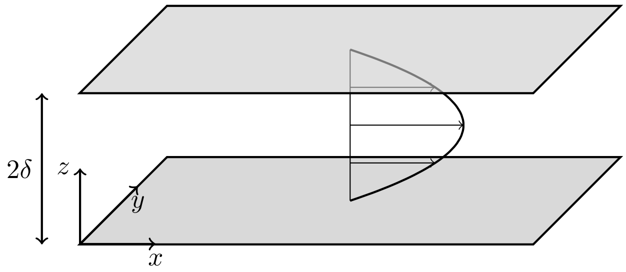

Figure 3.1: Sketch of the channel flow configuration. A parabolic profile is used to indicate the mean flow direction.

A channel flow can be thought to as being the flow inside a long duct of rectangular cross section having a high aspect ratio between its height, 2δ, and its lateral extent, b. The requirement of $2\delta/b \ll 1$ assures that, at least in the central part of the duct, the effects of the lateral walls of the duct can be discarded and the flow, in this region, becomes independent on shifts in the lateral (spanwise) direction. In this work, only *fully-developed* channel flows are considered, meaning that the flow is also invariant upon shifts in the longitudinal (streamwise) direction. In a real-world duct, this condition is usually matched sufficiently downstream of its inlet section, provided that the duct is sufficiently long.

Under these assumptions, a fully-developed channel flow can be represented as in the sketch of figure 3.1. The flow, aligned along the streamwise, $x = x_1$, direction, is confined between two plates of indefinite extension along the streamwise and spanwise ($y = x_2$) directions and varies along the wall-normal coordinate, $z = x_3$. In case of a laminar flow, an analytical solution to the equations (2.3) and (2.4) in the channel exists and is represented by a parabolic velocity profile (*Poiseuille* flow). When the flow is turbulent, the assumptions of a fully-developed channel flow are still applicable, but they must be intended in a statistical sense; the invariance of the flow in the streamwise and spanwise directions applies only to flow statistics and not to instantaneous quantities, as the latter are unsteady and three-dimensional in nature. Hence, the flow is said to be statistically homogeneous in the stream and spanwise directions.

Integrating the momentum balance (2.2) in the channel volume enables to relate the mean pressure gradient used to drive the flow, *i.e.* the external volumetric force, $\overline{f} = \overline{f}_1$, and the mean momentum flux at the channel walls,

$$\overline{f} = \frac{\tau_w}{\rho\delta}. \tag{3.1}$$

The mean momentum flux at the walls is embodied by the mean wall stress, τ_w, defined as

$$\tau_w = \frac{1}{\mathcal{A}} \int_{\mathcal{A}_w} \overline{\tau}_{ij} n_j \delta_{1i} \, \mathrm{d}\mathcal{A}_w \tag{3.2}$$

where $\mathcal{A}$ and $\mathcal{A}_w$ are, respectively, the plan area of the channel and the wetted surface of one channel wall; n_j is the jth component of the unit outward normal vector to the channel wall. Note that, for a flat, smooth channel, $\mathcal{A}_w = \mathcal{A}$ and $\tau_w = \mu\langle\overline{u}\rangle_{,z}|_w$, where the w subscript denotes quantities evaluated at the channel bottom wall, angular brackets indicate spatial averaging in the streamwise and spanwise directions, and $u = u_1$ is the streamwise velocity component. Note that, throughout this work, the following notations are used interchangeably: $u = u_1$, $v = u_2$, and $w = u_3$, and similarly for the spatial coordinates, $x = x_1$, $y = x_2$, and $z = x_3$.

The analogous to relationship (3.1) for the scalar transfer is readily obtained by integrating (2.9) in the channel volume,

$$\overline{q} = \frac{q_w}{\rho c\delta}. \tag{3.3}$$

The mean scalar flux at the walls is represented by q_w, defined as

$$q_w = \frac{1}{\mathcal{A}} \int_{\mathcal{A}_w} \rho c\alpha \, \frac{\partial\overline{\vartheta}}{\partial x_i} n_i \, \mathrm{d}\mathcal{A}_w. \tag{3.4}$$

The relationships (3.1) and (3.4) represent a static equilibrium balance: at statistically stationary conditions, a fully-developed flow is maintained upon feeding it, on average, with the amount of streamwise momentum and scalar that are lost through fluxes at the walls. As such, these relations do not enable to get further information on the connection between the flow and the mean wall fluxes. In fact, this information can be recovered for smooth-wall channels by careful integration of the spatially-averaged equation (2.4) in the wall-normal direction, as shown by Fukagata et al. [26]. The result is the *Fukagata-Iwamoto-Kasagi* (FIK) relationship, which relates the mean wall-momentum flux to a weighted integral of the Reynolds shear stress in the channel volume (with the wall-normal distance being the weight). Similarly, Hasegawa and Kasagi [37] derive an equivalent expression for the mean scalar transfer by wall-normal integration of the spatially-averaged equation (2.9).

These FIK type of relationships, though useful for investigating the turbulence contribution to the mean momentum and scalar wall fluxes apply mainly to smooth wall channels and are difficult to extend in more complex scenarios, such as rough wall channel flows. An alternative approach consists in considering the integral balances (2.12) and (2.13) in the channel volume $\mathcal{V}$. These read:

$$0 = \int_{\mathcal{V}} \overline{f u_1} \mathrm{d}\mathcal{V} + \oint_{\partial\mathcal{V}} \left(-\overline{\mathcal{B} u_i} + \nu \frac{\partial \overline{\mathcal{B}}}{\partial x_i} \right) n_i \, \mathrm{d}\partial\mathcal{V} - \int_{\mathcal{V}} \nu \overline{\omega_i \omega_i} \, \mathrm{d}\mathcal{V}, \tag{3.5}$$

$$0 = \int_{\mathcal{V}} \overline{q\vartheta} \, \mathrm{d}\mathcal{V} \; + \oint_{\partial\mathcal{V}} \left(-\overline{\mathcal{G} u_i} + \alpha \frac{\partial \overline{\mathcal{G}}}{\partial x_i} \right) n_i \, \mathrm{d}\partial\mathcal{V} - \int_{\mathcal{V}} \alpha \overline{\vartheta_{,i} \, \vartheta_{,i}} \, \mathrm{d}\mathcal{V}. \tag{3.6}$$

It is straightforward to show that the integral on the channel boundary, $\partial\mathcal{V}$, vanish. Due to the statistical homogeneity of the stream and spanwise directions, the integrals on the lateral boundaries give equal, but opposite in sign, contributions with a zero outcome on the balances (3.5) and (3.6). The convective terms, $\overline{\mathcal{B} u_i} n_i$ and $\overline{\mathcal{G} u_i} n_i$, are identically zero, provided that the channel walls are stationary and impermeable. This assumption will be considered retained throughout the present work. For the same reason, the mechanical energy flux on the two channel walls also vanishes,

$$\oint_{\partial\mathcal{V}} \nu \mathcal{B}_{,i} \, n_i \, \mathrm{d}\partial\mathcal{V} = \oint_{\partial\mathcal{V}} \nu (\mathcal{K} + (p/\rho))_{,i} \, n_i \, \mathrm{d}\partial\mathcal{V} = \oint_{\partial\mathcal{V}} \nu u_j u_{j,i} \, \mathrm{d}\partial\mathcal{V} - \oint_{\partial\mathcal{V}} \nu u_j u_{i,j} \, \mathrm{d}\partial\mathcal{V} = 0, \tag{3.7}$$

where (2.14) has been used for the pressure term. Finally, assuming homogeneous boundary conditions for ϑ at the channel walls, the flux of $\mathcal{G}$ across them is also identically zero. By further dividing the integral balances (3.5) and (3.6) by the channel volume, they can be rearranged to give:

$$\overline{f \overline{U}}_b = \overline{f} \, \overline{U}_b = \frac{1}{\mathcal{V}} \int_{\mathcal{V}} \nu \overline{\omega_i \omega_i} \, \mathrm{d}\mathcal{V}, \tag{3.8}$$

$$\overline{q \overline{\Theta}}_b = \overline{q} \overline{\Theta}_b = \frac{1}{\mathcal{V}} \int_{\mathcal{V}} \alpha \overline{\vartheta_{,i} \, \vartheta_{,i}} \, \mathrm{d}\mathcal{V}, \tag{3.9}$$

where U_b and Θ_b denote, respectively, the mean bulk velocity and scalar (*i.e.* the volume averages of the mean streamwise velocity and of the mean scalar).

The total power exerted by the flow is represented by the left-hand side of (3.8) and must balance, at statistically stationary conditions, the amount of mechanical energy that is dissipated within the channel volume. Analogously, the product of the volumetric scalar source by the mean bulk scalar realized in the flow must be in equilibrium with the bulk dissipation of $\mathcal{G}$. Differently from the integral momentum and scalar balances (3.1) and (3.4), equations (3.8) and (3.9) express a link between an integral measure, such as the total power realized by the flow, and a field quantity such as the dissipation rate fields. In addition, relationships (3.8) and (3.9) can be further specialized to establish a relationship between the wall fluxes and the bulk dissipation fields. This is shown in sections 3.1.1, 3.1.2, and 3.1.3 for different strategies through which the flow is driven in the channel.

Furthermore, equations (3.8) and (3.9) can be used in the definition of the scalar transfer efficiency (2.23). In particular, integrating equation (2.9) in the channel volume and dividing the result by the channel volume gives: $\pi_\vartheta = c\overline{q}$; moreover, taking into account equation (3.9), the net scalar power flux across the channel boundary can be expressed as:

$$\pi_\vartheta = \overline{q} c = \frac{1}{\overline{\Theta}_b} \frac{1}{\mathcal{V}} \int_{\mathcal{V}} c \alpha \overline{\vartheta_{,i} \, \vartheta_{,i}} \, \mathrm{d}\mathcal{V}. \tag{3.10}$$

On the other hand, the consumed mechanical power is simply $\pi_M = f\overline{U}_b$, and thus it is given by equation (3.8). Therefore, the scalar transfer efficiency η, defined in (2.23), becomes:

$$\eta = \frac{\pi_\vartheta}{\pi_M} = \frac{1}{\overline{\Theta}_b} \left(\int_{\mathcal{V}} c \alpha \overline{\vartheta_{,i} \, \vartheta_{,i}} \, \mathrm{d}\mathcal{V} \right) \times \left(\int_{\mathcal{V}} \nu \overline{\omega_i \omega_i} \, \mathrm{d}\mathcal{V} \right)^{-1}. \tag{3.11}$$

The latter expression shows that the scalar transfer efficiency of a channel flow can be linked to the bulk dissipation rates of the mean mechanical energy and of the mean squared scalar field. According to different flow driving strategies, different characteristic physical scales can be used to formulate the problem in non-dimensional settings. Accordingly, different expressions for the Reynolds analogy efficiency factor, RA_π, defined in equation (2.27), are obtained. This is shown in the following for the constant pressure gradient, constant flow rate, and constant power input strategies.

3.1.1 Constant pressure gradient

A common way of enforcing a flow rate in a channel is that of prescribing a constant pressure gradient (CPG) between the inlet and outlet sections of the channel. In practice, this translates into prescribing the constant forcing term f and, in turn, due to the momentum balance (3.1), the mean momentum flux. Hence, the natural velocity scale, suitable for representing the problem in dimensionless form, is the *friction velocity* $u_\tau = (\tau_w/\rho)^{\frac{1}{2}} = (f\delta)^{\frac{1}{2}}$. Using the *viscous length*, $\delta_\nu = \nu/u_\tau$, as the scaling length, the integral energy balance (3.8) becomes:

$$\overline{U}_b^+ = \frac{Re_\tau}{\mathcal{V}^+}\int_{\mathcal{V}^+} \overline{\omega_i^+\omega_i^+}\,\mathrm{d}\mathcal{V}^+, \tag{3.12}$$

where the friction Reynolds number is $Re_\tau = u_\tau\delta/\nu$ and a + superscript indicates viscous-scaled quantities (*i.e.* made dimensionless using u_τ and δ_ν).

According to the CPG driving strategy, the momentum wall flux is prescribed by the chosen mean pressure gradient that drives the flow. The momentum transfer effectiveness of the channel flow can be measured with the mean flow rate that the prescribed forcing is capable of realizing. Hence, the mean bulk velocity is a meaningful measure of the momentum transfer: the lower the mean bulk velocity is, the more effective is the momentum transfer. According to (3.12), effective momentum transfer translates into low values of the CPG units-scaled mean bulk dissipation.

A common measure of the mean momentum wall flux is the friction coefficient, defined as:

$$C_f = \frac{2\tau_w}{\rho\overline{U}_b^2} = \frac{2}{\overline{U}_b^{+2}}. \tag{3.13}$$

The higher the friction coefficient, the more effective momentum transfer is; a scenario that is realized when a small flow rate is achieved for a given driving pressure gradient or, equivalently, when the flow is not capable of realizing a large mean bulk dissipation of mechanical energy.

The strategy for forcing the scalar field, equivalent to the CPG momentum forcing, consists in prescribing a constant and uniform source term, q. Given the integral balance (3.4), this is implicitly equivalent to prescribing a wall scalar flux, q_w. In these settings, the natural choice for a scalar scale to make the problem dimensionless is the friction scalar, $\vartheta_\tau = q_w/(\rho c u_\tau) = \delta q/u_\tau$. A viscous length scale can be defined as $\delta_\alpha = \alpha/u_\tau$; the latter is related to the viscous length scale through $\delta_\alpha = \delta_\nu/Pr$, where $Pr = \nu/\alpha$ is the Prandtl number, which expresses the ratio between the momentum and scalar molecular diffusivities of the fluid. The non-dimensional form of (3.9) reads:

$$\overline{\Theta}_b^+ = \frac{Pe_\tau}{\mathcal{V}^\#}\int_{\mathcal{V}^\#} \overline{\vartheta^+{}_{,i^\#}\,\vartheta^+{}_{,i^\#}}\,\mathrm{d}\mathcal{V}^\# = \frac{Re_\tau}{Pr\mathcal{V}^+}\int_{\mathcal{V}^+} \overline{\vartheta^+{}_{,i^+}\,\vartheta^+{}_{,i^+}}\,\mathrm{d}\mathcal{V}^+, \tag{3.14}$$

where $Pe_\tau = PrRe_\tau$ is the friction Péclet number and a # superscript denotes lengths made dimensionless using δ_α.

For a prescribed wall scalar flux, the scalar transfer effectiveness can be measured in terms of the mean bulk scalar, $\overline{\Theta}_b^+$: the lower its value, the more effective is the scalar transfer. According to (3.14), a better mean scalar transfer is achieved for low values of the CPG units-scaled mean bulk dissipation of $\mathcal{G}$. Similarly to the momentum transfer, a scalar transfer coefficient can be defined as:

$$C_h = \frac{q_w}{\rho c \overline{U}_b \overline{\Theta}_b} = \frac{1}{\overline{U}_b^+ \overline{\Theta}_b^+}. \tag{3.15}$$

Note that, in case of heat transfer analysis, C_h coincides with the Stanton number. C_h measures the effectiveness of the scalar transfer for a given flow rate; scalar transfer is more effective when a low mean bulk scalar is achieved for a prescribed volumetric scalar source term or, equivalently, when the flow is not capable of dissipating $\mathcal{G}$ under prescribed scalar forcing conditions.

The degree of similarity between the mean scalar and momentum transfer in a channel flow can be measured through the Reynolds analogy factor, defined as $RA = 2C_h/C_f$. Using (3.13),(3.15), (3.12), and (3.14), the Reynolds analogy factor becomes:

$$RA = \frac{\overline{U}_b^+}{\overline{\Theta}_b^+} = Pr \left(\int_{\mathcal{V}^+} \overline{\omega_i^+ \omega_i^+} \, \mathrm{d}\mathcal{V}^+ \right) \times \left(\int_{\mathcal{V}^+} \overline{\vartheta^+{}_{,i^+} \vartheta^+{}_{,i^+}} \, \mathrm{d}\mathcal{V}^+ \right)^{-1} \tag{3.16}$$

Using the CPG scaling, the scalar transfer efficiency (3.11) becomes:

$$\eta = \frac{c\overline{\Theta}_b}{\overline{U}_b^2} Pr \left(\int_{\mathcal{V}^+} \overline{\omega_i^+ \omega_i^+} \, \mathrm{d}\mathcal{V}^+ \right) \times \left(\int_{\mathcal{V}^+} \overline{\vartheta^+{}_{,i^+} \vartheta^+{}_{,i^+}} \, \mathrm{d}\mathcal{V}^+ \right)^{-1} = \frac{c\overline{\Theta}_b}{\overline{U}_b^2} RA. \tag{3.17}$$

With the comparison between (3.17) and (2.28) it is readily realized that, for a channel flow, the classical Reynolds analogy factor, RA, coincides with the Reynolds analogy efficiency factor, RA_π, defined with equation (2.26). Hence, the Reynolds analogy factor is an indicator of the scalar transfer efficiency of a channel flow driven using the CPG framework. The same result applies also to the other two driving strategies presented in this work.

3.1.2 Constant flow rate

Another commonplace strategy for driving a flow through a channel consists in prescribing a constant flow rate (CFR). Naturally, the mean bulk velocity is a suitable velocity scale for making the problem dimensionless; using δ as scaling length, the mechanical energy balance (3.8) reads:

$$\overline{f}^* = \frac{1}{Re_b \mathcal{V}^*} \int_{\mathcal{V}^*} \overline{\omega_i^* \omega_i^*} \, \mathrm{d}\mathcal{V}^*, \tag{3.18}$$

where the bulk Reynolds number is $Re_b = \overline{U}_b \delta / \nu$ and a $*$ superscript denotes normalization based on the outer units $\overline{U}_b$ and δ.

At CFR, the momentum transfer performances are directly measured in terms of the mean momentum flux at the wall which, due to (3.1), is equivalent to the mean pressure gradient that drives the flow (in outer units, $\overline{f}^*$). A high momentum transfer corresponds to a high mean momentum flux; according to (3.18), this is achieved by maximizing the bulk dissipation of mechanical energy. From a physical perspective, for a prescribed flow rate, as the momentum transfer increases, so does the mean pressure gradient that is required to drive the flow. The friction coefficient directly embodies this fact, for it is given by:

$$C_f = 2\overline{f}^*. \tag{3.19}$$

The equivalent strategy of driving the flow at CFR for the scalar field is prescribing a constant mean bulk scalar, $\overline{\Theta}_b$. The latter is therefore the natural scale for making the scalar field dimensionless. Accordingly, the non-dimensional form of the integral balance (3.14) is:

$$\overline{q}^* = \frac{1}{Pr Re_b \mathcal{V}^*} \int_{\mathcal{V}^*} \overline{\vartheta^*{}_{,i^*}\, \vartheta^*{}_{,i^*}}\, \mathrm{d}\mathcal{V}^*, \tag{3.20}$$

where $\overline{q}^* = q\delta/(\overline{U}_b\overline{\Theta}_b)$.

At constant mean scalar conditions, high scalar transfer is achieved through high mean scalar fluxes at the wall; equivalently, this condition is realized for low values of the mean scalar source and, therefore, of the mean bulk dissipation of $\mathcal{G}$, as stated by equation (3.20). In terms of the scalar coefficient, high scalar transfer rates reflect as high values of C_h, given that:

$$C_h = \overline{q}^*. \tag{3.21}$$

The Reynolds analogy factor, for the CFR case, becomes:

$$RA = \frac{\overline{q}^*}{\overline{f}^*} = \frac{1}{Pr}\left(\int_{\mathcal{V}^*} \overline{\vartheta^*{}_{,i^*}\, \vartheta^*{}_{,i^*}}\, \mathrm{d}\mathcal{V}^*\right) \times \left(\int_{\mathcal{V}^*} \overline{\omega_i^*\omega_i^*}\, \mathrm{d}\mathcal{V}^*\right)^{-1} \tag{3.22}$$

Using the CFR scaling, the scalar transfer efficiency (3.11) becomes:

$$\eta = \frac{c\overline{\Theta}_b}{\overline{U}_b^2}\frac{1}{Pr}\left(\int_{\mathcal{V}^*} \overline{\vartheta^*{}_{,i^*}\, \vartheta^*{}_{,i^*}}\, \mathrm{d}\mathcal{V}^*\right) \times \left(\int_{\mathcal{V}^*} \overline{\omega_i^*\omega_i^*}\, \mathrm{d}\mathcal{V}^*\right)^{-1} = \frac{c\overline{\Theta}_b}{\overline{U}_b^2} RA. \tag{3.23}$$

Hence, similarly to the CPG case, the Reynolds analogy factor expresses the scalar transfer efficiency of the channel flow driven at constant flow rate and it coincides with the Reynolds analogy efficiency factor, RA_π.

3.1.3 Constant power input

A third possibility consists in driving the flow by providing it with a constant power input (CPI). This amounts to prescribing, on average, the mechanical power per unit density:

$$\pi_M = \frac{1}{\mathcal{V}}\int_{\mathcal{V}} \overline{fu}\, \mathrm{d}\mathcal{V} = \frac{1}{\mathcal{V}}\int_{\mathcal{V}} \nu\overline{\omega_i\omega_i}\, \mathrm{d}\mathcal{V}. \tag{3.24}$$

CPI can be realized in different ways. For instance, Hasegawa et al. [38] introduce CPI channel flow simulations in the context of flow control for skin friction drag reduction. In particular, they define a velocity scale that corresponds to the bulk velocity achieved in a laminar channel for a given pumping power. Normalization of equations (2.3) and (2.4) with the thus defined velocity scale and δ leads to their similar form with the resulting Reynolds number expressing the prescribed power input.

In the present work, CPI is achieved in an alternative fashion, without relating the velocity scale to the laminar solution in the channel. The latter is well-defined for a smooth wall channel, but it is not, in general, otherwise. The integral balance (3.24) shows that, at CPI, the volume averaged dissipation rate must be prescribed. Hence, CPI can be enforced by fixing the mean dissipation rate of mechanical energy. It is natural to define a characteristic frequency scale based on $\overline{\omega_i\omega_i}$; namely:

$$\Omega = \left(\frac{1}{\mathcal{V}}\int_{\mathcal{V}} \overline{\omega_i\omega_i}\, \mathrm{d}\mathcal{V}\right)^{\frac{1}{2}}, \tag{3.25}$$

which, together with ν, allows the definition of the velocity scale, $u_\Omega = (\nu\Omega)^{1/2}$, and the length scale, $\delta_\Omega = (\nu/\Omega)^{1/2}$.

Assuming the volumetric forcing, f, to be uniform in the channel volume (but variable in time), the balance (3.24) becomes:

$$\pi_M = \overline{fU_b} = \nu\Omega^2 = \frac{u_\Omega^3}{\delta_\Omega}. \tag{3.26}$$

Further, independently on the forcing strategy, $\overline{f} = u_\tau^2/\delta$ must be always satisfied; consequently,

$$\overline{f}\,\overline{U_b} = \frac{u_\tau^3}{\delta}\overline{U_b^+} = \pi_M. \tag{3.27}$$

In other words, the covariance of the driving force and bulk velocity temporal fluctuations must be identically zero, $\overline{f'U_b'} = 0$ (a prime superscript indicates fluctuations with respect to the mean in time). Thus, combining (3.26), (3.27) and using (3.1), the prescribed power input becomes:

$$\pi_M = \overline{fU_b} = \overline{f}\,\overline{U_b} = \frac{\tau_w}{\rho\delta}\overline{U_b} = \frac{u_\Omega^3}{\delta_\Omega}. \tag{3.28}$$

The latter equation can be solved for the mean momentum wall flux as a function of the mean bulk velocity. The result can be inserted in the definition of the friction coefficient, (3.13), to give:

$$C_f = \frac{2Re_\Omega}{\overline{U_b}^{\Omega 3}}, \tag{3.29}$$

where $Re_\Omega = u_\Omega\delta/\nu$ represents the ratio between the half-channel height and δ_Ω; namely, $Re_\Omega = \delta/\delta_\Omega$. Further, normalization based on u_Ω and δ_Ω is denoted by a Ω superscript.

At CPI, the product of the mean momentum flux and the mean bulk velocity is a prescribed constant. Hence, high momentum transfer, *i.e.* high momentum flux, is achieved for small values of the mean bulk velocity; a relationship that is clearly embodied by the friction coefficient in (3.29), which shows that C_f increases as the mean bulk velocity decreases.

The analogous approach to CPI for driving the scalar problem is achieved by fixing the volume averaged mean dissipation of the squared-scalar field, $\mathcal{G}$, which is,

$$\frac{1}{\mathcal{V}}\int_{\mathcal{V}} \overline{q\vartheta}\,\mathrm{d}\mathcal{V} = \frac{1}{\mathcal{V}}\int_{\mathcal{V}} \alpha\overline{\vartheta_{,i}\,\vartheta_{,i}}\,\mathrm{d}\mathcal{V}. \tag{3.30}$$

This is equivalent to prescribing the quantity:

$$\Xi = \left(\frac{1}{\mathcal{V}}\int_{\mathcal{V}} \overline{\vartheta_{,i}\,\vartheta_{,i}}\right)^{\frac{1}{2}}, \tag{3.31}$$

which has the physical units of the scalar per unit length. Jointly with α and u_Ω, it can be used to form a length scale, $\delta_\Xi = \alpha/u_\Omega$, and a scalar scale, $\vartheta_\Xi = \delta_\Xi\Xi$.

For a uniform-in-space, but non-constant in time, volumetric source, the integral balance (3.30) becomes

$$\overline{q\Theta_b} = \alpha\Xi^2 = \frac{\vartheta_\Xi^2 u_\Omega}{\delta_\Omega}. \tag{3.32}$$

Regardless of the forcing strategy, the mean volumetric source must be $\overline{q} = \vartheta_\tau u_\tau/\delta$, and so,

$$\overline{q}\,\overline{\Theta_b} = \frac{\vartheta_\tau^2 u_\tau}{\delta}\overline{\Theta_b^+} = \alpha\Xi^2 = \overline{q\Theta_b}. \tag{3.33}$$

Given the inverse proportionality between $\overline{q}$ and $\overline{\Theta}_b$, scalar transfer (*i.e.* $\overline{q}$) is particularly effective when a low mean bulk scalar is realized. This fact is well represented by the scalar transfer coefficient,

$$C_h = \frac{PrRe_\Omega}{\overline{U}_b^{\Omega}\,\overline{\Theta}_b^{\Xi\,2}}, \tag{3.34}$$

which shows that, for the CPI-established flow rate, the mean scalar transfer increases as lower values of the mean bulk scalar are achieved.

Expressions (3.29) and (3.34) can be used to evaluate the Reynolds analogy factor,

$$RA = \frac{2Ch}{C_f} = Pr\left(\frac{\overline{U}_b^{\Omega}}{\overline{\Theta}_b^{\Xi}}\right)^2 . \tag{3.35}$$

Similarly to the CPG strategy, the dissimilarity between the mean momentum and scalar transfer in the channel can be measured as a ratio between the mean bulk velocity and scalar.

The CPI scaling can also be used to express the scalar transfer efficiency, (3.11). This becomes:

$$\eta = \frac{c\overline{\Theta}_b}{\overline{U}_b^2}Pr\left(\frac{\overline{U}_b^{\Omega}}{\overline{\Theta}_b^{\Xi}}\right)^2 = \frac{c\overline{\Theta}_b}{\overline{U}_b^2}RA, \tag{3.36}$$

thus showing, even for the CPI case, that the classical Reynolds analogy factor, RA, coincides with the Reynolds analogy efficiency factor, RA_π, for a channel flow.

At CPG, momentum and scalar transfer performances can be measured in terms of the mean bulk velocity and scalar realized in the flow. These are directly related to the volume averages of the mean dissipation rates of the square magnitudes of momentum and scalar. At CFR, similarly, the performances of momentum and scalar transfer are measured in terms of the mean driving force and volumetric source, which are linked to the volume averages of the dissipation fields. At CPI, the latter are prescribed and the momentum and scalar transfer performances can be measured either in terms of the mean bulk velocity and scalar, or by considering the mean momentum and scalar fluxes. In either case, these quantities contain the same information, for their product is proportional to the prescribed mean dissipation rate in the channel.

These considerations suggest that the assessment the dissipation rates can be instrumental for the understanding of dissimilar momentum and scalar transfer. In particular, it could be expected that local variations from similar dissipation rates can inform about flow mechanisms that induce a net dissimilar momentum and scalar transfer. This scenario is showcased on smooth and rough wall channel flow in section (5.1).

3.2 Boundary layers

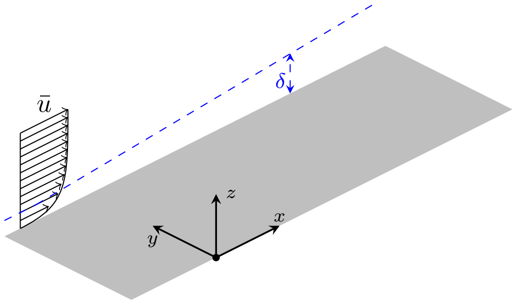

Figure 3.2: Sketch of the boundary layer configuration. A blue dashed line depicts the mean boundary layer thickness, δ.

Boundary layers describe the portion of a flow in which the convection of streamwise momentum is mainly balanced by its molecular diffusion across a thin region of space. Of particular interest are boundary layers that develop along solid walls, as is the case for the flow developing around the wings of an aircraft or on the hull of a ship. In practical applications, the Reynolds number of the flow is high, so that the balancing between momentum convection and diffusion occurs within a very narrow region close to the wall. Within the thickness of this layer, vorticity is produced by the action of the wall friction and it is convected downstream, without abandoning the boundary layer thickness. Hence, if the upstream flow is irrotational, it remains so at a sufficient distance from the wall; this region, where the velocity field is determined (up to a constant) by the gradient of a potential function, is named *outer flow*. According to the boundary layer theory, the streamwise development of the outer flow completely determines the streamwise pressure gradient within the boundary layer, where pressure propagates unchanged in the wall normal direction [78].

Naturally, a scalar field injected in the flow develops a boundary layer in the wall vicinity, where the convection of the scalar is balanced by its molecular diffusion, mainly in the wall normal direction. For a unit Prandtl number and in the absence of an outer pressure gradient, the scalar and momentum boundary layers are expected to be similar. The Reynolds analogy factor can be defined as the ratio between the mean friction and scalar flux coefficients, C_f and C_h, in a similar fashion as for a channel flow; namely, $RA = 2C_f/C_h$. However, here it is emphasized that, differently from a fully-developed channel, the momentum and scalar wall fluxes, respectively τ_w and q_w, are functions of the streamwise location, as they change with the flow development along the wall.

In particular, the action of friction at the wall forces the flow to slow down; in consequence to a streamwise decrease of the wall parallel velocity, u, at a given wall distance, the incompressibility constraint determines the formation of a wall normal velocity component, w, which carries low-streamwise momentum and scalar farther away from the wall and determines the thickening of the momentum and scalar boundary layer thicknesses. Here it is assumed that the velocity field and the passive-scalar field satisfy analogous boundary conditions at the wall and in the outer, free stream, flow. As a result, the mean velocity and scalar gradients at the wall decrease with the streamwise distance, thus determining a decrease in the mean momentum and scalar fluxes.

An integral momentum balance across the boundary layer thickness can be used to relate the mean momentum wall flux, τ_w, to the streamwise rate of change of momentum and to the action of the mean streamwise pressure gradient. The result is usually expressed in terms of the well-known von Kármán integral momentum equation,

$$\frac{\tau_w}{\rho u_\infty^2} = \frac{\mathrm{d}\delta_2}{\mathrm{d}x} + u_\infty \frac{\mathrm{d}u_\infty}{\mathrm{d}x}\left(\delta_1 + 2\delta_2\right), \tag{3.37}$$

where u_∞ is the free stream outer velocity, and δ_1 and δ_2 denote, respectively, the displacement and momentum thicknesses [78]. Note that in (3.37), Bernoulli's equation has been used to relate the streamwise pressure gradient to the free-stream velocity; namely $\frac{\mathrm{d}p}{\mathrm{d}x} = -u_\infty \frac{\mathrm{d}u_\infty}{\mathrm{d}x}$.

Equation (3.37) can be rearranged to explicitly relate the wall momentum flux to the streamwise rate of change of mechanical energy $\mathcal{B}$. To this end, the time-averaged momentum equation (2.4) is rewritten in the form,

$$\frac{\partial \overline{\mathcal{B}}}{\partial x_i} = \overline{\mathcal{L}}_i + \nu \frac{\partial \overline{u}_i}{\partial x_j \partial x_j}, \tag{3.38}$$

where $\mathcal{L}_i = \epsilon_{mni} u_m \omega_n$ denotes the ith component of the Lamb vector. The wall normal integration of the streamwise component of (3.38) leads, upon neglecting the streamwise molecular diffusion of momentum, to the integral momentum equation:

$$\frac{\tau_w}{\rho} = \frac{\mathrm{d}}{\mathrm{d}x}\int_0^\infty \overline{\mathcal{B}}\,\mathrm{d}z - \int_0^\infty \overline{\mathcal{L}}_1, \tag{3.39}$$

with $\overline{\mathcal{L}}_1 = \overline{v\omega_z} - \overline{w\omega_y}$. In view of (3.39), the wall stress balances the streamwise rate of change of mechanical energy and the transport of vorticity due to the wall normal and spanwise velocity components. For instance, in a steady state laminar boundary layer, the Lamb vector reduces to $\mathcal{L}_1 = -w\omega_y = -wu_{,z}$ and the second integral on the right-hand side of (3.39) represents the stress that results from the wall normal convection of streamwise momentum.

The scalar analogous of the integral equation (3.37), or equivalently (3.39), is obtained by integrating the time-averaged equation (2.9) in the wall normal direction and neglecting the streamwise and spanwise scalar molecular diffusion. The result reads [78]:

$$\frac{q_w}{\rho c} = \frac{\mathrm{d}}{\mathrm{d}x}\left(u_\infty \vartheta_\infty \delta_2^\vartheta\right) = \frac{\mathrm{d}}{\mathrm{d}x}\left[u_\infty \vartheta_\infty \int_0^\infty \left(\frac{\overline{u}}{u_\infty} - \frac{\overline{u\vartheta}}{u_\infty \vartheta_\infty}\right)\right]\mathrm{d}z, \tag{3.40}$$

where ϑ_∞ denotes the scalar value in the outer flow region and δ_2^ϑ is the scalar energy thickness, which is the analogous to the momentum thickness, δ_2.

Equations (3.39) and (3.40) can be used to relate the wall momentum and scalar fluxes to the transport of mechanical energy, streamwise momentum and scalar field in the boundary layer thickness and are, therefore, a natural option for assessing the local analogy between the momentum and the scalar transfer in terms of the classical Reynolds analogy factor, RA. Nevertheless, unlike in the fully developed channel flow case, the classical Reynolds analogy factor is not necessarily representative of the scalar transfer efficiency of the boundary layer flow. While the mean scalar flux at the wall is representative of the net scalar energy transfer through the system, it is not straightforward to establish a relationship between the mean momentum wall flux and the mechanical energy consumed by the flow. In order to determine the scalar transfer efficiency in terms of the Reynolds analogy efficiency factor, (2.27), an analysis on the energetics of the system is required.

Such an assessment can be accomplished with an integral analysis of equations (2.12) and (2.13), upon setting to zero the external volumetric forcing and source terms, f_i and q. In the following, it is assumed that the scalar field satisfies analogous wall boundary conditions to the velocity field, *i.e.* that $\vartheta_w = 0$. The wall normal integration of equations (2.12) and (2.13) leads to the following balances:

$$\frac{\mathrm{d}}{\mathrm{d}x}\int_0^\infty \left(\overline{u}\mathcal{B}_\infty - \overline{u\mathcal{B}}\right)\,\mathrm{d}z = \int_0^\infty \nu\overline{\omega_i\omega_i}, \tag{3.41}$$

$$\frac{\mathrm{d}}{\mathrm{d}x}\int_0^\infty \left(\overline{u}\mathcal{G}_\infty - \overline{u\mathcal{G}}\right)\,\mathrm{d}z = \int_0^\infty \alpha\overline{\vartheta_{,i}\,\vartheta_{,i}}. \tag{3.42}$$

Equations (3.41) and (3.42) show that the net streamwise loss in the mean mechanical power and mean squared-scalar magnitude, which occur due to the momentum and scalar transfer at the wall, balances the integral dissipation rates.

The application of (3.41) and (3.42) to a control volume of finite streamwise size helps in clarifying the analysis. To this end, a boundary layer over a smooth wall is considered and (3.41) and (3.42) are further integrated in the streamwise direction from the leading edge of the flat plate, at $x = 0$, up to an arbitrary distance from it,

$$\underbrace{\int_0^\infty u_\infty\mathcal{B}_\infty\,\mathrm{d}z}_{\Pi_{IN}} - \underbrace{\left(\int_0^\infty \overline{u\mathcal{B}}\,\mathrm{d}z + \int_0^x w_\infty\mathcal{B}_\infty\,\mathrm{d}x\right)}_{\Pi_{OU}} = \int_0^x\int_0^\infty \nu\overline{\omega_i\omega_i}\,\mathrm{d}z\,\mathrm{d}x, \tag{3.43}$$

$$\underbrace{\int_0^\infty u_\infty\mathcal{G}_\infty\,\mathrm{d}z}_{\Pi_{IN}^{\mathcal{G}}} - \underbrace{\left(\int_0^\infty \overline{u\mathcal{G}}\,\mathrm{d}z + \int_0^x w_\infty\mathcal{G}_\infty\,\mathrm{d}x\right)}_{\Pi_{OU}^{\mathcal{G}}} = \int_0^x\int_0^\infty \alpha\overline{\vartheta_{,i}\,\vartheta_{,i}}\,\mathrm{d}z\,\mathrm{d}x, \tag{3.44}$$

where the incompressibility constraint has been used to replace the streamwise rate of change of the wall normal integral of $\overline{u}$ with the wall normal velocity at infinity, w_∞. Note that (3.43) and (3.44) express the integral mean mechanical energy and squared-scalar field across the control volume depicted in figure 3.3.

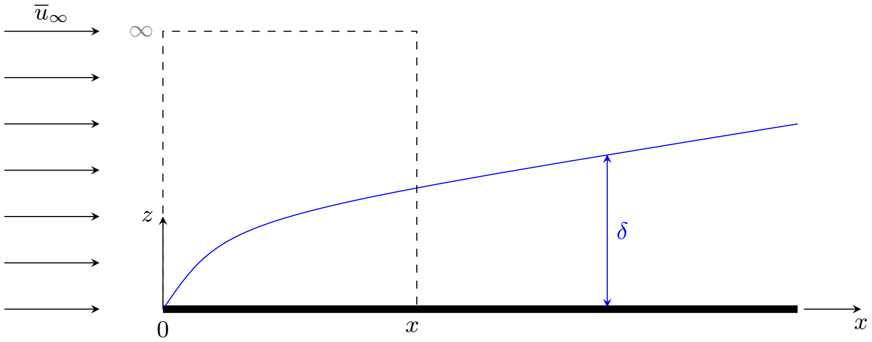

Figure 3.3: Flat plate boundary layer. A black dashed line indicates the control volume used for the analysis of the mean mechanical energy and squared-scalar field. A blue line depicts the mean boundary layer thickness, δ.

Π_{IN} and $\Pi_{IN}^{\mathcal{G}}$ represent the mean mechanical energy and squared-scalar carried by the flow at the input of the control volume; conversely, Π_{OU} and $\Pi_{OU}^{\mathcal{G}}$ are the output mean mechanical energy and squared-scalar across the top and downstream surfaces of the control volume. The net difference between inputs and outputs amounts to the bulk dissipation of $\overline{\mathcal{B}}$ and $\overline{\mathcal{G}}$ that occurs due to the mean wall momentum and scalar fluxes. The no slip boundary condition for the velocity at the wall determines the generation of vorticity which diffuses and is transported within the boundary layer, with the consequent increase in dissipated mechanical energy; similarly, the scalar flux at the wall determines the diffusion and convection of the scalar flux across the boundary layer, thus determining an increase in the dissipation of the squared-scalar field.

Equations (3.43) and (3.44) provide a means for assessing the integral analogy between the mean mechanical energy and mean squared-scalar field evolution along the boundary layer. Equation (3.43) links the mean mechanical power lost by the flow in traversing the control volume to the mean dissipation rate, $\nu\overline{\omega_i\omega_i}$, thus providing a suitable means for relating the mean mechanical energy consumption with flow features. An analogous link between the net scalar wall flux, Π^{ϑ}_{IN}, and the dissipation field of the mean squared scalar field is however less straightforward to find. Note that the net scalar wall flux is defined as:

$$\Pi^{\vartheta}_{IN} = \int_0^x q_w\,\mathrm{d}x = \int_0^x \rho c\alpha\overline{\vartheta_{,z}}\big|_w\,\mathrm{d}x. \tag{3.45}$$

The link between Π^{ϑ}_{IN} and the bulk dissipation on the right-hand side of (3.44) can be found considering the passive-scalar field $\varphi = \vartheta_\infty - \vartheta$ and half of its squared magnitude, $\mathcal{G}^{\varphi} = \varphi^2/2$. Thanks to the linearity of the scalar problem, φ satisfies (2.9) and, consequently, $\mathcal{G}^{\varphi}$ satisfies an unsteady advection-diffusion equation as (2.11), with the dissipation rate $\alpha\varphi_{,i}\,\varphi_{,i}$. It is further assumed for the outer scalar, ϑ_∞, to be constant and uniform, so that its gradient is identically zero and $\alpha\vartheta_{,i}\,\vartheta_{,i} = \alpha\varphi_{,i}\,\varphi_{,i}$. Due to the homogeneus wall boundary condition of ϑ, the scalar field φ satisfies $\varphi_w = \vartheta_\infty$ at the wall; in the far-field, the scalar field φ is $\varphi_\infty = 0$.

Integrating the governing equation for $\overline{\mathcal{G}^{\varphi}}$ over the control volume of figure 3.3 gives:

$$\underbrace{-\int_0^x \alpha\varphi_w\overline{\varphi_{,z}}\,\mathrm{d}x}_{\Pi^{\mathcal{G}^{\varphi}}_{IN}} \underbrace{-\int_0^\infty \overline{u\mathcal{G}^{\varphi}}\,\mathrm{d}z}_{\Pi^{\mathcal{G}^{\varphi}}_{OU}} = \int_0^x\int_0^\infty \alpha\overline{\varphi_{,i}\,\varphi_{,i}}\,\mathrm{d}z\,\mathrm{d}x = \int_0^x\int_0^\infty \alpha\overline{\vartheta_{,i}\,\vartheta_{,i}}\,\mathrm{d}z\,\mathrm{d}x, \tag{3.46}$$

where $\Pi^{\mathcal{G}^{\varphi}}_{IN} = \varphi_w\Pi^{\vartheta}_{IN}/(\rho c) = \vartheta_\infty\Pi^{\vartheta}_{IN}/(\rho c)$, since $\varphi_{,z} = -\vartheta_{,z}$ and the scalar at the wall, $\varphi_w = \vartheta_\infty$ is prescribed. Clearly, (3.46) establishes a link between the scalar power transferred at the wall and the dissipation of either $\overline{\mathcal{G}}$ or $\overline{\mathcal{G}^{\varphi}}$.

The scalar transfer efficiency (2.23) can be applied to the boundary layer flow. In order to assess the local scalar transfer efficiency, its evaluation is performed over the control volume in figure 3.3. In this case, the total mechanical power consumed within the control volume is

$$\pi_M = \frac{\Pi_{IN} - \Pi_{OU}}{\mathcal{V}} = \frac{1}{\mathcal{V}}\oint_{\partial\mathcal{V}} \overline{\mathcal{B}u_i}n_i\,\mathrm{d}\partial\mathcal{V} = \frac{1}{\mathcal{V}}\int_{\mathcal{V}} \nu\overline{\omega_i\omega_i}\,\mathrm{d}\mathcal{V}, \tag{3.47}$$

where $\mathcal{V}$ denotes the volume of the control volume and $\partial\mathcal{V}$ is its boundary. Assuming negligible molecular scalar fluxes across the vertical faces of the control volume, the net scalar scalar flux transferred across the boundary of the control volume reduces to the scalar flux across the bottom wall, namely,

$$\pi_\vartheta = \left|\frac{1}{\mathcal{V}}\oint_{\partial\mathcal{V}} c\alpha\overline{\vartheta_{,i}}n_i\,\mathrm{d}\partial\mathcal{V}\right| \approx \frac{\Pi^{\vartheta}_{IN}}{\rho\mathcal{V}}. \tag{3.48}$$

Therefore, the scalar transfer efficiency can be evaluated as:

$$\eta = \frac{\pi_\vartheta}{\pi_M} = \left(\frac{\Pi^{\vartheta}_{IN}}{\rho}\right) \times \left(\int_{\mathcal{V}} \nu\overline{\omega_i\omega_i}\,\mathrm{d}\mathcal{V}\right)^{-1}. \tag{3.49}$$

Further, the first term on the right-hand side of equation (3.49) can be related to the integral balance of $\overline{\mathcal{G}^{\varphi}}$ over the control volume, as it stems from equation (3.46). This leads to the following expression for the scalar transfer efficiency:

$$\eta = \frac{c}{\vartheta_\infty}\left(\oint_{\partial\mathcal{V}} \overline{\mathcal{G}^{\varphi}u_i}n_i\,\mathrm{d}\partial\mathcal{V} + \int_{\mathcal{V}} \alpha\overline{\varphi_{,i}\,\varphi_{,i}}\right) \times \left(\int_{\mathcal{V}} \nu\overline{\omega_i\omega_i}\,\mathrm{d}\mathcal{V}\right)^{-1}. \tag{3.50}$$

The latter expression shows that, unlike the channel flow case, whereby the efficiency depends only on the bulk dissipation rates of mechanical energy and of the squared-scalar field, for the boundary layer case, the scalar transfer efficiency depends also on the convection of the squared-scalar field. For a low concentration fluid flowing over a high-concentration wall, the efficiency increases as the convection of the squared concentration magnitude transported by the fluid increases, for a fixed amount of dissipated mechanical energy.

The expressions (3.49) and (3.50) can be rewritten upon using the non-dimensional form of the flow variables,

$$\eta = \frac{c\vartheta_\infty}{u_\infty^2}\frac{1}{Pr}\left(\oint_{\partial\mathcal{V}^*}\overline{\vartheta^*{}_{,i}}n_i\,\mathrm{d}\partial\mathcal{V}^*\right)\times\left(\int_{\mathcal{V}^*}\overline{\omega_i^*\omega_i^*}\,\mathrm{d}\mathcal{V}^*\right)^{-1}, \tag{3.51}$$

or, equivalently,

$$\eta = \frac{c\vartheta_\infty}{u_\infty^2}\frac{1}{Pr}\left(\oint_{\partial\mathcal{V}^*}\overline{\mathcal{G}^{\vartheta*}u_i^*}n_i\,\mathrm{d}\partial\mathcal{V}^* + \int_{\mathcal{V}^*}\overline{\varphi_{,i}^*\,\varphi_{,i}^*}\,\mathrm{d}\mathcal{V}^*\right)\times\left(\int_{\mathcal{V}^*}\overline{\omega_i^*\omega_i^*}\,\mathrm{d}\mathcal{V}^*\right)^{-1}, \tag{3.52}$$

where the $*$ superscript denotes a non-dimensional quantity.

Comparing the last two expressions with equation (2.28), suggests that the Reynolds analogy efficiency factor for a boundary layer flow can be computed as:

$$RA_\pi = \frac{1}{Pr}\left(\oint_{\partial\mathcal{V}^*}\overline{\vartheta^*{}_{,i}}n_i\,\mathrm{d}\partial\mathcal{V}^*\right)\times\left(\int_{\mathcal{V}^*}\overline{\omega_i^*\omega_i^*}\,\mathrm{d}\mathcal{V}^*\right)^{-1} = \tag{3.53}$$

$$= \frac{1}{Pr}\left(\oint_{\partial\mathcal{V}^*}\overline{\mathcal{G}^{\varphi*}u_i^*}n_i\,\mathrm{d}\partial\mathcal{V}^* + \int_{\mathcal{V}^*}\overline{\varphi_{,i}^*\,\varphi_{,i}^*}\,\mathrm{d}\mathcal{V}^*\right)\times\left(\int_{\mathcal{V}^*}\overline{\omega_i^*\omega_i^*}\,\mathrm{d}\mathcal{V}^*\right)^{-1}. \tag{3.54}$$

While for a fully developed channel flow $RA_\pi = RA$, the same is not true for a boundary layer flow, whereby RA_π can be considered as a generalization of the classical Reynolds analogy factor, enabling the assessment of the scalar transfer efficiency of the system. In fact, a direct relationship between the momentum wall flux and the bulk dissipation cannot be established based on the integral mechanical energy balance, as it is done for the fully-developed channel flow case, *i.e.* through equation (3.8). Nevertheless, based on physical arguments, the mean mechanical energy dissipated within a thin slice of flow in the wall normal direction should amount to the product of the mean wall stress and the mean bulk velocity through the boundary layer at the considered streamwise location. In practice, this leads to the following balance:

$$\frac{\tau_w}{\rho\delta}\int_0^\delta \overline{u}\,\mathrm{d}z \sim \int_0^\delta \nu\overline{\omega_i\omega_i}\,\mathrm{d}z, \tag{3.55}$$

where δ is a suitable measure of the boundary layer thickness that ensures the convergence of the dissipation rate integral on the right-hand side of the equation. From the last expression, the friction coefficient can be deduced to be:

$$C_f \approx \frac{2\delta}{u_\infty^3(\delta-\delta_1)}\int_0^\infty \nu\overline{\omega_i\omega_i}\,\mathrm{d}z. \tag{3.56}$$

Although not exact, equation (3.56) provides a relationship between the wall friction and the bulk mechanical energy dissipation, thus enabling the comparison between RA_π and the classical Reynolds analogy factor, RA. In fact, for a narrow control volume of infinitesimal width $\Delta x \to 0$ centered at position x, the scalar transfer efficiency (3.51) reduces, using equation (3.56), to

$$\eta = \frac{c\vartheta_\infty}{u_\infty^2}RA_\pi = \frac{c\vartheta_\infty}{u_\infty^2}\frac{\delta}{\delta-\delta_1}RA. \tag{3.57}$$

From the last expression, it follows that:

$$RA_\pi = \frac{\delta}{\delta-\delta_1}RA. \tag{3.58}$$

The last equation establishes a link between the scalar transfer efficiency and the classical Reynolds analogy factor. The expression shows that, for a negligibly small displacement thickness, relatively to the boundary layer thickness, the two definitions of the Reynolds analogy factors become equivalent. When this is not the case, RA_π becomes larger than RA, due to the fact that the displacement thickness is expected to be smaller than the thickness δ. Hence, for a smooth wall boundary layer, for which $RA \approx 1$ (as it is shown in section 5.2), the Reynolds analogy efficiency factor, RA_π is expected to be larger than one, indicating that the net scalar flux exchanged at the wall exceeds the amount of mechanical energy dissipated across the boundary layer thickness over the same region.

Using analogous arguments as those used for the derivation of (3.56), an expression relating the scalar transfer coefficient, C_h, and the bulk dissipation of the squared-scalar field is found to be:

$$C_h \approx \frac{\delta^\vartheta}{u_\infty \vartheta_\infty^2 (\delta^\vartheta - \delta_1^\vartheta)} \int_0^\infty \alpha \overline{\vartheta_{,i}\, \vartheta_{,i}}\, \mathrm{d}z, \tag{3.59}$$

where δ^ϑ is a suitable height spanning the scalar boundary layer thickness and δ_1^ϑ is the scalar analogous to the displacement thickness, defined as

$$\delta_1^\vartheta = \int_0^\infty \left(1 - \frac{\vartheta}{\vartheta_\infty}\right) \mathrm{d}z. \tag{3.60}$$

The validity of (3.56) and (3.59) is tested on direct numerical simulation data of smooth and rough wall boundary layers in section 5.2 of the present work, where the scalar transfer efficiency of the system is also assessed in terms of the Reynolds analogy factors, RA and RA_π, thus providing a comparison between the classical Reynolds analogy approach and the energetic framework presented in this work.

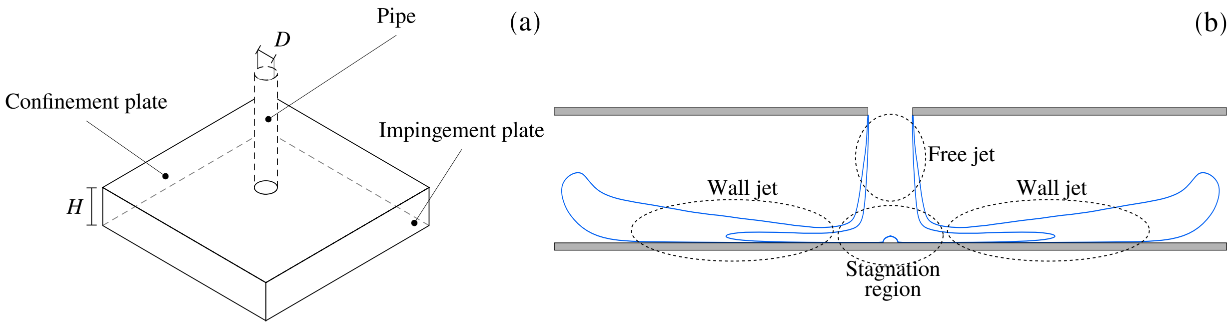

Figure 3.4: Impinging jet: geometrical configuration, (a); mean flow regions, (b). The figure has been adapted from [85].

3.3 Impinging jets

Jet impingement is realized by directing a jet flow against a solid wall. The configuration of interest in the present study is shown in figure 3.4a; in particular, a fully-developed turbulent pipe flow, with diameter D, is used to generate a jet that impinges orthogonally onto a solid plate located at a distance H from the nozzle. Further, the configuration under investigation includes a confinement plate located at the same height as the nozzle exit section. The top plate avoids the entrainment of flow from the far outside and mimics engineering applications that target the scalar transfer in closed environment (*e.g.* cooling systems of electric circuitry or inside turbine blades [9]). As displayed in figure 3.4b, the mean flow realized by jet impingement can be categorized in markedly different regions. For a sufficient separation between the nozzle and the target plate, a *free jet* region can be observed, where the flow behaves akin to a turbulent jet expanding in an unconfined environment. As the flow approaches the impingement plate, its deflection takes place through the action of an adverse pressure gradient. This part of the flow is usually referred to as *stagnation region*. The deflected flow is made to accelerate radially along the impingement plate and to develop as a *wall jet*. The latter is a wall-bounded flow that is generated by injecting high-momentum fluid through a narrow gap and letting it to develop between a solid wall and quiescent fluid [52]. As such, the flow develops an inner boundary layer, due to the presence of the wall, and an outer free-shear boundary layer with the still fluid.

Momentum and scalar transfer along the impingement plate can be quantified through the mean radial distributions of the momentum and scalar fluxes,

$$\tau_w = \frac{1}{2\pi r} \int_{\mathscr{L}_w} \overline{\tau}_{ij} n_j \hat{r}_i \, \mathrm{d}\mathscr{L}_w, \tag{3.61}$$

$$q_w = \frac{1}{2\pi r} \int_{\mathscr{L}_w} \rho c \alpha \, \overline{\vartheta_{,i}} n_i \, \mathrm{d}\mathscr{L}_w, \tag{3.62}$$

where r denotes the radial distance from the jet axis, $\hat{r}_i$ is the ith component of the unit radial vector, and $\mathscr{L}_w(r)$ is a closed circumferential contour that follows the target plate geometry; for a smooth-wall plate, $\mathscr{L}_w(r)$ coincides with the circumference of radius r centred at the intersection of the jet axis with the impingement plate. Angular brackets denote the spatial averaging operator in the circumferential direction, implicitly defined in equations (3.61) and (3.62).

The mean momentum and scalar wall fluxes can be made non-dimensional to define the mean friction and scalar coefficients, respectively,

$$C_f = \frac{2\tau_w}{\rho \overline{U}_b^2}, \tag{3.63}$$

$$C_h = \frac{q_w}{\rho c \Delta\Theta \overline{U}_b}, \tag{3.64}$$

where $\overline{U}_b$ indicates the mean bulk velocity in the pipe flow issuing the jet, and $\Delta\Theta = \vartheta_w - \vartheta_J$ denotes the prescribed scalar difference between the impingement plate scalar, ϑ_w, and the jet scalar, ϑ_J. In this study it is assumed that $\Delta\Theta > 0$ and that the issuing jet and the confinement plate have the same prescribed scalar value, ϑ_J. In case of a heat transfer analysis, this scenario corresponds to the case in which a cold jet at thermal equilibrium with the confinement plate impinges on a warm plate.

The radial distributions of C_f and C_h are known to present several differences along the impingement plate and, correspondingly, the impinging jet is considered to be a classical case in which the Reynolds analogy does not hold [9, 74, 103] (*i.e.* mean momentum and scalar transfer are dissimilar along the target plate). In the stagnation region, the departure from the analogy favours the scalar wall flux compared to the momentum wall flux. In this region, the presence of a solid wall is felt on the incoming flow predominantly through the action of the pressure gradient, which constitutes the main factor in changing the fluid's momentum and to redirect it along the wall parallel direction. The wall shear stress becomes correspondingly vanishing small for $r \to 0$. At the same time, the pressure does not actively influence the scalar exchange over the same region, and the mean scalar wall flux, (3.62), is usually maximum in this region [14, 85, 103].

As the flow develops downstream in the wall jet, the mean momentum and scalar wall fluxes are expected to become similar to each other and to follow a radial decrease that can be predicted from the classical boundary layer theory (see section 3.2). At a sufficiently long distance from the stagnation region, it is assumed that the mean radial pressure gradient is small enough so that the transport of the radial momentum over a distance r is balanced by its wall normal diffusion across the boundary layer thickness, δ_m. The latter can be identified as the wall normal distance at which the mean radial velocity profile reaches its maximum, $\overline{u}_m$, at the considered radial location. The flow rate conservation reflects in a decreasing mean bulk radial velocity, $\overline{u}_b = \left(\int_{\mathcal{A}_L} \overline{u_r}\, \mathrm{d}\mathcal{A}_L\right)/\mathcal{A}_L$, as $\overline{u}_b \sim u_0/r$, with u_0 being a suitable constant ($\mathcal{A}_L$ indicates a cylindrical circular surface with radius r and whose axis coincides with the jet axis). It is legitimate to assume for the maxima of the mean radial velocity profiles, $\overline{u}_m$, to also decrease in the same fashion along the radial direction. As a result of these assumptions, an order-of-magnitude analysis of (2.4) yields the following estimation for the velocity boundary layer thickness:

$$\frac{\delta_m}{r} \sim \left(\frac{\nu}{u_0}\right)^{\frac{1}{2}}, \tag{3.65}$$

suggesting a linear increase of the velocity boundary layer thickness with the radial distance from the jet axis.

A similar estimation can be performed for the scalar boundary layer thickness, δ_m^{ϑ}. The latter is defined, analogously to δ_m, to be the wall normal distance at which the mean scalar profile reaches its maximum (or minimum, depending on the actual scalar boundary conditions), ϑ_m, at the considered radial location. Unlike the mean radial velocity maxima, the outer scalar scale, ϑ_m, is not constrained from mass conservation to decrease as $\sim 1/r$; in fact, it can be assumed to increase, or to decrease, depending on whether the flow is accumulating or losing its mean scalar concentration moving away from the jet axis. For instance, for a

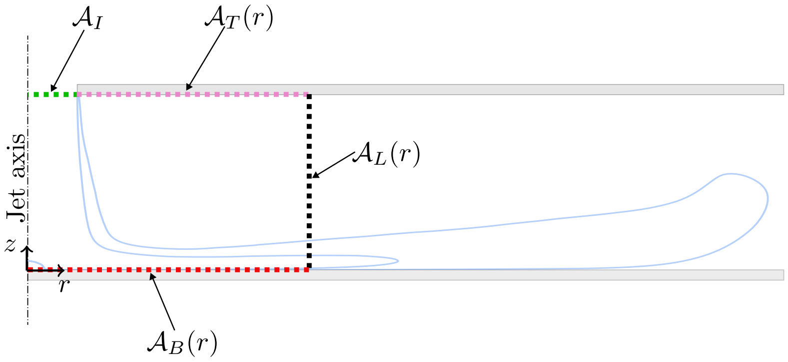

Figure 3.5: Two-dimensional sketch of the control volume used for the impinging jet analysis.

cold jet impinging on a warm plate, it can be expected that the mean temperature of the fluid increases for increasing the radial distance due to the continuous heat exchange at the impingement plate.

The order-of-magnitude analysis of (2.9) leads to the estimation of the scalar boundary layer thickness to be,

$$\frac{\delta_m^\vartheta}{r} \sim \left(\frac{\alpha}{u_0}\right)^{\frac{1}{2}}. \tag{3.66}$$

According to (3.65) and (3.66), the velocity and scalar boundary layer thicknesses should grow linearly with the radial distance and, for a unit Prandtl number, their thickness should be approximately comparable.

The above assumptions, together with the estimates (3.65) and (3.66), can be used to predict the radial development of the mean momentum and scalar wall fluxes (3.61) and (3.62); namely,

$$\frac{\tau_w}{\rho} = \nu \left.\frac{\partial\langle\overline{u_r}\rangle}{\partial z}\right|_{z=0} \sim \frac{1}{r^2}, \tag{3.67}$$

$$\frac{q_w}{\rho c} = \alpha \left.\frac{\partial\langle\overline{\vartheta}\rangle}{\partial z}\right|_{z=0} \sim \frac{1}{r}. \tag{3.68}$$

The same functional dependence on the radial distance is also foreseen for the mean momentum and scalar transfer coefficients (3.63) and (3.64), given that the reference quantities used to make the wall fluxes non-dimensional are constants. Thus, the Reynolds analogy factor increases linearly with the radial distance, $RA = 2C_h/C_f \sim r$, hence predicting a more favourable scalar transfer in comparison to the momentum transfer in the wall jet region of the flow. It is emphasized that this departure from analogy is entirely related to the radial decrease of the outer velocity scale, as $\overline{u_m} \sim u_0/r$, imposed by mass conservation.

Similarly to the canonical boundary layers, as presented in section 3.2, the assessment of the analogy between momentum and scalar transfer through the the mean wall fluxes is limited, at best. Impinging jets usually target the scalar transfer at the impingement plate; in this respect, the mean scalar flux, (3.62), provides information about the local scalar flux exchanged at the impingement plate. In contrast, the mean momentum flux, (3.61), is not informative regarding the mechanical power that is necessary to drive the flow through the system. This information can be retrieved from an integral analysis of equations (2.12) and (2.13).

To this end, the control volume depicted in figure 3.5 is considered in the following. In particular, the analysis considers cylindrical control volumes, $\mathcal{V}(r)$, centred on the jet axis and with a circular cross section of radius r. The lateral surface is denoted by $\mathcal{A}_L$, while the bottom surface, which lies on the impingement plate, is $\mathcal{A}_B$. The top surface lies on the same plane as the nozzle exit section and the confinement plate and is divided into $\mathcal{A}_I$, which coincides with the nozzle exit section, and the remaining par, $\mathcal{A}_T$.

Integration of (2.12) and (2.13) (with $f_j = 0$ and $q = 0$) in the control volume $\mathcal{V}$ results in the following integral balances:

$$0 = \underbrace{-\int_{\mathcal{A}_I} \overline{\mathcal{B}u_z}\,\mathrm{d}\mathcal{A}_I}_{\Pi_{IN}} \underbrace{-\int_{\mathcal{A}_L} \overline{\mathcal{B}u_r}\,\mathrm{d}\mathcal{A}_L}_{\Pi_{OU}} + \underbrace{\oint_{\partial\mathcal{V}} \nu\overline{\mathcal{B}_{,i}}n_i\,\mathrm{d}\partial\mathcal{V}}_{\mathcal{D}} \underbrace{-\int_{\mathcal{V}} \nu\overline{\omega_i\omega_i}\,\mathrm{d}\mathcal{V}}_{\mathcal{E}}, \tag{3.69}$$

$$0 = \underbrace{-\int_{\mathcal{A}_I} \overline{\mathcal{G}u_z}\,\mathrm{d}\mathcal{A}_I}_{\Pi^{\mathcal{G}}_{IN}} \underbrace{-\int_{\mathcal{A}_L} \overline{\mathcal{G}u_r}\,\mathrm{d}\mathcal{A}_L}_{\Pi^{\mathcal{G}}_{OU}} + \underbrace{\oint_{\partial\mathcal{V}} \alpha\overline{\mathcal{G}_{,i}}n_i\,\mathrm{d}\partial\mathcal{V}}_{\mathcal{D}^{\mathcal{G}}} \underbrace{-\int_{\mathcal{V}} \alpha\overline{\vartheta_{,i}\,\vartheta_i}\,\mathrm{d}\mathcal{V}}_{\mathcal{E}^{\mathcal{G}}}, \tag{3.70}$$

where $\partial\mathcal{V}$ denotes the boundary of the control volume $\mathcal{V}$.

At the inlet section, the inflow conditions are assumed to be prescribed. Thus, Π_{IN} and $\Pi^{\mathcal{G}}_{IN}$ correspond to the prescribed mechanical power and squared-scalar entering the system. On the other hand, Π_{OU} and $\Pi^{\mathcal{G}}_{OU}$ indicate the amount of mechanical power and squared-scalar that are convected away from the control volume lateral surface. Their difference with respect to the inflow conditions amounts to the mechanical power and squared-scalar that are lost through molecular diffusion at the boundaries, $\mathcal{D}$ and $\mathcal{D}^{\mathcal{G}}$, and through viscous dissipation in the bulk of the flow, $\mathcal{E}$ and $\mathcal{E}^{\mathcal{G}}$.

The molecular diffusion of mechanical energy does not necessarily vanish over the closed boundary $\partial\mathcal{V}$, but numerical results presented in section 5.3 indicate that its contribution can be neglected in comparison with the other terms in the balance. Hence, the mean mechanical energy balance (3.69) reduces to $\Pi_{IN} - \Pi_{OU} = \mathcal{E}$, enabling the assessment of the consumed mechanical energy in terms of the mean mechanical energy dissipation. Measuring the efficiency of scalar transfer at the impingement plate can be achieved by comparing the amount of exchanged scalar power, $\Pi^{\vartheta}_{IN} = -\int_{\mathcal{A}_B} \rho c\,\alpha\overline{\vartheta_{,z}}\,\mathrm{d}\mathcal{A}_B$, and $\mathcal{E}$. Note that the negative sign in the definition of Π^{ϑ}_{IN} is introduced assuming a negative mean scalar gradient at the impoingement plate (*i.e.* the flow adsorbs scalar concentration at the wall). As (3.69) links the consumed mechanical power to the dissipation rate of mechanical energy, a similar relationship is delivered by (3.70) between Π^{ϑ}_{IN} and the mean dissipation rate of the squared-scalar magnitude. The exchanged scalar flux appears in the balance (3.70) through the molecular diffusion of $\mathcal{G}$ at the impingement plate. More precisely,

$$\int_{\mathcal{A}_B} \alpha\overline{\mathcal{G}_{,i}}n_i\,\mathrm{d}\mathcal{A}_B = -\int_{\mathcal{A}_B} \alpha\vartheta_w\overline{\vartheta_{,z}}\,\mathrm{d}\mathcal{A}_B = \frac{\vartheta_w}{\rho c}\Pi^{\vartheta}_{IN}. \tag{3.71}$$

The relationship between Π^{ϑ}_{IN} and $\mathcal{E}^{\mathcal{G}}$ depends on the actual boundary conditions for the scalar field, which determine the flux of scalar energy in the system. In the numerical results presented in section 5.3, the focus is on the case in which $\vartheta_w = 1$ and $\vartheta_J = 0$; in case ϑ represented the fluid temperature, this scenario mimics a cold jet impinging on a warm, constant temperature, wall and, as such, is representative of a cooling system. Under these boundary conditions for the scalar, the integral balance (3.70) becomes $\vartheta_w\Pi^{\vartheta}_{IN}/(\rho c) - \Pi^{\mathcal{G}}_{OU} = \mathcal{E}^{\mathcal{G}}$. A relationship that, similarly to the mean balance of mechanical energy, links the scalar power exchanged at the impingement plate to the mean dissipation rate of the squared-scalar field.

The scalar transfer efficiency, (2.23), is applied to the impinging jet configuration using the control volume, $\mathcal{V}$, depicted in figure 5.3. The net scalar flux, π_ϑ, across the control volume boundary, $\partial\mathcal{V}$, accounts for the scalar transfer at the impingement and the confinement plates, namely,

$$\pi_\vartheta = \frac{1}{\mathcal{V}}\left(-\int_{\mathcal{A}_B} c\alpha\,\overline{\vartheta_{,z}}\,\mathrm{d}\mathcal{A}_B + \int_{\mathcal{A}_T} c\alpha\,\overline{\vartheta_{,z}}\,\mathrm{d}\mathcal{A}_T\right). \tag{3.72}$$

It can be expected that the scalar transfer at the target impingement plate exceeds significantly the net scalar flux through the confinement plate. As it is shown in section 5.3.6, this is true for control volumes of relatively small radius. In this case, the net scalar flux, (3.72), reduces to:

$$\pi_\vartheta \approx -\frac{1}{\mathcal{V}} \int_{\mathcal{A}_B} c\alpha \overline{\vartheta_{,z}} \, \mathrm{d}\mathcal{A}_B = \frac{\Pi_{IN}^{\vartheta}}{\rho \mathcal{V}}. \tag{3.73}$$

From the integral mechanical energy balance, equation (3.69), the mechanical energy consumption per unit volume is given by:

$$\pi_M = \frac{\mathcal{E}}{\mathcal{V}} = \frac{1}{\mathcal{V}} \int_{\mathcal{V}} \nu \overline{\omega_i \omega_i} \, \mathrm{d}\mathcal{V}. \tag{3.74}$$

Based on the definition in equation (2.23), the scalar transfer efficiency for the impinging jet configuration can be computed as:

$$\eta = \frac{\pi_\vartheta}{\pi_M} = \left(-\int_{\mathcal{A}_B} c\alpha \, \overline{\vartheta_{,z}} \, \mathrm{d}\mathcal{A}_B + \int_{\mathcal{A}_T} c\alpha \, \overline{\vartheta_{,z}} \, \mathrm{d}\mathcal{A}_T \right) \times \left(\int_{\mathcal{V}} \nu \overline{\omega_i \omega_i} \, \mathrm{d}\mathcal{V} \right)^{-1}. \tag{3.75}$$

Expressing the flow variables in (3.75) in dimensionless form allows to write the scalar transfer efficiency in the form of equation (2.28), where the Reynolds analogy efficiency factor for the impinging jet flow is given by:

$$RA_\pi = \frac{1}{Pr} \left(-\int_{\mathcal{A}_B^*} \overline{\vartheta^*{}_{,z^*}} \, \mathrm{d}\mathcal{A}_B^* + \int_{\mathcal{A}_T^*} \overline{\vartheta^*{}_{,z^*}} \, \mathrm{d}\mathcal{A}_T^* \right) \times \left(\int_{\mathcal{V}^*} \overline{\omega_i^* \omega_i^*} \, \mathrm{d}\mathcal{V}^* \right)^{-1}. \tag{3.76}$$

According to (3.73), for control volumes of small radii, RA_π can be approximated by accounting only the non-dimensional scalar flux through the impingement plate; namely,

$$RA_\pi \approx \frac{1}{Pr} \left(-\int_{\mathcal{A}_B^*} \overline{\vartheta^*{}_{,z^*}} \, \mathrm{d}\mathcal{A}_B^* \right) \times \left(\int_{\mathcal{V}^*} \overline{\omega_i^* \omega_i^*} \, \mathrm{d}\mathcal{V}^* \right)^{-1}. \tag{3.77}$$

Unlike for the fully developed channel flow and for the boundary layer cases, presented in sections 3.1 and 3.2, a direct relationship between RA_π and the classical Reynolds analogy factor, RA, cannot be found for the impinging jet. First of all, the net scalar flux across the system boundary involves the contributions from both the impingement and the confinement plates. Hence, the Reynolds analogy factor should contain information about the momentum and scalar fluxes across both walls. Further, even in case one considered only the momentum and scalar fluxes though the impingement plate, an explicit relationship between the mechanical energy consumption and the mean momentum wall flux cannot be determined in this case. As a result, the classical Reynolds analogy factor is of little use for the assessment of the energetic scalar transfer performances of the system. In contrast, this information can be ascertained from the Reynolds analogy efficiency factor (3.76), as it is shown in section 5.3 using direct numerical simulation data of turbulent jets impinging on smooth and rough plates.

4 Numerical methods for data generation

In this study, the theoretical framework presented in chapter 2 is investigated on the flow configurations of chapter 3. The analysis requires the assessment of the flow in great detail and the evaluation of quantities, such as the dissipation fields $\nu\omega_i\omega_i$ and $\alpha\vartheta_{,i}\,\vartheta_{,i}$, in the bulk of the flow and over a wide range of space and time scales. All of this information is not retrievable from an experiment, even using the most sophisticated equipment currently available. Neither is it imaginable that such detailed experiments will be possible in the near future, especially considering the wide variety of flow conditions that are considered here, spanning from fully-developed channel flow, to impinging jets. While experiments remain an invaluable tool for scientific investigations, nowadays numerical simulations have become a well-established alternative for the investigation of turbulent flows.

In a direct numerical simulation (DNS), the governing equations (2.3) and (2.4) are discretized in space over a computational domain and are numerically integrated in time, starting from a specified initial condition. Provided that suitable boundary conditions are given to the problem and that the space and time resolution are sufficient to resolve all the relevant scales of motion, the results obtained using a DNS should provide a complete description of the simulated flow. In fact, a DNS can be thought to as being a digital experiment, which, differently from a real-world experiment, enables to access any flow detail, in principle. The main limitation of a DNS is the high computational cost associated with the resolution requirements, especially when turbulent flows are investigated. This fact constrains drastically the span of Reynolds numbers achievable using DNSs, which, in most cases, fall well behind the Reynolds numbers typical of applications of engineering interest. For this reason, DNSs remain a research tool that, together with experiments, can be used to understand the physical mechanisms at play in a turbulent flow.

There exist several strategies for the space discretization of equations (2.3) and (2.4). In the present study, two different methods, based on a spectral representation of the solution, are used and are briefly summarized in this chapter.

4.1 Spectral element method

The spectral element method used in the present investigation is based on the method proposed by Patera [62] and is implemented in the flow solver `Nek5000`[20]. The governing equations (2.3) and (2.4) are written in weak form according to the classical Galerkin formalism, common to finite element methods. Namely, the equations are multiplied by suitable test functions and the resulting equations are integrated over the entire flow domain. The resulting variational formulation of the problem is an integral equivalent of the strong formulation (2.3) and (2.4) which enables to reduce the regularity requirements on the solution.

The computational domain is discretised into E hexahedral elements with contiguous faces on which the solution is required to be continuous. On each element, the spatial discretization of the weak equations occurs by approximating the solution and test function spaces with the finite-dimensional space spanned by Lagrange polynomials of degree N based on Gauss-Legendre-Lobatto (GLL) nodes in the unit cubic element $[-1,\,1]^3$. For the simulations presented in this study, the same polynomial degree is used for the pressure and velocity spaces, *i.e.* a $\mathrm{P}_N - \mathrm{P}_N$ formulation is used. Gaussian quadrature on GLL nodes is used to approximate the integrals arising from the weak formulation of the problem and to assemble the discretised system of equations. This procedure grants a great flexibility in terms of mesh deformation and it allows the treatment of complex geometries using body-fitted meshes. As it will be further detailed in section 4.3.2, this fact is conveniently exploited in the present study to resolve surface roughness into the simulations.

Time advancement of the discretized system of equations is performed semi-implicitly using a third-order backward differencing and extrapolation scheme. More specifically, the advective non-linear terms of the discretised momentum equation are extrapolated using a third-order extrapolation scheme, whereas the viscous terms are implicitly advanced using a third-order backward differencing formula. An operator splitting technique is employed to decouple the pressure and velocity computation. As a result, at each time-step the problem is split into solving one pressure Poisson equation and a Helmholtz system for each velocity component. Once the velocity field has been computed, an additional Helmholtz system, arising from the discretization of (2.9), has to be solved for each simulated passive-scalar field.

4.2 Pseudo spectral method

A pseudo spectral method is used in this study to perform the DNS of turbulent boundary layers presented in section 5.2. The method implemented in the flow solver `SIMSON` [11]. The governing equations (2.3) and (2.4) are re-arranged in the wall normal velocity wall normal vorticity formulation. In practice, instead of discretizing equation (2.4) for the three velocity components, two equations, one for the wall normal velocity component and one for the wall normal vorticity component, are considered instead. It can be shown that, once these two equations are solver, upon complementing them with suitable boundary conditions, the remaining velocity components can be recovered from the incompressibility constraint, (2.3), and the definition of the wall normal vorticity component. In essence, the problem in primitive variables, *i.e.* using the three velocity components, or in the wall normal velocity-vorticity formulation are two equivalent approaches.

Time advancement is performed using a semi-implicit scheme which uses a third-order, three-stages, Runge-Kutta method. The spatial discretization of the governing equations is performed by expanding the flow variables in Fourier series in the wall parallel directions, thereby assuming the periodicity of the solution in these directions. Due to the wall presence, the wall normal direction cannot be periodic; hence, in the wall normal direction the equations are discretized using Chebyshev polynomials. Naturally, the assumption of periodicity in the streamwise direction is not compatible with a boundary layer flow, whereby the flow develops moving downstream. To enable the simulation of spatially developing flow, the solver implements a fringe method to enforce the periodicity on the solution. In practice, a volumetric forcing is applied within a fringe region, near the outlet of the computational domain, which is tuned to rescale the solution to its conditions at the inlet. More specifically, the volumetric forcing, f_i, is set to $f_i = \gamma(x)(\mathcal{U}_i - u_i)$, where $\gamma(x)$ is the fringe function, which is non-negative and different from zero only in the fringe region; $\mathcal{U}_i$ is the target velocity field, which blends to the inlet velocity field at the outlet section of the computational domain.

At the inlet section of the domain, the velocity is set equal to the Blasius solution of the boundary layer, whose displacement thickness, δ_{1IN}, is used as the characteristic length scale to make the problem dimensionless. Tripping is applied downstream of the inlet to trigger turbulence; this requires a sufficient streamwise length for the development of the disturbances into a turbulence downstream of the tripping region. Further details about the actual computational domain used in this study are presented in section

5.2. On the top surface of the computational domain, which represents a plane in the free stream outer flow, the velocity field is prescribed to match the free-stream velocity, u_∞, in the streamwise direction and allowed to have transpiration in the wall-normal direction.

4.3 Surface roughness representation

4.3.1 Immersed boundary method

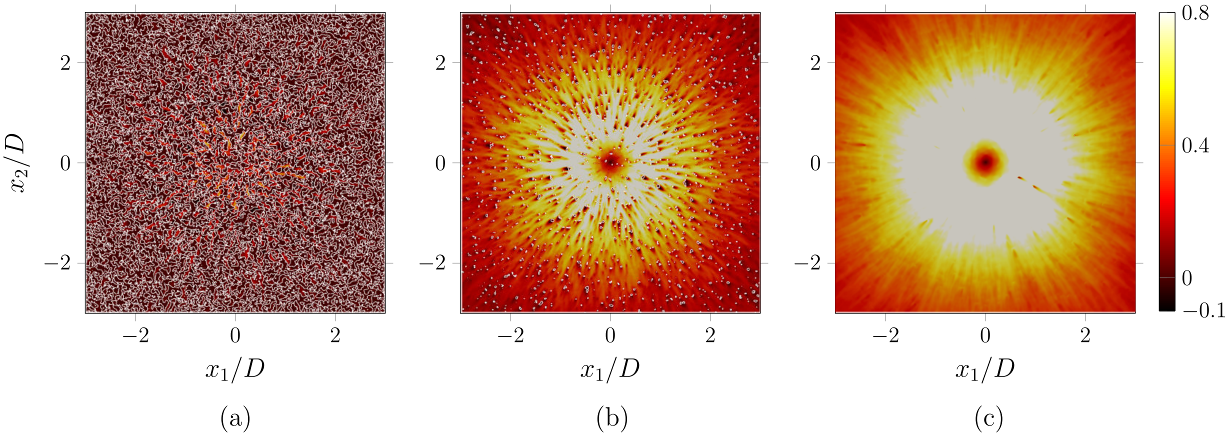

(a) (b) (c)

Figure 4.1: IBM-resolved surface roughness in the impinging jet configuration of Secchi et al. [81]. The figure shows colour maps of the time averaged radial velocity component at different wall-normal heights. (a) $z = 0.05D$; (b) $z = 0.07D$; (c) $z = 0.09D$. The figure has been adapted from [81].

Resolving the roughness topography in the simulations is a non-trivial task due to the high irregularity of its geometry and the multitude of length scales that characterize its in-plane distribution. To address this challenge, *immersed boundary methods* (IBM) are a viable approach that enable the enforcement of velocity boundary conditions on complex surfaces without requiring body-conforming grids. With IBM, flow boundaries are fully immersed within a computational grid, independently on the actual grid node locations. Boundary conditions are imposed using various techniques specific to the chosen method [47, 57].

For a broad class of IBM, no-slip boundary conditions on impermeable surfaces are enforced through a volume force field distributed along the boundary. For rigid boundaries, a widely adopted approach is the method introduced by [29], where the volume force acts as the control input of a closed-loop system designed to maintain the boundary velocity at a prescribed value. Specifically, the force at each boundary point is updated at each time step based on the local velocity error and its time integral, forming a proportional-integral (PI) control scheme. While this method requires the specification of two model constants for the proportional (P) and integral (I) terms, it has proven effective in various scenarios. [29] and [30] applied it to DNS of two-dimensional flow around a cylinder and three-dimensional fully developed turbulent channel flows over riblets.

According to [29], a volume force field, f_i^{IBM}, is added to the right-hand side of equation 2.4. At a stationary immersed boundary, the force field is specified by:

$$f_i^{IBM} = -\alpha_{IB} \int_0^t u_i, \mathrm{d}t' - \beta_{IB} u_i, \qquad i = 1,\, 2,\, 3, \tag{4.1}$$

where α_{IB} and β_{IB} denote the integral and proportional constants. The proportional term aims at damping local velocity fluctuations with respect to the local prescribed boundary velocity (in this case zero, since the boundary is stationary), whereas the integral term is necessary to achieve a zero steady state error between the enforced velocity and the prescribed one.

The volumetric forcing in (4.1) has to be applied at a selected number of Lagrangian control points located on the boundary surface. In accordance with IBM principles, these discrete boundary points do not need to coincide with computational grid nodes. Discrete delta functions are then used to link the boundary and fluid regions, spreading forces from the Lagrangian markers to neighbouring grid nodes. This inevitably results in a non-sharp fluid-solid interface, where the thickness of the diffused interface layer depends on the support of the chosen discrete delta function. Furthermore, applying this approach to non-uniform computational grids adds significant complexity [67].

To circumvent these discretization challenges, some IBM implementations with volume forcing avoid the use of discrete delta functions altogether, instead prescribing a momentum sink term, in the form of (4.1), at every grid node within the boundary volume. However, this simplification comes at a significant cost: it only permits a staircase-like resolution of surface boundaries, limiting the method's accuracy [33, 51].

Nevertheless, IBM employing this forcing strategy has been used for DNS of fully developed turbulent channel flows over homogeneous [24, 108] and heterogeneous [89] surface roughness. The application of the method to three-dimensional turbulent developing flows over homogeneous rough surfaces has also been reported in the literature. For instance, von Deyn et al. [98] use a similar approach to investigate surface roughness in turbulent boundary layers. In the context of spectral element methods, Weber et al. [102] show that such a simple implementation of the Goldstein IBM delivers accurate results in terms of quantities that are averaged in space over sufficiently large window, thus limiting its applicability to flows featuring at least one statistically homogeneous direction. A similar outcome is observed in the analysis of Secchi et al. [80] and Secchi et al. [81] where a similar implementation of this IBM is used to resolve surface roughness topographies in the DNS of turbulent impinging jets. In particular, selected results from the latter two investigations are discussed in detail in section 5.4. Further, the same IBM approach is used to resolve surface roughness in the boundary layer DNS presented in section 5.2.

4.3.2 Mesh deformation

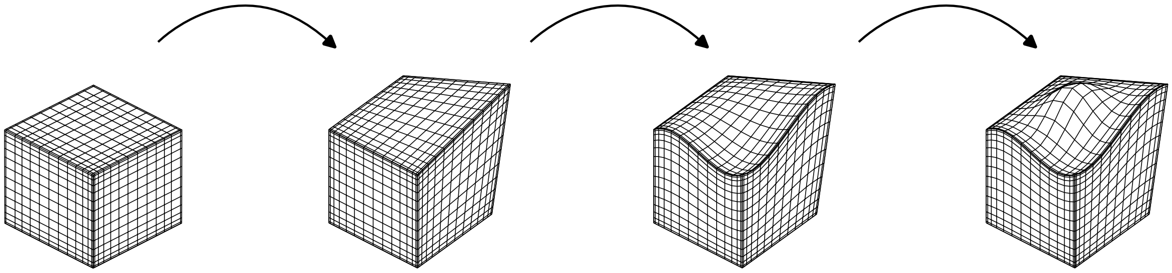

Figure 4.2: Successive transformations applied to a single element following the Gordon-Hall procedure [31]. Figure adapted from [16].

One advantage of spectral element methods is that they can be applied in a straightforward manner to complex geometries, a character that they share in common with finite element methods. The flow domain is discretized into E elements, to which a deformation can be applied to adapt to the boundary's geometry. Assembling the stiffness and mass matrices, arising from the discretization of the weak problem, requires

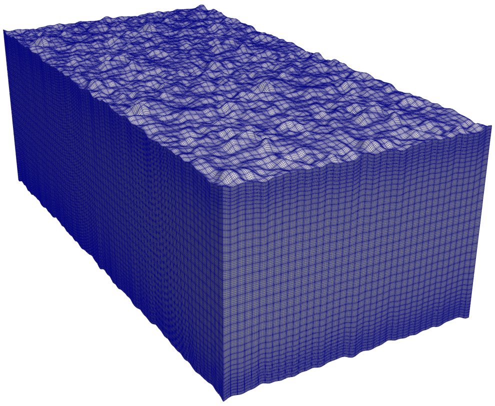

Figure 4.3: Spectral element mesh for a channel flow configuration deformed according to the roughness topographies at the bottom and top walls of the channel.

the knowledge of the function that maps any point of the deformed element to a point that belongs to the unit cubic element, $[-1,\,1]^3$. This feature can be conveniently exploited to resolve surface roughness into the simulations. Naturally, the roughness in-plane distribution cannot be completely arbitrary: the requirement is that a transformation, mapping the deformed elements to the unit cubic element, with a non-vanishing Jacobian can be found. In particular this requires the vertex angles of each element to be bounded away from 0 and π. Hence, some regularity requirements are imposed on the types of surface roughness that can be resolved in the simulations.

As discussed in detail by Deville et al. [16], the geometry of the element is represented on the reference cubic element by using the same polynomial representation as the one used for the solution within the spectral element framework. The nodal values of the geometrical transformation of the element into the reference one are determined using the Gordon-Hall procedure [31]. In practice, three successive transformations are applied to determine a correspondence between the deformed and the reference elements according to the prescribed nodal values distributions of the deformed element. A first transformation takes the reference element and maps it to a deformed one having the same vertices as the prescribed one. A trilinear interpolation is used for the other nodes of the element. The second and third transformations take into account, respectively, the edge and surface information. The successive application of these transformations is clarified in figure 4.2. Note that this procedure can be stopped at any of the three successive transformations depending on the desired degree of approximation of the surface. The polynomial representation of the geometrical mapping allows to easily compute the Jacobian of the transformation and any spatial derivatives that arise in the computation of the stiffness and mass matrices of the discretized problem.

The application of mesh deformation in the spectral element flow solver `Nek5000`[20] is used in the work of Secchi et al. [82] and Secchi et al. [83] to resolve surface roughness in the DNS of turbulent impinging jets, and by Secchi et al. [86] to simulate turbulent flows in rough wall channel flows. The results of these studies are discussed in detail in sections 5.1 and 5.4.2 of the present work. For all the considered cases, surface roughness is represented by an in-plane random distribution of the roughness wall height, $z_w = z_w(x, y)$, where x and y indicate the wall-parallel coordinates. The mesh deformation is applied during the simulation initialization on a non-deformed Cartesian grid. In particular, the wall normal coordinate of each grid point on the bottom plane of the computational box is transformed to match the roughness height at the considered in-plane location. Grid points at higher wall normal distances are accordingly displaced following a linear transformation that vanishes at a sufficiently large distance from the wall. For the rough wall channel flow in [86], the zero-displacement plane occurs at $z = \delta$ and the z-coordinate transformation continues linearly in the top half of the channel, so that the two rough walls are symmetrically deformed with respect to the plane $z = \delta$. The result of the mesh deformation is shown in figure 4.3. For the rough wall impinging jets in [82, 83] the zero-displacement plane is set at $z = D$, and the coordinates of grid points at higher wall normal distances are left unchanged. Hence, the configuration has a rough wall impingement plate and a smooth wall confinement plate.

5 Direct numerical simulation results

This chapter uses DNS data to perform momentum and scalar transfer analysis of the flow configurations presented in chapter 3. The data have been generated using the methods presented in chapter 4. The first configuration consists in fully developed turbulent channel flows with smooth and rough walls. As shown in chapter 3, in this case the classical Reynolds analogy factor is representative of the scalar transfer efficiency of the system. This fact is used to link the roughness-induced departures from an analogous momentum and scalar transfer to the time-averaged dissipation fields of the mean mechanical energy and the squared-scalar field.

Flow development in the streamwise direction is introduced by considering canonical turbulent boundary layers subject to a zero-pressure gradient. The flow development introduces a marked difference with respect to the fully developed channel flows. The classical Reynolds analogy, which still embodies the analogy between the local mean momentum and scalar wall fluxes, is no more representative of the local scalar transfer efficiency of the flow. The DNS data are used to confirm this observation for a smooth and a rough wall boundary layer. For the rough wall case, the investigated roughness topography has a large characteristics size in comparison to the boundary layer thickness. Although this characteristic prevents the generalization of the present results to canonical rough wall boundary layers, the investigated settings are similar to those encountered in the boundary layers that develop near the stagnation region of impinging jets.

The latter, which are the most complex flow configuration investigated in the present study, are characterized by very thin boundary layers in the near impingement region. As the flow develops radially, a quick increase in the boundary layer thickness occurs due to the rapid deceleration of the flow that follows its radial development. DNS data for smooth and rough wall impinging jets are used to characterize the mean flow features and to highlight the dissimilarities between the mean momentum and scalar transfer. The energetic approach introduced in chapters 2 and 3 is applied to the impinging jet DNS data to determine the Reynolds analogy efficiency factor along the impingement plate. In accordance with the findings of canonical boundary layers, at sufficiently large distances from the jet axis the local scalar transfer efficiency is found to be significantly greater than one, even for the smooth wall case. However, near the impingement region, the local scalar transfer efficiency becomes severely less than unity, highlighting that the very high scalar transfer rates in this region are achieved in spite of a much greater consumption of mechanical energy.

5.1 Smooth- and rough-wall channel flow

This section contains quotations from the author's publication [86]. All cited passages are placed in quotation marks.

The framework developed in chapters 2 and 3 is applied to the study of the dissimilar scalar momentum and scalar transfer in smooth and rough wall channel flows. In particular, "[...] the numerical simulations replicate two cases of the rough-wall fully-developed turbulent channel flow simulations [of] Thakkar [91], Thakkar

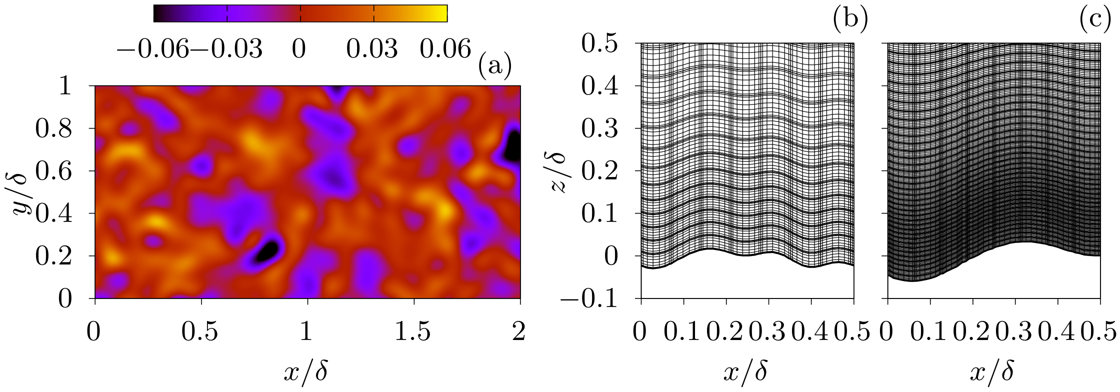

Figure 5.1: Height map of the roughness topography for the $k^+ = 15$ case, (a). Computational mesh: $k^+ = 15$ case, (b); $k^+ = 90$ case, (c). The figure has been adapted from [86].

k^+	Re_τ	k/δ	L_x/δ	L_y/δ	n_x	n_y	n_z	P	DOF	$T_{avg}\overline{U}_b/\delta$
0	180	0	4π	2π	40	20	36	9^{th}	29×10^6	1875.6
15	180	1/12	5.63	2.815	80	40	36	7^{th}	59×10^6	1042.7
90	540	1/6	5.63	2.815	90	45	108	7^{th}	224×10^6	140.9

Table 5.1: Simulation and resolution parameters. P denotes the polynomial degree of the solution and DOF is the total number of degrees of freedom. Table modified from [86].

et al. [92, 93] and Peeters and Sandham [63]. In particular, in one case the flow is transitionally rough, but close to smooth-wall conditions, with $k^+ = 15$ (here $k^+ = ku_\tau/\nu$, and k is the mean peak-to-trough height of the roughness topography), whereas for the second case, the flow is close to fully rough conditions, with $k^+ = 90$. The roughness topography is obtained from a scan of a real grit-blasted surface and is statistically homogeneous in the wall-parallel directions $x_1 = x$ and $x_2 = y$. A sample of the roughness topography is shown in figure 5.1. The physical size of the roughness is $k = \delta/12$, for the $k^+ = 15$ case, and $k = \delta/6$, for the $k^+ = 90$ case. The friction Reynolds number is $Re_\tau = 180$ for the former case and $Re_\tau = 540$ for the latter. An additional smooth-wall channel flow at $Re_\tau = 180$ is also simulated. For all the cases, a unit Prandtl number is considered" (from Secchi et al. [86]).

The numerical simulations are performed using the flow solver `Nek5000` [20], which implements the numerical method presented in chapter 4. The use of a computational mesh consisting of spectral elements leaves great flexibility for the spatial discretization of the computational domain; this fact is exploited to model the roughness topography in the simulations. In particular, as stated in [86], "surface roughness is introduced into the simulations using a body-fitted mesh, obtained by deforming, in the wall-normal direction z, the spectral elements of a plane-channel box having the bottom and top walls at, respectively, $z = 0$ and $z = 2\delta$. The mesh deformation is symmetric with respect to the channel centre line and varies linearly with the wall-normal distance from the bottom wall of the non-deformed channel. As a result, the mean height of the deformed channel is 2δ. Figure 5.1b and 5.1c illustrate the details of the body-conforming computational meshes used in the two rough-wall cases.

The non-deformed computational domain has size $L_x \times L_y \times 2\delta$ in the streamwise, spanwise, and wall-normal directions, respectively. Correspondingly, the number of elements in the three coordinate directions are denoted by n_x, n_y, and n_z. A uniform distribution of elements is used in the streamwise and spanwise directions, whereas, in the wall-normal direction, elements are clustered near the channel walls. The domain size, the number of elements in each direction, the polynomial degree of the solution, and the total number of degrees of freedom (DOF) are reported in table 5.1. The total number of DOF corresponds to the number of grid-points in the physical space and is given by $n_x \times n_y \times n_z \times (P+1)^3$, since each element is divided into $P+1$ grid points. The points distribution along each element direction is non uniform and follows the Gauss-Legendre-Lobatto distribution of quadrature nodes. This can be appreciated in the panels (a) and (b) of figure 5.1 for the case $P = 7$."

Relatively little experimental data is available in the literature for turbulent flows over surface roughness, especially when the statistics of a scalar field are of interest. Hence, validating numerical results is not a straightforward task. In principle, DNS enable the resolution of all the relevant scales of motion and are capable of delivering detailed information about the investigated flow. However, this is true only when the DNS results have been carefully checked against their independence on the mesh resolution and the convergence of statistical quantities. Whenever possible, the comparison with DNS data in the literature can further improve the confidence on the results. Citing from [86], "[the] numerical setup is validated against the reference data of Thakkar [91] and Peeters and Sandham [63]. As an example, [figure 5.2] shows a comparison of the mean streamwise-velocity and temperature profiles with the available reference data. In the figure and throughout the text, angular brackets denote *intrinsic averaging, i.e.*, spatial averaging along the homogeneous channel directions performed in fluid regions only; namely, $\langle \cdot \rangle = \left(\int_{A_f} \cdot \, \mathrm{d}A_f \right) / A_f$, where A_f indicates the plan-area covered by the fluid at a given wall-normal height. Time-statistics reported in this work have been collected for different time integration intervals, T_{avg}, depending on the considered case. For each simulated case, T_{avg}, expressed in terms of external time units, δ/U_b, is reported in table 5.1. For the $k^+ = 90$ case, a significantly shorter integration time interval was used, in comparison to the other cases, to save on computational resources. For this case, the convergence of the statistics was checked by comparing the results for $T_{avg} = 140.9\delta/U_b$ and $T_{avg} = 94.7\delta/U_b$ and no significant differences were observed in the acquired statistics". Further details about the grid and time convergence of the flow statistics are reported in section A.1.

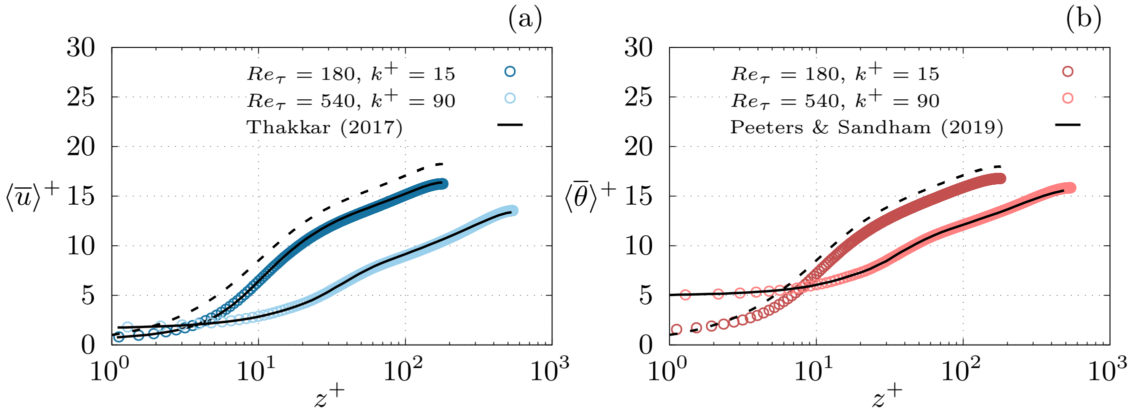

Figure 5.2: CPG-scaled mean streamwise-velocity profiles, (a), and mean scalar profiles, (b). Black dashed lines indicate smooth-wall data at $Re_\tau = 180$. The figure has been adapted from [86].

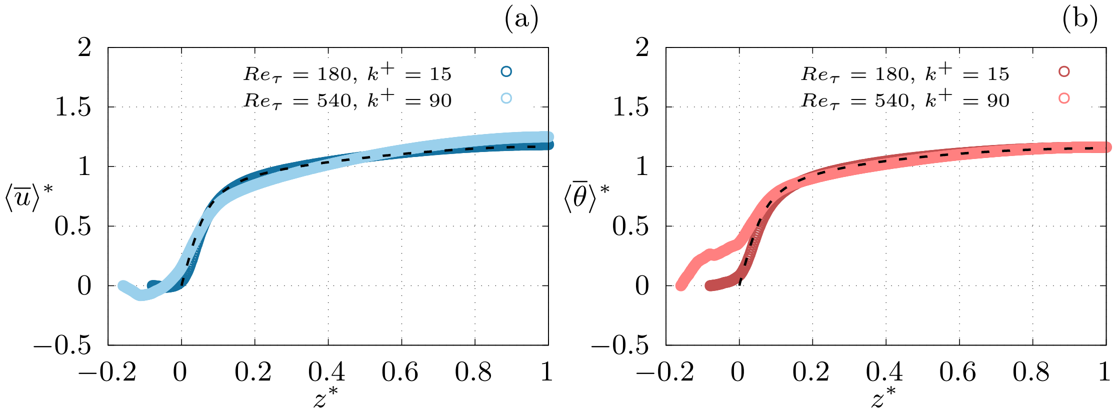

Figure 5.3: CFR-scaled mean streamwise-velocity profiles, (a), and mean scalar profiles, (b). Black dashed lines indicate smooth-wall data at $Re_\tau = 180$.

5.1.1 Integral momentum and scalar transfer

As presented in section 3.1, the evaluation of the integral momentum and scalar transfer performances of channel flow need to consider different parameters, depending on the driving flow conditions. When the flow is driven by a constant pressure gradient, better momentum and scalar transfer is measured in terms of the mean flow rate and the average scalar value attained in the channel; this is reflected by the friction and scalar transfer coefficients, respectively, (3.13) and (3.15), being inversely proportional to the squared mean bulk velocity, for the former, and to the mean bulk scalar, for the latter. Compared to a smooth wall flow, roughness emphasizes momentum and scalar transfer. In particular, it is well-established that, "from an integral perspective, the roughness effect results in a decrease in the mean bulk velocity and scalar, $\overline{U}_b^+$ and $\overline{\Theta}_b^+$, respectively. The latter, computed using [(3.12) and (3.14)], and the Reynolds-analogy factor [(3.16)] are reported in [table 5.2]. As expected, as the roughness Reynolds-number, k^+, increases, so does the departure from the Reynolds analogy. This is shown by the faster decrease of $\overline{U}_b^+$ compared to $\overline{\Theta}_b^+$ for increasing k^+. Correspondingly, the Reynolds-analogy factor decreases, from $RA = 1$ for the smooth-wall case, to $RA = 0.8$ for the $k^+ = 90$ case. As expected, while surface roughness promotes momentum and scalar exchange, the former is much favoured compared to the latter" (from Secchi et al. [86]).

The mean momentum and scalar transfer increase can be perceived also from the comparison of the mean velocity and scalar profiles in the channel with smooth wall data. In this respect, "compared to a smooth-wall flow at matched Re_τ, a rough-wall flow exhibits increased momentum and scalar transfer which manifest themselves as a downward shift of the logarithmic regions of the mean streamwise-velocity and scalar profiles [13]. This can be appreciated in [figure 5.2], where the mean velocity and scalar profiles are shown for all the simulated cases"(from Secchi et al. [86]). Note that smooth wall profiles in figure 5.2 are for $Re_\tau = 180$ and, therefore, only the $k^+ = 15$ data should be compared to them. However, for higher friction Reynolds numbers, the slope of the logarithmic region and intercept become universal; hence, for the $k^+ = 90$ case, a qualitative understanding of the logarithmic shift of the profiles, induced by the roughness, can also be gained by comparison with the logarithmic region of the smooth wall case at low Reynolds number.

Once the ratio between the characteristic physical scales associated with the different channel flow driving strategies (*i.e.* CPG, CFR, and CPI presented in sections 3.1.1, 3.1.2, and 3.1.3, respectively) are known, it is possible to rescale the data and analyse them according to the considered strategy. In essence, it is not necessary to run a different simulation for each driving strategy, for the three approaches should

k^+	Re_τ	$\overline{U}_b^+$	$\overline{\Theta}_b^+$	$\overline{f}^*$	$\overline{q}^*$	$\overline{U}_b^\Omega$	$\overline{\Theta}_b^\Xi$	RA
0	180	15.63	15.59	0.0041	0.0041	28.80	28.75	1.00
15	180	13.72	14.44	0.0053	0.0050	26.11	26.78	0.95
90	540	10.84	13.62	0.0085	0.0068	28.80	32.28	0.80

Table 5.2: Mean bulk streamwise velocity, scalar, and volumetric forcing and source terms in CPG, CFR and CPI scaling. The last column reports the classical Reynolds analogy factor.

give the same physical result. In fact, the choice of the forcing strategy is not completely irrelevant, but small differences appear in terms of very low probability events, whose effect does not compromise the main flow statistics [72]. With this remark, the CPG data presented in [86] can be rescaled in terms of CFR or CPI variables to gain different insights on the dissimilar mean momentum and scalar transfer. At CFR, the mean bulk velocity and scalar are fixed and, therefore, a higher momentum and scalar transfer shows as higher volumetric forcing and source terms or, equivalently, as higher mean wall fluxes. The mean streamwise pressure gradient and mean source term for all the cases are reported, scaled in CFR units, in table 5.2. It is evident that the roughness-induced increase in mean momentum and scalar transfer reflects into higher mean volumetric forcing and source terms. At CFR the mean bulk velocity and scalar are prescribed, thus minor differences are expected in the bulk of the channel for the mean profiles. This can be appreciated in figure 5.3, which shows the CFR-scaled mean streamwise velocity and scalar profiles for all the simulated cases. Note that, differently from the CPG-scaled profiles of figure 5.2, the plots in figure 5.3 do not use a logarithmic scale in the wall normal distance, since CFR-scaled mean profiles are not expected to show a logarithmic behaviour. Further, this allows to visualize the flow within the roughness canopy, where significant effects of the roughness can be observed. Especially for the $k^+ = 90$ case, the mean velocity profiles exhibits back-flow within the roughness sublayer, as a consequence of recirculating flow in the separated regions of the roughness canopy. For the same case, the mean scalar is particularly high within the roughness sublayer, where the formation of a plateau of approximately constant mean scalar is apparent.

The mean streamwise velocity and scalar profiles, normalized using CPI units, are reported in figure 5.4. For the rough wall case at the lowest roughness Reynolds number, the mean profiles show a downward shift in comparison to the smooth wall data at the same friction Reynolds number. In this case, the CPI-scaled data shows clearly a logarithmic region for $20 \lesssim z^\Omega \lesssim 80$. In contrast, the $k^+ = 90$ case displays a markedly different behaviour. The mean velocity profiles shows a net downward shift and a change in slope of its logarithmic region, in comparison to the smooth wall case. The same, however, does not occur for the mean scalar profile, whereby the data show a logarithmic behaviour without displaying a clear shift with respect to the smooth wall data. In this case, the largest differences are seen in the near wall region, where the $k^+ = 90$ mean scalar has significantly larger values in comparison to the smooth wall and $k^+ = 15$ cases.

5.1.2 Mechanical energy and squared-scalar budgets

It is instructive to analyse the similarities between time- and space-averaged budgets (2.12) and (2.13). For CPG scaling, the mean profiles of each term appearing in the budgets are shown in figure 5.5; the definition of the transport, viscous diffusion, dissipation, and power-input terms is reported in the table 5.3. According to the CPG approach, the power input terms, $\mathscr{P}$ and $\mathscr{P}^\mathcal{G}$, are simply the mean streamwise velocity and scalar divided by the Reynolds and Péclet numbers. $\mathscr{P}$ represents the mean power realized by the flow, as a function of the wall normal distance, for the prescribed driving force term. An analogous

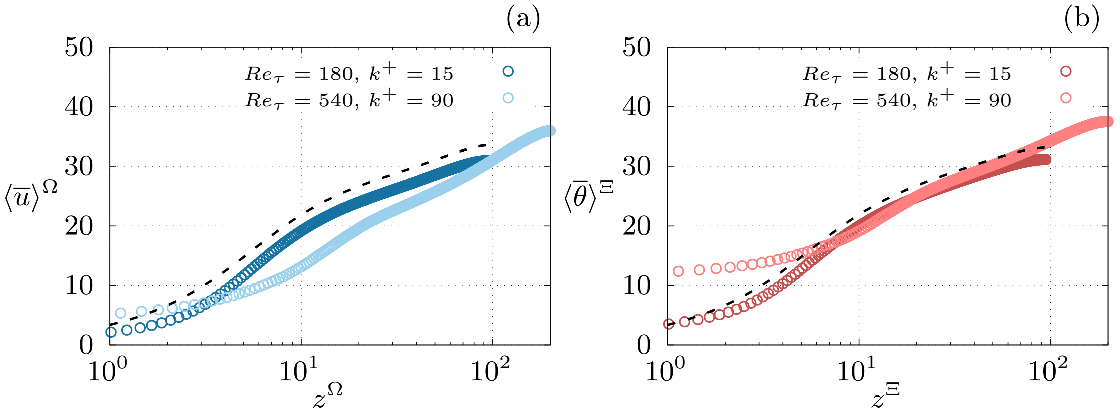

Figure 5.4: CPI-scaled mean streamwise-velocity profiles, (a), and mean scalar profiles, (b). Black dashed lines indicate smooth-wall data at $Re_\tau = 180$.

	Mechanical	Scalar
Transport	$\mathscr{T} = \left\langle \overline{u_i^+ \mathcal{B},_i^+} \right\rangle$	$\mathscr{T}^{\mathcal{G}} = \left\langle \overline{u_i^+ \mathcal{G},_i^+} \right\rangle$
Diffusion	$\mathscr{D} = \left\langle \overline{\mathcal{B}},_{ii}^+ \right\rangle$	$\mathscr{D}^{\mathcal{G}} = \left\langle \overline{\mathcal{G}},_{ii}^+ \right\rangle$
Dissipation	$\varepsilon = \left\langle \overline{\omega_i^+ \omega_i^+} \right\rangle$	$\varepsilon^{\mathcal{G}} = \left\langle \overline{\vartheta,_i^+ \vartheta,_i^+} \right\rangle$
Power input	$\mathscr{P} = \frac{1}{Re_\tau} f^+ \delta_{1i} \left\langle \overline{u_i}^+ \right\rangle$	$\mathscr{P}^{\mathcal{G}} = \frac{1}{Pe_\tau} q^+ \left\langle \overline{\vartheta}^+ \right\rangle$

Table 5.3: Definition of time- and space-averaged terms of the budget equations for $\overline{\mathcal{B}}$ and $\overline{\mathcal{G}}$. Table adapted from [86].

interpretation can be associated with $\mathscr{P}^{\mathcal{G}}$, even though $\mathscr{P}^{\mathcal{G}}$ does not have the physical dimensions of power. Nevertheless, for the sake of analogy between (2.12) and (2.13), $\mathcal{P}$ will be referred to as the mean scalar power realized by the flow as a function of the wall normal distance.

In figure 5.5 it is possible to see the relative importance of the various terms in the mean budget equations as a function of the wall distance. “For all the cases, towards the channel centre line, the viscous diffusion and the dissipation terms become negligible compared to the other terms, and $\mathscr{P} \approx \mathscr{T}$, and $\mathscr{P}^{\mathcal{G}} \approx \mathscr{T}^{\mathcal{G}}$. Closer to the wall, all terms in the budgets become relevant and each case needs to be addressed separately.

For the smooth-wall case, an almost perfect overlap is observed everywhere between the terms in the mechanical- and the scalar-energy equations. It should be noted that, at higher Reynolds numbers, such a perfect correspondence might be lost. As shown by Abe and Antonia [2], at $Pr = 1$, and for sufficiently high Reynolds numbers, $\overline{U}_b^+ = 2.54\log(Re_\tau) + 2.41$, and $\overline{\Theta}_b^+ = 2.18\log(Re_\tau) + 4$. These two relations predict diverging $\overline{U}_b^+$ and $\overline{\Theta}_b^+$ as the Reynolds number increases, with the scalar transfer becoming more effective than momentum transfer for sufficiently large Reynolds numbers [...]. Hence, differences can appear also in the budget terms shown in the figure.

For the $k^+ = 15$ case, figure 5.5b shows that roughness produces changes in the [mechanical energy and squared-scalar budget terms] only well within the roughness canopy, leaving the distributions practically unaltered farther from the wall. Within the roughness canopy, the viscous diffusion is almost exclusively balanced by the dissipation term for both the mechanical and [squared-scalar] budgets. Further, [$\varepsilon^{\mathcal{G}}$ and $\mathscr{D}^{\mathcal{G}}$] are amplified compared to ε and $\mathscr{D}$. This scenario differs for the $k^+ = 90$ case in figure 5.5c. Within the roughness canopy, the largest differences occur, whereas, away from the wall, the terms of the

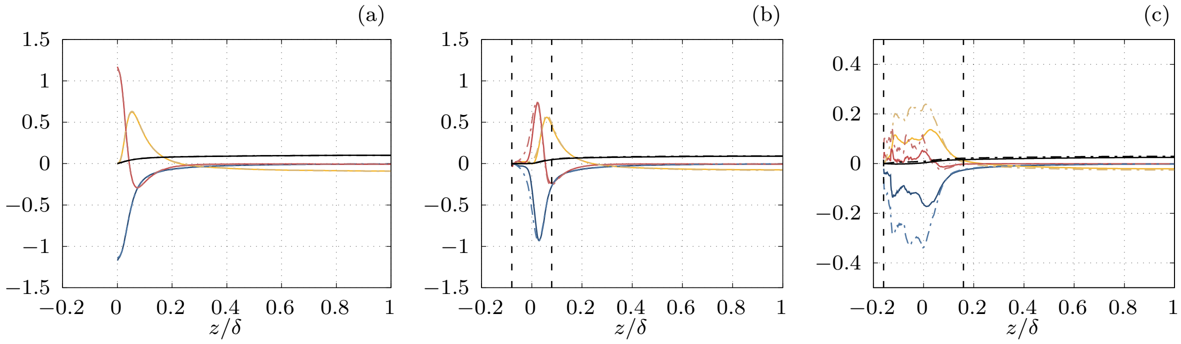

Figure 5.5: CPG-scaled mechanical energy and squared-scalar budgets. (a) Smooth wall, $Re_\tau = 180$; (b) $k^+ = 15$, $Re_\tau = 180$; (c) $k^+ = 90$, $Re_\tau = 540$. ———, $-\varepsilon$; -·-·-·, $-\varepsilon^{\mathcal{G}}$; ———, $-\mathscr{T}$; -·-·-·, $-\mathscr{T}^{\mathcal{G}}$; ———, $\mathscr{D}$; -·-·-·, $\mathscr{D}^{\mathcal{G}}$; ———, $\mathscr{P}$; -·-·-·, $\mathscr{P}^{\mathcal{G}}$. The vertical black dashed lines in panels (b) and (c) indicate the boundaries of the roughness canopy. Figure adapted from [86].

mechanical and scalar energy-budgets tend to overlap, with the exception of $\mathscr{T}^{\mathcal{G}}$ and $\mathscr{P}^{\mathcal{G}}$ which remain larger in magnitude than $\mathscr{T}$ and $\mathscr{P}$, respectively. Focusing on the mechanical-energy budget, the transport term $\mathscr{T}$ penetrates deep in the roughness sublayer, where it exceeds in magnitude the viscous diffusion $\mathscr{D}$. Concurrently, the mechanical energy dissipation exceeds, in magnitude, the joint contribution of $\mathscr{T}$ and $\mathscr{D}$, thus realizing a slightly negative power input for $z \lesssim -0.045\delta$. The same cannot occur for the scalar power input $\mathscr{P}^{\mathcal{G}}$, for the scalar ϑ, and thus $\mathscr{P}^{\mathcal{G}}$, is bounded to vary in the interval [0, 1]. Consistently, within the roughness canopy, $\varepsilon^{\mathcal{G}}$ retains a smaller magnitude compared to the joint contribution of $\mathscr{T}^{\mathcal{G}}$ and $\mathscr{D}^{\mathcal{G}}$, therefore realizing a small, positive, $\mathscr{P}^{\mathcal{G}}$. Interestingly, the profiles of $\mathscr{T}^{\mathcal{G}}$, $\mathscr{D}^{\mathcal{G}}$, and $\varepsilon^{\mathcal{G}}$ are qualitatively similar in shape to the corresponding mechanical-energy budget terms, even though they are larger in magnitude" (from Secchi et al. [86]).

Rescaling the budget terms according to CFR or CPI strategies does not change the nature of the mean profiles reported in figure 5.5, since the scaling factors are constant throughout the channel volume and they equally affect each term in the budgets. Hence, the result of scaling the data according to these two approaches is not shown here.

5.1.3 Bulk dissipation rates

As discussed in section 3.1.1, $\overline{U}_b^+$ and $\overline{\Theta}_b^+$ represent a suitable measure to assess the dissimilarity between momentum and scalar transfer according to the CPG framework. The computed values of $\overline{U}_b^+$ and $\overline{\Theta}_b^+$ as functions of the friction Reynolds number is displayed in figure 5.6(a) for all the simulated cases. The plot also presents the logarithmic distributions expected for smooth-wall channel flow [1, 2]. The enhancement of momentum and scalar transfer due to roughness results in the rough-wall data falling below the smooth-wall asymptotes. The CPG scaling enables the computation of the mean bulk velocity and scalar through the mean bulk dissipation rates of mechanical energy, in equation (3.12), and squared-scalar field, with equation (3.14). This fact can be exploited to differentiate between the mean- and turbulent-flow contributions to

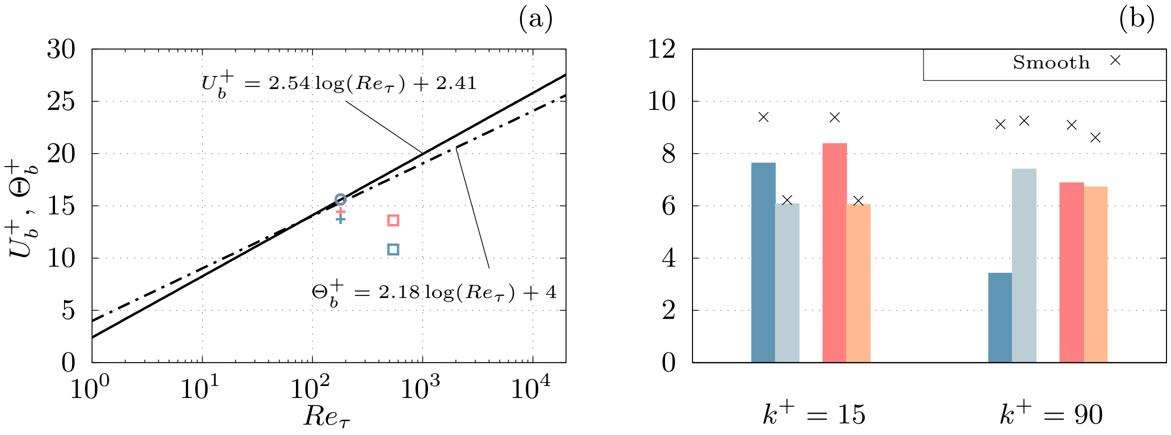

Figure 5.6: (a) Mean bulk velocity (blue) and scalar (red) as functions of the friction Reynolds number. Smooth wall, circle markers; rough wall $k^+ = 15$, cross markers; rough wall $k^+ = 90$, square markers. (b) Mean and turbulent contributions to the volume-averaged dissipation rates. 🟦, $Re_\tau \mathcal{E}^{m+}$; ⬜, $Re_\tau \mathcal{E}^{t+}$; 🟥, $Re_\tau \mathcal{E}_\mathcal{G}^{m+}/Pr$; 🟧, $Re_\tau \mathcal{E}_\mathcal{G}^{t+}/Pr$. Figure adapted from [86].

the mean momentum and scalar transfer. In particular, following Secchi et al. [86], the bulk dissipation rates, $\mathcal{E}^+$ and $\mathcal{E}_\mathcal{G}^+$, are defined as

$$\mathcal{E}^+ = \frac{1}{\mathcal{V}^+} \int_{\mathcal{V}^+} \overline{\omega_i^+ \omega_i^+} \, \mathrm{d}\mathcal{V}^+, \tag{5.1}$$

$$\mathcal{E}_\mathcal{G}^+ = \frac{1}{\mathcal{V}^+} \int_{\mathcal{V}^+} \overline{\vartheta,_i^+ \vartheta,_i^+} \, \mathrm{d}\mathcal{V}^+, \tag{5.2}$$

and are split into their mean, $\mathcal{E}^{m+}$ and $\mathcal{E}_\mathcal{G}^{m+}$, and turbulent, $\mathcal{E}^{t+}$ and $\mathcal{E}_\mathcal{G}^{t+}$, contributions by using the classical Reynolds decomposition [71]. By denoting with a prime superscript the stochastic turbulent fluctuations, these are defined as:

$$\mathcal{E}^{m+} = \frac{1}{\mathcal{V}^+} \int_{\mathcal{V}^+} \overline{\omega}_i^+ \, \overline{\omega}_i^+ \, \mathrm{d}\mathcal{V}^+, \tag{5.3}$$

$$\mathcal{E}^{t+} = \frac{1}{\mathcal{V}^+} \int_{\mathcal{V}^+} \overline{\omega_i' \omega_i'}^+ \, \mathrm{d}\mathcal{V}^+, \tag{5.4}$$

$$\mathcal{E}_\mathcal{G}^{m+} = \frac{1}{\mathcal{V}^+} \int_{\mathcal{V}^+} \overline{\vartheta,_i}^+ \, \overline{\vartheta,_i}^+ \, \mathrm{d}\mathcal{V}^+, \tag{5.5}$$

$$\mathcal{E}_\mathcal{G}^{t+} = \frac{1}{\mathcal{V}^+} \int_{\mathcal{V}^+} \overline{\vartheta,_i' \, \vartheta,_i'}^+ \, \mathrm{d}\mathcal{V}^+. \tag{5.6}$$

Note that $\mathcal{V}^+$ denotes the channel volume scaled using the viscous length, δ_ν. According to (3.12) and (3.14), the contributions to the mean bulk velocity and scalar are obtained by simply multiplying the mean and turbulent contributions by Re_τ, given that $Pr = 1$ in the present case. The mean- and turbulent-flow contributions to $\overline{U}_b^+$ and $\overline{\Theta}_b^+$ are shown in figure 5.6(b) for all the computed cases. For the smooth-wall case at $Re_\tau = 540$, these contributions have been estimated using the asymptotic relationships of Abe and Antonia [1] and Abe and Antonia [2]. The plot is helpful in highlighting how the mean-flow and the stochastic turbulent fluctuations contribute in shaping the mean momentum and scalar transfer at different roughness Reynolds numbers.

“At $k^+ = 15$, the mean flow contribution exceeds that due to the stochastic turbulent field. It is interesting to observe that $\mathcal{E}^{t+}$, $\mathcal{E}_\mathcal{G}^{t+}$ attain similar values, which are also close to the smooth-wall data at the same

Reynolds number. Conversely, $\mathcal{E}^{m+}$ and $\mathcal{E}_{\mathcal{G}}^{m+}$ are reduced from the corresponding smooth-wall values, and $\mathcal{E}_{\mathcal{G}}^{m+}$ is approximately 10% larger than $\mathcal{E}^{m+}$. Compared to the smooth-wall predictions at $Re_\tau = 540$, the rough-wall data at $k^+ = 90$ shows that $\mathcal{E}^{m+}$ suffers the largest decrease, whereas $\mathcal{E}^{t+}$, still being significantly lower than its corresponding smooth-wall counterpart, exceeds $\mathcal{E}^{m+}$. On the other hand, $\mathcal{E}_{\mathcal{G}}^{m+}$ and $\mathcal{E}_{\mathcal{G}}^{t+}$ appear similar to each other.

Interestingly, figure 5.6(b) shows that, for both rough-wall cases, the largest contribution to the breaking of the Reynolds analogy appears to be caused by the mean-field: at $k^+ = 15$, $\mathcal{E}_{\mathcal{G}}^{m+} \approx 1.10\mathcal{E}^{m+}$ and $\mathcal{E}_{\mathcal{G}}^{t+} \approx \mathcal{E}^{t+}$; at $k^+ = 90$, $\mathcal{E}_{\mathcal{G}}^{m+} \approx 1.96\mathcal{E}^{m+}$ and $\mathcal{E}_{\mathcal{G}}^{t+} \approx 0.93\mathcal{E}^{t+}$” (from Secchi et al. [86]). In other words, at higher roughness Reynolds numbers, roughness seems to affect more significantly the mean-flow bulk dissipation rates and, in particular, the effect is different for the mechanical and squared-scalar dissipation rates. The former is significantly less intense than the latter, thus resulting in an impaired mean scalar transfer compared to the mean momentum transfer.

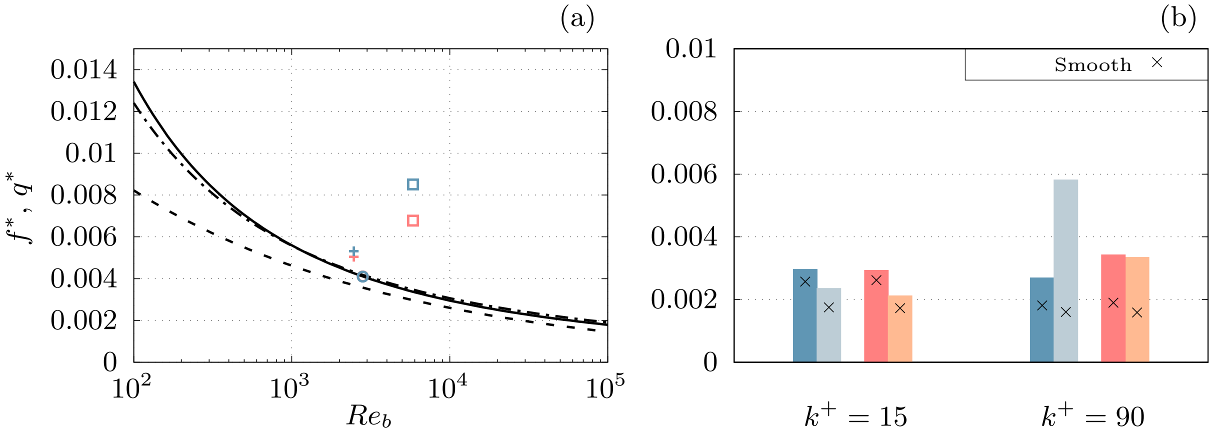

Figure 5.7: (a) Mean volumetric forcing (blue) and scalar source (red) terms as functions of the bulk Reynolds number. Smooth wall, circle markers; rough wall $k^+ = 15$, cross markers; rough wall $k^+ = 90$, square markers; solid line, [1]; dash-dot line, [2]; dashed line, [15]. (b) Mean and turbulent contributions to the volume-averaged dissipation rates. 🟦, $\mathcal{E}^{m*}/Re_b$; ⬜, $\mathcal{E}^{t*}/Re_b$; 🟥, $\mathcal{E}_{\mathcal{G}}^{m*}/(PrRe_b)$; 🟧, $\mathcal{E}_{\mathcal{G}}^{t*}/(PrRe_b)$.

The CFR scaling of the data offers an alternative perspective on the analysis. The CFR analogous of the mean bulk velocity and scalar as functions of the friction Reynolds number is reported in figure 5.7(a), which shows the volumetric forcing and source terms, f^* and q^*, as functions of the bulk Reynolds number. For smooth-wall flows, the plot shows also the same quantities predicted by the asymptotic momentum and scalar transfer laws of Abe and Antonia [1] and Abe and Antonia [2] and the Dean's correlation for the volumetric forcing f^* [15]. To maintain a prescribed mean flow rate and a prescribed mean scalar, the volumetric forcing and source terms increase for increased mean momentum and scalar transfer. Hence the effects of roughness are seen in figure 5.7(a) as higher f^* and q^* compared to a smooth-wall flow at the same bulk Reynold number.

The mean- and turbulent-flow contributions to the mean bulk dissipation rates, $\mathcal{E}^*$ and $\mathcal{E}_{\mathcal{G}}^*$, scaled in CFR units, are displayed in figure 5.7(b). Both k^+ cases show an increase in all bulk dissipation contributions, in comparison to a smooth-wall flow at matched bulk Reynolds number. Note that, in both cases, the smooth-wall reference data has been estimated using the asymptotic relationships of Abe and Antonia [1] and Abe and Antonia [2]. The present smooth-wall DNS at $Re_\tau = 180$ is not reported in figure 5.7(b), since its bulk Reynolds number differs from that of the $k^+ = 15$ case. At $k^+ = 15$, the variation with respect to smooth-wall conditions affect very similarly the mean- and the turbulent-flow contributions of both the mechanical energy and squared-scalar bulk dissipations. The increase in $\mathcal{E}^{t*}$ is slightly more enhanced than the increase in $\mathcal{E}_{\mathcal{G}}^{t*}$, thus resulting in a more pronounced momentum transfer increase in comparison to the increase of mean scalar transfer that occurs between the smooth- and rough-wall cases. At $k^+ = 90$ a manifest change, compared to smooth-wall conditions at matched bulk Reynolds number, occurs for the turbulent-flow contribution to the bulk dissipation rate of mechanical energy. Hence, the roughness-induced increase in momentum transfer appears to be dominated by the turbulent-flow contribution, $\mathcal{E}^{t*}$, whereas $\mathcal{E}^{m*}$ changes relatively less in comparison to its smooth-wall value. For the scalar transfer, very similar changes occur to both the mean- and turbulent-flow contributions to $\mathcal{E}_{\mathcal{G}}^{*}$, with respect to the smooth-wall reference.

The scenarios depicted by figures 5.6(b) and 5.7(b) seem contradictory at a first glance: for the CPG scaling, the main roughness-induced variation of the bulk dissipation rates affects the mean-flow contribution, whereas for the CFR scaling the main change is observed for the turbulent-flow contributions. In fact, the ambiguity vanishes considering that the rough-wall cases are compared to different smooth-wall references; in figure 5.6(b), the smooth-rough comparison is made at matched friction Reynolds number, whereas in figure 5.7(b) the same is done at fixed bulk Reynolds number. Hence, at CPG, *i.e.* at fixed mean momentum and scalar wall fluxes, the flow response to the roughness-induced momentum and scalar transfer increase manifests itself primarily through a decrease in the mean-flow bulk dissipation rates, $\mathcal{E}^{m+}$, and $\mathcal{E}_{\mathcal{G}}^{m+}$. In contrast, at CFR, *i.e.* at fixed flow rate and mean scalar, the flow responds to the increased momentum and scalar transfer with an increase of the turbulent-flow contributions to the bulk dissipation rates.

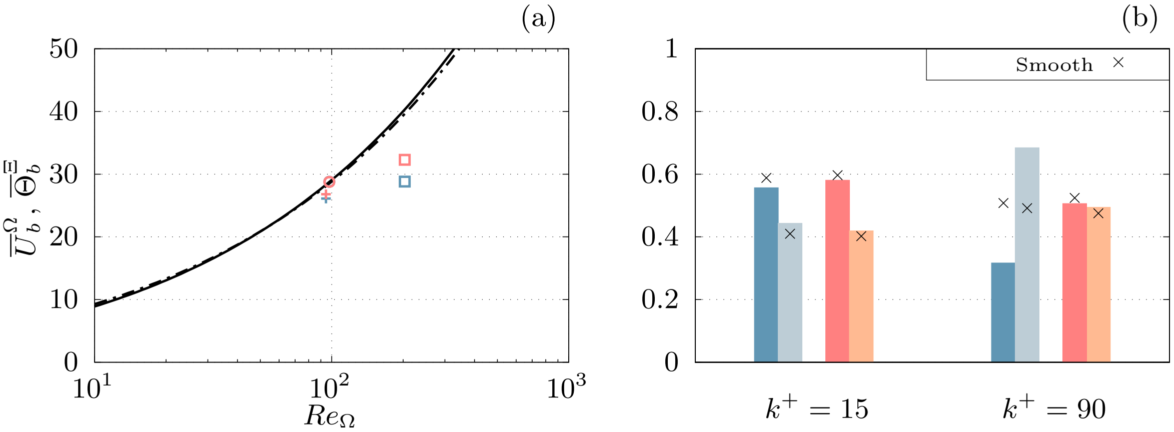

Figure 5.8: (a) Mean bulk velocity (blue) and scalar (red) as functions of the Reynolds number Re_Ω. Smooth wall, circle markers; rough wall $k^+ = 15$, cross markers; rough wall $k^+ = 90$, square markers. (b) Mean and turbulent contributions to the volume-averaged dissipation rates. 🟦, $\mathcal{E}^{m\Omega}$; ⬜, $\mathcal{E}^{t\Omega}$; 🟥, $\mathcal{E}_{\mathcal{G}}^{m\Xi}$; 🟧, $\mathcal{E}_{\mathcal{G}}^{t\Xi}$.

Momentum and scalar transfer performances for the CPI-scaled quantities are visualized, in terms of the mean bulk velocity and scalar, in figure 5.8(a). At matched Re_Ω, the roughness-induced momentum and scalar transfer increase, in comparison to a smooth-wall flow, manifests itself through a decreases in the mean bulk velocity and scalar. For a prescribed power input, the augmentation of the non-dimensional volumetric driving force and source terms, or equivalently of the mean wall fluxes, is given by the reciprocal of the CPI-scaled mean bulk velocity and scalar. Figure 5.8(b) shows the mean- and turbulent flow bulk dissipation rates for both the rough-wall cases in comparison with the smooth-wall cases at the same

Re_Ω. According to the CPI normalization, the non-dimensional mean- and turbulent-flow bulk dissipation contributions must sum up to unity and, as such, $\mathcal{E}^\Omega$ and $\mathcal{E}_\mathcal{G}^\Xi$ are not a meaningful measure of the mean momentum and scalar transfer. However, their mean- and turbulent-flow contributions are informative in regard to how the dissipation fields respond to the momentum and scalar transfer increase brought about by the roughness. From figure 5.8(b), it is observed that, at matched Re_Ω, the mechanical energy bulk dissipation responds significantly differently from the bulk dissipation of the squared scalar. This is particularly evident for the $k^+ = 90$ case, where it is observed that $\mathcal{E}^{m\Omega}$ and $\mathcal{E}^{t\Omega}$ depart from their smooth-wall values, whereas $\mathcal{E}_\mathcal{G}^{m\Omega}$ and $\mathcal{E}_\mathcal{G}^{t\Omega}$ do not change appreciably from the smooth wall case at matched Re_Ω. The same scenario is seen also at $k^+ = 15$, even though the change in $\mathcal{E}_\mathcal{G}^{m\Omega}$ and $\mathcal{E}_\mathcal{G}^{t\Omega}$ produced by the roughness is also marginal.

5.1.4 Dispersive dissipation rates

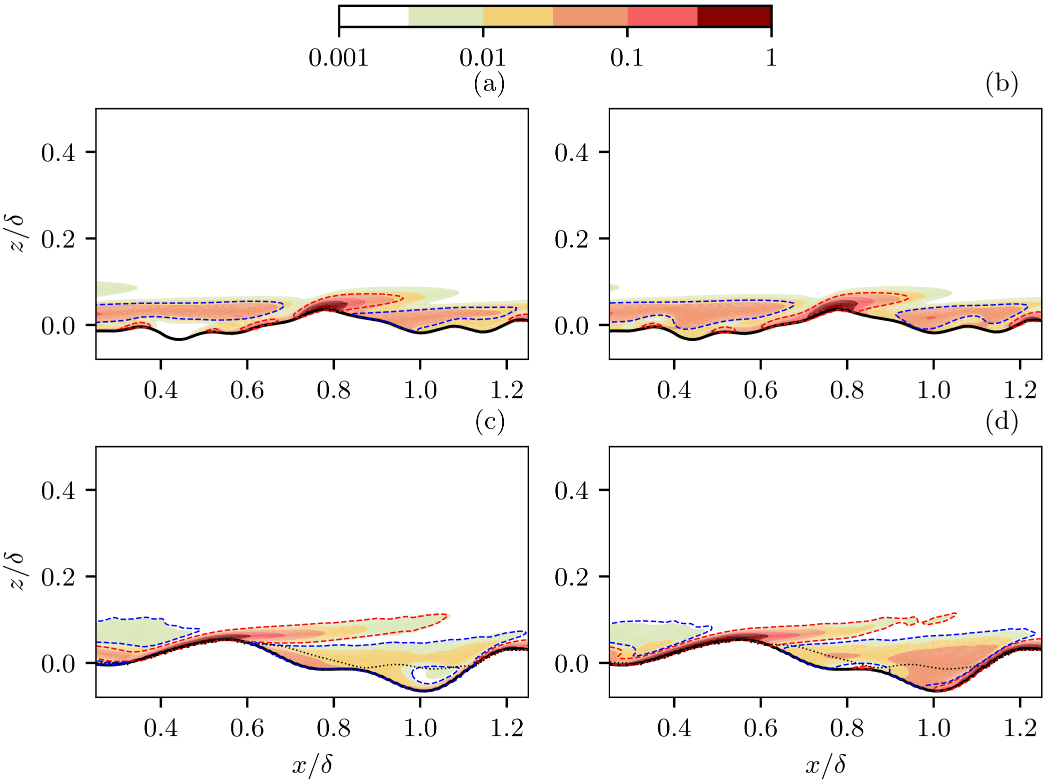

Figure 5.9: Dispersive dissipation rates for the $k^+ = 15$ (a, b), and $k^+ = 90$ (c, d) cases. (a, c) $\overline{\omega_i}''^+\overline{\omega_i}''^+$; (b, d) $\overline{\vartheta_{,i}}''^+\overline{\vartheta_{,i}}''^+$. Dashed lines represent lines of constant $\overline{\omega_y}''^+ = \pm 0.046$ (a, c) and $\overline{\vartheta_{,z}}''^+ = \pm 0.046$ (b, d). Blue and red colours indicate, respectively, negative and positive values. In panels (c) and (d), a black dotted line represents the iso-contour line of zero mean streamwise velocity. Figure adapted from [86].

The time averaged dissipation rates, $\nu\overline{\omega_i\omega_i}$ and $\nu\overline{\vartheta_{,i}\,\vartheta_{,i}}$, let themselves to be further decomposed into a mean-in-space part and a spatial fluctuation determined by the roughness topography. Namely, $\nu\overline{\omega_i\omega_i} = \nu\langle\overline{\omega_i}\rangle\langle\overline{\omega_i}\rangle + \nu\langle\overline{\omega_i''}\ \overline{\omega_i''}\rangle$ and $\nu\overline{\vartheta_{,i}\,\vartheta_{,i}} = \nu\langle\overline{\vartheta_{,i}}\rangle\langle\overline{\vartheta_{,i}}\rangle + \nu\langle\overline{\vartheta_{,i}''}\ \overline{\vartheta_{,i}''}\rangle$, where the double prime superscript denotes the spatial, or dispersive, fluctuation of a time-averaged quantity with respect to its time- and space-mean value. The analysis of the spatial distribution of the dispersive fields, $\overline{\omega_i}''\overline{\omega_i}''$ and $\overline{\vartheta_{,i}}''\overline{\vartheta_{,i}}''$, can be used to

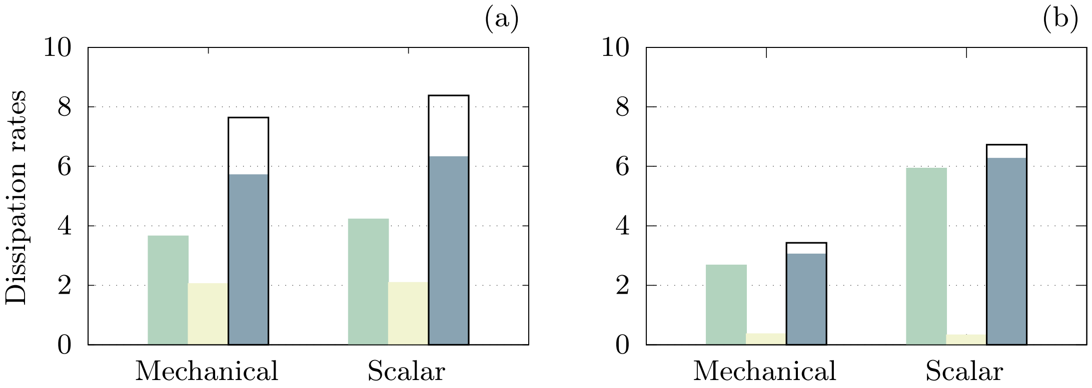

Figure 5.10: Attached, exposed regions (AER) and well-mixed regions (WMR) contributions to $Re_\tau \mathcal{E}^{m+}$ and $Re_\tau \mathcal{E}_{\mathcal{G}}^{m+}/Pr$. (a), $k^+ = 15$; (b), $k^+ = 90$. 🟩, AER; 🟨, WMR; 🟦, sum of AER and WMR contributions; a black solid outline indicates $Re_\tau \mathcal{E}^{m+}$ and $Re_\tau \mathcal{E}_{\mathcal{G}}^{m+}/Pr$. Figure adapted from [86].

identify flow regions whose response to the presence of a rough-wall geometry differs in terms of momentum and scalar transfer.

The spatial distribution of the dispersive dissipation rates, $\nu\overline{\omega_i}''\overline{\omega_i}''$ and $\nu\overline{\vartheta_{,i}}''\overline{\vartheta_{,i}}''$, are shown in figure 5.9 in CPG scaling for two representative sections of the roughness topographies for both roughness Reynolds number cases. As observed in [86], "high shear near roughness peaks leads to intense local heat and momentum transfer, where both fluxes exhibit a similar behaviour, as noted by [110]. Locally, the strong, positive, velocity and scalar gradients exceed significantly their spatial mean at the same wall-normal height, thus resulting in intense positive dispersive fluctuations $\overline{\omega_i}''^+$ and $\overline{\vartheta_{,i}}''^+$. Correspondingly, the dispersive dissipation fields, $\overline{\omega_i}''^+\overline{\omega_i}''^+$ and $\overline{\vartheta_{,i}}''^+\overline{\vartheta_{,i}}''^+$, attain their maxima. In figure 5.9, these regions are identified by isocontour lines for positive values of $\overline{\omega_y}''^+$ (figure 5.9a,c) and $\overline{\vartheta,z}''^+$ (figure 5.9b,d). They grow attached to the windward side of roughness hills and develop, exposed to high shear, up to the hill's crest, where they eventually detach from the roughness contour".

A markedly different behaviour is observed in flow regions between roughness hills. In particular, "large roughness elements tend to shelter their downstream regions from the incoming flow, thereby generating pockets of slow-moving, recirculating flow, which entrain outer fluid towards the bottom of the roughness valleys (Forooghi et al. [23]). These regions are characterized by nearly uniform scalar distributions and smaller scalar gradients compared with their mean value at the same wall-normal height. This results in negative dispersive fluctuations of the scalar gradient, $\overline{\vartheta_{,i}}''^+$, which, in turn, increase the local dispersive dissipation rate $\overline{\vartheta_{,i}}''^+\overline{\vartheta_{,i}}''^+$" (from Secchi et al. [86]).

It is possible to distinguish flow regions in the roughness sublayer that contribute dissimilarly to the mean momentum and scalar transfer. These are attached, exposed regions (AER) and well-mixed regions (WMR). In particular, the dispersive fluctuating field, $\overline{\vartheta_{,z}}''$, can be used to qualitatively identify AER and WMR by setting a suitable threshold value to this field. For instance, considering the iso-contour lines in figure 5.9, AER and WMR can be defined as the regions where $\overline{\vartheta_{,z}}''^+ > 0.046$ and $\overline{\vartheta_{,z}}''^+ < -0.046$, respectively. It is emphasized that these particular values are arbitrarily chosen based on the good visual correlation of the thus identified regions with the phenomenological description provided for AER and WMR. Albeit the arbitrariness of the thresholds, conditional integration of the mean dissipation rates, $\overline{\omega_i^+\,\omega_i^+}$ and $\overline{\vartheta_{,i}^+\,\vartheta_{,i}^+}$ enables the quantification that these regions have on the mean-flow momentum and scalar transfer. As reported in [86], the result of the conditional integration is shown in figure 5.10 for the investigated rough-wall cases. As observed by Secchi et al. [86], “for both cases, the largest contribution to $\mathcal{E}^{m+}$ and $\mathcal{E}_{\mathcal{G}}^{m+}$ is introduced by AER, whereas the contribution of WMR, despite being significant at $k^+ = 15$, becomes marginal at $k^+ = 90$. Interestingly, the contribution of WMR is very similar for the mechanical and scalar dissipation rates at both roughness Reynolds numbers. Namely, the dissimilarity between $\mathcal{E}^{m+}$ and $\mathcal{E}_{\mathcal{G}}^{m+}$ can be attributed to the differences displayed by the dissipation rates in AER alone. Note that the joint contribution of AER and WMR accounts for a large part of $\mathcal{E}^{m+}$ and $\mathcal{E}_{\mathcal{G}}^{m+}$, especially at $k^+ = 90$, where it represents more than 90% of $\mathcal{E}^{m+}$ and $\mathcal{E}_{\mathcal{G}}^{m+}$. The residual represents the contribution of the mean-flow dissipation rates that takes place in the core of the channel”.

5.2 Smooth and rough wall boundary layer

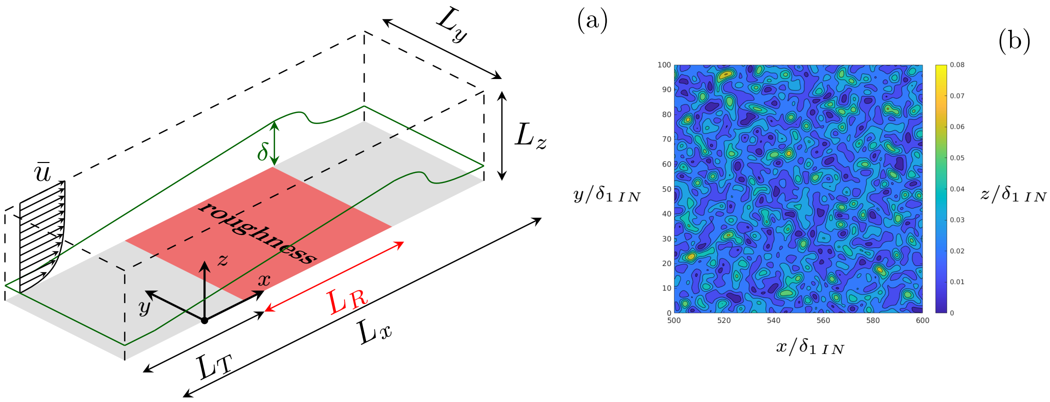

Figure 5.11: Sketch of the boundary layer computational domain, (a); surface roughness patch, (b). The sketch on the left has been adapted from [84].

Smooth and rough wall turbulent boundary layers are analysed in this section using DNS data presented in [84]. Differently from the other DNS studies reported in the present work, the simulations of boundary layer flows were carried out using the pseudo-spectral flow solver `SIMSON` [11]. The solver discretizes the governing equations in the Fourier space, for the wall-parallel directions, and Chebyshev polynomials for the wall normal direction. Further details about the numerical procedure are presented in chapter 4. The computational domain used for the simulations is illustrated in figure 5.11a. The domain is defined by a rectangular computational box with dimensions $L_x = 3000\delta_{1\,IN}$, $L_y = 124\delta_{1\,IN}$, and $L_z = 100\delta_{1\,IN}$ in the streamwise, spanwise, and wall-normal directions, respectively. Here, $\delta_{1\,IN}$ represents the displacement thickness of the Blasius boundary layer at the inlet of the computational domain.

A homogeneous roughness patch of length $L_R = 2350\delta_{1\,IN}$ is placed along the bottom wall, beginning at $x = L_T = 150\delta_{1\,IN}$. To ensure a smooth transition from the smooth to the rough wall, a sigmoid scaling function is applied to the roughness height distribution in the vicinity of $x = L_T$. The location L_T is chosen so that the flow reaches a fully turbulent state at the start of the roughness patch, independent of the specific tripping mechanism used to induce turbulence in the boundary layer [77]. The simulation parameters for both cases are summarized in table 5.4. In the table, n_x, n_y, and n_z denote, respectively, the number of grid nodes in the physical streamwise, spanwise, and wall normal directions.

Since the flow solver uses a spectral discretisation in the wall parallel directions, periodic boundary conditions are required at the inlet and outlet sections, as well as at the front and rear planes at $y = 0$ and

	$L_x/\delta_{1,in}$	$L_y/\delta_{1,in}$	$L_z/\delta_{1,in}$	$L_T/\delta_{1,in}$	$L_R/\delta_{1,in}$	n_x	n_y	n_z
Smooth-wall	3000	120	100	-	-	3072	256	301
Rough-wall	3000	120	100	150	2350	5760	288	401

Table 5.4: Smooth and rough wall DNS parameters.

$y = L_y/\delta_{1\,IN}$. To account for the streamwise development of the flow, the re-scaling strategy introduced by Chevalier et al. [11] is employed. In practice, $x > L_T + L_R$ represents a fringe region where a volumetric forcing is applied to re-scale the flow to the laminar Blasius boundary layer at $Re_1 = u_\infty \delta_{1\,IN}/\nu = 450$ that is prescribed at the inlet section of the computational domain.

At the bottom wall, no-slip and no-penetration boundary conditions are enforced using an IBM based on the approach of [29], similar to the method presented in section 4.3.1. A similar method is applied to impose a Dirichlet boundary condition for the scalar field, maintaining a uniform wall scalar concentration $\vartheta_w = 0$. On the top boundary of the computational domain, the streamwise velocity is set to the free-stream velocity u_∞, while the wall-normal velocity is permitted to have transpiration, following the methodology of [11]. The scalar field at the top boundary is prescribed to match the free-stream scalar ϑ_∞, with $\vartheta_\infty < \vartheta_w$. A unit Prandtl number is used for both the smooth and rough wall cases, $Pr = 1$.

The investigated surface roughness is based on a filtered three-dimensional scan of a real sandpaper rough surface. The same roughness topography is investigated in fully developed turbulent channel flow in [25] and is a $P60$ grit sandpaper. A colour map of the roughness topography is visualized in figure 5.11b. As reported by Frohnapfel et al. [25], the roughness distribution is obtained from tactile measurements and three-dimensional reconstruction of high resolution images of a real sandpaper rough patch. The measurements were used to obtain the power spectrum and probability density function of the roughness height in-plane distribution. The characteristic roughness height k is defined as $k_t = 4\delta_{1\,IN}$, where k_t represents the mean peak-to-trough height of the roughness topography.

5.2.1 Mean momentum and scalar transfer

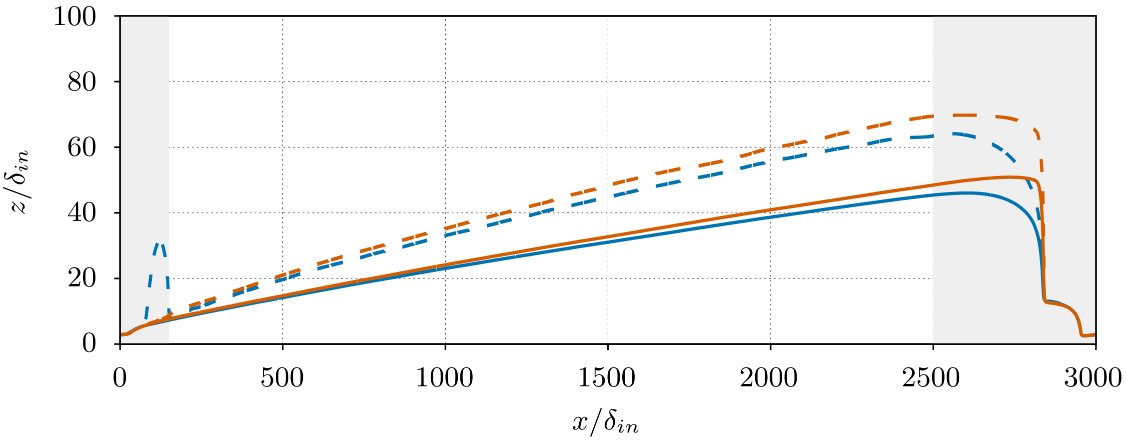

Figure 5.12: Velocity boundary layer thickness, δ_{99}, (blue) and scalar boundary layer thickness, δ_{99}^{ϑ} (orange). Solid lines, smooth wall; dashed lines, rough wall.

The velocity and scalar boundary layers development are visualized in figure 5.12 through the thicknesses, δ_{99} and δ_{99}^{ϑ}, measured as the wall normal height at which the mean streamwise velocity and the mean scalar are the 99% of their respective free stream values. The boundary layer thicknesses are compared, between the smooth and the rough wall cases, at fixed streamwise location. The light-grey areas in the plot correspond to the smooth wall flow regions. The one upstream of the roughness patch is necessary to let the flow develop from the Blasius profiles at the inlet section of the computational domain, whereas the smooth wall part downstream of the roughness patch is the region where the flow is rescaled to the inlet profiles to match the streamwise periodicity of the simulation. Therefore, the solution in this region cannot be considered physical, as it can be observed from the non-natural development of the boundary layer thicknesses in this region. The smooth and rough wall boundary layer thicknesses exhibit an evidently different development over the roughness patch. The δ_{99} thickness of the rough wall case spikes upstream of the roughness region due to the smooth-to-rough transition which generates a local mean pressure gradient. The same is not observed for the scalar boundary layer thickness. The mean flow quickly recovers downstream of the roughness leading edge. However, compared to the smooth wall case, the boundary layer thickness increases at a faster rate with the streamwise distance as a manifestation of the higher mean momentum transfer induced by the roughness. Further, the mean scalar boundary layer thickness departs significantly, for the rough wall data, from the velocity boundary layer thickness, indicating a dissimilar mean momentum and scalar transfer.

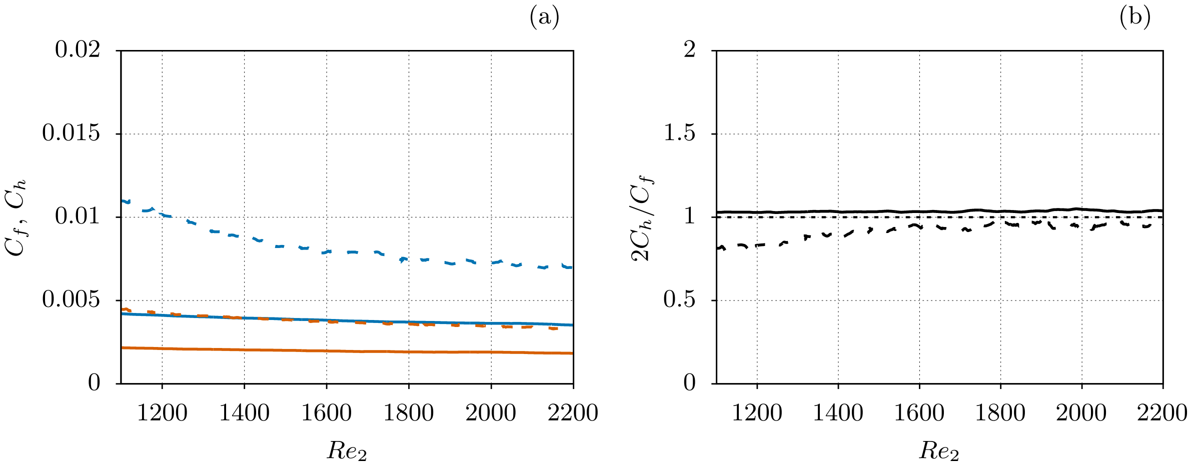

Figure 5.13: Friction coefficient (blue) and scalar transfer coefficient (orange), (a); Reynolds analogy factor, RA, (b). Solid lines, smooth wall; dashed lines, rough wall.

The comparison of smooth and rough wall statistics at a fixed streamwise location might be relevant for practical applications, since it is indicative of how dissimilar are the two flows at the same physical location. However, when comparing the momentum and scalar transfer capabilities of the smooth and rough wall flows, it is probably more meaningful to compare their statistics under similar conditions as, for instance, comparing the momentum and scalar transfer performances at matched boundary layer thickness. Naturally, this condition is met at different streamwise locations, since the rough wall boundary layer has a faster growing thickness in comparison to the smooth wall flow.

Following this observation, the mean momentum and scalar wall fluxes are shown in figure 5.13a through the distributions of the friction and scalar transfer coefficients, C_f and C_h, as functions of the momentum Reynolds number, $Re_2 = u_\infty \delta_2/\nu$. Note that the smooth and rough wall cases span different ranges of momentum Reynolds numbers, but the comparison in the figure is restricted to $1100 \leq Re_2 \leq 2200$, for which data is available for both cases. At matched Re_2, *i.e.* for a fixed boundary layer momentum thickness, the rough wall flow exhibit a significantly higher friction and scalar transfer coefficients in comparison to the smooth wall case. As expected, the roughness-induced increase in the mean momentum flux exceeds appreciably the increase in the mean scalar wall flux. This is especially true at small Re_2, a condition that occurs physically close to the leading edge of the roughness topography, where roughness elements are large in comparison to the thickness of the boundary layer. In this region, a large contribution to the momentum loss at the wall is expected to be caused by the pressure drag of roughness elements; an analogous effect is naturally missing in terms of the mean scalar transfer and, consequently, the mean scalar wall flux is not subject to a similar increase over the same region. This discrepancy becomes evident in figure 5.13b, which shows the Reynolds analogy factor, $RA = 2C_h/C_f$, as a function of Re_2. At low Re_2, the Reynolds analogy factor of the rough wall case is notably much less than 1, evidencing a higher momentum transfer in comparison to the mean scalar transfer. At larger Re_2, which corresponds at downstream locations, where the boundary layer becomes significantly thicker than the roughness size, RA approaches unity. In this region, the roughness affects very similarly the mean momentum and scalar transfer.

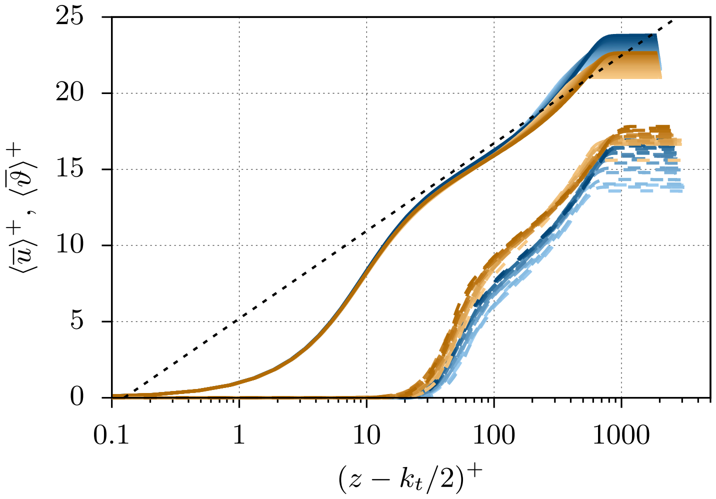

Figure 5.14: Mean streamwise velocity profiles (solid) and mean scalar profiles (dashed) in viscous units at different streamwise locations. Curves are colour-coded, from light to dark colours, to denote profiles at increasing distance from the roughness leading edge. Blue colour scale, $\langle\overline{u}\rangle^+$; brown colour scale, $\langle\overline{\vartheta}\rangle^+$. The black-dashed line indicates the logarithmic law $2.5\log(x) + 5.2$.

Mean streamwise velocity and scalar profiles scaled in viscous units are reported in figure 5.14 for the smooth and the rough wall cases. Several profiles, at different streamwise stations are reported in the figure. The smooth wall data shows a good collapse of the profiles sampled at different streamwise positions, both for the mean velocity and the mean scalar profiles. In contrast, the rough wall mean profiles exhibit a noticeable scatter when scaled in viscous units. This is especially true fort the mean streamwise velocity profiles, whereas a better collapse of the data is observed for the mean scalar profiles. In fact, at different streamwise positions, the relative size of the roughness changed in comparison to both, outer layer length scales, such as the boundary layer thickness, and the viscous length scale. Close to the roughness leading edge, roughness elements are large in comparison to the boundary layer thickness and to the viscous length scale. Hence, roughness plays a prominent effect on the flow in this region, which reflects into large downward shifts of the mean profiles. In fact, the flow has characteristics similar to a flow in the fully-rough regime. However, as the flow develops downstream, the separation between the roughness characteristic size and the boundary layer thickness and the viscous length scale increases. Roughness elements become increasingly smaller compared to both flow length scales. Correspondingly, the roughness-induced effects on the flow become more marginal and the mean flow behaves as a transitionally rough flow. In terms of the mean profiles in figure 5.14, this is seen as a decreasing downward shift of the rough wall profiles, in comparison to the smooth wall ones, for the profiles sampled at greater streamwise stations.

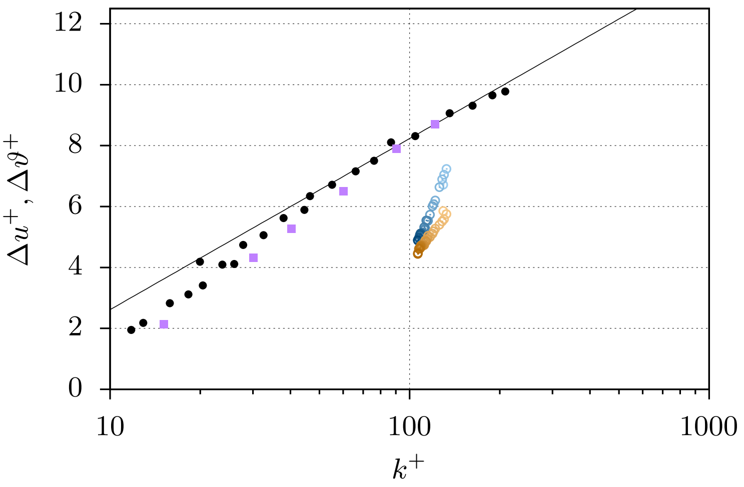

Figure 5.15: Roughness functions, Δu^+ and $\Delta\vartheta^+$, as functions of the local roughness Reynolds number, k^+. The streamwise location of data sampling is denoted by the colour gradient of symbols, from light to dark colours to indicate the increasing distance from the roughness leading edge. Blue colour scale, Δu^+; Brown colour scale, $\Delta\vartheta^+$. The black solid line represents $\log(k^+)/0.41 - 3.0$. Black symbols are from [59]; purple symbols are from [93].

The quantification of roughness effects based on the mean velocity and scalar profiles can be achieved by computing the roughness functions, Δu^+ and $\Delta\vartheta^+$, measuring the shift between the logarithmic regions of the viscous-scaled mean profiles of the smooth and rough wall cases [13]. This procedure introduces the issue of defining a meaningful reference plane for measuring the wall normal distances of the rough wall profiles. This problem is of high relevance when comparing the roughness function values between different data sets of different investigations. In plotting the mean profiles in figure 5.14, the wall normal distances are measured from the plane $k_t/2$. However, the evaluation of the roughness functions from the present data remains challenging: while the mean velocity profiles exhibit, reasonably well, a logarithmic region, the same is not true for the rough wall profiles. This is especially true for the mean profiles sampled near the roughness leading edge, a symptom of the large relative size of the roughness elements in comparison with the flow length scales in this region. To avoid these issues, the roughness functions are evaluated as the difference of the viscous-scaled free stream velocity and scalar of the smooth and rough wall cases at matched streamwise location; namely, $\Delta u^+ = u^+_{\infty S} - u^+_{\infty R}$, and $\Delta\vartheta^+ = \vartheta^+_{\infty S} - \vartheta^+_{\infty R}$, where the subscripts S and R denote, respectively the smooth and rough wall cases.

This definition is used to compute the roughness functions reported in figure 5.15 as functions of the local roughness Reynolds number, $k^+ = u_\tau k/\nu$. The figure shows also the roughness function values in rough wall pipe flows measured by Nikuradse [59], and the DNS data of rough wall channel flow of Thakkar et al. [93]. Despite the large values of the roughness Reynolds number, the Δu^+ of the present case shows a markedly dissimilar slope from the reference asymptotic behaviour. In particular, it is observed that the largest values of k^+ are realized near the roughness leading edge, where the friction at the wall is maximum. In this region, the boundary layer is rather thin, so that there is not enough separation between the roughness size and the the outer length scale of the flow. For instance, from figure 5.12, and recalling that $k_t = 4\delta_{1in}$, it is seen that, even close to the far-downstream end of the roughness patch, the roughness is only approximately 15 times smaller than the boundary layer thickness. The lack of separation between the roughness size and the outer flow length scale prevents the realization of the classical roughness flow regimes. The roughness elements do not act on the flow as small corrugations of the wall, but they are rather large obstacles that produce large modifications to the flow. These are seen, for instance, in the roughness function values of figure 5.15, or in the lack of a clearly identifiable logarithmic region in the rough wall mean profiles of figure 5.14.

5.2.2 Energetic aspects

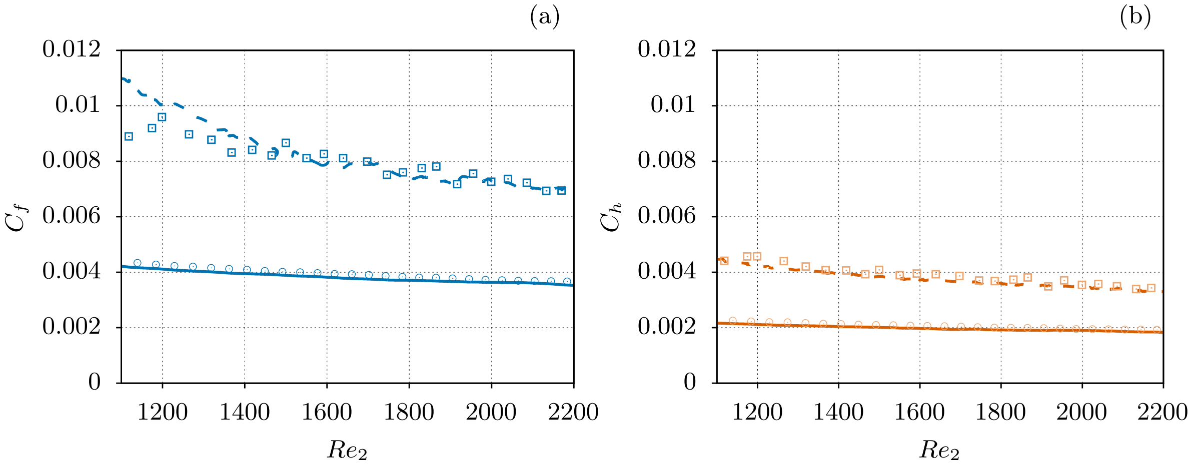

Figure 5.16: Friction coefficient (a), and scalar transfer coefficient (b) computed using (3.39) and (3.40) (lines), and using (3.55) and (3.59) (symbols). Smooth wall, solid lines and circles; rough wall, dashed lines and square markers.

Due to its large relative size, the investigated rough wall geometry cannot be regarded as surface roughness in a classical sense. Thus, its effects on the flow cannot be interpreted on the basis of rough wall turbulent flow results [13, 41]. Nevertheless, the approach presented in section 3.2 offers a valid alternative for assessing the similar momentum and scalar transfer and its modifications induced by the investigated rough wall topography.

The approximate expressions for the friction and scalar transfer coefficients, (3.56) and (3.59), are tested with the present DNS data for both the smooth and the rough wall cases in figure 5.16. The C_f and C_h values, computed from the bulk dissipation rates and the boundary layer thicknesses, $\delta = \delta_{99}$ and δ_1, are compared with the C_f and C_h values computed using the integral momentum and scalar equations (3.44) and (3.45), respectively. The agreement between the curves is remarkable for both cases, with relatively small deviations for the C_f computed with (3.56) at small momentum Reynolds numbers. In particular, the estimated values appear to capture very well the decreasing trend of the friction and scalar transfer coefficients for increasing the momentum Reynolds number.

The scalar transfer efficiency is reported in terms of the Reynolds analogy efficiency factor, RA_π, in figure 5.17. The figure shows that, even for the smooth wall case, RA_π is greater than one. In particular, the present data shows that $RA_\pi \approx 1.2$ for this case. This behaviour is expected on the basis of equation (3.58) and the Reynolds analogy factor distribution, RA, shown in figure 5.13. For a smooth wall boundary layer,

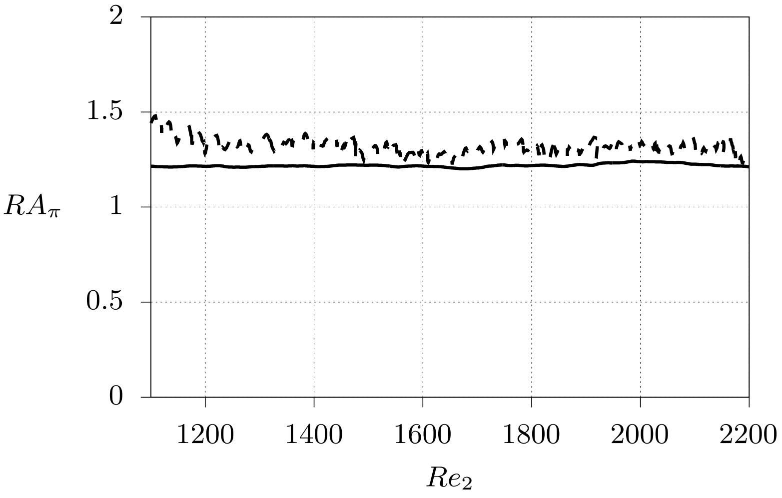

Figure 5.17: Reynolds analogy efficiency factor, RA_π. Smooth wall, solid line; rough wall, dashed line.

the classical Reynolds analogy factor is expected to be one, reflecting the similarity between the mean momentum and scalar fluxes at the wall. Due to the non-negligible displacement thickness, in comparison to the boundary layer thickness, δ_{99}, the Reynolds analogy efficiency factor, RA_π, results amplified in comparison to RA. This fact indicates that the scalar transfer along the wall of a flat plate boundary layer occurs in a particularly effective way: the thickening of the boundary layer emphasizes the scalar transport and, in turn, the net scalar transfer at the wall, while consuming a relatively smaller amount of mechanical energy. The presence of roughness on the wall further emphasizes the thickening of the boundary layer in comparison to the smooth wall case. Correspondingly, the net scalar transfer and the dissipated mechanical energy increase, but, as shown in figure 5.17, the augmentation of scalar transfer exceeds that of the consumed mechanical energy, thus determining an appreciably higher Reynolds analogy factor, RA_π.

5.3 Smooth-wall impinging jet

This section investigates momentum and scalar transfer of turbulent jets impinging on hydrodynamically smooth plates. The geometry of the flow configuration is that displayed in figure 3.4 and considers a separation between the impingement plate and the nozzle exit section of $H = 2D$, where D represents the diameter of the pipe used to generate the jet. In particular, the jet issues from a fully-developed turbulent pipe flow at a bulk Reynolds number, $Re_b = 5300$. The latter is based on the mean bulk velocity in the pipe, $\overline{U}_b$, and the pipe diameter. No-slip boundary conditions are applied on the confinement and impingement plates for the velocity field, whereas at the lateral open boundary, the boundary condition presented in [18] are applied. The jet and the confinement plate have a prescribed scalar, $\vartheta_J = 0$; on the impingement plate, the scalar is fixed to $\vartheta_w = 1$. On the lateral boundary, the boundary conditions presented in [54] are enforced on the scalar field. Details regarding the computational mesh, the independence of the results from the lateral domain size, the grid convergence study, and the validation of the numerical framework are provided in appendix A.2. Parts of the results shown in this section are presented in the author's publications [81, 85]; cited passages from these publications are placed in quotation marks.

5.3.1 Mean flow description

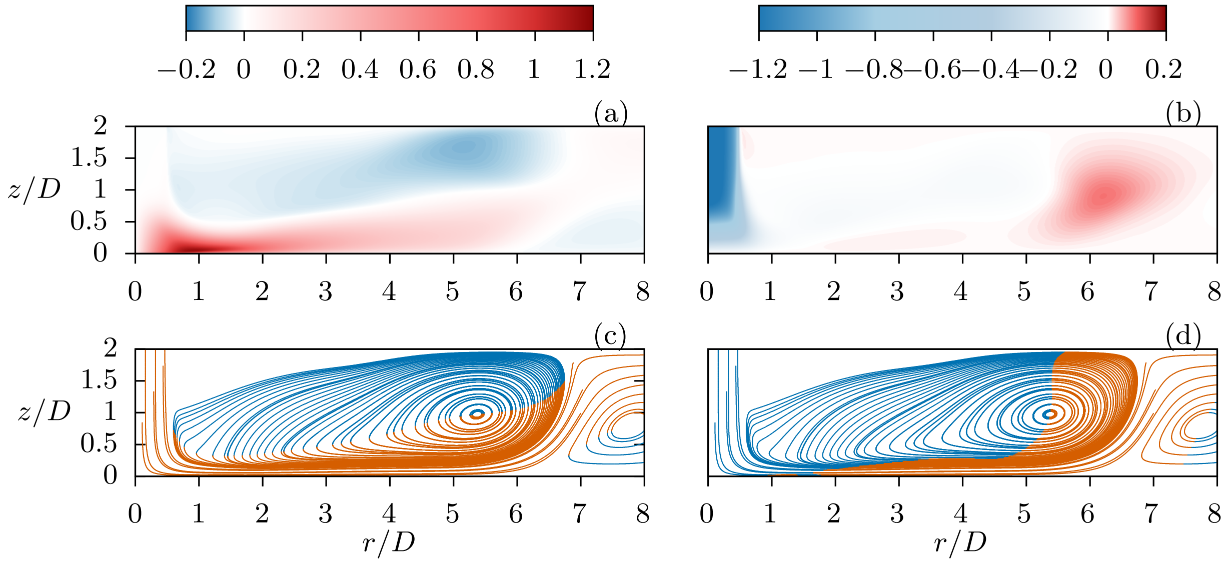

Figure 5.18: Illustration of the mean velocity field. (a) The mean radial velocity, denoted as $\langle\overline{u_r}\rangle^*$. (b) The mean axial velocity, represented by $\langle\overline{u_z}\rangle^*$. Panels (c) and (d) present streamlines corresponding to the mean velocity field. These streamlines are colour-coded to distinguish different regions: in panel (c), orange indicates positive values and blue represents negative values of the mean radial velocity $\langle\overline{u_r}\rangle^*$; similarly, in panel (d), the same colour scheme is applied to visualize the positive and negative values of the mean axial velocity $\langle\overline{u_z}\rangle^*$. Figure adapted from [85].

The macroscopic structure of the mean flow is visualized in figure 5.18 through the time- and space-averaged radial and axial velocity components, $\langle\overline{u_r}\rangle^*$ and $\langle\overline{u_z}\rangle^*$, respectively. Here and in the following, angular brackets denote averaging in the circumferential direction, and the $*$ superscript denotes normalization with $\overline{U}_b$ and D. The colour maps in panels (a) and (b) of figure 5.18 evidence the free jet region, which features a highly negative mean axial velocity, $\langle \overline{u_z} \rangle^*$, near the jet axis, and the wall jet region, characterized by strong mean radial velocities near the impingement plate. Selected streamlines of the mean flow are shown in panels (c) and (d) of figure 5.18 and are used to clarify the structure of the mean flow. As observed by Secchi et al. [85], the latter is characterized by two large-scale recirculating regions; the primary recirculating cell is centred at $r \approx 5.4D$ and $z \approx D$ and forms due to the continuous momentum supply from the wall jet and the no-slip boundary conditions on the confinement and impingement plates. The secondary recirculating zone appears near the open boundary of the computational domain, causing inflow through the lower half and outflow through the upper half of this boundary. However, the velocity magnitude in this region remains relatively low, reaching at most $\approx 5\%$ of the mean bulk velocity of the free jet.

The presence of the main recirculating cell has been observed by different authors in the literature (see, for instance, the review of Jambunathan et al. [40]). The recent experimental measurements of Chen et al. [10] also highlight the formation of the primary recirculating cell under similar boundary conditions to those of the present study. This is shown in figure 5.19, where selected streamlines of the mean flow are compared to those reported in [10]. Although some noticeable differences are evident, a qualitatively good agreement is observed between the present DNS data and the experimental measurements. The remaining differences are likely to be associated with slight discrepancies between the present configuration and that in [10]. In particular, Chen et al. [10] address a slightly different Reynolds number ($Re_b = 5084$), and the authors report that flow statistics at the inlet section of the jet domain depart from those associated with a jet issuing from a fully-developed turbulent pipe flow. Further, it is remarked that differences can also originate from the unavoidable uncertainties introduced by the modelling of the lateral open boundary of the computational domain [75]. In this respect, the independence of the present results on the domain size is further detailed in the appendix A.2. Further comparison with experimental literature data and details about the independence of the results on the mesh resolution and on the time averaging window are reported in the appendix A.2.

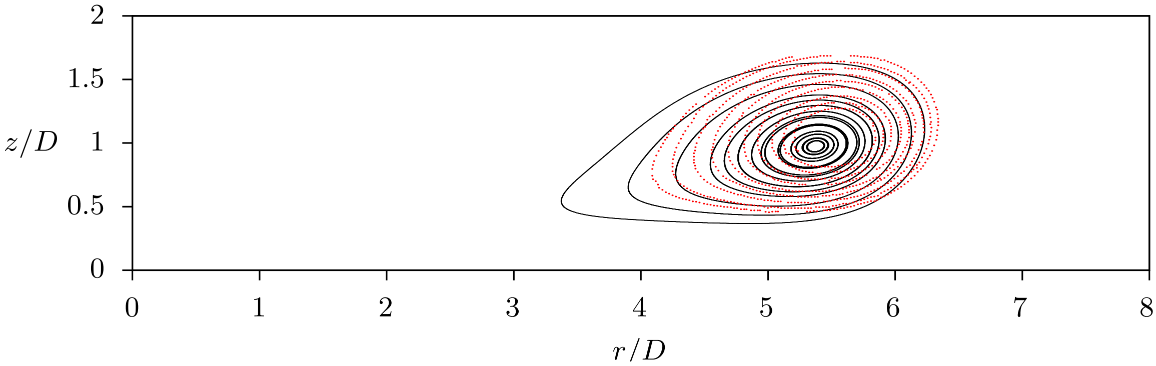

Figure 5.19: Selected streamlines of the mean velocity field. Black lines, present DNS; red symbols, data from Chen et al. [10]. Figure adapted from [85].

Mean radial velocity profiles at selected radial stations are reported in figure 5.20. "[The] mean profiles well represent the characteristic shape of a wall-jet that is generated by the injection of high momentum fluid through a narrow gap between a solid wall and a quiescent fluid. Such a momentum inflow determines a two-layered flow in which the maximum velocity is attained in a region of the flow bounded by an inner wall-boundary layer and an outer free-shear flow. In the present case, it must be noted that the outer region of the flow is not characterized by a perfectly quiescent fluid, but rather, by a mild back-flow which is induced, in the upper part of the domain, by the primary recirculating cell [...]. Due to the recirculating

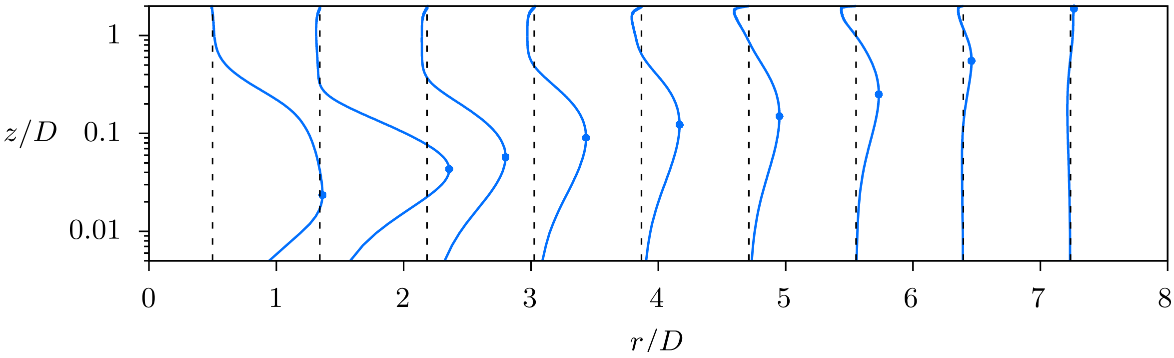

Figure 5.20: Mean radial velocity profiles at selected radial stations. Symbols denote the maxima of the mean radial velocity at each radial location. Black-dashed vertical lines indicate the radial location at which the profiles are sampled. Figure adapted from [85].

flow, a wall jet also develops on the confinement plate, whose direction opposes that developing along the impingement plate, and with comparatively little streamwise momentum" (from Secchi et al. [85]).

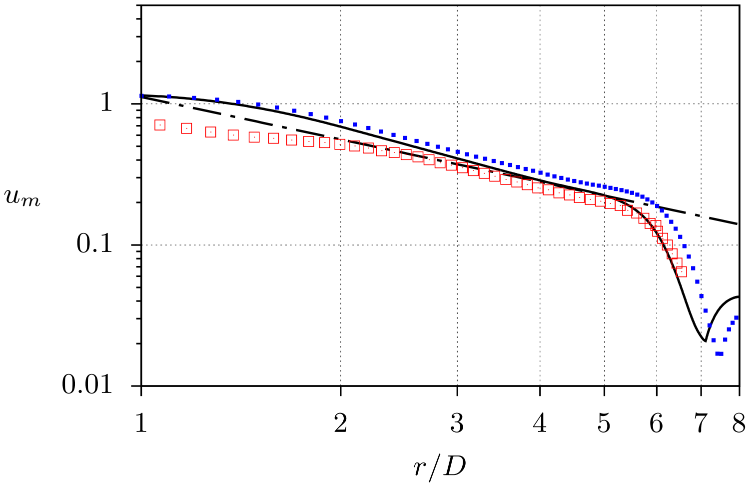

Figure 5.21: Radial distribution of the mean radial velocity maxima, u_m. The solid black line (———) represents the results obtained from the present DNS. Red squares correspond to the data from [10]. Blue symbols are from [81] (case $J00$ in table 5.5). The black dashed line represents the curve $1.12/(r/D)$. Figure adapted from [85].

As stated in section 3.3, the wall normal distance, δ_m, at which the mean radial velocity reaches its maximum, u_m, is a representative measure of the boundary layer thickness that develops along the impingement plate. A suitable velocity scale for the outer flow in the boundary layer is u_m. In fact, it is standard practice to use these quantities as characteristic physical scales in the analysis of wall jets [52]. Note that, for each mean radial velocity profile shown in figure 5.20, the corresponding velocity maximum value is also highlighted. As argued in section 3.3, the mean radial velocity maxima are constrained to develop radially as $u_m \sim r^{-1}$ as a consequence of mass conservation. This hypothesis is tested in figure 5.21, which shows the radial distribution of u_m for the present DNS, together with experimental data of Chen et al. [10] at $Re_b = 5084$, and the DNS data of Secchi et al. [81] at $Re_b = 10\,000$. The data shows that the magnitude of the radial velocity maxima is not particularly sensitive to changes in the bulk Reynolds number of the jet. Further, it is evident that the radial decrease of u_m follows a behaviour that closely matches the predicted decay $\sim r^{-1}$, especially in the range $3D \lesssim r \lesssim 5D$.

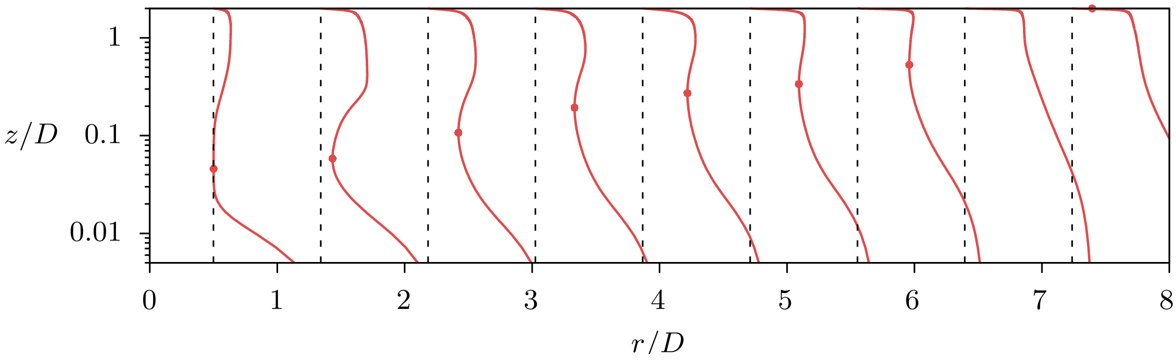

Figure 5.22: Mean scalar profiles at selected radial stations. Symbols denote the minima of the mean scalar, ϑ_m at each radial location. Black-dashed vertical lines indicate the radial location at which the profiles are sampled. Figure adapted from [85].

Mean scalar profiles at selected radial locations are shown in figure 5.22. Due to the different boundary conditions on the scalar and velocity fields at the impingement and confinement plates, the mean scalar profiles are dissimilar to the mean radial velocity profiles shown, at the same radial locations, in figure 5.20. At the impingement plate the scalar is prescribed to be $\vartheta_w = 1$, whereas at the confinement plate, the scalar is $\vartheta_T = 0$. The jet carries low concentration scalar near the impingement plate and, as the flow develops in the wall jet, the low concentration scalar is seen to determine the formation of local minima in the mean scalar profiles of figure 5.22. The local minima, ϑ_m, and their wall normal location, δ_m^ϑ, are suitable scalar and length scales to characterize the scalar boundary layer. As argued in section 3.3, the mean scalar minima, ϑ_m, are not constrained by mass conservation to follow a power law radial decrease $\sim r^{-1}$. In fact, ϑ_m is expected to grow with the radial distance, for the mean scalar is expected to increase due to the scalar exchange with the impingement plate. This is verified in figure 5.23, where the radial distribution of ϑ_m is shown. Note that, ϑ_m is shown only up to $r \approx 6D$, as at greater radial distances the mean scalar profiles do not exhibit local minima any more. Overall, the figure shows that ϑ_m increases in intensity with the radial distance; at small radial distances, where the scalar transfer is particularly intense, its increase is relatively fast, whereas a lower increase is observed for $r \gtrsim 3D$.

According to the estimates (3.65) and (3.66), the velocity and scalar boundary layer thicknesses are expected to grow linearly with the radial distance. δ_m/r and δ_m^ϑ/r are shown, as functions of the radial distance, in figure 5.24. The figure shows that the boundary layer thicknesses reach an approximately linear radial growth in the range $3D \lesssim r \lesssim 5D$, where δ_m/r and δ_m^ϑ/r become approximately constant. It is observed that, over the same range, the mean radial velocity maxima exhibit, approximately, a power law decay $\sim r^{-1}$, thus supporting the arguments exposed in section 3.3. Nevertheless, it is apparent that the velocity and scalar boundary layers have a markedly different thickness throughout the wall jet, with $\delta_m^\vartheta > \delta_m$. Yet, this result is not expected from the estimates 3.65 and 3.66, which predict similar boundary layer thicknesses provided that the the fluid has similar molecular momentum and scalar diffusivities (as is the present case, where a unit Prandtl number is assumed). It can be argued that the dissimilarity is driven by the different boundary conditions on the velocity and scalar fields at the two walls. “The different temperature boundary conditions on the bottom and top plates drive a [scalar] exchange, via molecular diffusion, which does not have an equivalent for the momentum transfer. This observation suggests the decomposition of the [scalar] field into $\vartheta = \vartheta_B + \Theta$; where ϑ_B is the base steady-state [scalar] distribution realized when

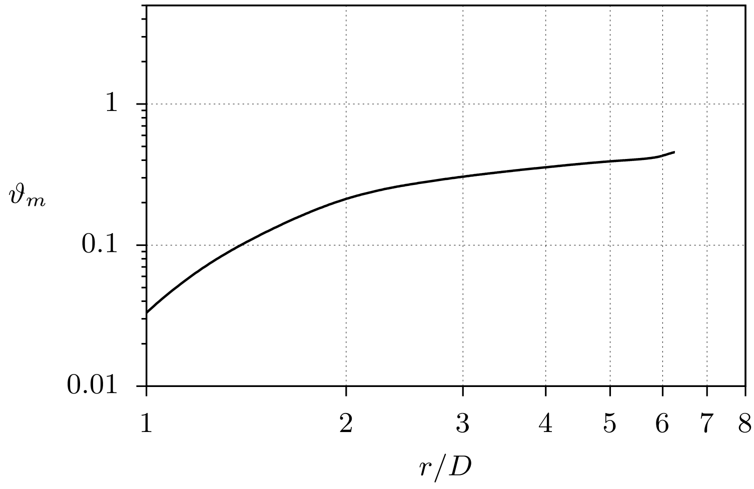

Figure 5.23: Distribution of the mean scalar minima, ϑ_m, as a function of the radial distance from the jet axis.

there is no flow. More precisely, it is the solution of $\alpha\vartheta_{B,ii} = 0$ with $\vartheta_B = 1$ at the impingement plate and $\vartheta_B = 0$ at the confinement plate [...]. In particular, it is given by $\vartheta_B = 1 - z/2$. On the other hand, Θ represents the local deviation of ϑ from the base solution, ϑ_B, and thus represents a measure of how strongly the flow affects the [scalar] field. Substituting $\vartheta = \vartheta_B + \Theta$ into [equation (2.9)] gives

$$\frac{\partial\Theta}{\partial t} + u_j\frac{\partial\Theta}{\partial x_j} = \frac{1}{Pe_b}\frac{\partial^2\Theta}{\partial x_j\partial x_j} + \frac{u_z}{2}, \tag{5.7}$$

with homogeneous boundary conditions for Θ on the bottom and top plates. Equation (5.7) shows that local deviations from the base [scalar] distribution, ϑ_B, are driven by the wall-normal velocity u_z" (from Secchi et al. [85]).

A boundary layer thickness can also be defined for the mean field $\langle\overline{\Theta}\rangle$. From Secchi et al. [85], "Along the impingement plate, the boundary layer thickness for $\langle\overline{\Theta}\rangle$ can be defined as the smallest wall-normal height, [δ_m^Θ], at which $\langle\overline{\Theta}\rangle$ has a stationary point (*i.e.* it has a minimum or a maximum)". The distribution of δ_m^Θ along the impingement plate is also shown in figure 5.24; Despite a weak decrease within the range $3D \lesssim r \lesssim 5D$, δ_m^Θ appears very similar in magnitude to δ_m.

5.3.2 Wall jet self similarity

Planar wall jets are self-preserving and velocity statistics show a self-similar character in the streamwise direction when scaled by suitable velocity and length scales. Several studies report on the self-similarity of velocity statistics scaled with the maxima of the mean streamwise velocity, u_m, and the wall normal height of their occurrence, δ_m [28, 52, 79]. In particular, based on theoretical arguments, George et al. [28] discuss that u_m and δ_m are suitable scales for normalizing velocity statistics in the outer layer of the wall jet. Their analysis explicitly assumes a high Reynolds number flow, so that sufficient separation of scales exists between viscosity-driven phenomena and large-scales of the outer flow. In practice, this assumption allows the distinction in the wall jet of an inner and an outer layer, which possibly interact through an overlap layer. For very high Reynolds numbers, the intrusion of the outer layer into the inner one should

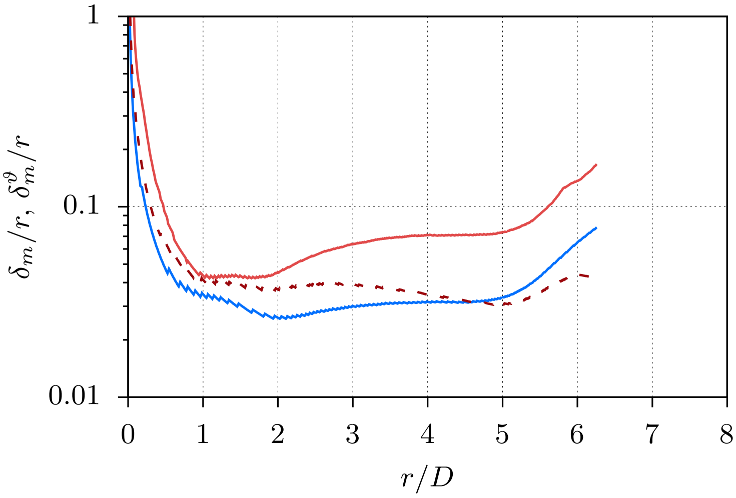

Figure 5.24: Boundary layer thicknesses along the impingement plate. ——, δ_m/r; ——, δ_m^ϑ/r; - - - - -, δ_m^Θ/r. Figure adapted from [85].

become marginal and the inner layer of the wall jet should resemble closely a canonical boundary layer flow. Hence, the characteristic velocity and length scales for the inner region of the wall jet should be the friction velocity, $u_\tau = (\tau_w/\rho)^{(1/2)}$, and the viscous length scale, $\delta_\nu = \nu/u_\tau$.

The extension of similarity arguments to radial wall jets is straightforward, in principle. Nevertheless, as discussed in sections 3.3 and 5.3.1, the radial expansion of the flow has tangible consequences on the radial distribution of mean flow statistics. These can be the result of the structural dissimilarities between planar and radial wall jets discussed in [7]. For impinging jets, the self-similar character of velocity statistics in the wall jet region has been investigated by the author in [81]. For smooth-wall impingement plates, self-similarity is observed, in a narrow range of radial distances, for the mean radial velocity profiles and Reynolds stresses scaled using both the outer region scales, u_m and δ_m, and the inner region scales, u_τ and δ_ν. The good collapse of the data in the inner and outer regions of the wall jet with both sets of scaling variables can be attributed to the very low Reynolds number achieved along the impingement plate. The lack of separation of scales between the two layers reflects into similar characteristic physical scales, which then lead to a similar collapse of the velocity statistics after normalization with either set of variables.

A similar result is observed for the present dataset; in particular, it is shown that an analogous scaling works also for the scalar statistics. Figure 5.25 reports velocity and scalar statistics scaled in inner layer variables. The normalization is denoted with a + superscript, as in the CPG channel flow (see section 3.1.1), since the scaling variables are the viscous units, u_τ, δ_ν and ϑ_τ. The wall normal profiles shown in the figure are sampled in the range $3D \leq r \leq 5D$. A very good collapse of the data is observed for the mean radial velocity (panel a), scalar (panel b), Reynolds stresses (panel c), and wall normal turbulent scalar fluxes (panel d) profiles, with minor scattering observed for the radial component of the Reynolds stress tensor. It is evident from panels (a, b) of figure 5.25 that the mean radial velocity and scalar profiles do not exhibit a logarithmic region, suggesting the limited separation of scales between the inner and the outer flow regions. This observation is consistent with the author's findings [81], whereby the lack of a distinguishable logarithmic region in the mean radial velocity profiles is observed for an even higher jet bulk Reynolds number, $Re_b = 10\,000$.

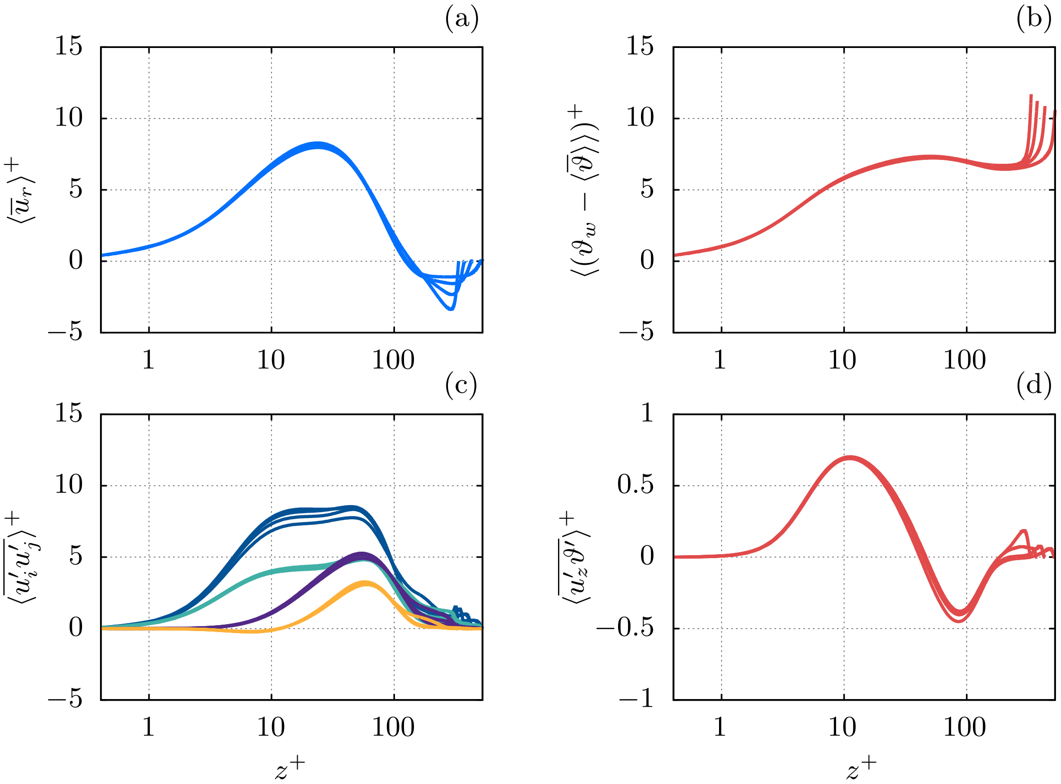

Figure 5.25: Inner units-scaled mean radial velocity profiles (a), mean scalar profiles (b), Reynolds stresses (c), wall normal turbulent heat flux (d). In panel (c), different colours indicate: ——, $\langle \overline{u_r'^2} \rangle^+$; ——, $\langle \overline{u_\phi'^2} \rangle^+$; ——, $\langle \overline{u_z'^2} \rangle^+$; ——, $\langle \overline{u_r' u_z'} \rangle^+$.

The scaling of velocity and scalar statistics in outer units, u_m, δ_m, and δ_m^ϑ, is reported in figure 5.26 for the same range of radial distances. A † superscript is used to denote outer units-scaled quantities. It can be observed that the normalization determines a good collapse for all the presented statistics throughout the wall jet thickness.

As discussed in section 5.3.2, the boundary layer developing along the impingement plate lacks sufficient separation of scales so that inner and outer layer regions cannot be unambiguously identified. The resulting flow statistics are likely to be affected by the strong interaction between the two layers. Naturally, for higher Reynolds number impinging jets, it can be expected for the flow along the impingement plate to also develop sufficient separation of scales and to eventually present features similar to those of a canonical boundary layer. However, data in the literature [34, 106] suggest that such an analysis would require the assessment of Reynolds number flows that are currently out of reach of DNS studies.

5.3.3 Mean momentum and scalar budgets

In this section the mean flow developing along the impingement plate is investigated by computing the budgets of the mean momentum and scalar equations (2.4) and (2.9) (with the volumetric forcing and

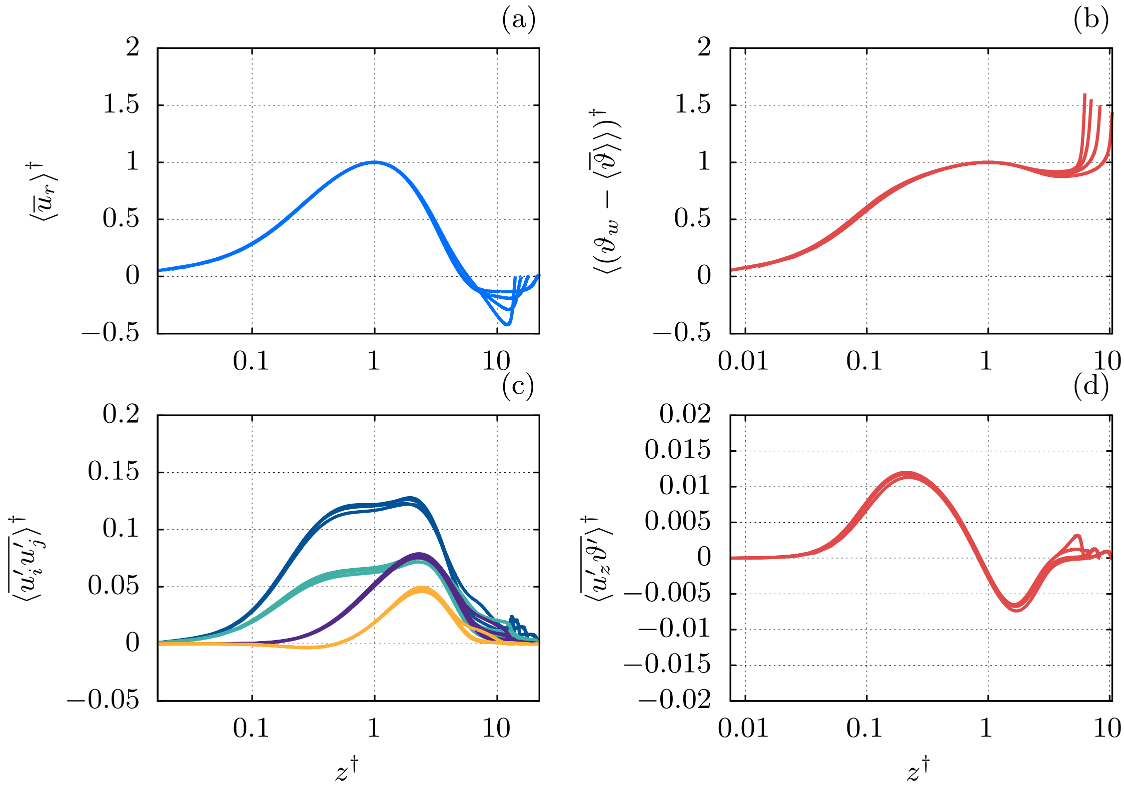

Figure 5.26: Outer units-scaled mean radial velocity profiles (a), mean scalar profiles (b), Reynolds stresses (c), wall normal turbulent heat flux (d). In panel (c), different colours indicate: ——, $\langle\overline{u_r'^2}\rangle^\dagger$; ——, $\langle\overline{u_\phi'^2}\rangle^\dagger$; ——, $\langle\overline{u_z'^2}\rangle^\dagger$; ——, $\langle\overline{u_r' u_z'}\rangle^\dagger$.

source terms, f_j and q set to zero). In particular, the following mean momentum and scalar equations are considered:

$$0 \approx \underbrace{-\left(\frac{1}{r}\langle r\overline{u_r^2}\rangle_{,r} + \langle\overline{u_r u_z}\rangle_{,z}\right)}_{NL_r} \underbrace{-\langle\overline{p}\rangle_{,r}}_{G_r} + \underbrace{\frac{1}{Re_b}\langle\overline{u_r}\rangle_{,zz}}_{V_r}, \tag{5.8a}$$

$$0 \approx \underbrace{-\left(\frac{1}{r}\langle r\overline{u_r u_z}\rangle_{,r} + \langle\overline{u_z^2}\rangle_{,z}\right)}_{NL_z} \underbrace{-\langle\overline{p}\rangle_{,z}}_{G_z}, \tag{5.8b}$$

$$0 \approx \underbrace{-\left(\frac{1}{r}\langle r\overline{u_r\vartheta}\rangle_{,r} + \langle\overline{u_z\vartheta}\rangle_{,z}\right)}_{NL_\vartheta} + \underbrace{\frac{1}{Pe_b}\langle\overline{\vartheta}\rangle_{,zz}}_{V_\vartheta}. \tag{5.8c}$$

Equation (5.8a) represents the Prandtl's boundary layer equation for the streamwise velocity component in a radial boundary layer. Unlike a canonical boundary layer, the present case requires equation (5.8b) to account for the possible existence of a wall-normal mean pressure gradient across the boundary layer developing along the impingement plate. Equation (5.8c) expresses the balance between scalar flux convection and the wall-normal molecular diffusion of the scalar field.

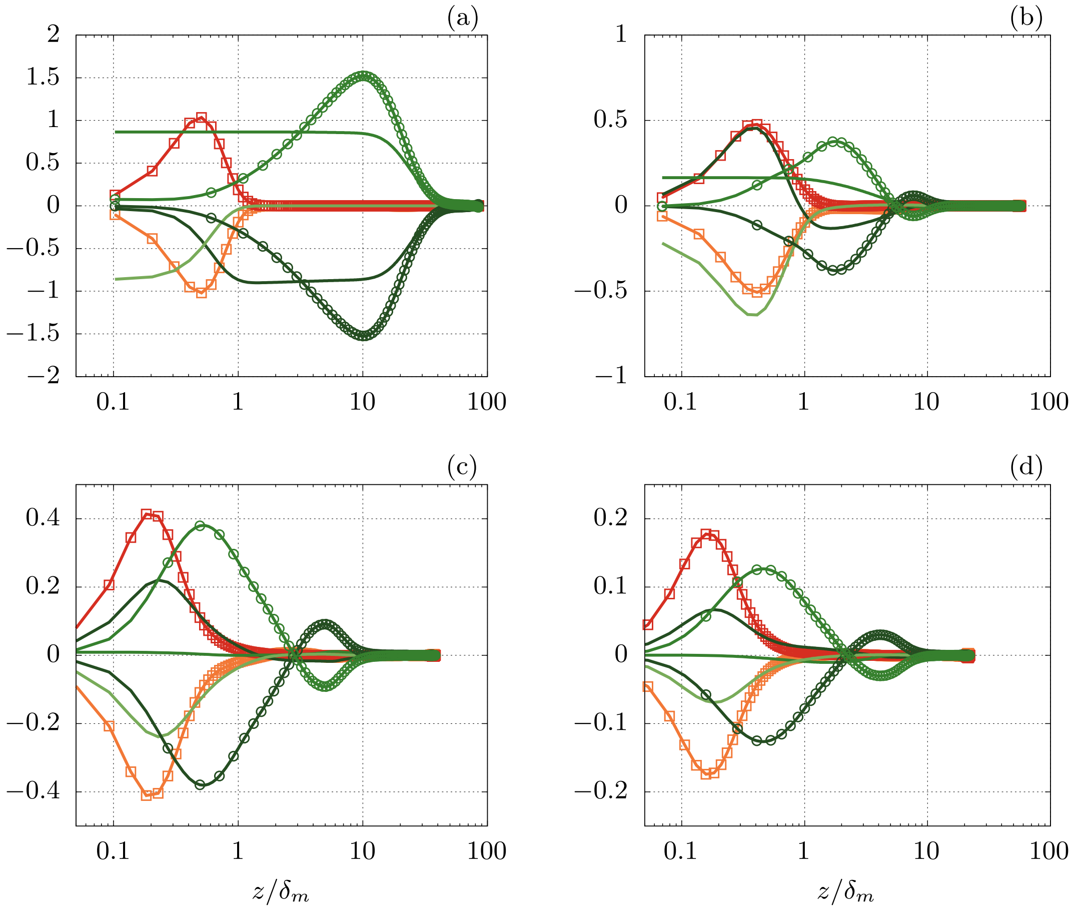

Figure 5.27: Mean momentum and scalar budgets at selected radial locations. (a) $r/D = 0.25$; (b) $r/D = 1$; (c) $r/D = 2$; (d) $r/D = 3$. ——, NL_r; ——, G_r; ——, V_r; —○—, NL_z; —○—, G_z; —□—, NL_ϑ; —□—, V_ϑ. Figure adapted from [85].

Figure 5.27 presents the individual terms of equations (5.8a), (5.8b), and (5.8c) as functions of the wall normal distance at various radial positions. To facilitate the distinction between the inner and outer layers of the wall jet, the abscissa in each plot is scaled by the boundary layer thickness δ_m. "[At] $r = 0.25D$ (figure [5.27a]), well within the stagnation region of the flow, a strong, favourable radial pressure gradient, G_r, exists which stays constant up to large distances from the wall, approximately up to [$z = 10\,\delta_m$]. For [$z < \delta_m$], the radial pressure gradient is balanced by the combined action of the advection, NL_r, and the wall-normal molecular diffusion of radial momentum, V_r, even though, for [$z \lesssim 0.3\delta_m$], the advection term becomes negligible. Conversely, in the outer region of the flow, for [$z > \delta_m$, V_r] becomes quickly negligible and the radial pressure gradient is balanced by the radial momentum advection alone. This scenario is observed further downstream of the stagnation region, at $r = D$ (panel b in the figure), where the radial pressure gradient still has a significant contribution to the momentum balance. However, with increasing radial distance from the jet axis (panels c and d in the figure display the budgets ad $r = 2D$ and $r = 3D$, respectively), the action of the radial pressure gradient becomes quickly negligible compared to the advection and molecular diffusion of radial momentum within the boundary layer. Hence, sufficiently

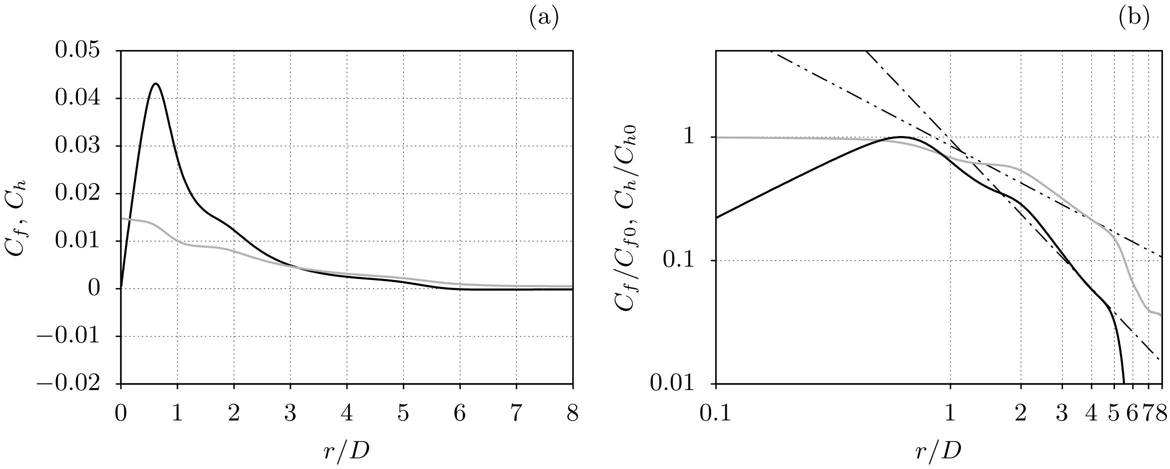

Figure 5.28: Mean friction and scalar transfer coefficients along the impingement plate. (a) ———, C_f; ———, C_h. (b) ———, C_f/C_{f0}; ———, C_h/C_{h0}; dash-dot line, $\sim (r/D)^{-2}$; dash-dot-dot line, $\sim (r/D)^{-1}$. Figure adapted from [85].

downstream of the stagnation region, for $r \gtrsim 1.5D$, the flow develops radially similarly to a zero pressure gradient boundary layer.

However, much differently form a canonical boundary layer, across the boundary layer thickness, the pressure does not remain constant. In fact, the mean wall-normal pressure gradient, G_z, is, in magnitude, comparable to the terms appearing in the mean momentum equation [(5.8a)] at every radial location, as shown in [figure 5.27]. Within the stagnation region, figure [figure 5.27a], the flow coming from the free-jet core experiences a strongly adverse pressure gradient which deflects the flow and aligns it parallel to the impingement wall. This process takes place essentially away from the boundary layer, so that the intrusion of the mean pressure gradient is only marginal for [$z < \delta_m$]. Nevertheless, downstream of the stagnation region (panels a, b and c in the figure), the penetration of the mean wall-normal pressure gradient into the boundary layer becomes apparent. The rise of a wall-normal pressure gradient within the wall jet region is a direct consequence of the recirculating flow structure, which was shown with the mean streamlines in panels c and d of figure 5.27. The mean, wall-normal directed, flow, entrained in the outer region of the wall jet, aligns along the radial direction through the action of an adverse pressure gradient, relative to the local flow direction, which is balanced by the streamwise advection of wall-normal momentum.

The mean [scalar equation (5.8c)] consists of the balance of simply two terms, NL_ϑ and V_ϑ, showing that in the inner layer of the wall jet, the convection of [scalar flux] balances the wall-normal molecular diffusion of the [scalar field]. Even if it is not shown in the plots of [figure 5.27], at sufficiently large radial distances, $r \gtrsim 2D$, the dominant term of NL_ϑ is that due to the wall-normal [scalar flux], namely $\langle \overline{u_z \vartheta} \rangle_{,z}$, whereas $\langle r\overline{u_r \vartheta} \rangle_{,r}/r$ is negligible at the same radial locations. Thus, at large radial distances, the wall-normal molecular diffusion of the [scalar] is balanced by the wall-normal [scalar flux] alone. The same scenario does not occur for the radial momentum equation (5.8a), in which case all terms, except the radial pressure gradient term, remain of comparable magnitude at large radial distances" (from Secchi et al. [85]).

5.3.4 Momentum and scalar wall fluxes

The structure of the flow near the impingement plate influences the distributions of the mean momentum and scalar fluxes at the wall. These are depicted in figure 5.28a in terms of the friction and scalar transfer coefficients defined in equations (3.63) and (3.64), respectively. In the stagnation region of the flow, the scalar flux at the wall reaches its maximum, whereas the friction coefficient approaches zero as the radial distance decreases. In this region, the mean momentum and scalar behaviours exhibit notable differences. The deflection of the flow, which involves a redistribution of wall-normal momentum into radial momentum, occurs due to the influence of the pressure field, which does not directly affect the scalar field.

As the flow accelerates radially, the friction coefficient increases rapidly with radial distance, reaching a peak at $r \approx D/2$, before decreasing further downstream as the flow expands and decelerates radially. Ultimately, at $r \approx 5.8D$, flow separation occurs, and the skin friction coefficient becomes negative. In contrast, the scalar transfer coefficient decreases from the stagnation region onward, except in the range $r \approx 1.5D - 2D$, where a bump in C_h distribution appears. Notably, in this same region, C_f exhibits a similar trend. It is well-established in the literature [for instance, 14] that in this region, a secondary peak in the scalar transfer rate arises due to the unsteady interaction of coherent vortical structures with the wall. However, under the present conditions, this secondary peak is not yet well-developed. Nevertheless, it is interesting to observe that, downstream of this region, the mean distributions of C_f and C_h become more similar, even though for $r \gtrsim 3D$, C_h significantly exceeds C_f in magnitude. Furthermore, near and downstream of the flow separation, the two distributions differ substantially.

The distributions of C_f and C_h, normalized by their respective maxima, C_{f0} and C_{h0}, are useful for highlighting differences in the evolution of the mean radial momentum and scalar wall-fluxes along the impingement plate. These distributions, shown in figure 5.28b, emphasize two primary regions where dissimilar behaviour is observed. In the stagnation region, as the radial distance increases, the wall scalar transfer gradually decreases from its peak value at the jet centreline, in contrast to the rapidly increasing wall-normal momentum flux. In the wall jet region, for $2D \lesssim r \lesssim 5D$, both the friction coefficient and the scalar transfer coefficient decrease following a power law behaviour, consistent with the experimental observations of Woodworth et al. [103]. Despite the similar magnitude of C_f and C_h, as seen in figure 5.28a, their decay rate along the radial direction differs significantly.

This discrepancy can be explained by considering an order-of-magnitude analysis of the momentum and scalar equations, (5.8a) and (5.8b), in the boundary layer. This analysis is reported in section 3.3 of the present work. The crucial aspect of the analysis is realizing that, due to mass conservation, the outer velocity scale, u_m, is constrained to decrease radially as $\sim r^{-1}$, at least in a region where the wall jet has reached a self-preserving character. In the present flow, this occurs, approximately, in the range $3D \lesssim r \lesssim 5D$, as shown in sections 5.3.1 and 5.3.2. The result predicts the mean momentum and scalar fluxes to decrease according to the estimates (3.67) and (3.68), and, thus the friction and scalar transfer coefficients are expected to decrease as $C_f \sim r^{-2}$ and $C_h \sim r^{-1}$. A behaviour that is approximately well-matched by the present data in the range $3D \lesssim r \lesssim 5D$, as observed in figure 5.28b.

5.3.5 Mechanical energy and squared-scalar budgets

The analysis on the energetics of impinging jets, presented from a theoretical perspective in section 3.3, is applied to the available DNS data. In particular, the mean mechanical energy and squared-scalar budget equations (3.69) and (3.70) are applied to control volumes, similar to that depicted in figure 3.5, of increasing radial size. The computed budget terms for the mechanical energy balance, (3.69), are shown in figure 5.29. Note that the molecular diffusion of mechanical energy, $\mathcal{D}$, is negligible compared to the other terms in the budget and, therefore, it is not reported in the figure. “The power input to the system, Π_{IN} is fixed by the prescribed inflow condition at the nozzle exit section. For increasing r, the power input gets consumed by the bulk energy dissipation, $\mathcal{E}$, thus determining the decrease of the output power, Π_{OU}, which represents the available mechanical power for the downstream flow. For $3D \lesssim r \lesssim 5D$, Π_{OU}

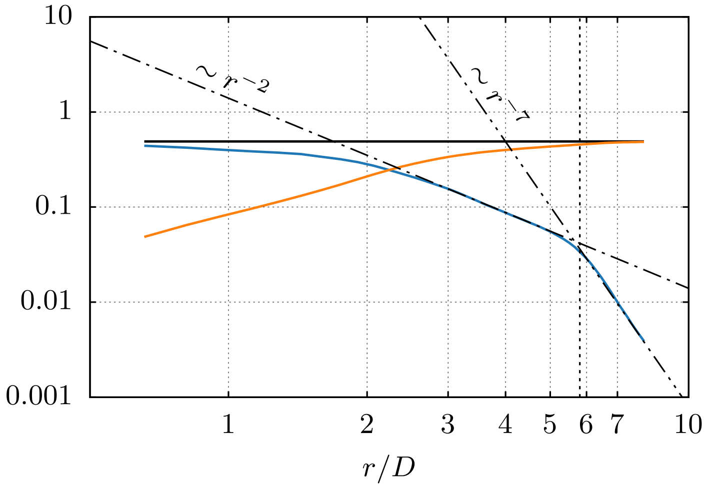

Figure 5.29: Mechanical energy integral budget for control volumes, $\mathcal{V}(r)$ of increasing radius. ———, Π_{in}; ———, Π_{out}; ———, $\mathcal{E}$. A black-dashed line indicates the radial location of flow separation on the impingement plate. Figure adapted from [85].

clearly exhibits a power-law decay $\Pi_{OU} \sim r^{-2}$. This behaviour can be explained by assuming that the mean convection of mechanical energy, $\langle \overline{Bu_r} \rangle$, scales with $u_m^3 \sim r^{-3}$, based on the same arguments as in [section 3.3]. Downstream of the separation point, for $r \gtrsim 5.8D$, the radial rate of decay of Π_{OU} increases further, as Π_{OU} tends to vanish with the radial distance as $\sim r^{-7}$" (from Secchi et al. [85]).

The mean squared-scalar budget terms of equation (3.70) are shown in figure 5.30 for the present data. As observed in 3.3, the mean molecular flux of the squared-scalar field at the wall is directly related to the exchanged scalar power at the impingement plate, Π^{ϑ}_{IN}, as stated by equation (3.71). Given that, in the present case $\vartheta_w = 1$, $\Pi^{\mathcal{G}}_{IN}$ is numerically equal to Π^{ϑ}_{IN}. With reference to figure 5.30, the latter increases with increasing the radial extension of the control volume, due to the increasing surface area over which the scalar transfer takes place. Further, "at small radial distances, for $r \lesssim 2D$, the convection of $\overline{\mathcal{G}}$ across $\mathcal{A}_L(r)$ is significantly smaller than the other terms, and $\vartheta_w \Pi^{\theta}_{IN} \approx \mathcal{E}^{\mathcal{G}}(r)$. Namely, near the impingement region, all the [scalar power] extracted at the impingement plate goes into the bulk dissipation of $\overline{\mathcal{G}}$. For larger control volumes, the flow becomes increasingly less capable of dissipating the net [scalar] power input across the impingement plate, and the convection of $\overline{\mathcal{G}}$ across $\mathcal{A}_L(r)$, $\Pi^{\mathcal{G}}_{OU}$, becomes relevant for large r/D" (from Secchi et al. [85]).

5.3.6 Scalar transfer efficiency

The energetic balances presented in the previous section can be used to further investigate the scalar transfer efficiency of the system. Jet impingement is known to produce very high scalar transfer rates, especially in the stagnation region of the flow. This is also seen in the friction coefficient and the scalar transfer coefficient distributions in figure 5.28, where it is observed that the scalar transfer coefficient number reaches its maximum at the jet axis, whereas the friction coefficient goes to zero over the same area. Other regions of the impingement plate exhibit dissimilar mean momentum and scalar wall fluxes, with one of the two exceeding significantly the magnitude of the other. Yet, this plot does not provide information about the energetic cost required to sustain the observed scalar transfer distribution.

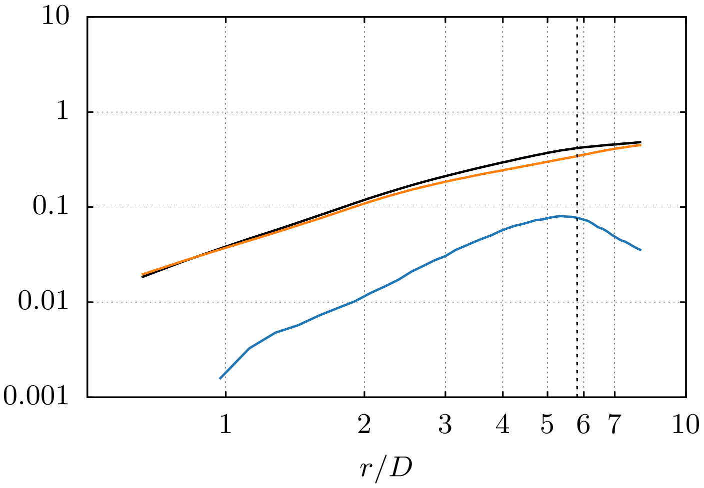

Figure 5.30: Mean squared-scalar, $\overline{\mathcal{G}}$ budget for control volumes, $\mathcal{V}(r)$ of increasing radius. ———, $\theta_w \Pi_\theta$; ———, $\Pi_{\mathcal{G}\,out}$; ———, $\mathcal{E}_{\mathcal{G}}$. A black-dashed line indicates the radial location of flow separation on the impingement plate. Figure adapted from [85].

The scalar transfer efficiency can be measured through the Reynolds analogy efficiency factor, RA_π, defined in equation (3.76). The radial distribution of RA_π is shown in figure 5.31a. The figure reports also the distribution of the Reynolds analogy efficiency factor that is obtained by considering only the scalar flux at the impingement plate, *viz.* using equation (3.77). Furthermore, a third distribution of the Reynolds analogy efficiency factor is computed using (3.77) and subtracting the net scalar flux associated with the base passive-scalar ϑ_b (defined in section 5.3.2), thus removing from the scalar transfer efficiency computation the scalar flux that is present also with the fluid at rest. In practice, in the latter case, RA_π represents a comparison between the net scalar wall flux increment driven by the flow and the mechanical power necessary for the sustainment of the flow.

In either case, figure 5.31a shows that the scalar transfer efficiency of the system "is significantly smaller than unity for any considered size of the control volume $\mathcal{V}(r)$, suggesting that jet impingement is not an energetically efficient means for [exchanging a scalar at a solid surface]. This result is particularly interesting, given that jet impingement is usually referred to as an example of a Reynolds analogy breaking flow, for a finite wall [scalar] transfer is realized in the stagnation region in spite of a vanishingly small wall-shear stress. Indeed, as reported in [section 5.3.4], for $r \lesssim D/2$ the [wall scalar flux] significantly exceeds the wall momentum flux. However, such high [scalar transfer] rates are realized at a comparatively higher mechanical energy expense. As a result, at small radial distances, a very low [scalar transfer] efficiency is observed, with $\eta < 0.6$ for $r \lesssim 2.5D$. For increasing the radial extent of the control volume $\mathcal{V}(r)$, the [scalar transfer] efficiency increases at different rates depending on the considered flow region and, particularly, the increase is approximately linear in the range $3D \lesssim r \lesssim 5D$. Notably, in correspondence of the separation point, the efficiency is still appreciably less than unity" (from Secchi et al. [85]).

To gain localized insights into the integral balances at different radial positions, the preceding analysis can be applied to control volumes in the form of hollow circular cylinders. These cylinders are coaxial with the jet axis, with their bottom and top surfaces located on the impingement and confinement plates, respectively. The volume of such a cylinder is expressed as $[\mathcal{V}(r)] = \mathcal{V}(r + \Delta r/2) - \mathcal{V}(r - \Delta r/2)$, where $[\cdot]$ denotes the variation of a quantity computed over the control volumes of the circular cylinders $\mathcal{V}(r + \Delta r/2)$

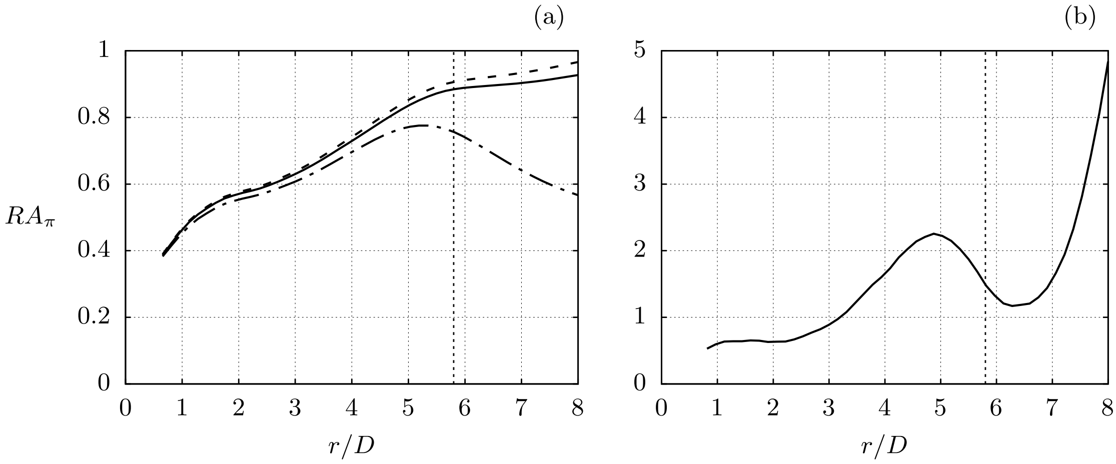

Figure 5.31: (a), Reynolds analogy efficiency factor, RA_π, for control volumes, $\mathcal{V}(r)$ of increasing radius. Dashed-line, equation (3.77); solid line, equation (3.77) without including the constant scalar flux associated with the base solution, ϑ_B; solid dashed-line, equation (3.76). (b), local Reynolds analogy efficiency factor for control volumes $[\mathcal{V}(r)]$ computed with equation (3.77) without including the constant scalar flux associated with the base solution, ϑ_B. In both panels, a vertical black dashed line marks the radial position of flow separation on the impingement plate. Figure adapted from [85].

and $\mathcal{V}(r - \Delta r/2)$. For such control volumes, figure 5.31b reports the Reynolds analogy efficiency factor, RA_π, computed only considering the net scalar flux at the impingement plate and removing the scalar flux associated with the base solution, ϑ_b. For $r \lesssim 3D$, the flow-driven enhancement of scalar transfer is notably inefficient, as the mechanical power dissipated within $[\mathcal{V}(r)]$ greatly exceeds the scalar power exchanged at its base. In contrast, at larger radial distances, RA_π rises above unity, reaching a local maximum of $RA_\pi \approx 2.3$ at $r \approx 5D$. Interestingly, in the wall jet region ($r \gtrsim 3D$), the dissipation of mechanical energy is relatively low compared to the scalar transfer enhancement at the impingement plate. Beyond the local peak, as the flow approaches separation, RA_π declines to a global minimum of approximately 1.3 just downstream of the separation point. At even greater radial distances, despite the diminishing availability of mechanical energy, scalar transfer at the base of $[\mathcal{V}(r)]$ remains significant, as reflected in the sharp increase of RA_π for $r \gtrsim 6.5D$.

Focusing on the region upstream of the separation point, a parallel can be drawn between the local Reynolds analogy efficiency factor distributions in figure 5.31b and that of the zero pressure gradient boundary layer in figure 5.17. The boundary layer shows an efficiency factor greater than one even for the smooth wall case. In that case, the upward moving flow, generated by the wall friction-induced boundary layer thickening, determines a net scalar flux that exceeds the dissipated mechanical energy. A similar scenario is seen for the impinging jet for $r \gtrsim 3D$, where the wall jet thickens even more drastically due to the radial expansion of the flow. This can be seen, for instance, in the coloured streamlines of figure 5.18d, which evidence the net dominance of upward moving fluid in the near wall region at these radial locations. Correspondingly, the local Reynolds analogy efficiency factor increases rapidly, to values larger than $RA_\pi = 1$, until reaching its local maximum. In contrast, radial distances $r \lesssim 2D$ are dominated by negative wall normal velocities in the near wall region. Although these generate high local heat transfer rates, they are produced in spite of a much higher mechanical energy dissipation; as a result, figure 5.31b evidences a local Reynolds analogy efficiency factor significantly less than unity.

5.3.7 Mechanical energy and squared-scalar dissipation rates

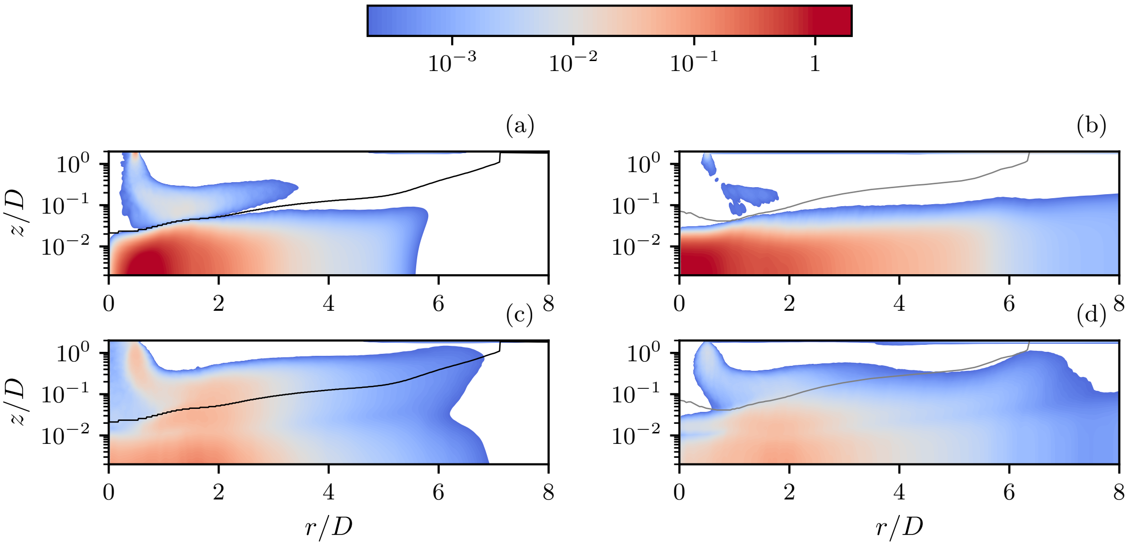

Figure 5.32: Mean and turbulent dissipation rates. (a), $\langle\overline{\omega_i}\;\overline{\omega_i}\rangle/Re$; (b), $\langle\overline{\theta_{,i}}\;\overline{\theta_{,i}}\rangle/Pe$; (c), $\langle\overline{\omega_i'\omega_i'}\rangle/Re$; (d), $\langle\overline{\theta_{,i}'\,\theta_{,i}'}\rangle/Pe$. ———, z_m/D; ———, $z_{\theta\,m}/D$. Figure adapted from [85].

The integral dissipation rates, $[\mathcal{E}]$ and $\left[\mathcal{E}^{\mathcal{G}}\right]$, are relevant for the assessment of the scalar transfer efficiency of the system. The former quantifies the total mechanical power dissipated within $[\mathcal{V}]$, while the latter can be related with the scalar flux across its base. To gain further insight, it is useful to examine the time-averaged mechanical and scalar dissipation fields, $\nu\overline{\omega_i\omega_i}$ and $\alpha\overline{\theta_{,i}\,\theta_{,i}}$, respectively. The Reynolds decomposition of these quantities enables the assessment of the mean- and turbulent-flow contributions to a dissimilar momentum and scalar transfer. This comparison is done in figure 5.32, which shows the mean-flow, $\nu\langle\overline{\omega_i}\;\overline{\omega_i}\rangle$ and $\alpha\langle\overline{\vartheta_{,i}}\;\overline{\vartheta_{,i}}\rangle$, and the turbulent-flow, $\nu\langle\overline{\omega_i'\omega_i'}\rangle$ and $\alpha\langle\overline{\vartheta_{,i}'\,\vartheta_{,i}'}\rangle$, contributions to the time-averaged dissipation fields, $\nu\overline{\omega_i\omega_i}$ and $\alpha\overline{\vartheta_{,i}\,\vartheta_{,i}}$. The visualizations focus on the near wall region, since the dissipation fields are the highest in this region. In the figure, the boundary layer thicknesses, δ_m and δ_m^{ϑ}, are also shown.

“The mean flow contributions exhibit evident differences across the entire flow domain. The main difference occurs within the stagnation region of the flow, where the mean scalar dissipation reaches its global maximum in correspondence with the jet axis; conversely, $\nu\langle\overline{\omega_i}\;\overline{\omega_i}\rangle$ becomes maximum further downstream of it, around $r \approx D/2$. This dissimilarity is driven by the fact that in the stagnation region, momentum is predominantly affected by the action of the pressure which determines the deflection of the flow along the impingement plate. Consequently, the fluid near the wall is characterized by low streamwise-momentum, and, in turn, the molecular momentum flux at the wall remains small close to the jet axis. In contrast, the [fluid scalar concentration] is not directly affected by the action of the pressure field, thus allowing cold, low-momentum- fluid to approach the impingement plate and to determine intense wall-normal [scalar] gradients, which result in high [scalar transfer] rates. The strong radial acceleration of the mean flow produces high shear in the vicinity of the wall which reflects into large values of the mean mechanical and scalar dissipation rates. Note that $\nu\langle\overline{\omega_i}\;\overline{\omega_i}\rangle$ peaks in this region at $r \approx D/2$. Further downstream, the flow decelerates in the radial direction and the mean mechanical and scalar dissipation rates consequently decrease. A region of apparent dissimilarity between the mean mechanical and scalar dissipation rates occurs where flow separation takes place, at $r \approx 5.8D$. There, a vanishingly small $\nu\langle\overline{\omega_i}\;\overline{\omega_i}\rangle$ is observed, in contrast to $\alpha\langle\overline{\vartheta_{,i}}\;\overline{\vartheta_{,i}}\rangle$ which remains visibly larger over the same region. Away from the boundary layer, the mean mechanical and scalar dissipation rates are large in the region of the shear layer of the free jet and in the outer shear layer of the wall jet. It is interesting to observe that $\nu\langle\overline{\omega_i}\;\overline{\omega_i}\rangle$ appears more intense than $\alpha\langle\overline{\vartheta_{,i}}\,\overline{\vartheta_{,i}}\rangle$ in these flow regions, indicating that the mean scalar distribution tends to be more diffused across these shear layers, compared to the mean momentum components

The distributions of the turbulent dissipation rates of mechanical energy and $\overline{\mathcal{G}}$, $\nu\langle\overline{\omega_i'\omega_i'}\rangle$ and $\alpha\langle\overline{\vartheta_{,i}'\,\vartheta_{,i}'}\rangle$, are shown in [figure 5.32(c, d)]. In both cases, the turbulent contribution to the dissipation fields is qualitatively similar, especially within the boundary layers thickness, where the dissipation rates show a two-layered structure in which two regions of high values of $\nu\langle\overline{\omega_i'\omega_i'}\rangle$ and $\alpha\langle\overline{\vartheta_{,i}'\,\vartheta_{,i}'}\rangle$ are separated by local minima. From the figure it can be appreciated how the wall-normal height of these local minima increases with the radial distance from the jet axis. The turbulent contributions to the dissipation rates are maxima at the wall and reach their highest values within the range $D \lesssim r \lesssim 2.5D$. Over the same range, $\nu\langle\overline{\omega_i'\omega_i'}\rangle$ and $\alpha\langle\overline{\vartheta_{,i}'\,\vartheta_{,i}'}\rangle$ show very large intensities also at large wall-normal distances, and, in the case of $\nu\langle\overline{\omega_i'\omega_i'}\rangle$, even outside of the boundary layer, in the outer region of the wall-jet” (from Secchi et al. [85]).

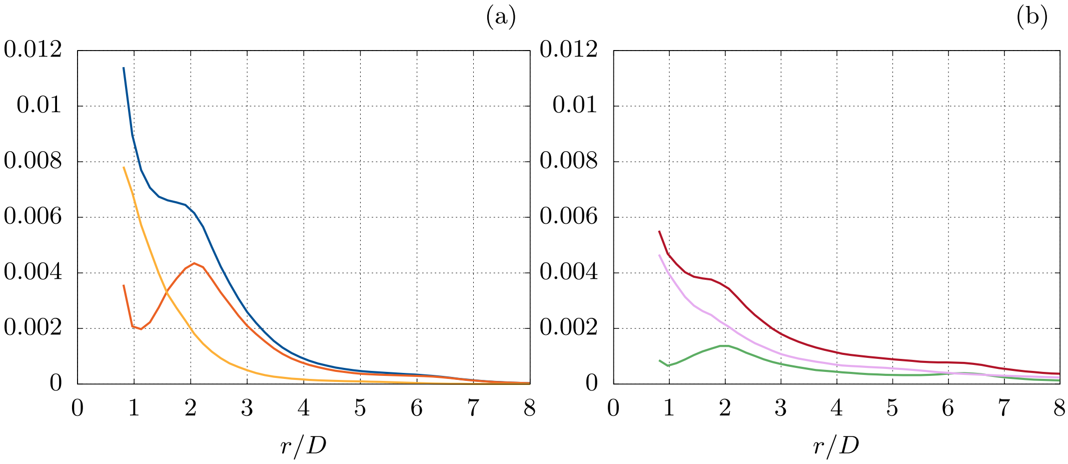

Figure 5.33: Mean and turbulent contributions to the mechanical (a) and squared-scalar (b) bulk dissipation rates. ——, $[\mathcal{E}]$; ——, $[\mathcal{E}^m]$; ——, $[\mathcal{E}^t]$; ——, $[\mathcal{E}_{\mathcal{G}}]$; ——, $[\mathcal{E}_{\mathcal{G}}^m]$; ——, $[\mathcal{E}_{\mathcal{G}}^t]$. Figure adapted from [85].

The observations about the mean- and turbulent-flow dissipation rates are made quantitative by considering their integral contributions, $[\mathcal{E}] = [\mathcal{E}^m] + [\mathcal{E}^t]$ and $\left[\mathcal{E}^{\mathcal{G}}\right] = \left[\mathcal{E}^{\mathcal{G}m}\right] + \left[\mathcal{E}^{\mathcal{G}t}\right]$, where the superscripts m and t indicate, respectively, the mean and turbulent components. More precisely, $\mathcal{E}^m = \int_{\mathcal{V}(r)} \nu\langle\overline{\omega_i}\;\overline{\omega_i}\rangle\,\mathrm{d}\mathcal{V}$, $\mathcal{E}^{\mathcal{G}m} = \int_{\mathcal{V}(r)} \alpha\langle\overline{\vartheta_{,i}}\;\overline{\vartheta_{,i}}\rangle\,\mathrm{d}\mathcal{V}$, $\mathcal{E}^t = \int_{\mathcal{V}(r)} \nu\langle\overline{\omega_i'\omega_i'}\rangle\,\mathrm{d}\mathcal{V}$, and $\mathcal{E}^{\mathcal{G}t} = \int_{\mathcal{V}(r)} \alpha\langle\overline{\vartheta_{,i}'\,\vartheta_{,i}'}\rangle\,\mathrm{d}\mathcal{V}$.

The radial distributions of $[\mathcal{E}]$, $[\mathcal{E}^m]$, $[\mathcal{E}^t]$, $\left[\mathcal{E}^{\mathcal{G}}\right]$, $\left[\mathcal{E}^{\mathcal{G}m}\right]$, and $\left[\mathcal{E}^{\mathcal{G}t}\right]$ are shown in figure 5.33. From the figure, it is evident that turbulent fluctuations contribute the most to $[\mathcal{E}]$ throughout most of the flow field. However, at small radial distances, a significant portion of the dissipation originates from the intense mean shear near the impingement plate. This contribution from the mean flow diminishes rapidly as the radial distance increases. In contrast, $[\mathcal{E}_{\mathcal{G}}]$ is primarily governed by the combined effects of mean-flow and turbulent dissipation across the entire domain. Notably, both $\left[\mathcal{E}^{\mathcal{G}m}\right]$ and $\left[\mathcal{E}^{\mathcal{G}t}\right]$ play a significant role in determining $\left[\mathcal{E}^{\mathcal{G}}\right]$, with the mean-flow contribution consistently exceeding the turbulent contribution. As shown in figure 5.33, both $[\mathcal{E}^t]$ and $\left[\mathcal{E}^{\mathcal{G}t}\right]$ increase rapidly for $r > D$, reaching their peak at $r \approx 2D$, before decreasing further downstream. This process culminates at $r \approx 2D$, where $[\mathcal{E}^t]$ and $[\mathcal{E}\mathcal{G}^t]$ reach their maximum values.

In reference to figure 5.33it is further noted that, in the range $D \lesssim r \lesssim 2D$, “$[\mathcal{E}^t]$ is significantly more amplified compared to $\left[\mathcal{E}^t_{\mathcal{G}}\right]$, indicating a clear dissimilarity between the velocity and scalar gradients fluctuations. While the physical reason for such a dissimilarity still remains an open question, the present findings show how its effects can have important practical consequences, especially in determining the [scalar transfer] efficiency of the system” (from Secchi et al. [85]).

5.4 Rough-wall impinging jet

Investigating the effects of surface roughness on the momentum and scalar transfer of impinging jets is of high practical relevance; for instance jet cooling typically intervenes on the inner surfaces of turbine blades or on electric circuitry, which are corrugated, at least, up to a certain extent. Extending results available for rough wall fully-developed channel flow (see section 5.1), or boundary layers (see section 5.2), is not a trivial task due to the complexity of impinging jet flows (see section 5.3). Hence, dedicated studies are required to investigate the effects of rough walls on the momentum and scalar transfer of jet impingement.

Nevertheless, only a relatively little number of investigations report on this account; the review presented in [19] compiles most of the available findings on this topic. The majority of the studies focus on global wall-heat transfer enhancements for specific configurations, such as arrays of multiple jets or engineered rough surfaces featuring dimples or fins. However, only a few investigations have examined a single circular turbulent jet impinging on plates with homogeneous random surface roughness, focusing only on the mean momentum transfer ([106], and the author’s publications [80, 81]). The recent author’s contributions [82, 83] report high-fidelity DNS results on the mean scalar transfer of impinging jets on random surface roughness.

This section explores the current knowledge about surface roughness effects on the mean momentum and scalar transfer of turbulent impinging jets, summarizing the author’s results published in [80–83] and revisiting them in view of the energetic framework presented in chapter 2. Excerpts from these works of the author are reported in this section within quotation marks. The flow configuration is the same as the smooth wall impinging jet presented in section 5.3. However, the impingement plate is rough with a random and homogeneous distribution of the wall normal height. As detailed in [80–83], the investigated roughness topographies are generated using the iterative approach developed by Pèrez-Ràfols and Almqvist [65], which allows for the creation of surfaces with a prescribed power spectrum (PS) and probability density function (PDF). The algorithm begins with a roughness distribution that matches the desired PDF but has an initially unknown PS. The surface is then transformed into Fourier space, where corrections are applied to adjust the PS. After transforming back to the physical domain, the modified distribution may no longer match the target PDF, requiring further corrections. This process is repeated iteratively until both the PDF and PS converge to their prescribed values.

For all cases, the roughness distribution has been generated with a Gaussian PDF; In [80, 81], the author investigates different surfaces by varying the characteristic size of the roughness, identified as the 99% of the confidence interval of the PDF of the roughness height distribution $k = k_{99}$. The PS of the in-plane distribution was taken from [21]. Conversely, the author’ studies [82, 83] use a PS for the in-plane roughness height distribution that is essentially a low-wave lengths pass filter. Both investigations consider two different surfaces, with equal $k = k_{99}$, but featuring a different wave length threshold, λ_{min}. The latter corresponds to the smallest wave length that is resolved in the roughness topography. The parameters for all the available cases are summarized in table 5.5.

Case	Literature	Re_b	k_{99}/D	λ_{min}	Scalar analysis
$J00$	[80, 81]	10 000	Smooth	-	No
$J01$	[80]	10 000	0.04	-	No
$J02$	[80, 81]	10 000	0.05	-	No
$J03$	[80, 81]	10 000	0.12	-	No
$J04$	[80, 81]	10 000	0.15	-	No
$J05$	[82, 83, 85]	5300	Smooth	-	Yes
$J06$	[82, 83]	5300	0.05	0.08	Yes
$J07$	[82, 83]	5300	0.05	0.04	Yes

Table 5.5: Parameters of the rough wall impinging jet DNS data.

5.4.1 Mean momentum transfer

The momentum transfer analysis of Secchi et al. [80] is supported by experimental measurements of the same flow configuration carried out by collaboration partners within the SFB-TRR 150 project. In the study, particle image velocimetry (PIV) measurements are reported for both smooth and rough wall conditions at the same bulk Reynolds number as in the DNS. Surface roughness in the experiment was realized by additive manufacturing of the digital roughness topography of the $J01$ case.

Figure 5.34 shows the comparison between DNS and experimental data for smooth and rough wall conditions. Mean radial velocity profiles at different radial locations are shown in panels (a) and (b) for the cases $J00$ and $J01$, respectively. Very good agreement is observed between the DNS and the experimental data for both cases. The uncertainty of the PIV measurements reflects into a larger scatter of the data near the wall; further, for the rough wall case, the measurements cannot resolve the flow field inside the roughness canopy, as can be seen from figure 5.34b.

In panels (c) and (d) of the figure, the radial development of the flow is compared between the DNS and the experiments through the radial distributions of the boundary layer thickness, δ_m, and the thickness $\delta_{1/2}$. The latter is an alternative measure of the wall jet thickness commonly found in the literature [52]. It represents the largest wall normal distance at which the mean streamwise velocity profile equals one-half of the maximum velocity at the same streamwise location, *i.e.* u_m in the present case. The parameter k_m in panel (d) indicates the melt-down roughness height. In fact, in [80], the roughness is laid on top of the plane $z = 0$ as to mimic the roughness formed by deposition of sediments. For comparison with the smooth wall data, it is reasonable to take $z = k_m$ as a reference roughness height. For the smooth wall case, DNS and PIV measurements show a remarkable agreement. For the rough wall case, the agreement is particularly good at small radial distances, but at larger radial distances, a discrepancy appears in the rate of growth of the wall jet thicknesses. Secchi et al. [80] note that this differences could be attributed to the absence of a confinement plate in the experiment and to the averaging time of the DNS data. In fact, due to the high computational cost, the simulations could not be run for a sufficiently long integration time (differently from the data at lower Reynolds number of Secchi et al. [82, 83, 85]). Further details in this respect are given in the appendix A.3.

For the smooth wall data, the comparison of the non-dimensional momentum flux at the wall is reported in figure 5.34e. The same cannot be done for the rough wall data, since the experimental measurements do not enable the estimation of this quantity. Conversely, panel (f) in the figure compares, for the rough

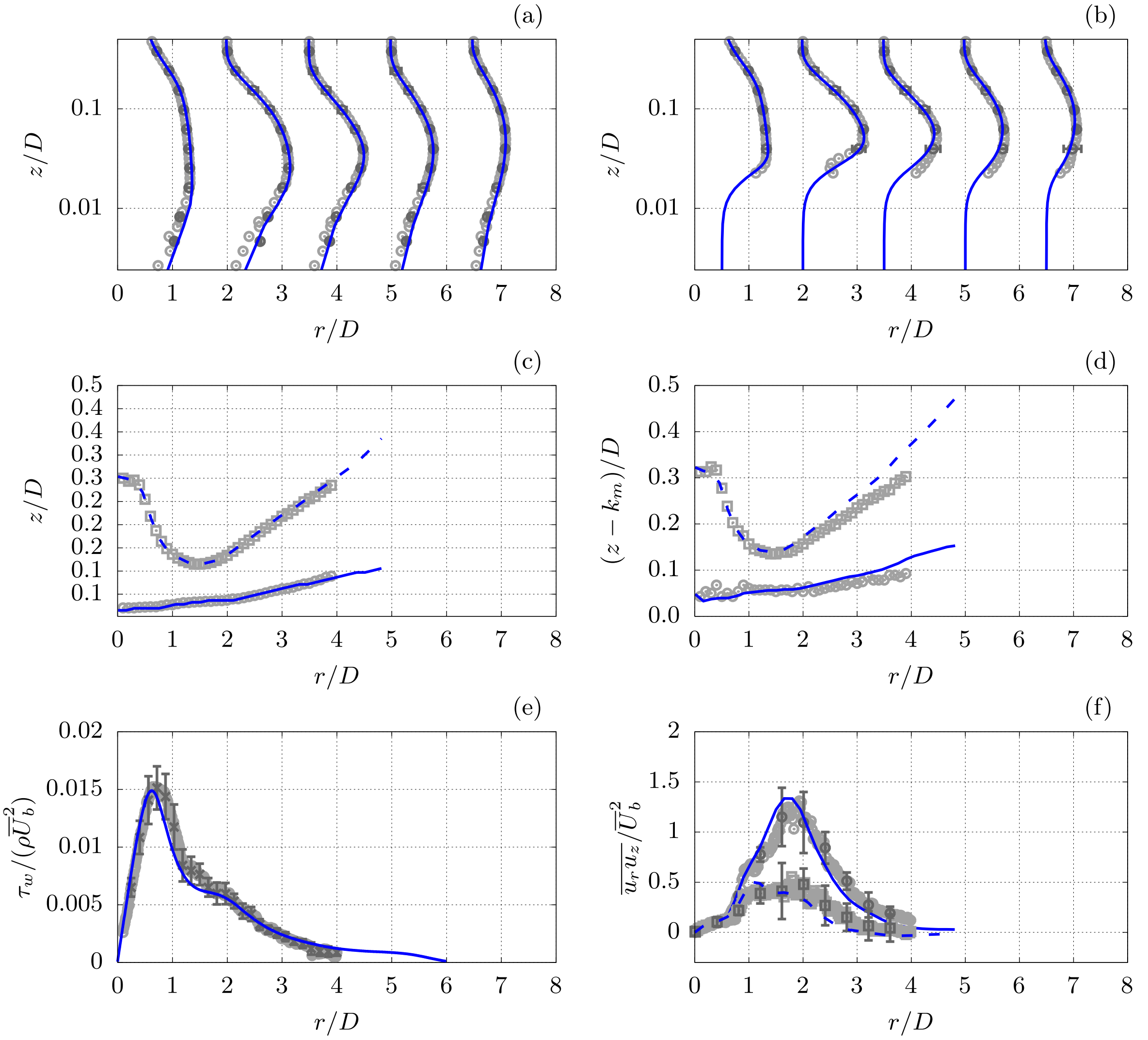

Figure 5.34: Comparison between DNS data and PIV measurements from [80]. Smooth wall, case $J00$, (a, c, e); rough wall, case $J01$, (b, d, f). Selected mean radial velocity profiles, (a, b); boundary layer thicknesses, δ_m/D (solid lines), and $\delta_{1/2}/D$ (dashed lines); momentum wall stress, (e); Reynolds shear stress radial distribution at $z-k_m = 0.06D$ (dashed line), and at $z-k_m = 0.1D$ (solid line). Grey symbols indicate experimental measurements. Error bars are three times the standard deviation of independent measurements. The figure is adapted from [80].

wall case, the Reynolds shear stress distribution at two wall normal heights as a function of the radial distance.

The effects of roughness on the mean flow developing along the impingement plate are discussed in [81], with a particular emphasis on the self-similar character of velocity statistics normalized with inner and outer units. For smooth wall conditions, this analysis has been reported in section 5.3.2 of the present work. Therein, it is discussed that the low Reynolds numbers currently achievable with DNSs translate in insufficient scales separation between the inner and outer regions of the wall jet and the lack of a visible overlap layer where the inner-units scaled mean streamwise velocity exhibit a logarithmic layer. In this context, it is observed that normalization with either inner or outer units determines a reasonable collapse of the velocity statistics, at least in a narrow range of radial distances (refer to figures 5.25 and 5.26).

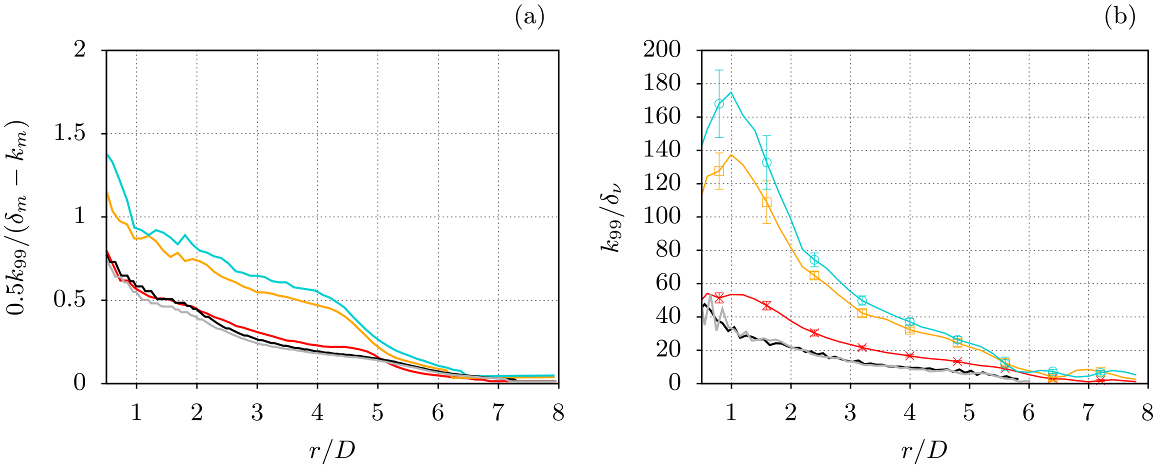

Figure 5.35: Characteristic roughness size in comparison with flow length scales as a function of the radial coordinate. $k_{99}/[2(\delta_m - k_m)]$, (a); k_{99}/δ_ν, (b). —, $J02$; —, $J03$; —, $J04$; —, $J06$; —, $J07$. Figure adapted from [81].

As discussed by the author in [81], roughness introduces, at least, one additional length scale that needs to be compared with the boundary layer thickness, δ_m and the viscous length scale, δ_ν. This comparison is reported in figure 5.35 for the rough wall cases $J02 - J04$, $J06$, and $J07$. In particular, one-half of the roughness height k_{99} is compared to the boundary layer thickness. $0.5k_{99}$ is chosen since it represents a measure of the height of the roughness peaks with respect to the reference plane at $z = k_m$ for cases $J02 - J04$ and $z = 0$ for the cases $J06$ and $J07$. In fact, the latter two cases are from [82] and [83], whereby the mean plane of the roughness topographies coincides with $z = 0$. From panel (a) of figure 5.35, it is apparent that the roughness is relatively large compared to the boundary layer thickness for all the cases. This is particularly the case at small radial distances, where the boundary layers are very thin. Moving downstream, the relative roughness size decreases as the boundary layer thickens. The cases $J02$, $J06$ and $J07$ have very similar distributions. This is consistent with the fact that the roughness topographies are all characterized by the same height k_{99}. However, the higher Reynolds number for the $J02$ case determines a thinner boundary layer developing on the impingement plate and, consequently, the roughness-to-boundary layer thickness ratio is slightly higher than for the $J06$ and $J07$ cases.

The comparison between the roughness size, k_{99} and the viscous length scale is shown in figure 5.35(b). At small radial distances, very large values of k_{99}^+ are attained for the cases $J03$ and $J04$. In fact, this region is characterized by relatively high wall shear stress which, in turn, results in a relatively small viscous length scale. Such large values of k_{99}^+ could suggest that the flow behaves as if it were in the fully rough regime. However, from panel (a) in figure 5.35, it is clear that the roughness topography of these cases has a size that is comparable to the boundary layer thickness over the same region. Hence, roughness elements represent large obstacles to the local flow and cannot be considered as small corrugations of the surface as it is done in the turbulence-roughness interaction theory Chung et al. [13].

The effects of roughness on the self-similar character of the mean radial velocity profiles, scaled in inner units, is shown in figure 5.36. The profiles are sampled in the range $2D \leq r \leq 4D$ for cases $J02 - J04$, and

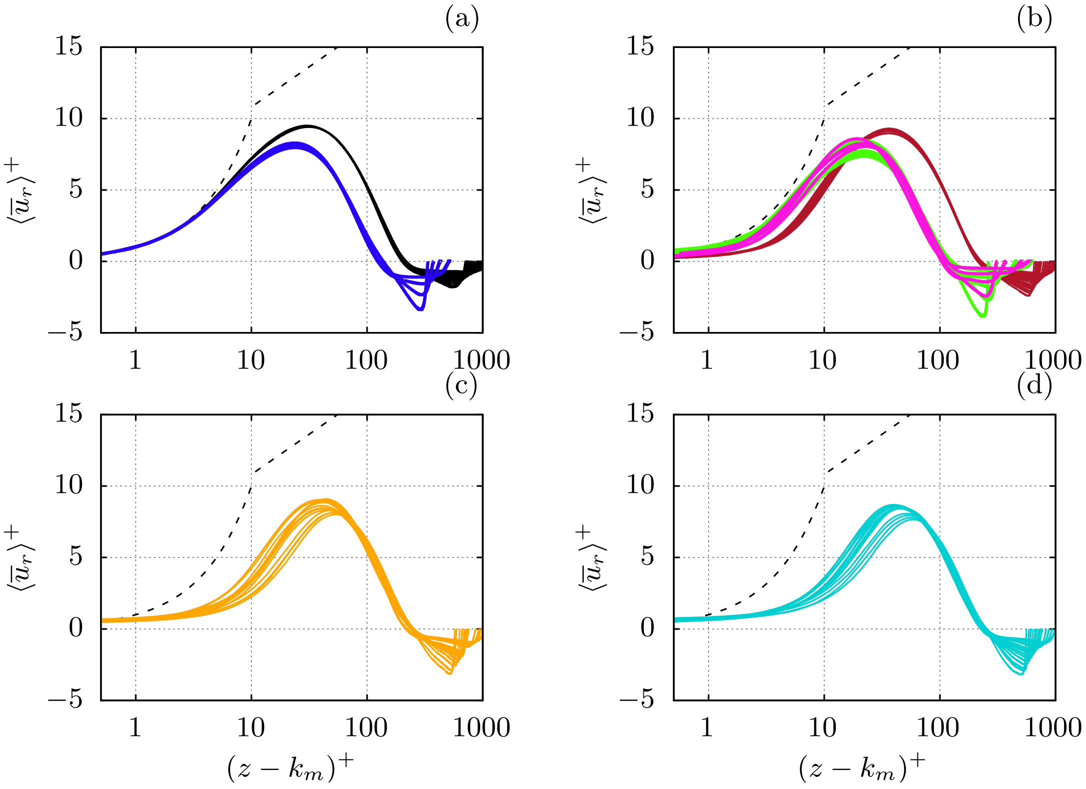

Figure 5.36: Inner units-scaled mean radial velocity profiles in the wall jet region of the flow. Smooth wall, (a); ——, $J00$; ——, $J05$. Rough wall: (b), —— $J02$, —— $J06$, —— $J07$; (c), —— $J03$; (d), ——, $J04$. Black dashed lines indicate the law of the wall. Figure adapted from [81].

in $3D \leq r \leq 5D$ for the $J05 - J07$ cases. “All the plotted smooth wall case profiles collapse consistently well for approximately $z^+ < 200$. On the other hand, the presence of roughness deteriorates the self-similar character of the inner units scaled mean radial velocity profiles, with the decline becoming more significant for increasing size of the roughness. Nevertheless, it must also be considered that the roughness size in the three cases is large relative to the local values of the viscous length scale δ_ν, as it can be appreciated in [figure 5.35]. Therefore, it is expected that, for all the three cases, the roughness sub-layer extends to wall-normal distances comparable to $[\delta_m^+]$. With this perspective, it is in fact remarkable to observe that the similar character of the velocity profiles is not completely compromised” (from Secchi et al. [81]).

From panel (a) in the figure, it is apparent that, even for the smooth wall case at high Reynolds number, case $J00$, the mean radial velocity profiles do not exhibit a logarithmic range. For reference, the figure shows also the linear and logarithmic velocity profiles expected from the classical law of the wall. The comparison between the radial velocity profiles of the $J05$ and $J00$ cases, it appears that, as the Reynolds number increases, the viscous units-scaled velocity maxima tend become more intense at an increasingly greater distance from the wall, *i.e.* the local Reynolds number $\delta_m^+ = \delta_m/\delta_\nu$.

Figure 5.36b compares cases $J02$, $J06$, $J07$, for which the roughness topography is characterized by the same k_{99}. Cases $J06$ and $J07$ have a different λ_{min}, but the figure shows that the mean radial velocity profiles in the wall jet are not sensibly affected by changes of small wave length of the roughness topography. In contrast, the effect of the Reynolds number change is more visible. close to the wall, the mean velocity profiles are more damped for the higher Reynolds number case. Nevertheless, as in the smooth wall case, the viscous-scaled velocity peaks and the local $\delta_m^+ = \delta_m/\delta_\nu$ increase for the higher inlet Reynolds number case.

Similar observations are made in [81] in reference to the outer-units scaled mean radial velocity profiles of the cases $J00$, $J02 - J04$. Albeit roughness introduces some scattering in the normalized profiles, their self-similar character is observed in the range $2D \leq r \leq 4D$. Further, the same authors observe that self similarity is also observed, over the same range of radial distances, for the Reynolds stress components scaled in both inner and outer units. Similar results have been shown in figures 5.25 and 5.26 for the smooth wall case, $J05$, and are not further shown here.

5.4.2 Mean scalar transfer

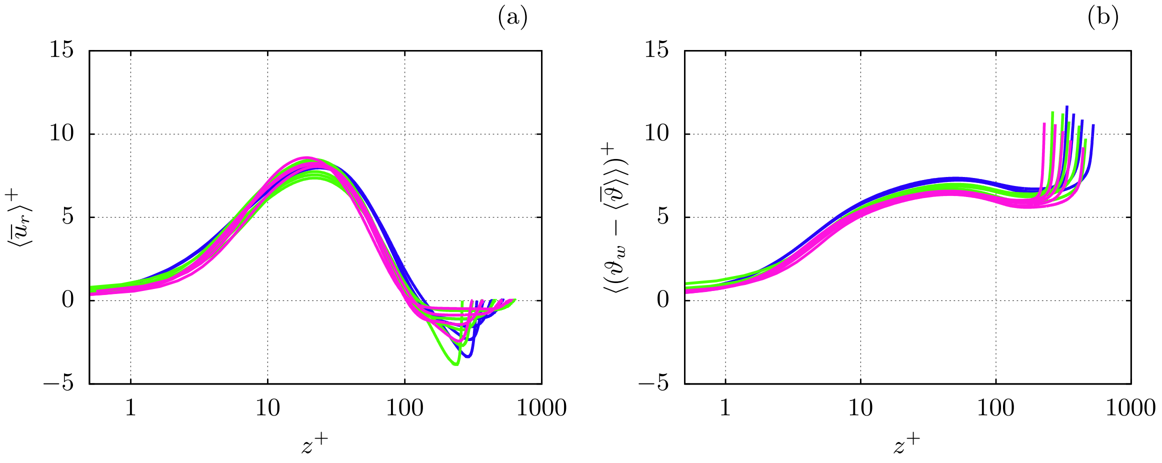

Figure 5.37: Inner units-scaled mean radial velocity profiles (a) and scalar profiles (b) in the wall jet region. ——, $J05$; ——, $J06$; ——, $J07$. Figure adapted from [83].

As noted in the analysis of figure 5.36, changes in λ_{min} of the investigated roughness topography does not produce significant changes in the mean radial profiles of the wall jet region of the flow. This is further shown in figure 5.37(a), where the comparison is extended to also include the smooth wall data. The figure highlights how the investigated roughness, under the considered conditions, does not have a significant impact compared to smooth conditions. In panel (b), it is shown that something similar occurs also for the mean scalar profiles, $(\vartheta_w - \langle \overline{\vartheta} \rangle)^+$. However, in this case, a small and systematic downward shift of the mean scalar is observed for the rough wall cases. In particular, the shift appears to increase for decreasing λ_{min}, implying a local scalar transfer increase for the rough wall case characterized by smaller roughness elements.

The small influence that roughness appears to have on the mean radial velocity and scalar profiles in the wall jet suggests that roughness, in the present cases, is only capable of marginally affecting the mean momentum and scalar wall fluxes. These are shown, in terms of the friction and scalar transfer coefficients, in figure 5.38 for the smooth wall case, $J05$, and for the rough wall cases $J06$ and $J07$. The figure only shows radial distances $r \geq D$ since large fluctuations in the wall shear stress occur in the azimuthally-averaged data due to small relative size of the averaging area over the roughness elements size. Large fluctuations are also observed at greater radii, but with a decreasing amplitude. Compared to the smooth wall data, a net increase is observed for the friction coefficient for $r \lesssim 3D$. In contrast, at greater radial distances, the friction coefficient oscillates around the smooth wall value at matched radial location. Consistently

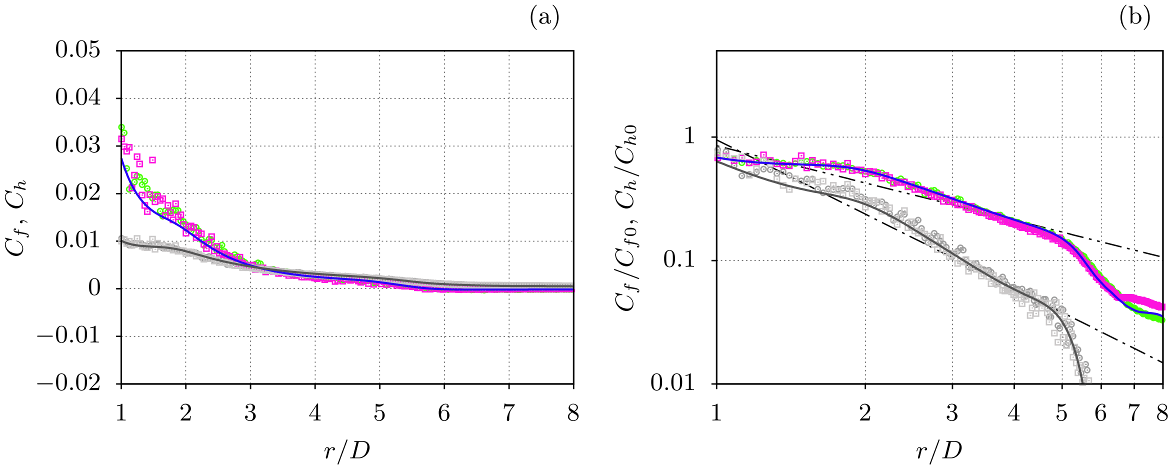

Figure 5.38: Panel (a): mean friction coefficient and scalar transfer coefficient distributions along the impingement plate for the smooth and rough wall cases, $J05 - J07$. Panel (b): distributions of C_f/C_{f0} and C_h/C_{h0} in the wall jet region. Friction coefficient: ——, $J05$; ○ ○ ○, $J06$; □ □ □, $J07$. Scalar transfer coefficient: ——, $J05$; ○ ○ ○, $J06$; □ □ □, $J07$. In panel (b) the dash-dot line represents $\sim (r/D)^{-2}$, and the dash-dot-dot line is $\sim (r/D)^{-1}$. Adapted from [85].

with the observations made in reference to figure 5.36, the parameter λ_{min} does not influence significantly the results, even though, for the smaller λ_{min} case, $J07$, the C_f fluctuations are somewhat more intense compared to the $J06$ case.

Differently from the friction coefficient, the scalar transfer coefficient does not change appreciably from the smooth wall data at matched radial location. The only differences observed, for both the $J06$ and $J07$ cases, are small oscillations around the smooth wall data. Notably, as shown in figure 5.38b, the rough wall data appears to also follow the estimates (3.67) and (3.68) in the range $3D \lesssim r \lesssim 5D$.

The changes induced by the roughness on the mean friction coefficient and scalar transfer coefficient at small radial locations evidence a roughness-induced departure from local classical Reynolds analogy. While the rough wall mean friction coefficient is appreciably larger than its smooth wall counterpart for $r \lesssim 3D$, the scalar transfer coefficient does not show a comparable change. This observation might suggest that the increase in friction coefficient could be attributed to the pressure drag induced by roughness elements on the flow. This scenario is further investigated in figure 5.39a by showing the viscous and pressure contributions to the mean friction coefficient. For the rough wall cases, the figure shows that, while there is a significant pressure contribution to C_f, the viscous contribution is significantly lower than the smooth wall C_f value at matched radial location. Hence, the departure from analogous momentum and scalar transfer appears to be caused, in a non-trivial way, by both the viscous and pressure contributions. However, comparing the smooth and rough wall data at matched radial location can be misleading when such an interpretation of the local departure from Reynolds analogy is considered. Due to the presence of roughness, the flow develops under different conditions compared to the smooth wall case and, locally, the smooth and rough wall flows exhibit markedly different conditions. For instance, their boundary layer thicknesses and outer velocity scales are likely to be different.

In view of this observation, it seems reasonable to perform the rough and smooth wall data comparison by fixing the outer conditions of the boundary layer. For the viscous and pressure contributions to C_f, this is done in figure 5.39b by comparing the smooth and rough wall data at matched outer Reynolds number, $Re_m = \overline{U}_b \delta_m / \nu$. In other words, the comparison is done by comparing the data extracted at different

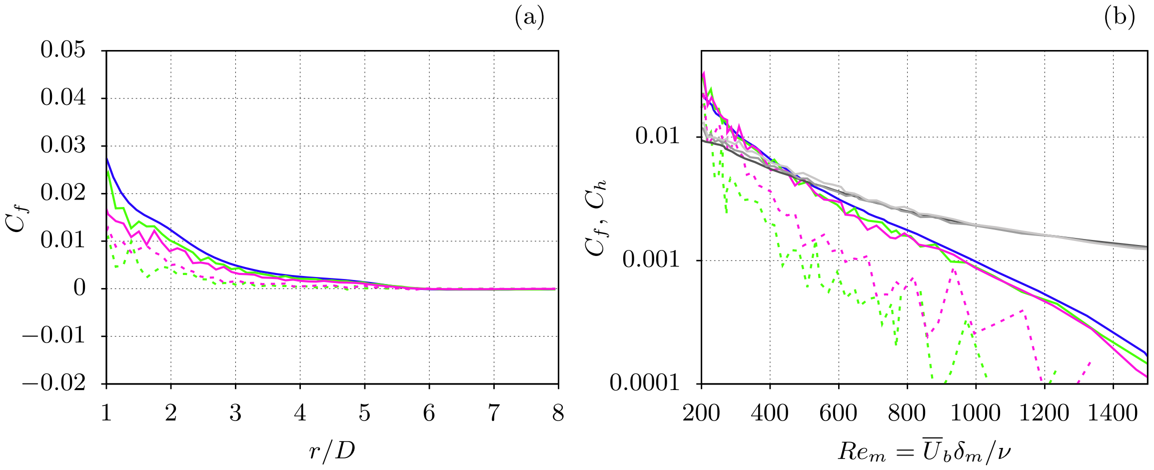

Figure 5.39: Viscous (solid) and pressure (dashed) contributions to the friction coefficient at matched radial coordinate (a) and at matched local Reynolds number, Re_m, (b). Panel (b) also reports the scalar transfer coefficient distributions. —, $J05$; —, $J06$; —, $J07$. In panel (b), the scalar transfer coefficient curves are: —, $J05$; —, $J06$; —, $J07$.

radial locations, but having the same boundary layer thickness. The figure also reports the scalar transfer coefficient at matched Re_m. In these settings, it is observed that the viscous contribution to C_f does not significantly change compared to the smooth wall data. Hence, at matched Re_m, the roughness-induced increase in C_f is exclusively to be attributed to the pressure contribution. The latter, decreases and becomes negligible at large Re_m, *i.e.* when the boundary layer is much thicker than the roughness size. The comparison of the scalar transfer coefficient at fixed Re_m confirms the previous observations and highlights that the roughness-induced change in mean scalar flux, compared to smooth wall conditions, is essentially negligible for the investigated cases. Hence, the analysis of figure 5.39b shows that, at matched Re_m, the viscous contribution to the momentum wall flux and the scalar wall flux respond very similarly to the presence of surface roughness; thus, the main reason of the roughness-induced departure from analogous momentum and scalar flux can be attributed to the action of the pressure drag, in agreement with the well-established scenario scenario described in section 1.2.1 and in the literature (for instance, in [36]).

Thus far, the analysis highlighted how the investigated roughness does not produce significant changes on the mean flow under the present flow conditions. For the $J05$ and $J06$, this is seen in the mean radial velocity and scalar profiles, shown in figure 5.37, and in the mean friction coefficient and scalar transfer coefficient in figure 5.38. In particular, the latter figure shows that the roughness effects become less pronounced at greater radial distances. The apparent insensitivity of the flow on the roughness can be attributed to two different causes. The low Reynolds number achieved along the impingement plate prevents the occurrence of the turbulence regeneration mechanisms that are typical of turbulent wall-bounded flows. This scenario is illustrated in figure 5.40 which shows, for the smooth wall case $J05$, wall normal profiles of turbulent kinetic energy, in panel (a), and of turbulent kinetic energy production and dissipation, in panel (b). From Secchi et al. [83], “the turbulent kinetic energy exhibits two distinct peaks: one in the inner region of the wall jet and one in its shear layer. Contrary to the outer peak, the inner one gets quickly damped with increasing radial distance. In fact, as shown in [figure 5.40(b)], while the production and dissipation of turbulent kinetic energy are substantially balanced in the outer region of the wall jet, an imbalance between dissipation and production exists in the inner region which favours the dissipation of turbulent kinetic energy”. This observation highlights that the inner region of the wall jet is in non-equilibrium, with a clear advantage of the dissipation of turbulent kinetic energy over its dissipation. It can be expected that

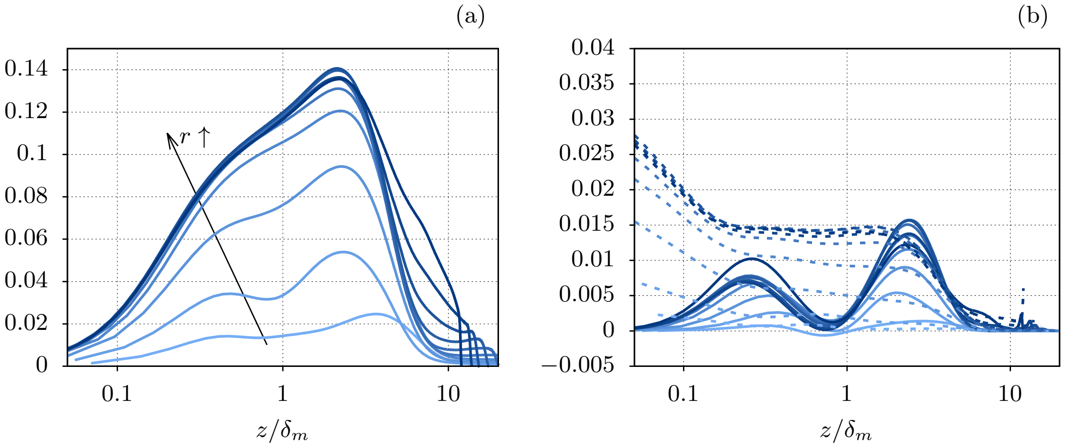

Figure 5.40: Turbulent kinetic energy, panel (a), and production and dissipation of turbulent kinetic energy at different radial locations, panel (b), for the case $J05$. In panel (b), solid lines represents the production profiles and dashed lines display the dissipation profiles. Radial locations are distinguished varying the colours of the curves, from light blue for the profiles at $r = D$, to dark blue for profiles at $r = 5D$. Figure adapted from [83].

this scenario changes with increasing the Reynolds number, however the present dataset does not allow to confirm this speculation.

The presence of roughness does not determine significant changes. In fact, "[this scenario] seems to be unaltered for the rough wall case, even though a slight increase in the production of turbulent kinetic energy is observed in the inner region. The shear-driven turbulent kinetic energy production mechanism in the inner region of the wall jet appears to be weak and, correspondingly, surface roughness only marginally affects flow properties in this region" (from Secchi et al. [83]). Further, it is argued that "the near-wall turbulence is sustained at the expenses of the outer layer flow through redistribution mechanisms. This scenario appears not to be affected by the small scales that characterize the considered roughness topography, suggesting that such production and redistribution of turbulence fluctuations phenomena are associated with relatively much larger flow structures" (from Secchi et al. [83]).

Further support to this observation is provided in figure 5.41, where the turbulence energy spectra for radial velocity fluctuations are shown at three different radial locations of the wall jet region of the smooth wall case $J05$. In the figure, k_ϕ denotes the wave number in the azimuthal direction. A red dashed line in the three plots indicates the boundary layer thickness at the corresponding radial location and is used to distinguish between the inner and outer regions of the wall jet. Further, a vertical blue dashed line denotes the wave number corresponding to the characteristic size roughness topography, k_{99}, for the cases $J06$ and $J07$. At $r = 0.75D$, an energy peak is clearly visible in the outer layer having a relatively narrow support of wave numbers slightly less than $k_\phi \approx 10/D$. At downstream radial locations, the energy peak spreads over a broader range of wave numbers and partially intrudes inside the inner layer. However, the figure suggests that most of the energy of turbulent fluctuations is located in the outer layer of the wall jet, *i.e.* at large distances from the rough wall, and involves scales of motion that are significantly separated from the characteristic size of the roughness.

These arguments justify the observed marginal effects that surface roughness has on the present flow. It is to be expected that, at much higher Reynolds numbers, more significant effects of roughness could start to come into play. However, the author's results in [80] and [81] highlight that, even for an inlet

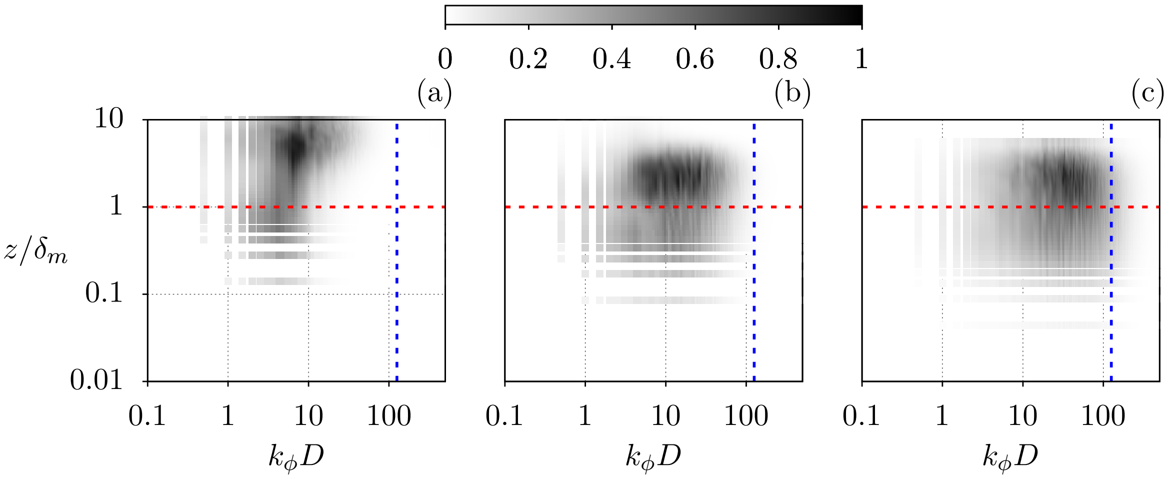

Figure 5.41: Premultiplied azimuthal spectra for radial velocity fluctuations, $k_\phi \Phi_{u_r u_r}/(\overline{U}_b^2)$ at $r = 0.75D$ (a), $r = 1.5D$ (b), $r = 3D$ (c). A red dashed line highlight the local height of the boundary layer, δ_m, whereas the blue-dashed line represents $2\pi/k_{99}$.

Reynolds number as high as $Re_b = 10\,000$, only minor effects of roughness are registered. To the best of the author's knowledge, $Re_b = 10\,000$ corresponds to the highest inlet Reynolds number currently achieved by a DNS study [14, 80, 81]. Due to the high cost associated with performing DNS of impinging jet flows, it is foreseeable that future studies on the topic will have to address the problem experimentally or using large eddy simulations.

5.4.3 Scalar transfer efficiency

The effects of surface roughness on the flow do not only exhibit in terms of changes in the momentum and scalar wall fluxes. The roughness is expected to emphasize the dissipation of mechanical energy and, in turn, the necessary power input required to drive the flow. In general, the scalar exchange at the rough wall is also expected to increase, even though only marginally for the present cases, as seen in section 5.4.2. At statistically stationary conditions, an increase in the scalar wall flux should result in an increase in the mean convected scalar across the lateral surface, $\mathcal{A}_L(r)$, of the control volume $\mathcal{V}(r)$ shown in figure 5.3. Consequently, a high mean scalar transfer at the impingement plate should manifest itself also through a larger convection of $\overline{\mathcal{G}}$ across $\mathcal{A}_L(r)$. In other words, the scalar concentration that the flow carries across the lateral surface of $\mathcal{V}(r)$ is an index of the total scalar exchange that occurs through the base of $\mathcal{V}(r)$; hence, the higher the convection of $\overline{\mathcal{G}}$ through $\mathcal{A}_L(r)$, the higher the mean scalar transfer at the impingement plate. However, the integral balance (3.70), and the use of (3.71), indicate that, at a fixed mean scalar flux through the base of $\mathcal{V}(r)$, the amount of mean squared-scalar concentration that the flow carries through the lateral surface is determined by the bulk dissipation of $\overline{\mathcal{G}}$, $\mathcal{E}^{\mathcal{G}}(r)$. The lower is the bulk dissipation, the higher is the lateral convection of $\overline{\mathcal{G}}$.

As surface roughness can potentially increase the mean scalar flux at the wall, it is meaningful to consider how the mean bulk dissipation of $\overline{\mathcal{G}}$ responds to the presence of surface roughness. Figure 5.42 shows the radial distributions of $\mathcal{E}(r)$ and $\mathcal{E}^{\mathcal{G}}(r)$ for the smooth wall case, $J05$, and the rough wall cases $J06$ and $J07$. Note that the plots restrict the analysis up to radial locations upstream of the separation point of the $J05$ case at $r \approx 5.8D$. The figure shows a systematic increase in the bulk dissipation rates, $\mathcal{E}(r)$ and $\mathcal{E}^{\mathcal{G}}_(r)$, compared to the smooth wall case, at approximately all radial distances, with the increase being more

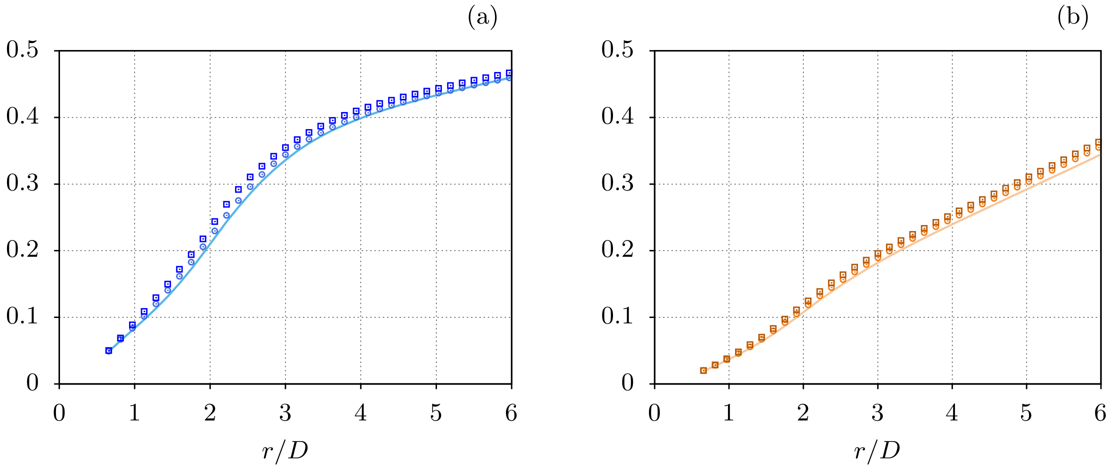

Figure 5.42: Mechanical energy bulk dissipation, $\mathcal{E}(r)$, (a) and squared-scalar bulk dissipation, $\mathcal{E}^{\mathcal{G}}(\nabla)$, (b) for control volumes $\mathcal{V}(r)$ of increasing radius. Solid lines, $J05$; circles, $J06$; squares, $J07$.

pronounced for the smallest λ_{min} case, $J07$. Despite the marginal roughness-induced change in the mean momentum and scalar wall fluxes reported in sections 5.4.2 and 5.4.3, it is observed from figure 5.42 that roughness determines a net increase in the dissipation of mechanical energy and squared-scalar field. The former results in a larger mechanical energy consumption, and hence in a greater power required to drive the flow, whereas the latter, at matched scalar exchanged at the impingement plate, results in a lower mean scalar concentration convected downstream.

A different scenario is observed for the local bulk dissipation rates. These are analysed in a similar fashion to what is presented in section 5.3.6 for the smooth wall case $J05$. In particular, the bulk dissipation rates, $[\mathcal{E}]$ and $\left[\mathcal{E}^{\mathcal{G}}\right]$ are computed over the control volumes $[\mathcal{V}] = \mathcal{V}(r + \Delta r/2) - \mathcal{V}(r - \Delta r/2)$, where Δr is an arbitrary thickness for $[\mathcal{V}]$ (see the related discussion about the definition of the control volumes $[\mathcal{V}]$ in section 5.3.6). The result is shown in figure 5.43 for the smooth wall case, $J05$, and the rough wall cases $J06$ and $J07$. Note that the bulk dissipation rates in the figure are normalized with the volume $[\mathcal{V}]$. Further, the figure compares the mean and turbulent flow contributions to the dissipation rates. At small radial distances, a net increase in the local bulk dissipations is evident for both rough wall cases in comparison to the smooth wall values over the same region. In this area, the net increase appears to be determined by both the mean and turbulent flow contributions. However, further downstream, the turbulent flow contributions, $[\mathcal{E}^t]$ and $\left[\mathcal{E}^{\mathcal{G}t}\right]$, of the rough wall cases become smaller compared to their smooth wall values at the same radial locations. An opposite behaviour is observed for the mean flow contributions, which are greater for the rough wall cases. The net outcome is a slight decrease of the rough wall cases local bulk dissipation, $[\mathcal{E}^t]$, whereas $\left[\mathcal{E}^{\mathcal{G}}\right]$ does not change appreciably from the smooth wall case at matched radial distance.

The scalar transfer efficiency is assessed in terms of the Reynolds analogy efficiency factor, (3.77), which considers only the scalar flux at the impingement plate. As seen for the smooth wall case, at small radial distance the net scalar flux across the confinement plate plays a marginal role (see figure 5.31a). The distribution of RA_π along the radial direction is reported in figure 5.44a for the $J05-J07$ cases. In all cases, the the scalar flux due to the base solution ϑ_B, defined in section 5.3.1, is removed from the computation of RA_π, even though at small radial distance its contribution is marginal. The Reynolds analogy efficiency factor shown in figure 5.44a reflects the previous observations about the roughness-induced variations of mean scalar wall flux and consumed mechanical energy. Since the former remains approximately unaltered,

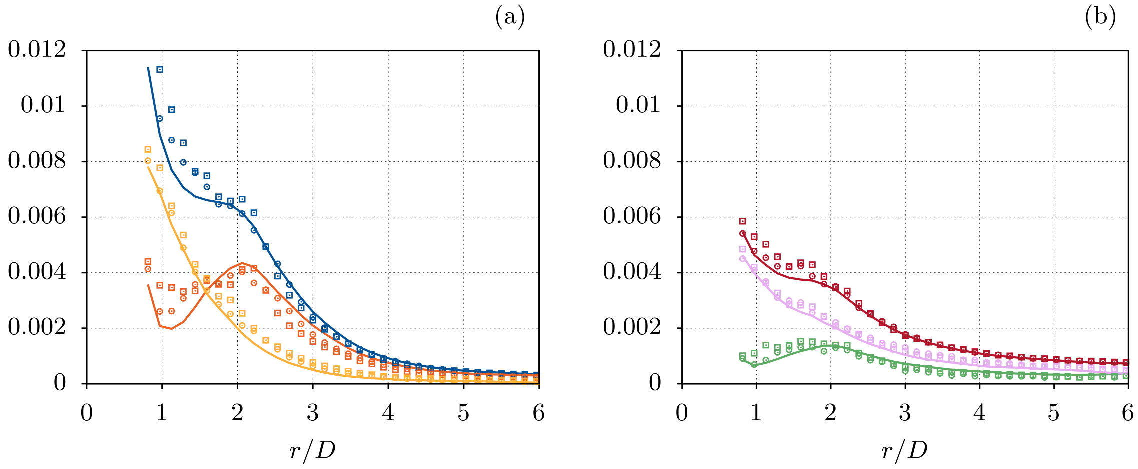

Figure 5.43: Local mean mechanical energy bulk dissipation (a), and mean squared-scalar bulk dissipation (b) for control volumes $[\mathcal{V}(r)]$. $J05$: ——, $[\mathcal{E}]$; ——, $[\mathcal{E}^m]$; ——, $[\mathcal{E}^t]$; ——, $[\mathcal{E}_\mathcal{G}]$; ——, $[\mathcal{E}_\mathcal{G}^m]$; ——, $[\mathcal{E}_\mathcal{G}^t]$. $J06$: ○○○, $[\mathcal{E}(r)]$; ○○○, $[\mathcal{E}^m(r)]$; ○○○, $[\mathcal{E}^t(r)]$; ○○○, $[\mathcal{E}^\mathcal{G}(r)]$; ○○○, $[\mathcal{E}^{\mathcal{G}m}(r)]$; ○○○, $[\mathcal{E}^{\mathcal{G}t}(r)]$. $J07$: □□□, $[\mathcal{E}(r)]$; □□□, $[\mathcal{E}^m(r)]$; □□□, $[\mathcal{E}^t(r)]$; □□□, $[\mathcal{E}^\mathcal{G}(r)]$; □□□, $[\mathcal{E}^{\mathcal{G}m}(r)]$; □□□, $[\mathcal{E}^{\mathcal{G}t}(r)]$; Adapted from [85].

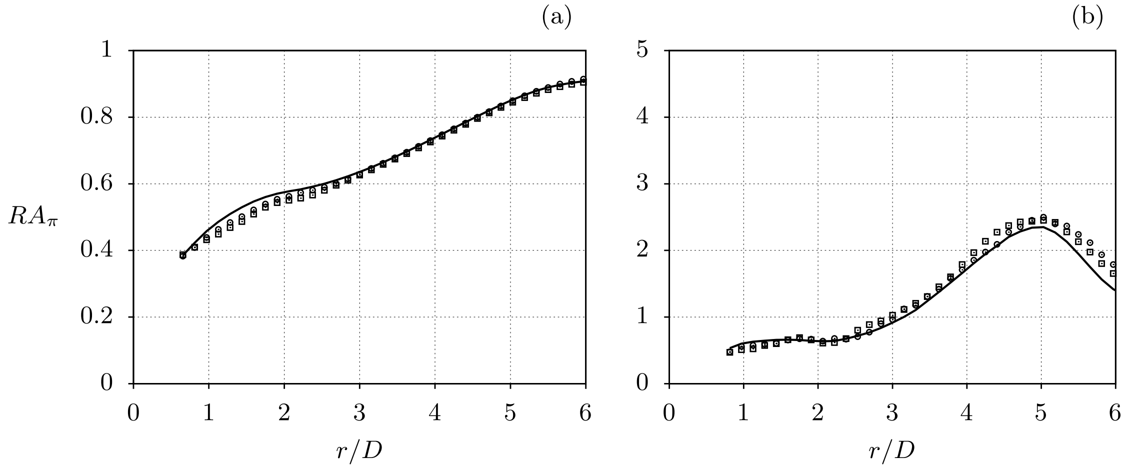

Figure 5.44: (a), Smooth and rough wall comparison of Reynolds analogy efficiency factor, RA_π, for control volumes, $\mathcal{V}(r)$, of increasing radius. (b), local Reynolds analogy efficiency factor for the control volumes, $[\mathcal{V}(r)]$. In both panels RA_π is computed computed using equation (3.77) without including the constant scalar flux associated with the base solution, ϑ_B. A solid line represents the smooth wall data, $J05$, circles are case $J06$, and square markers are case $J07$. Adapted from [85].

whereas the latter increases, especially at small radial locations, the global efficiency of the rough wall cases decreases in comparison to the smooth wall flow at fixed size of the control volume $\mathcal{V}(r)$. In contrast, the Reynolds analogy efficiency factor computed on the control volumes $[\mathcal{V}(r)]$ increases at sufficiently large radial distances ($r \gtrsim 3D$) in comparison to the smooth wall case, as it can be seen in figure 5.44b. This behaviour is consistent with the observations about the roughness-induced changes to the local Reynolds analogy efficiency factor in the rough wall boundary layer of section 5.2.2. In fact, while the bulk dissipation of mechanical energy does not change appreciably due to roughness, in fact it actually decreases slightly, as shown in figure 5.43a, the net scalar exchange through the base of $[\mathcal{V}(r)]$ increases for the rough wall cases due to the larger wetted surface area in comparison to the smooth wall case. As a result, the local Reynolds analogy efficiency factor results slightly higher in comparison to the smooth wall case at matched radial location.

6 Conclusions and outlook

This thesis investigates analogous momentum and passive-scalar transfer in incompressible wall-bounded flows. Unlike previous studies, the analogy is explored from an energetic perspective, beginning with the similarity between the governing equations for the instantaneous kinetic energy, $\mathcal{K}$, and half the squared scalar concentration, $\mathcal{G}$. For statistically stationary flows, this analogy extends to the mean mechanical energy, $\overline{\mathcal{B}}$—defined as the sum of kinetic energy and pressure per unit density—and the time-averaged squared scalar field, $\overline{\mathcal{G}}$. Under such conditions, it is shown that the conservation of these quantities may exhibit dissimilar behaviour, particularly in how $\overline{\mathcal{B}}$ and $\overline{\mathcal{G}}$ are dissipated by the mean dissipation rates $\nu\overline{\omega_i\omega_i}$, and $\alpha\overline{\vartheta_{,i}\,\vartheta_{,i}}$.

The balance equation for $\mathcal{G}$ can be related to an evolutive equation for a scalar entropy-like quantity, $\mathcal{S}$; the latter coincides with the thermodynamic entropy of the flow in case the scalar field represents the temperature of the fluid. In general, the scalar entropy increases or decreases according to the local molecular scalar flux weighted by the scalar concentration value. A net increase in scalar entropy is generated by a non-negative source term which corresponds to the local dissipation rate of the squared scalar field, $\mathcal{G}$, weighted by the squared magnitude of the scalar concentration. It is shown that an analogous equation can also be written for a mechanical entropy-like quantity, $\mathcal{Z}$. Its local variation depends on the molecular flux of mechanical energy and pressure transport weighted by the local momentum magnitude. However, unlike for the scalar entropy equation, it is not straightforward to relate the dissipation rate of mechanical energy to a positive-definite source term of mechanical entropy, thus evidencing a possible structural difference between the evolution of mechanical energy and the squared scalar field.

The similarities between the governing equations of the mean mechanical energy and the squared scalar field are further exploited to assess analogies in their integral balances across finite-size control volumes. In particular, integral changes in the mean mechanical energy of the flow are linked to the bulk dissipation of mechanical energy within the considered control volume, providing a means for the evaluation of the mechanical power input required to drive a given flow. Analogously, it is shown that the net scalar flux across the control volume's boundary can be related to the bulk dissipation of the squared scalar field in the control volume. The integral balances of mechanical energy and squared scalar are used to evaluate the scalar transfer efficiency of a given wall-bounded flow. In particular the efficiency is evaluated as the ratio between the net scalar flux, occurring at the boundary of a control volume, and the amount mechanical energy that gets dissipated within the control volume. In practice, the scalar transfer efficiency provides with a way of quantifying the energy cost associated with the scalar flux achieved by the flow. In non-dimensional settings, the assessment of the scalar transfer efficiency reduces to the evaluation of the *Reynolds analogy efficiency factor*, RA_π. This newly defined parameter is representative of the similarity between the integral momentum and scalar transfer from an energetic perspective.

The proposed framework for assessing the analogy between momentum and scalar transfer is tested on three different turbulent flow configurations. These are fully developed channel flows, zero pressure gradient boundary layers, and circular impinging jets. For each case, the smooth and rough wall conditions are investigated. The application of the framework is presented from a theoretical perspective and the results of the analysis are tested against DNS of the considered flow configurations.

For fully developed channel flows, the analysis follows closely the investigation reported in [86], where the same channel flow data is analysed. Adding on to the results of Secchi et al. [86], the present investigation shows how momentum and scalar transfer performances of channel flows, with and without surface roughness, can be interpreted according to different flow driving strategies. In the common cases of CPG and CFR, improved momentum transfer shows as a decrease in the mean streamwise bulk velocity and in an increase in the mean pressure gradient required to pump the flow, respectively. In an analogous fashion, increases in the mean scalar transfer reflect into lower values of the mean bulk scalar, for the CPG strategy, and into higher volumetric scalar source values for the CFR strategy.

A third possible flow driving strategy is introduced in the present study; namely this consists in feeding the flow with a constant power input. Differently from existing studies in the literature [38, 72], the CPI approach is achieved by prescribing the mean value, over the channel volume, of $\overline{\omega_i \omega_i}$. Similarly, fixing $\overline{\vartheta_{,i}\, \vartheta_{,i}}$ enables to achieve an analogous driving strategy for the scalar transfer problem. Prescribing these quantities, together with the fluid's molecular diffusivities, sets new velocity, length, and scalar characteristic scales that can be used to rescale the available data according to the CPI approach. In particular, channel flow data obtained by driving the flow with a CPG are rescaled into CPI variables to asses the momentum and scalar transfer performances. At CPI, the mean bulk velocity and volumetric driving force are inversely proportional: increased momentum transfer manifests itself through a decrease of the mean bulk velocity and a corresponding increase in the necessary volumetric force that drive the flow. A similar result holds for the scalar transfer enhancement: it occurs through a decrease in the mean scalar value and a corresponding increase in the volumetric scalar source term.

Regardless of the considered flow driving approach, information about the mean momentum and scalar transfer performances are conveyed by the mean friction and scalar transfer coefficients, C_f and C_h, respectively. The latter are expressed in terms of the bulk dissipation rates of mean mechanical energy and mean squared scalar field, thus enabling the evaluation of the classical Reynolds analogy factor, $RA = 2C_h/C_f$, in terms of the dissipation fields. The relationships between the friction and scalar transfer coefficients and the bulk dissipation rates is used to show that, for fully developed channel flows, the Reynolds analogy efficiency factor coincides exactly with the classical Reynolds analogy factor. Therefore, in this case, the Reynolds analogy factor of fully developed channel flows not only informs about the similarity between the mean momentum and scalar wall fluxes, but it provides information about the energetic scalar transfer efficiency of the system.

As it is well established in the literature, for a smooth wall channel flow, $RA \approx 1$, whereas for the rough wall case, a departure from analogous momentum and scalar transfer is measured through a Reynolds analogy factor being less than unity. Following the results of Secchi et al. [86], the relationships between C_f, C_h and the respective bulk dissipation rates is exploited to further explore the origins of a roughness-induced dissimilar mean momentum and scalar transfer. In particular the analysis of the spatial distributions of the mean dissipation rates highlights the flow regions most responsible for scalar and momentum transfer dissimilarities within the roughness sublayer. These are the attached, exposed regions (AER) forming on the windward slopes of roughness elements, and the well-mixed regions (WMR) located in the topographic valleys. AER consistently dominate the contributions to both mean bulk dissipation rates, whereas the effect of WMR is seen to disappear by increasing the roughness Reynolds number, k^+. Notably, WMR contribute almost equally to mechanical and scalar dissipation rates across the investigated roughness Reynolds numbers. This suggests that the observed roughness-induced dissimilarity between the momentum and scalar transfer stems mainly from differing dissipation behaviours within the AER.

DNS data of smooth and rough wall zero-pressure gradient boundary layers are used investigate the mean momentum and scalar transfer analogies in spatially developing flows. At matched streamwise location, the rough wall flow is characterized by thicker momentum and scalar boundary layers in comparison to smooth wall conditions. By performing the comparison at matched momentum Reynolds number, Re_2, the rough wall boundary layer exhibits significantly more intense momentum and scalar wall fluxes. Similarly to the channel flow case, the similarity between the mean momentum and scalar transfer can be evaluated through the classical Reynolds analogy factor. For the smooth wall data, $RA \approx 1$ for the entire range of momentum Reynolds numbers achieved in the DNS. In contrast, the rough wall case shows that the classical Reynolds analogy factor is significantly less than unity for small Re_2, but it approaches $RA \approx 1$ for increasing Re_2. This dependency on the local Reynolds number is, in fact, the result of the variation of the relative size of the roughness topography in comparison to local flow scales. Since the roughness size is prescribed, but the characteristic scales of the flow, such as the boundary layer thickness and the viscous length scale, change with respect to the streamwise location, the way the flow perceives the flow changes with the streamwise position.

Close to the leading edge of the roughness patch, the boundary layer thickness is relatively small in comparison to the characteristic size of the roughness topography. Similarly, the viscous length scale is also relatively small, in comparison to the roughness size, due to the high momentum flux in this region. Accordingly, surface roughness produces significant effects on the mean flow. These are seen, for instance in large downward shifts of the viscous units-scaled mean streamwise velocity and scalar profiles. Moving downstream, the roughness effects tend to become less prominent as the the boundary layer thickness and the viscous length scale tend to increase. Correspondingly, the viscous units-scaled mean streamwise velocity and scalar profiles show a decreasing downward shift in comparison to the smooth wall data. Despite the prominent effects induced by the roughness on the present data, the computed values of the roughness function, Δu^+, measuring the roughness-induced shift of the viscous units-scaled mean streamwise velocity profiles, highlight a behaviour that differs markedly from that of a fully-rough flow. In fact, the roughness function values measured at different streamwise locations fail to show the logarithmic slope, as a function of the roughness Reynolds number, k^+, that would be expected for fully rough conditions [13]. The reason lies in the lack of separation between the characteristic size of roughness elements and the boundary layer thickness throughout the streamwise extent of the simulated flow. In practice, roughness elements are so large that they act as large-scale obstacles on the flow rather than as small corrugations of the wall.

Differently from the fully developed channel flow case, an exact relationship between the friction coefficient and the bulk dissipation rate of mechanical energy cannot be established. However, based on physical arguments, the study proposes an approximate expression relating these quantities. In particular, the relationship is derived assuming that the amount of mechanical energy dissipated across the boundary layer should balance the product of the total wall stress by the mean bulk velocity at the considered streamwise position. Based on analogous arguments, a similar expression is also derived for the mean scalar wall flux and the bulk dissipation of the squared scalar field. The resulting expressions allow to relate the friction coefficients and the scalar transfer coefficients to the bulk dissipation rates of mechanical energy and of the squared scalar field. The values of C_f and C_h estimated using these expressions agree well with the values computed using mean momentum and scalar balances. Notably, the approximate expression between C_f and the bulk mechanical energy dissipation rate enables to express the Reynolds analogy efficiency factor as $RA_\pi = RA/(1 - \delta_1/\delta)$; owing to the fact that $\delta_1/\delta \leq 1$, this result shows that $RA_\pi > RA$, even for the smooth wall case. The direct computation of the Reynolds analogy efficiency factor with the present data confirms this result and further shows that the rough wall case is characterized by an even larger value of RA_π in comparison to the smooth wall case.

The last application considers smooth and rough wall impinging jets and uses for the analysis the results presented in [80–83, 85]. The most comprehensive data analysis is carried out for the smooth wall configuration for a bulk Reynolds number, $Re_b = 5300$ (based on the pipe diameter and its mean bulk velocity). Consistently with studies in the literature, the study evidences the formation of three separated flow regions: a free jet, a stagnation region, and a wall jet. For all the cases investigated in [80–83], surface roughness produces only marginal effects on the flow. In particular, it produces only a minor increase in the mean momentum and scalar wall fluxes along the impingement plate. This study shows that, the former increases mainly due to the pressure drag contribution of the roughness elements at small radial distances from the jet axis. Conversely, the viscous contribution to the mean momentum transfer remains practically unchanged in comparison to the smooth wall case at matched radial location. Similarly, the mean scalar flux does not change significantly at any radial location when compared to the smooth wall data.

Two main reasons are identified that justify the marginal influence of the roughness on the flow. For the relatively low Reynolds numbers achievable with a DNS, the near wall turbulence is in strong non-equilibrium, whereby the viscous dissipation of turbulence exceeds significantly its production. The near wall self-sustaining mechanisms of turbulence seem not to be sufficiently developed under the present conditions along the impingement plate. Most of the energy-containing eddies are confined at very large distances from the rough surface. In fact, as the analysis of energy spectra of radial velocity fluctuations reveals, they convect in the outer layer of the wall jet and consist predominantly in eddies, whose size is well-separated from the characteristic size of the investigated surface roughness.

Nonetheless, even for the smooth wall case, the impinging jet displays a patent non-analogous mean momentum and scalar transfer. In the stagnation region, the incoming flow from the free jet region deflects due to the action of an adverse mean pressure gradient which redirects the mean momentum towards the wall parallel direction. An equivalent mechanism acting on the mean scalar field does not exist and, as a result, the mean momentum and scalar wall fluxes depart from each other in this region. The mean momentum flux vanishes in correspondence of the jet axis, whereas the mean scalar flux is maximum. The analysed data shows that the mean wall fluxes tend to become more similar in magnitude sufficiently downstream of the stagnation region. However, along the wall jet, the mean momentum flux decays with the radial distance more rapidly than the mean scalar wall flux. This discrepancy arises from the radial evolution of the flow, which imposes a decrease in mean radial velocity inversely proportional to the radial coordinate. While this constraint affects momentum transport, it does not impact the mean scalar field or its wall flux. In contrast, the mean momentum wall flux must decay with the square of the radial distance.

Although the analysis of the mean momentum and scalar wall fluxes evidence regions of very high scalar transfer rates and relatively low momentum flux, the integral energetic analysis presented in this work reveals that the impinging jet flow is characterized by a low scalar transfer efficiency. Namely, the elevated scalar flux resulting from jet impingement is accompanied by a substantially higher expenditure of mechanical energy. This is shown through the radial distribution of the Reynolds analogy efficiency factor considering cylindrical control volumes, coaxial with the jet, for increasing their radius. In particular, RA_π is evaluated by taking into account the scalar flux at the impingement plate alone, and by considering the net scalar flux through the top confinement plate. Both cases show that, especially for small radii of the control volume, RA_π is significantly less than unity. Its value increases for increasing the radius of the control volume, but it remains less than unity for all the considered control volumes. Excluding from the computation of RA_π the baseline scalar flux, present even in the absence of flow, further reduces the Reynolds analogy efficiency factor at large radial positions.

The Reynolds analogy efficiency factor is also analysed locally following a procedure similar to that presented for the canonical boundary layer flows. The local analysis of RA_π along the impingement plate delivers results that are consistent with what is observed for the boundary layer flows. In particular, at sufficiently large distances from the stagnation region, the local RA_π exhibits values significantly higher than unity. This region of the wall jet is characterized by a fast-growing boundary layer with an upward velocity component that raises to fulfil mass conservation. This is, of course, similar to the boundary layer flow; the main difference being that the thickening of the canonical boundary layer occurs due to the wall friction, whereas for the radial flow of the impinging jet case, the growth of the boundary layer is accelerated by the radial development of the flow. However, for both cases, the scalar transfer associated with these flows is particularly effective. The scalar wall flux exceeds significantly the dissipation of mechanical energy occurring in the flow. In contrast, the near-wall regions exhibiting particularly low local Reynolds analogy efficiency factors are characterized by downward-directed flow. This occurs in the impinging jet for small radial distances. While the presence of flow directed towards the wall has an intuitive beneficial effect in augmenting the local scalar wall flux, it determines a comparatively greater increase in the mechanical energy dissipation and, thus, is associated with a Reynolds analogy efficiency factor smaller than unity.

The present work offers several points which could potentially drive future research endeavours. As already noted by Secchi et al. [86], the analysis of the mean dissipation rates of mechanical energy and squared scalar field offers a promising approach for developing a scalar transfer law for rough wall channel flow at high Reynolds numbers. This result is not yet available in the literature and it is the object of active research in the community. In this respect, future investigations should include a larger parameters space considering different roughness topographies and varying a wider range of Reynolds numbers. It is further noted that the observations made in reference to canonical boundary layers and impinging jets might also be helpful in unravelling the physical mechanisms behind dissimilar momentum and scalar transfer in rough wall channels. Despite the evident differences between these flows, it is not difficult to imagine flow patterns, within the roughness sublayer, displaying properties common to boundary layers and impinging flows. In fact, as noted by [56], [110], and Secchi et al. [86], AER over the windward side of roughness hills may form due to local flow impingement. AER further develop along the roughness hills featuring properties akin to boundary layers and, as shown by Secchi et al. [86] (and reported in this work), these regions contribute differently to the integral mean momentum and scalar transfer. The analysis presented for boundary layers and impinging jets could then be extended and applied locally also for the detailed analysis of rough wall channel flows.

Another context in which the present work could offer a substantial contribution is in the development of flow control strategies aiming at dissimilar control of momentum and scalar transfer. Typically, applications require to minimize the momentum transfer while maximizing the transfer of a scalar field [37]. In this respect, the Reynolds analogy efficiency factor could be a key parameter worth considering in this types of investigations. For instance, for impinging jets, several studies investigate strategies for increasing the wall scalar transfer [27, 39, 95]. Yet, none of the existing studies addresses the corresponding increase in the mean mechanical energy consumption produced by the flow control strategy. Related to impinging jets, it is remarked here that the present data set are restricted to few configurations. Future investigations should aim at characterising the scalar transfer efficiency of impinging jets for varying the configuration parameters, such as the nozzle to plate distance, and the inlet Reynolds number.

Journal Publications

(peer reviewed journal publications cited in this thesis)

[Secchi et al., 2022a], F. Secchi, T. Häber, D. Gatti, S. Schulz, D. Trimis, R. Suntz, and B. Frohnapfel. Turbulent impinging jets on rough surfaces. *GAMM-Mitteilungen.* 2022, 45(1):e202200005, doi: https://doi.org/10.1002/gamm.202200005.

[Secchi et al., 2023a], F. Secchi, D. Gatti, and B. Frohnapfel. The wall-jet region of a turbulent jet impinging on smooth and rough plates. *Flow, Turbulence and Combustion.* 2023, 110(2):275–299, 2023, doi: 10.1007/s10494-022-00387-x.

[Secchi et al., 2025a], F. Secchi, D. Gatti, U. Piomelli and B. Frohnapfel. A framework for assessing the Reynolds analogy in turbulent forced convection over rough walls. *Journal of Fluid Mechanics.* 2025, 1006:R3, doi: 10.1017/jfm.2025.1.

[Secchi et al., 2025b], F. Secchi, D. Gatti, and B. Frohnapfel. Energetics of a turbulent impinging jet with passive scalar transport. *Journal of Fluid Mechanics.* Submitted.

(peer reviewed journal publications not cited in this thesis)

[Bopp et al. 2024], M. Bopp, S. Wegt, L. Krüger, F. Secchi, B. Frohnapfel and S. Jakirlić. Flow and thermal fields modeling in jet impingement configurations using a Reynolds stress turbulence closure within the RANS and Sensitized-RANS framework. *International Journal of Heat and Fluid Flow,.* 2024, 105:109264, doi:10.1016/j.ijheatfluidflow.2023.109264.

Conference contributions

[Magagnato et al. 2021a], F. Magagnato, F. Secchi, P. Forooghi, S. Straub and B. Frohnapfel. DNS of Turbulent Heat Transfer in Impinging Jets at Different Reynolds and Prandtl Numbers. *14th WCCM-ECCOMAS Congress 2020: Collection of papers presented at the 14th edition of the WCCM-ECCOMAS*, virtual congress, January, 11-15, 2021, doi:10.23967/wccm-eccomas.2020.299

[Secchi et al. 2021b], F. Secchi, D. Gatti, and B. Frohnapfel. DNS of turbulent impinging jets on rough surfaces using a parametric forcing approach. *13th International ERCOFTAC Symposium on Engineering, Turbulence, Modelling and Measurements* , Rhodes, Greece, September, 15-17, 2021

[Bopp et al. 2022], M. Bopp, S. Wegt, L. Krüger, S. Jakirlić, F. Secchi, and B. Frohnapfel. Heat flux modeling in wall-bounded turbulent flows by Reynolds stress models within RANS and sensitized-RANS frameworks. *Proceedings of the 12th International Symposium on Turbulence and Shear Flow Phenomena*, Osaka, Japan, July, 19-22, 2022

[Secchi et al. 2022b], F. Secchi, D. Gatti, and B. Frohnapfel. Impact of wall boundary conditions on passive scalars in complex turbulent flows. *Proceedings of the 12th International Symposium on Turbulence and Shear Flow Phenomena*, Osaka, Japan, July, 19-22, 2022. doi:10.5445/IR/1000154332

[Secchi et al. 2023b], F. Secchi, D. Gatti, and B. Frohnapfel. Turbulent jet impingement: surface roughness effects on wall-heat transfer. *Proceeding of 10th International Symposium on Turbulence, Heat and Mass Transfer, THMT-23*, Rome, Italy, 11-15 September 2023, 4, Begellhouse. doi:10.1615/ICHMT.THMT-23.970

[Secchi et al. 2023c], F. Secchi, D. Gatti, and B. Frohnapfel. Heat transfer of an impinging jet - sensitivity towards inflow conditions. *14th International ERCOFTAC Symposium on Engineering, Turbulence, Modelling and Measurements* , Barcelona, Spain, September, 6-8, 2023

[Secchi et al. 2024a], F. Secchi, J. Yang, D. Gatti, A. Stroh, P. Schlatter, and B. Frohnapfel. Direct numerical simulation of smooth and rough wall turbulent boundary layers with heat transfer. *Ercoftac Workshop on Direct and Large Eddy Simulation (DLES14 2024)*, Erlangen, Germany, 10.–12. April 2024. doi:10.5445/IR/1000175210

[Weber et al. 2024], L. Weber, F. Secchi, D. Gatti, B. Frohnapfel, and P. Schlatter. Feedback-forcing immersed boundaries in spectral element methods: capabilities and limitations. *Ercoftac Workshop on Direct and Large Eddy Simulation (DLES14 2024)*, Erlangen, Germany, 10.–12. April 2024

[Secchi et al. 2024b], F. Secchi, D. Gatti, and B. Frohnapfel. Turbulent impinging jets on smooth and rough plates. *13th International Symposium on Turbulence and Shear Flow Phenomena*, Montreal, Canada, June, 25-28, 2025. doi:10.5445/IR/1000175227

Bibliography

[1] H. Abe and R. A. Antonia. Relationship between the energy dissipation function and the skin friction law in a turbulent channel flow. *J. Fluid Mech.*, 798:140–164, 2016. doi: 10.1017/jfm.2016.299.

[2] H. Abe and R. A. Antonia. Relationship between the heat transfer law and the scalar dissipation function in a turbulent channel flow. *J. Fluid Mech.*, 830:300–325, 2017. doi: 10.1017/jfm.2017.564.

[3] W. Abu Rowin, Y. Xia, S. Wang, and N. Hutchins. Accurately predicting turbulent heat transfer over rough walls: a review of measurement equipment and methods. *Exp. Fluids*, 65(6):86, May 2024. ISSN 1432-1114. doi: 10.1007/s00348-024-03812-1.

[4] R. J. Adrian. Comment on “a note on poisson’s equation for pressure in a turbulent flow”. *Phys. Fluids*, 25(3):577–577, 03 1982. ISSN 0031-9171. doi: 10.1063/1.863774.

[5] F. Alcántara-Ávila, S. Hoyas, and M. Jezabel Pérez-Quiles. Direct numerical simulation of thermal channel flow for $Re_\tau = 5000$ and $Pr = 0.71$. *J. Fluid Mech.*, 916:A29, 2021. doi: 10.1017/jfm.2021.231.

[6] J. Atema. Chemical signals in the marine environment: dispersal, detection, and temporal signal analysis. *Proc. Natl. Acad. Sci. U.S.A.*, 92(1):62–66, 1995. doi: 10.1073/pnas.92.1.62.

[7] R. Banyassady and U. Piomelli. Interaction of inner and outer layers in plane and radial wall jets. *J. Turbul.*, 16(5):460–483, 2015. doi: 10.1080/14685248.2015.1008008.

[8] P. Bradshaw and Y. M. Koh. A note on Poisson’s equation for pressure in a turbulent flow. *Phys. Fluids*, 24(4):777–777, 04 1981. doi: 10.1063/1.863442.

[9] R. S. Bunker. Gas Turbine Cooling: Moving From Macro to Micro Cooling. volume Volume 3C: Heat Transfer of *Turbo Expo: Power for Land, Sea, and Air*, page V03CT14A002, 06 2013. doi: 10.1115/GT2013-94277.

[10] M. Chen, L. Yang, H. Huang, X. Zhou, W. Zhang, and D. Wang. Flow characteristics in a semi-confined circular-pipe impinging jet. *Phys. Fluids*, 36(2):025108, 02 2024. ISSN 1070-6631. doi: 10.1063/5.0181233.

[11] M. Chevalier, P. Schlatter, A. Lundbladh, and D. Henningson. SIMSON–A pseudo-spectral solver for incompressible boundary layer flow. *Technical Report TRITA-MEK*, pages 1–100, 2007.

[12] K. S. Choi, D. Gatti, and I. Mortazavi. Progress in flow control and drag reduction. *Flow Turbul. Combust.*, 113(1):1, 2024. doi: 10.1007/s10494-024-00557-z.

[13] D. Chung, N. Hutchins, M. P. Schultz, and K. A. Flack. Predicting the drag of rough surfaces. *Annu. Rev. Fluid Mech.*, 53:439–471, 2021. doi: https://doi.org/10.1146/annurev-fluid-062520-115127.

[14] F. Dairay, V. Fortuné, E. Lamballais, and L. E. Brizzi. Direct numerical simulation of a turbulent jet impinging on a heated wall. *J. Fluid Mech.*, 764:362–394, 2015.

[15] R. B. Dean. Reynolds number dependence of skin friction and other bulk flow variables in two-dimensional rectangular duct flow. *J. Fluids Eng.*, 100(2):215–223, 06 1978. ISSN 0098-2202. doi: 10.1115/1.3448633.

[16] M. O. Deville, P. F. Fischer, and E. H. Mund. *High-Order Methods for Incompressible Fluid Flow*. Cambridge Monographs on Applied and Computational Mathematics. Cambridge University Press, 2002.

[17] R. H. Dishington. Rate of surface-strain tensor. *Am. J. Phys.*, 33(10):827–831, 10 1965. ISSN 0002-9505. doi: 10.1119/1.1970994.

[18] S. Dong, G.E. Karniadakis, and C. Chryssostomidis. A robust and accurate outflow boundary condition for incompressible flow simulations on severely-truncated unbounded domains. *J. Comput. Phys.*, 261:83–105, 2014. ISSN 0021-9991. doi: https://doi.org/10.1016/j.jcp.2013.12.042.

[19] S. V. Ekkad and P. Singh. A modern review on jet impingement heat transfer methods. *J. Heat Transfer.*, 143(6):064001, 04 2021. ISSN 0022-1481. doi: 10.1115/1.4049496.

[20] P. F. Fisher, J. W. Lottes, and S. G. Kerkemeier. NEK5000 Version 19.0. 2019. Argonne National Laboratory, Illinois.

[21] F. Forooghi, A. Weidenlener, F. Magagnato, B. Böhm, H. Kubach, T. Koch, and B. Frohnapfel. Dns of momentum and heat transfer over rough surfaces based on realistic combustion chamber deposit geometries. *Int. J. Heat Fluid Flow.*, 69:83–94, 2018. ISSN 0142-727X. doi: https://doi.org/10.1016/j.ijheatfluidflow.2017.12.002.

[22] P. Forooghi, B. Frohnapfel, F. Magagnato, and A. Busse. A modified parametric forcing approach for modelling of roughness. *Int. J. Heat Fluid Flow*, 71:200–209, 2018.

[23] P. Forooghi, M. Stripf, and B. Frohnapfel. A systematic study of turbulent heat transfer over rough walls. *Int. J. Heat Mass Transf.*, 127:1157–1168, 2018. ISSN 0017-9310. doi: https://doi.org/10.1016/j.ijheatmasstransfer.2018.08.013.

[24] P. Forooghi, A. Stroh, P. Schlatter, and B. Frohnapfel. Direct numerical simulation of flow over dissimilar, randomly distributed roughness elements: A systematic study on the effect of surface morphology on turbulence. *Phys. Rev. Fluids*, 3:044605, Apr 2018. doi: 10.1103/PhysRevFluids.3.044605.

[25] B. Frohnapfel, L. von Deyn, J. Yang, J. Neuhauser, A. Stroh, R. Örlü, and D. Gatti. Flow resistance over heterogeneous roughness made of spanwise-alternating sandpaper strips. *J. Fluid Mech.*, 980: A31, 2024. doi: 10.1017/jfm.2024.40.

[26] K. Fukagata, K. Iwamoto, and N. Kasagi. Contribution of Reynolds stress distribution to the skin friction in wall-bounded flows. *Phys. Fluids*, 14(11):L73–L76, 11 2002. doi: 10.1063/1.1516779.

[27] C. Gau, W. Y. Sheu, and C. H. Shen. Impingement cooling flow and heat transfer under acoustic excitations. *J. Heat Transf.*, 119(4):810–817, 11 1997. ISSN 0022-1481. doi: 10.1115/1.2824187.

[28] W. K. George, H. Abrahamsson, J. Eriksson, R. I. Karlsson, L. Löfdahl, and M. Wosnik. A similarity theory for the turbulent plane wall jet without external stream. *J. Fluid Mech.*, 425:367–411, 2000. doi: 10.1017/S002211200000224X.

[29] D. Goldstein, R. Handler, and L. Sirovich. Modeling a no-slip flow boundary with an external force field. *J. Comput. Phys.*, 105(2):354–366, 1993. ISSN 0021-9991. doi: https://doi.org/10.1006/jcph.1993.1081.

[30] D. Goldstein, R. Handler, and L. Sirovich. Direct numerical simulation of turbulent flow over a modeled riblet covered surface. *J. Fluid Mecha.*, 302:333–376, 1995. doi: 10.1017/S0022112095004125.

[31] W. J. Gordon and C. A. Hall. Transfinite element methods: Blending-function interpolation over arbitrary curved element domains. *Numer. Math.*, 21:109–129, 1973.

[32] P. M. Gresho and R. L. Sani. On pressure boundary conditions for the incompressible navier-stokes equations. *Int. J. Numer. Methods Fluids*, 7(10):1111–1145, 1987. doi: https://doi.org/10.1002/fld.1650071008.

[33] B.E. Griffith and C.S. Peskin. On the order of accuracy of the immersed boundary method: Higher order convergence rates for sufficiently smooth problems. *J. Comput. Phys.*, 208(1):75–105, 2005. ISSN 0021-9991. doi: https://doi.org/10.1016/j.jcp.2005.02.011.

[34] M. Hadžiabdić and K. Hanjalić. Vortical structures and heat transfer in a round impinging jet. *J. Fluid Mech.*, 596:221–260, 2008. doi: 10.1017/S002211200700955X.

[35] J. M. Hamilton, J. Kim, and F. Waleffe. Regeneration mechanisms of near-wall turbulence structures. *J. Fluid Mech.*, 287:317–348, 1995. doi: 10.1017/S0022112095000978.

[36] Z. Hantsis and U. Piomelli. Numerical simulations of scalar transport on rough surfaces. *Fluids*, 9(7), 2024. ISSN 2311-5521. doi: 10.3390/fluids9070159.

[37] Y. Hasegawa and N. Kasagi. Dissimilar control of momentum and heat transfer in a fully developed turbulent channel flow. *J. Fluid Mech.*, 683:57–93, 2011. doi: 10.1017/jfm.2011.248.

[38] Y. Hasegawa, M. Quadrio, and B. Frohnapfel. Numerical simulation of turbulent duct flows with constant power input. *J. Fluid Mech.*, 750:191–209, 2014. doi: 10.1017/jfm.2014.269.

[39] S.D Hwang and H.H Cho. Effects of acoustic excitation positions on heat transfer and flow in axisymmetric impinging jet: main jet excitation and shear layer excitation. *Int. J. Heat Fluid Flow*, 24(2):199–209, 2003. ISSN 0142-727X. doi: https://doi.org/10.1016/S0142-727X(02)00236-9.

[40] K. Jambunathan, E. Lai, M. A. Moss, and B. L. Button. A review of heat transfer data for single circular jet impingement. *Int. J. Heat Fluid Flow*, 13(2):106–115, 1992. ISSN 0142-727X. doi: doi.org/10.1016/0142-727X(92)90017-4.

[41] J. Jiménez. Turbulent flows over rough walls. *Annu. Rev. Fluid Mech.*, 36:173–196, 2004. doi: 10.1146/annurev.fluid.36.050802.122103.

[42] J. Jiménez and A. Pinelli. The autonomous cycle of near-wall turbulence. *J. Fluid Mech.*, 389: 335–359, 1999. doi: 10.1017/S0022112099005066.

[43] B.A. Kader. Temperature and concentration profiles in fully turbulent boundary layers. *Int. J. Heat Mass Transf.*, 24(9):1541–1544, 1981. ISSN 0017-9310. doi: https://doi.org/10.1016/0017-9310(81)90220-9.

[44] M. Kadivar and H. Garg. Turbulent heat transfer over roughness: a comprehensive review of theories and turbulent flow structure. *Int. J. Thermofluids.*, 26:100967, 2025. ISSN 2666-2027. doi: https://doi.org/10.1016/j.ijft.2024.100967.

[45] V. V. Katti, S. N. Yasaswy, and S. V. Prabhu. Local heat transfer distribution between smooth flat surface and impinging air jet from a circular nozzle at low Reynolds numbers. *Heat Mass Transf.*, 47 (3):237–244, Mar 2011. ISSN 1432-1181. doi: 10.1007/s00231-010-0716-1.

[46] J. Kim and P. Moin. Transport of passive scalars in a turbulent channel flow. In *Turbulent Shear Flows 6*, pages 85–96. Springer, 1989. doi: 10.1007/978-3-642-73948-4_9.

[47] W. Kim and H. Choi. Immersed boundary methods for fluid-structure interaction: A review. *Int. J. Heat Fluid Flow*, 75:301–309, 2019. ISSN 0142-727X. doi: https://doi.org/10.1016/j.ijheatfluidflow.2019.01.010.

[48] P. K. Kundu, I. M. Cohen, and D. R. Dowling. Chapter 9 - Boundary layers and related topics. In *Fluid Mechanics (Fifth Edition)*, pages 404–406. Academic Press, Boston, fifth edition edition, 2012. ISBN 978-0-12-382100-3. doi: https://doi.org/10.1016/B978-0-12-382100-3.10009-5.

[49] P. K. Kundu, I. M. Cohen, and D. R. Dowling. Chapter 4 - conservation laws. In *Fluid Mechanics (Fifth Edition)*, pages 95–169. Academic Press, Boston, fifth edition edition, 2012. ISBN 978-0-12-382100-3. doi: https://doi.org/10.1016/B978-0-12-382100-3.10004-6.

[50] F. Laadhari. Reynolds number effect on the dissipation function in wall-bounded flows. *Phys. Fluids*, 19(3):038101, 03 2007. ISSN 1070-6631. doi: 10.1063/1.2711480.

[51] M.C. Lai and C.S. Peskin. An immersed boundary method with formal second-order accuracy and reduced numerical viscosity. *J. Computat. Phys.*, 160(2):705–719, 2000. ISSN 0021-9991. doi: https://doi.org/10.1006/jcph.2000.6483.

[52] B.E. Launder and W. Rodi. The turbulent wall jet. *Progress in Aerospace Sciences*, 19:81–128, 1979. ISSN 0376-0421. doi: https://doi.org/10.1016/0376-0421(79)90002-2.

[53] J. Lee and S. J. Lee. The effect of nozzle configuration on stagnation region heat transfer enhancement of axisymmetric jet impingement. *Int. J. Heat Mass Transf.*, 43(18):3497–3509, 2000. ISSN 0017-9310. doi: https://doi.org/10.1016/S0017-9310(99)00349-X.

[54] X. Liu, Z. Xie, and S. Dong. On a simple and effective thermal open boundary condition for convective heat transfer problems. *Int. J. Heat and Mass Transfer*, 151:119355, 2020. ISSN 0017-9310. doi: https://doi.org/10.1016/j.ijheatmasstransfer.2020.119355.

[55] Y. Lu, L. D. Monache, J. Weil, K. Ngan, and Q. Li. Predictability of passive scalar dispersion in atmospheric surface layers with urban-like roughness: A large-eddy simulations study. *Q. J. R. Meteorol. Soc.*, 149(752):994–1017, 2023. doi: https://doi.org/10.1002/qj.4445.

[56] M. MacDonald, N. Hutchins, and D. Chung. Roughness effects in turbulent forced convection. *J. Fluid Mech.*, 861:138–162, 2019. doi: 10.1017/jfm.2018.900.

[57] R. Mittal and G. Iaccarino. Immersed boundary methods. *Annu. Rev. Fluid Mech.*, 37(1):239–261, 2005. doi: 10.1146/annurev.fluid.37.061903.175743.

[58] V. Narayanan and V. A. Patil. Oscillatory thermal structures induced by unconfined slot jet impingement. *Exp. Therm. Fluid Sci.*, 32(2):682–695, 2007. ISSN 0894-1777. doi: https://doi.org/10.1016/j.expthermflusci.2007.09.002.

[59] J. Nikuradse. Strömungsgesetze in rauhen Rohren. Technical Report 361, VDI-Forschungsheft, Berlin, 1933.

[60] N. T. Obot. Effect of semi-confinement on impingement heat transfer. In *Proc. 7th Int. Heat Transf. Conf.*, pages 395–400, 1982. doi: 10.1615/IHTC7.2030.

[61] F. Pasquill and F. B. Smith. *Atmospheric diffusion*, volume 437. Ellis Horwood Chichester, 1983.

[62] A. J. Patera. A spectral element method for fluid dynamics: Laminar flow in a channel expansion. *J. Comput. Phys.*, 54(3):468–488, 1984.

[63] J. W. R. Peeters and N. D. Sandham. Turbulent heat transfer in channels with irregular roughness. *Int. J. Heat Mass Transf.*, 138:454–467, 2019. doi: https://doi.org/10.1016/j.ijheatmasstransfer.2019.04.013.

[64] A. Perez, R. Örlü, A. Talamelli, and P. Schlatter. Appraisal of cavity hot-wire probes for wall-shear-stress measurements. *Exp. Fluids*, 63, 09 2022. doi: 10.1007/s00348-022-03498-3.

[65] F. Pèrez-Ràfols and A. Almqvist. Generating randomly rough surfaces with given height probability distribution and power spectrum. *Tribol. Int.*, 131:591–604, 2019. ISSN 0301-679X. doi: https://doi.org/10.1016/j.triboint.2018.11.020.

[66] C. S. Peskin. Flow patterns around heart valves: A numerical method. *J. Comput. Phys.*, 10(2): 252–271, 1972. ISSN 0021-9991. doi: https://doi.org/10.1016/0021-9991(72)90065-4.

[67] A. Pinelli, I.Z. Naqavi, U. Piomelli, and J. Favier. Immersed-boundary methods for general finite-difference and finite-volume navier–stokes solvers. *J. Comput. Phys.*, 229(24):9073–9091, 2010. ISSN 0021-9991. doi: https://doi.org/10.1016/j.jcp.2010.08.021.

[68] S. Pirozzoli, M. Bernardini, and P. Orlandi. Passive scalars in turbulent channel flow at high Reynolds number. *J. Fluid Mech.*, 788:614–639, 2016. doi: 10.1017/jfm.2015.711.

[69] S. Pirozzoli, J. Romero, M. Fatica, R. Verzicco, and P. Orlandi. One-point statistics for turbulent pipe flow up to $Re_\tau \approx 6000$. *J. Fluid Mech.*, 926:A28, 2021. doi: 10.1017/jfm.2021.727.

[70] S. Pirozzoli, J. Romero, M. Fatica, R. Verzicco, and P. Orlandi. DNS of passive scalars in turbulent pipe flow. *J. Fluid Mech.*, 940:A45, 2022. doi: 10.1017/jfm.2022.265.

[71] S. B. Pope. *Turbulent Flows.* Cambridge University Press, 2000.

[72] M. Quadrio, B. Frohnapfel, and Y. Hasegawa. Does the choice of the forcing term affect flow statistics in dns of turbulent channel flow? *Eur. J. Mech. B Fluids.*, 55:286–293, 2016. ISSN 0997-7546. doi: https://doi.org/10.1016/j.euromechflu.2015.09.005.

[73] O. Reynolds. On the extent and action of the heating surface of steam boilers. *Proc. Lit. Phil. Soc. Manchester*, 14:7–12, 1874.

[74] A. Rouhi, S. Endrikat, D. Modesti, R. D. Sandberg, T. Oda, K. Tanimoto, N. Hutchins, and D. Chung. Riblet-generated flow mechanisms that lead to local breaking of Reynolds analogy. *J. Fluid Mech.*, 951:A45, 2022. doi: 10.1017/jfm.2022.880.

[75] R. L. Sani and P. M. Gresho. Résumé and remarks on the open boundary condition minisymposium. *Int. J. Numer. Methods Fluids.*, 18(10):983–1008, 1994. doi: https://doi.org/10.1002/fld.1650181006.

[76] S. Sarkar, R. Gupta, T. Roy, R. Ganguly, and C. M. Megaridis. Review of jet impingement cooling of electronic devices: Emerging role of surface engineering. *Int. J. Heat Mass Transf.*, 206:123888, 2023. ISSN 0017-9310. doi: https://doi.org/10.1016/j.ijheatmasstransfer.2023.123888.

[77] P. Schlatter and R. Örlü. Assessment of direct numerical simulation data of turbulent boundary layers. *J. Fluid Mech.*, 659:116–126, 2010. doi: 10.1017/S0022112010003113.

[78] H. Schlichting and K. Gersten. *Thermal Boundary Layers Without Coupling of the Velocity Field to the Temperature Field*, pages 209–230. Springer Berlin Heidelberg, Berlin, Heidelberg, 2017. ISBN 978-3-662-52919-5. doi: 10.1007/978-3-662-52919-5_9.

[79] W. H. Schwarz and W. P. Cosart. The two-dimensional turbulent wall-jet. *J. Fluid Mech.*, 10(4): 481–495, 1961. doi: 10.1017/S0022112061000299.

[80] F. Secchi, T. Häber, D. Gatti, S. Schulz, D. Trimis, R. Suntz, and B. Frohnapfel. Turbulent impinging jets on rough surfaces. *GAMM Mitt.*, 45(1):e202200005, 2022. doi: https://doi.org/10.1002/gamm.202200005.

[81] F. Secchi, D. Gatti, and B. Frohnapfel. The wall-jet region of a turbulent jet impinging on smooth and rough plates. *Flow Turbul. Combust.*, 110(2):275–299, 2023. ISSN 1573-1987. doi: 10.1007/s10494-022-00387-x.

[82] F. Secchi, D. Gatti, and Bettina Frohnapfel. Turbulent jet impingement: surface roughness effects on wall-heat transfer. In *Proc. 10th Int. Symp. Turbul. Heat Mass Transfer*, 2023. doi: 10.1615/ICHMT.THMT-23.970.

[83] F. Secchi, D. Gatti, and B. Frohnapfel. Turbulent impinging jets on smooth and rough plates. In *Proc. 13th Int. Symp. Turbul. Shear Flow Phenom.*, 2024. doi: 10.5445/IR/1000175227. URL `https://www.tsfp-conference.org/proceedings/2023/84.pdf`.

[84] F. Secchi, J. Yang, D. Gatti, A. Stroh, P. Schlatter, and B. Frohnapfel. Direct numerical simulation of smooth and rough wall turbulent boundary layers with heat transfer. In *Ercoftac Workshop on Direct and Large Eddy Simulation (DLES14 2024), Erlangen, Deutschland, 10.-12. April 2024*, 2024. doi: 10.5445/IR/1000175210.

[85] F. Secchi, D. Gatti, and B. Frohnapfel. Energetics of a turbulent impinging jet with passive scalar transport. *J. Fluid Mech. (Submitted)*, 2025.

[86] F. Secchi, D. Gatti, U. Piomelli, and B. Frohnapfel. A framework for assessing the Reynolds analogy in turbulent forced convection over rough walls. *J. Fluid Mech.*, 1006:R3, 2025. doi: 10.1017/jfm.2025.1.

[87] B. I. Shraiman and E. D. Siggia. Scalar turbulence. *Nature*, 405(6787):639–646, Jun 2000. ISSN 1476-4687. doi: 10.1038/35015000.

[88] A. Stroh, Y. Hasegawa, P. Schlatter, and B. Frohnapfel. Global effect of local skin friction drag reduction in spatially developing turbulent boundary layer. *J. Fluid Mech.*, 805:303–321, 2016. doi: 10.1017/jfm.2016.545.

[89] A. Stroh, K. Schäfer, B. Frohnapfel, and P. Forooghi. Rearrangement of secondary flow over spanwise heterogeneous roughness. *J. Fluid Mech.*, 885:R5, 2020. doi: 10.1017/jfm.2019.1030.

[90] C.S. Subramanian and R.A. Antonia. Effect of Reynolds number on a slightly heated turbulent boundary layer. *Int. J. Heat Mass Transf.*, 24(11):1833–1846, 1981. ISSN 0017-9310. doi: https://doi.org/10.1016/0017-9310(81)90149-6.

[91] M. Thakkar. *Investigation of turbulent flow over irregular rough surfaces using direct numerical simulations.* PhD thesis, University of Southampton, October 2017.

[92] M. Thakkar, A. Busse, and N. Sandham. Surface correlations of hydrodynamic drag for transitionally rough engineering surfaces. *J. Turb.*, 18(2):138–169, 2017. doi: 10.1080/14685248.2016.1258119.

[93] M. Thakkar, A. Busse, and N. D. Sandham. Direct numerical simulation of turbulent channel flow over a surrogate for nikuradse-type roughness. *J. Fluid Mech.*, 837:R1, 2018. doi: 10.1017/jfm.2017.873.

[94] N. Uddin, S. O. Neumann, and B. Weigand. LES simulations of an impinging jet: On the origin of the second peak in the nusselt number distribution. *Int. J. Heat Mass Transfer*, 57(1):356–368, 2013. ISSN 0017-9310. doi: https://doi.org/10.1016/j.ijheatmasstransfer.2012.10.052.

[95] N. Uddin, S. O. Neumann, B. Weigand, and B. A. Younis. LES investigation of a passively excited impinging jet. *Int. J. Heat Mass Transfer*, 165:120705, 2021. ISSN 0017-9310. doi: https://doi.org/10.1016/j.ijheatmasstransfer.2020.120705.

[96] C. Vanderwel, A. Stroh, J. Kriegseis, B. Frohnapfel, and B. Ganapathisubramani. The instantaneous structure of secondary flows in turbulent boundary layers. *J. Fluid Mech.*, 862:845–870, 2019. doi: 10.1017/jfm.2018.955.

[97] J. Vejrazka, J. Tihon, P. Marty, and V. Sobolík. Effect of an external excitation on the flow structure in a circular impinging jet. *Phys. Fluids*, 17(10):105102, 10 2005. ISSN 1070-6631. doi: 10.1063/1.2084207.

[98] L. H. von Deyn, P. Forooghi, B. Frohnapfel, P. Schlatter, A. Hanifi, and D. S. Henningson. Direct numerical simulations of bypass transition over distributed roughness. *AIAA Journal*, 58(2):702–711, 2020. doi: 10.2514/1.J057765.

[99] H. Wang, M. Sun, Y. Yang, and N. Qin. A passive scalar-based method for numerical combustion. *Int. J. Hydrogen Energy*, 40(33):10658–10661, 2015. ISSN 0360-3199. doi: https://doi.org/10.1016/j.ijhydene.2015.06.148.

[100] Z. Warhaft. Passive scalars in turbulent flows. *Annual Review of Fluid Mechanics*, 32(Volume 32, 2000):203–240, 2000. ISSN 1545-4479. doi: https://doi.org/10.1146/annurev.fluid.32.1.203.

[101] J. Warnatz, U. Maas, and R. W. Dibble. *Combustion: Physical and Chemical Fundamentals, Modeling and Simulation, Experiments, Pollutant Formation.* Springer, 2006. ISBN 978-3-540-45363-5. doi: 10.1007/978-3-540-45363-5.

[102] L. Weber, F. Secchi, D. Gatti, B. Frohnapfel, and P. Schlatter. Assessment of a feedback-forcing immersed boundary method in a spectral element framework for rough channel flows. In *Direct and Large Eddy Simulation XIV. DLES 2024. ERCOFTAC Series*, 2025.

[103] A. D. Woodworth, D. M. Salazar, and T. Liu. Heat transfer and skin friction: beyond the Reynolds analogy. *Int. J. Heat Mass Transfer*, 206:123960, 2023. ISSN 0017-9310. doi: https://doi.org/10.1016/j.ijheatmasstransfer.2023.123960.

[104] J. Z. Wu. A theory of three-dimensional interfacial vorticity dynamics. *Phys. Fluids*, 7(10):2375–2395, 10 1995. ISSN 1070-6631. doi: 10.1063/1.868750.

[105] J. Z. Wu, Y. Zhou, and M. Fan. A note on kinetic energy, dissipation and enstrophy. *Phys. Fluids*, 11(2):503–505, 02 1999. ISSN 1070-6631. doi: 10.1063/1.869866.

[106] W. Wu, R. Banyassady, and U. Piomelli. Large-eddy simulation of impinging jets on smooth and rough surfaces. *J. Turbul.*, 17(9):847–869, 2016. doi: 10.1080/14685248.2016.1181761.

[107] A. M. Yaglom. Similarity laws for constant-pressure and pressure-gradient turbulent wall flows. *Annu. Rev. Fluid Mech.*, 11(1):505–540, 1979. doi: 10.1146/annurev.fl.11.010179.002445.

[108] J. Yang, A. Stroh, D. Chung, and P. Forooghi. Direct numerical simulation-based characterization of pseudo-random roughness in minimal channels. *J. Fluid Mech.*, 941:A47, 2022. doi: 10.1017/jfm.2022.331.

[109] H. Yao, T. A. Zaki, and C. Meneveau. Entropy and fluctuation relations in isotropic turbulence. *J. Fluid Mech.*, 973:R6, 2023. doi: 10.1017/jfm.2023.808.

[110] K. Zhong, N. Hutchins, and D. Chung. Heat-transfer scaling at moderate Prandtl numbers in the fully rough regime. *J. Fluid Mech.*, 959:A8, 2023. doi: 10.1017/jfm.2023.125.

Nomenclature

Reynolds numbers

SYMBOL	DESCRIPTION
Re_b	bulk Reynolds number based on U_b and δ
Pe_b	bulk Péclet number based on Re_b
Re_τ	friction Reynolds number based on u_τ and δ
Pe_τ	friction Péclet number based on Re_τ
Re_Ω	dissipation Reynolds number based on u_Ω and δ
k^+	roughness Reynolds number based on u_τ and k
Re_1	displacement Reynolds number based on u_∞ and δ_1
Re_2	momentum Reynolds number based on u_∞ and δ_2
Re_m	local Reynolds number based on $\overline{U}_b$ and δ_m

Latin letters

upper case

SYMBOL	DESCRIPTION
$\mathcal{K}$	instantaneous kinetic energy
$\mathcal{G}$	one-half of the squared scalar magnitude
T	temperature
M	number of chemical species
$\mathcal{B}$	mechanical energy
$\mathcal{V}$	control volume
$\partial\mathcal{V}$	boundary of the control volume
$\mathcal{S}$	scalar entropy
$\mathcal{Z}$	mechanical entropy
$\mathcal{H}_{,i}$	imbalance between the molecular mechanical energy flux and the pressure transport
U_c	characteristic velocity scale of a system
L_c	characteristic length scale of a system
RA_π	Reynolds analogy efficiency factor

RA	Reynolds analogy factor
$\mathcal{A}$	plan area of the channel flow wall
$\mathcal{A}_w$	wetted area of the channel flow wall
U_b	bulk velocity
Pr	Prandtl number
C_f	friction coefficient
C_h	scalar transfer coefficient (Stanton number)
$\mathcal{L}_i$	ith component of the Lamb vector
$\mathcal{B}_\infty$	free stream mechanical energy of the boundary layer
$\mathcal{G}_\infty$	free stream (half) squared scalar magnitude of the boundary layer
$\mathcal{G}^\varphi$	squared scalar field associated with the passive scalar field φ
$\mathcal{L}_w$	closed circumferential contour following the impingement plate geometry
$\mathcal{A}_L$	lateral surface of the impinging jet control volume
$\mathcal{A}_B$	base surface of the impinging jet control volume
$\mathcal{A}_I$	inlet surface of the impinging jet control volume
$\mathcal{A}_T$	top surface of the impinging jet control volume
$\mathcal{E}$	bulk dissipation of mechanical energy within $\mathcal{V}$
$\mathcal{E}^\mathcal{G}$	bulk dissipation of $\mathcal{G}$ within $\mathcal{V}$
$\mathcal{D}$	integral molecular flux of mechanical energy across $\partial\mathcal{V}$
$\mathcal{D}^\mathcal{G}$	integral molecular flux of $\mathcal{G}$ across $\partial\mathcal{V}$
$\mathcal{U}_i$	target velocity in the fringe region of the boundary layer
L_x	computational domain length in x direction
L_y	computational domain length in y direction
P	polynomial degree of the solution in the spectral element framework
D	pipe diameter
T_{avg}	averaging time
$\mathscr{T}$	CPG units-scaled mean mechanical energy transport as a function of the wall normal distance
$\mathscr{T}^\mathcal{G}$	CPG units-scaled mean squared scalar transport as a function of the wall normal distance
$\mathscr{D}$	CPG units-scaled mean mechanical energy diffusion as a function of the wall normal distance
$\mathscr{D}^\mathcal{G}$	CPG units-scaled mean squared scalar diffusion as a function of the wall normal distance
ε	CPG units-scaled mean mechanical energy dissipation as a function of the wall normal distance
$\varepsilon^\mathcal{G}$	CPG units-scaled mean squared scalar dissipation as a function of the wall normal distance
$\mathscr{P}$	CPG units-scaled mean mechanical energy input as a function of the wall normal distance
$\mathscr{P}^\mathcal{G}$	CPG units-scaled mean squared scalar input as a function of the wall normal distance

L_R	length of the roughness patch in the boundary layer DNS
L_T	length of the transition region in the boundary layer DNS
H	nozzle to plate separation in the impinging jet configuration
NL_r	non-linear term in the radial component of the mean momentum equation in the wall jet
G_r	pressure gradient term in the radial component of the mean momentum equation in the wall jet
V_r	viscous diffusion term in the radial component of the mean momentum equation in the wall jet
NL_z	non-linear term in the wall normal component of the mean momentum equation in the wall jet
G_z	pressure gradient term in the wall normal component of the mean momentum equation in the wall jet
NL_ϑ	non-linear term in the mean passive scalar equation in the wall jet
V_ϑ	viscous diffusion term in the passive mean scalar equation in the wall jet
C_{f0}	maximum mean friction coefficient along the impingement plate
C_{h0}	maximum mean scalar transfer coefficient along the impingement plate
PS	power spectrum
PDF	probability density function

lower case

Symbol	Description
u_i	instantaneous velocity
u	streamwise velocity component
v	spanwise velocity component
w	wall normal velocity component
x_i	coordinate direction ith
x	streamwise coordinate direction
y	spanwise coordinate direction
z	wall normal coordinate direction
u_r	radial velocity component
u_ϕ	tangential velocity component
u_z	axial velocity component
r	radial coordinate
ϕ	angular coordinate
$\hat{r}_i$	ith component of the unit radial vector
t	time
f_j	body force per unit mass
f	mean pressure gradient driving the flow
p	pressure

s_{ij}	strain rate tensor
r_{ij}	rotation (vorticity) tensor
e	internal energy
c_{P}	heat capacity at constant pressure
q_{T}	temperature source term per unit mass
$q_{\mathrm{R}k}$	source term per unit mass of the kth species
q	source term per unit mass of the passive scalar field
n_i	unit outward normal vector to a surface
b_{ij}	superficial strain rate tensor
s	thermodynamic entropy
c	heat capacity analogous for a generic passive scalar field
δ	half-channel height
b	lateral extent of cross section of a duct
q_w	scalar wall flux
u_τ	friction velocity
u_Ω	velocity scale based on ν and Ω
u_∞	free stream velocity of the boundary layer
u_m	mean radial velocity maxima in the wall jet region of the impinging jet flow
u_b	mean bulk radial velocity in the impinging jet
u_0	constant with units of a squared length over time
k	roughness characteristic size
k_t	mean peak-to-trough height of the roughness topography
k_{99}	99% of the confidence interval of the PDF of the roughness distribution
k_m	melt-down height of the roughness topography
n_x	number of elements in the x direction
n_y	number of elements in the y direction
n_z	number of elements in the z direction
$u^+_{\infty S}$	smooth wall viscous units-scaled free stream velocity
$u^+_{\infty R}$	rough wall viscous units-scaled free stream velocity
f_i^{IBM}	immersed boundary body force
k_ϕ	azimuthal wave number
h	convective scalar transfer coefficient

Greek letters

upper case

Symbol	Description
Δt	time interval
$\Delta\Theta_c$	characteristic scalar variation within a system

Θ_b	bulk scalar
Ω	bulk dissipation-based frequency
Ξ	characteristic scalar per unit length based on mean bulk dissipation of $\mathcal{G}$
Π_{IN}	mean mechanical energy convected inside the control volume
Π_{OU}	mean mechanical energy convected out of the control volume
$\Pi^{\mathcal{G}}_{IN}$	mean squared scalar magnitude convected inside the control volume
$\Pi^{\mathcal{G}}_{OU}$	mean squared scalar magnitude convected out of the control volume
Π^{ϑ}_{IN}	mean input scalar flux at the control volume's boundary
$\Delta\Theta$	difference between ϑ_w and ϑ_J
Δu^+	streamwise velocity roughness function
$\Delta\vartheta^+$	scalar roughness function
Θ	local deviation of passive scalar field ϑ from the base solution ϑ_B
Δr	radial increment

lower case

Symbol	Description
ρ	density
τ_{ij}	stress tensor
μ	dynamic viscosity
ν	kinematic viscosity
ω_i	ith vorticity component
α_{T}	molecular thermal diffusivity
λ	thermal conductivity
ρ_k	mass concentration of species kth
$\alpha_{\mathrm{R}k}$	molecular concentration diffusivity
ϑ	passive scalar field
α	molecular diffusivity of the passive scalar field
η	scalar transfer efficiency
π_ϑ	net scalar flux per unit density
π_M	mechanical energy bulk dissipation per unit density
τ_w	stress at the wall
δ_ν	viscous length scale
ϑ_τ	friction scalar
δ_α	scalar molecular diffusivity length scale based on u_τ and α
δ_Ω	length scale based on ν and Ω
δ_Ξ	length scale based on α and u_Ω
ϑ_Ξ	scalar scale based on δ_Ξ and Ξ
δ_{99}	99% of u_∞ boundary layer thickness
δ_1	displacement boundary layer thickness

δ_2	momentum boundary layer thickness
ϑ_∞	free stream scalar value of the boundary layer
$\vartheta^+_{\infty S}$	smooth wall viscous units-scaled free stream scalar
$\vartheta^+_{\infty R}$	rough wall viscous units-scaled free stream scalar
δ^ϑ_{99}	99% of ϑ_∞ boundary layer thickness
δ^ϑ_1	scalar displacement thickness
δ^ϑ_2	scalar energy thickness
φ	complementary passive scalar field
ϑ_w	prescribed scalar value at the wall
ϑ_J	prescribed scalar value at the jet exit section
δ_m	boundary layer thickness along the impingement plate
δ^ϑ_m	scalar boundary layer thickness along the impingement plate
ϑ_m	maxima (or minima) of the mean scalar wall normal profiles in the wall jet region of the impinging jet flow
$\gamma(x)$	fringe function
δ_{1IN}	displacement thickness of the Blasius solution at the inlet of the boundary layer
α_{IB}	integral constant of the immersed boundary method
β_{IB}	proportional constant of the immersed boundary method
ϑ_B	steady-state base solution when no flow is present in the impinging jet configuration
λ_{min}	smallest resolved wave length in the roughness topography in-plane distribution

Mathematical symbols

SYMBOL	DESCRIPTION
δ_{ij}	identity second-order isotropic tensor
ε_{ijk}	Levi-Civita permutation tensor
$(\bar{\cdot})$	time averaging
$(\cdot)_{,i}$	partial differentiation with respect to the ith coordinate
$(\cdot)^\star$	normalization with U_c, L_c, ν, $\Delta\Theta_c$ and α
$(\cdot)^+$	normalization with u_τ and δ_ν
$(\cdot)^\#$	normalization with δ_α
$(\cdot)^*$	normalization with outer units. Channel flow, U_b and δ; impinging jet, U_b, D
$(\cdot)^\Omega$	normalization with u_Ω and δ_Ω
$(\cdot)'$	stochastic fluctuation with respect to the temporal mean
$(\cdot)''$	dispersive fluctuation with respect to the temporal and spatial mean
$\langle \cdot \rangle$	intrinsic spatial averaging. Channel flow, streamwise and spanwise directions; boundary layer, spanwise direction; impinging jet, circumferential direction.
$[\cdot]$	variation of a quantity computed over two coaxial control volumes of different radius

Abbreviations

SYMBOL	DESCRIPTION
DNS	direct numerical simulation
CFR	constant flow rate
CPG	constant pressure gradient
CPI	constant pressure gradient
FIK	Fukagata Iwamoto Kasagi
IBM	immersed boundary method
PI	proportional integral
DOF	degrees of freedom
PIV	particle image velocimetry

List of Figures

List of Tables

A Numerical simulations details

In this appendix, further technical details about the numerical simulations are provided for all the investigated configurations. In particular, the focus is put on the independence of the results from the mesh resolution and the time of acquisition of statistical data.

A.1 Rough wall channel flow

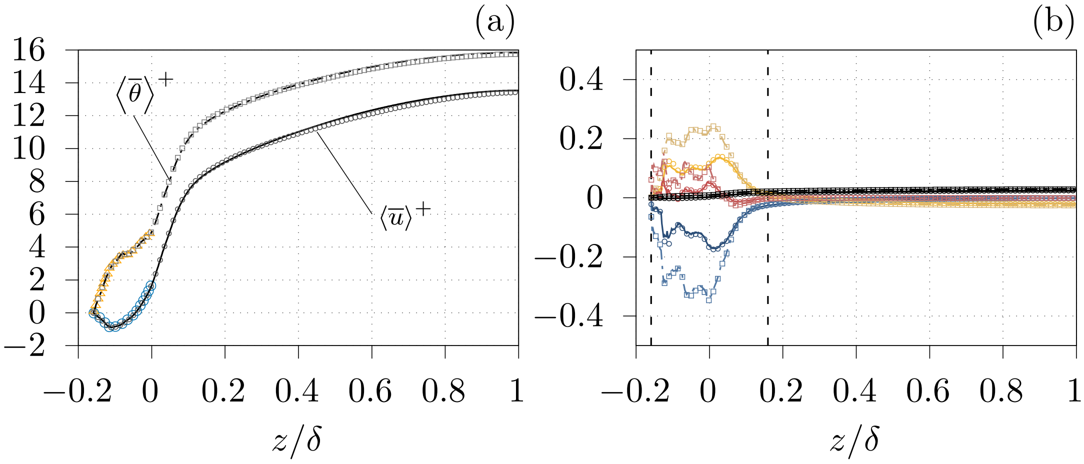

Figure A.1: Comparison between averaging time intervals, $T_{avg}U_b/\delta$, for the case $k^+ = 90$, $Re_\tau = 540$. Lines, $T_{avg}U_b/\delta = 140.9$; symbols, $T_{avg}U_b/\delta = 94.7$. (a), mean streamwise-velocity and scalar; blue and orange symbols represent data from [63]. (b), mean mechanical and scalar energy budgets. ——, $-\varepsilon$; -·-·-·, $-\varepsilon_\theta$; ——, $-T$; -·-·-·, $-T_\theta$; ——, D; -·-·-·, D_θ; ——, Π; -·-·-·, Π_θ. The vertical black dashed lines in panels (b) and (c) indicate the boundaries of the roughness canopy.

Details of the computational grid used in [86] are reported in table 5.1 of the present study. A full grid-independence study for the presented result is not available due to the high computational cost associated with simulating the rough wall channel flow configurations for multiple resolutions. The computational mesh adopted in the study was designed based on the simulations reported by Thakkar [91] and Thakkar et al. [93], who investigate the exact same roughness topographies under the same flow conditions. In particular, the simulations reported in [86] use a very similar resolution as that reported in [93]. It is important to highlight that the results of Secchi et al. [86] were obtained using a spectral element flow solver (described in Section 4.1 of this work), a high-order method that exhibits exponential convergence with the polynomial degree, provided the solution is sufficiently smooth [16]. In contrast, [93] use a finite difference method of the second order, ensuring that the spectral element method results presented here and in [86] are conservatively well-resolved.

L_x/D	L_y/D	H/D	n_{xc}	n_{xe}	n_{yc}	n_{ye}	n_z	E	N	DOF	$T_{avg}U_b/D$
16	16	2	98	29	98	29	48	1168128	7	598×10^6	500

Table A.1: Simulation parameters.

This can be appreciated from the good agreement between the present mean streamwise velocity and scalar profiles with the data from [93] and [63] shown in figure 5.2. Further, for the rough wall case with $k^+ = 90$, $Re_\tau = 540$, figure A.1 shows flow statistics computed over two different sampling times, T_{avg}. Solid lines and symbols in the figure compare, respectively, statistics collected over $T_{avg}U_b/\delta = 140.9$ (as the results presented in the present work) and $T_{avg}U_b/\delta = 94.7$. As it can be observed, differences between lines and symbols are marginal for both the mean streamwise-velocity and scalar, panel (a) in the figure, and in the mechanical and $\overline{\mathcal{G}}$ budget profiles, in panel (b) in the figure. Note also that, panel (a) in the figure provides a comparison of the mean streamwise velocity and scalar profiles within the roughness sublayer with the reference data from [93] and [63]. The data shows a remarkable agreement with the reference data for both averaging times.

It is further highlighted that the non-smooth profiles observed in figure 5.5c and in figure A.1b are due to the limited size of the roughness sample in the wall-parallel directions, and they are not an artifact due to the limited sampling time used to acquire the statistics.

A.2 Smooth wall impinging jet

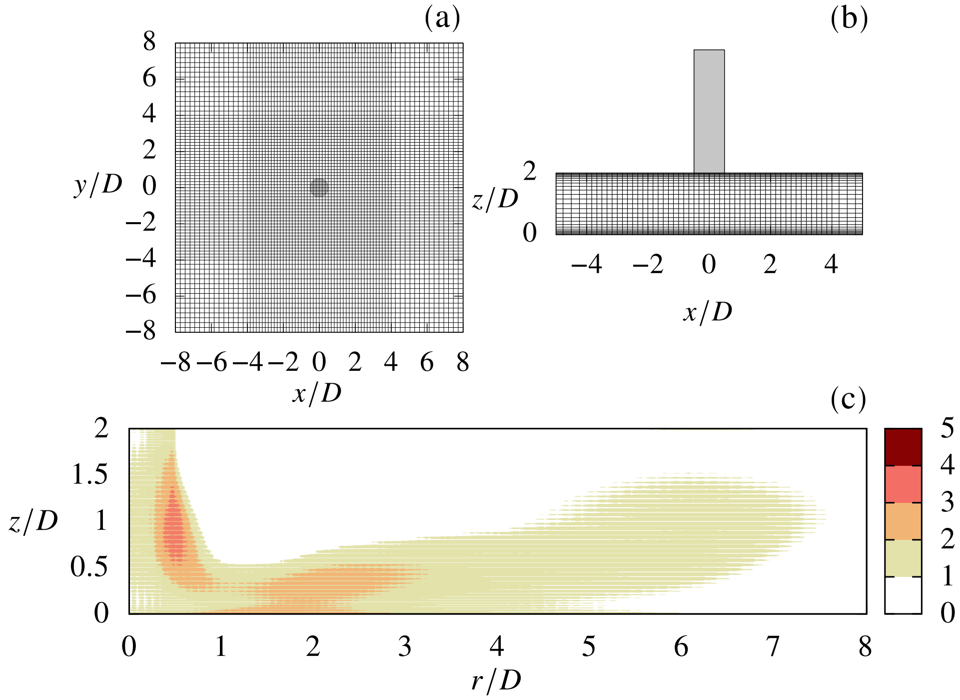

Figure A.2: Computational mesh of elements; (a) top view; (b) front view for $x \in [-5, 5]$. To ease the visualization, only one every two elements is shown in the figures. (c) Average local grid size to Kolmogorov length scaler ration, Δ/η.

The computational mesh used for the impinging jet DNS presented in section 5.3 and in [85] is displayed in figure A.2(a, b). As seen in panel (b) of the figure, the elements are stretched in the wall-normal direction to cluster elements toward the impingement and confinement plates. Additionally, the mesh is designed with a uniform in-plane element distribution over the square sub-domain $[-4D,\, 4D] \times [-4D,\, 4D]$. Table A.1 reports the mesh parameters and the total number of degrees of freedom (DOF). The latter corresponds to the number of grid points in the physical space and is computed as $DOF = E \times (N+1)^3$, where E denotes the total number of elements in the mesh and N indicates the polynomial degree of the solution. Referring to the table, the number of elements in the wall-parallel directions, x and y, is given by $2 \times n_{xe} + n_{xc}$, and $2 \times n_{ye} + n_{yc}$, respectively; the subscripts c and e indicate the central and external regions of the mesh. On the other hand, n_z denotes the number of elements in the wall-normal direction.

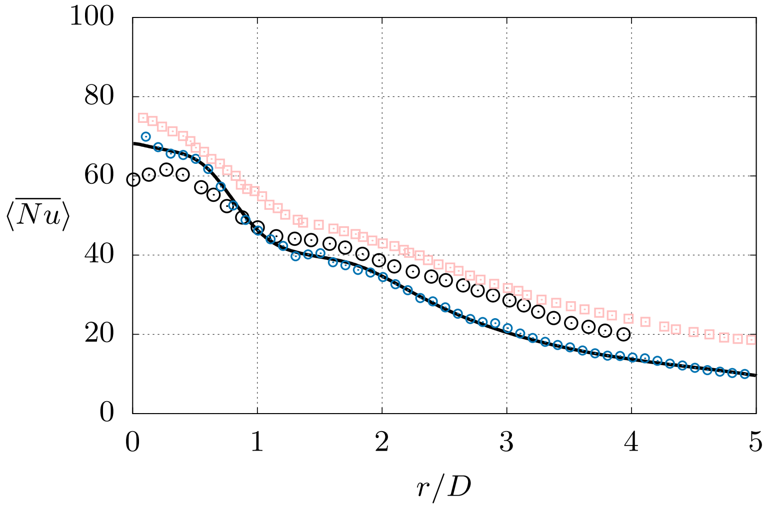

Figure A.3: Mean Nusselt number distribution along the impingement plate. ———, present DNS, $N = 7$; blue symbols, present DNS, $N = 5$; black symbols, experimental data of [53]; pink square markers, experimental data of Katti et al. [45]. DNS data is for a Prandtl number $Pr = 0.7$.

Results reported in section 5.3 refer to a numerical solution interpolated on each element with a Lagrange polynomial of degree $N = 7$. The mesh resolution in the flow domain is displayed in figure A.2c in terms of the ratio Δ/η, where $\Delta = (\Delta x \Delta y \Delta z)^{1/3}$, with Δx, Δy, and Δz being the local grid spacings in the coordinate directions, represents a measure of the local grid-size, and $\eta = \left(\nu^3/\varepsilon\right)^{1/4}$ is the Kolmogorov length scale (here ε represents the local mean dissipation rate of turbulent fluctuations). Grid independence of the results was tested by comparing the numerical solutions for $N = 5$ and $N = 7$ on a fixed mesh of elements. Figure A.3 shows the result of such an exercise on the time-, and space-averaged scalar wall flux distribution along the impingement plate for the two solutions. To enable the comparison with heat transfer measurements of Lee and Lee [53] and Katti et al. [45], the scalar wall flux is reported in terms of the Nusselt number, $Nu = hD/\lambda$, where h is the convective scalar transfer coefficient. Figure A.3 further suggests the independence of the flow statistics on the time-averaging window: once statistically stationary conditions were achieved, data were collected over a period $T_{avg} \approx 500D/U_b$, for the $N = 7$ case, and $T_{avg} \approx 200D/U_b$ for the case with $N = 5$.

The agreement with the experimental literature data is, on the other hand, somewhat poorer. At small radial locations the DNS data falls in between the two experimental data sets; however, at greater radial distances, the DNS data reports significantly smaller mean Nusselt number values in comparison to the reference

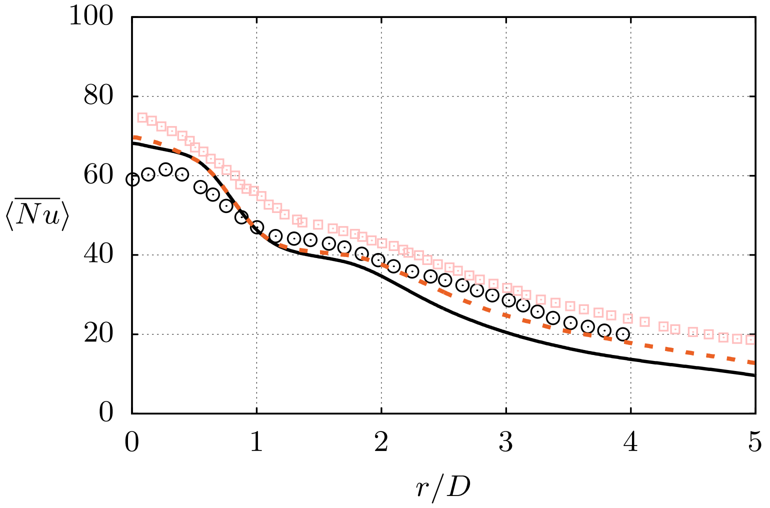

Figure A.4: Mean Nusselt number distribution along the impingement plate. Present DNS data: ———, statistically stationary conditions; - - - - -, transient of the flow. Black symbols, experimental data of [53]; pink square markers, experimental data of Katti et al. [45].

data. In this respect, it is noted that the experiments of Lee and Lee [53] and Katti et al. [45] consider slightly different configurations and Reynolds numbers. In particular, both literature studies do not include a confinement plate. In the present DNS investigation, the latter produces a semi-confined environment in which, at statistically stationary conditions, the scalar temperature field reaches a significantly higher mean bulk value in comparison to an equivalent non-confined flow. In fact, an open flow domain enables cold fluid to be continually entrained from the outside, thereby lowering the mean temperature in the impingement plate vicinity. In contrast, for the confined impinging jet, a larger mean bulk temperature is likely to determine overall lower mean scalar transfer rates with the warm impinging plate, as it is the case of the present DNS data. This is in agreement with observations in the literature, which evidence that the presence of a confinement plate reduces the mean heat-transfer rate along the impingement plate [40, 60].

Further, this argument is supported by the analysis of the transient of the flow. The smooth wall impinging jet case, $J05$, was initialized with the scalar field at equilibrium with the issuing jet and the confinement plate, *i.e.* with $\vartheta = 0$ everywhere away from the impingement plate. The latter is kept at a uniform and constant scalar value, $\vartheta_w = 1$. As the transient develops, the mean bulk scalar increases due to the scalar exchange at the impingement plate until the flow reaches statistically stationary conditions, and the mean bulk scalar fluctuates around a constant value between 0 and 1. Flow statistics are computed over this flow regime and give, for instance, the mean radial Nusselt number distributions in figure A.3. Performing the time-averaging over a selected time window during the transient of the flow results in a different distribution of the mean Nusselt number. This can be seen in figure A.4, where the mean Nusselt number distribution at statistically stationary conditions is compared to the distribution obtained by averaging over a time window, $T_{avg} \approx 18D/\overline{U}_b$, during which the bulk scalar was approximately 90% of the mean bulk scalar at statistically stationary conditions. The figure also shows the data of Lee and Lee [53] and Katti et al. [45]. At small radial distances, almost no differences are observed between the statistically stationary- and the transient-Nusselt number distributions. In contrast, at greater radii, the transient-Nusselt number is significantly larger than that of the statistically stationary case, indicating a locally more intense scalar transfer. In particular, the transient-Nusselt number distribution appears closer to the experimental measurements in this region.

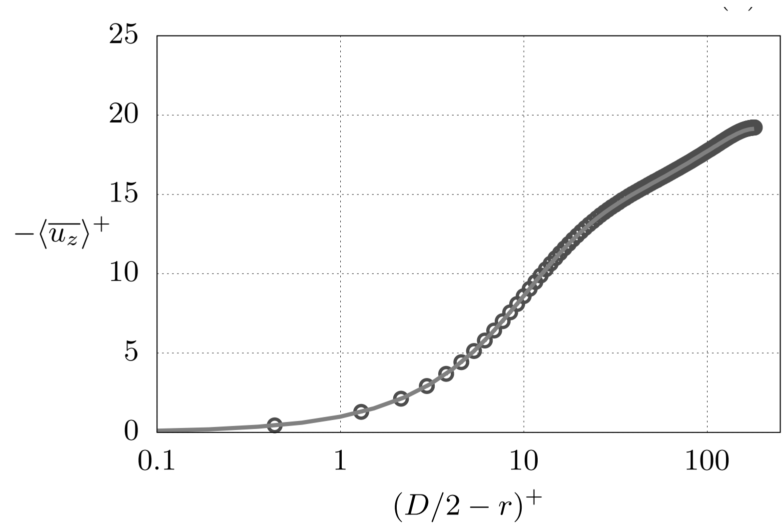

Figure A.5: Mean axial velocity profile at the inflow section of the jet domain (symbols); DNS data of Pirozzoli et al. [69] (solid line).

At the inflow section of the computational domain (i.e., at the nozzle exit), a turbulent velocity field is interpolated at each time step from a cross-section of a fully developed turbulent pipe flow simulation. Figure A.5 compares the mean axial velocity profile at the jet inflow section with the DNS data of [69] for pipe flow at a friction Reynolds number $Re_\tau = 180$, corresponding to a bulk Reynolds number of $Re = 5300$.

At the open boundary, inflow may occur due to the convection of vortical structures across the boundary. From an energetic perspective, the momentum influx can result in an unbounded increase in the kinetic energy of the system and, ultimately, it can lead to numerical instabilities. This is avoided by the application of the energy-stable boundary boundary condition of Dong et al. [18]. This prescribes the balance between the local total stress and the stress induced by the local momentum influx. In contrast, the total stress is set equal to zero if no inflow occurs, and the open boundary condition reduces to the well-known zero-gradient boundary condition. For the scalar field an analogous strategy, proposed by Liu et al. [54], is applied. In particular, at inflow regions on the open boundary, the scalar flux is set to balance the convected scalar influx; conversely, where no inflow occurs, the scalar flux is set to zero. The prescription of different values of the total stress and of the net scalar flux over inflow and outflow regions of the open boundary is achieved through a smooth step function which returns a unitary value where inflow occurs.

Nevertheless, open boundaries always introduce a certain degree of modelling error in a simulation, and thus the dependence of the results on the actual location of the open boundaries needs to be carried out [75]. This is done for the present data by comparing the mean mechanical energy budget, (3.69), shown in figure 5.29, with data from an additional DNS on a larger computational domain but similar spatial resolution. In particular, the larger computational domain has $L_x = 20D$ and $L_y = 20D$. The result is reported in figure A.6, where a good agreement can be observed between both data sets for each plotted quantity.

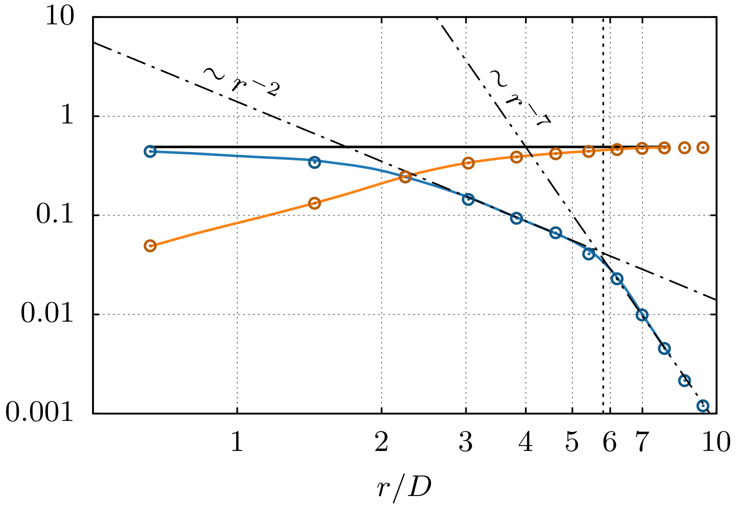

Figure A.6: Mechanical energy integral budgets. ———, Π_{in}; ———, Π_{out}; ———, $\mathcal{E}$. Symbols indicate data on the computational domain $L_x = 20D$ and $L_y = 20D$. A black-dashed line indicates the radial location of flow separation on the impingement plate.

R_{in}/D	N_{x1}	N_{x2}	N_{R1}	N_{R2}	N_{R3}	N_z
0.2	32	32	28	84	56	96

Table A.2: Mesh parameters of the jet flow domain. All the parameters reported in the table are depicted in figure A.7 for clarity. The first column in the table indicates the inner radius of the mesh, while the other columns report the number of elements in the respective direction.

A.3 Rough wall impinging jets

Rough wall impinging jet data presented in section 5.4 of the present investigation is from different sources. Cases $J01 - J04$ are from Secchi et al. [80] and Secchi et al. [81], whereas cases $J06 - J07$ are from Secchi et al. [82] and Secchi et al. [84]. Validating the numerical simulations is particularly challenging since practically no detailed data is available in the literature for rough wall impinging jets. In this respect, it is remarked that the DNS-to-experimental measurements comparison presented by Secchi et al. [80] and reported in figure 5.34 is, to the best of the author's knowledge, the only instance.

The computational mesh used in [80] is displayed in figure A.7 and the related parameters are reported in table A.2. The computational mesh consists in a total number of elements $E = 2\,034\,995$, which, for a representation of the solution with a polynomial degree $N = 7$, amounts to $\approx 1.042 \times 10^9$ DOF. The large number of DOF is required to simulate the relatively high Reynolds number, $Re = 10\,000$, and to accurately resolve the roughness topography using the IBM introduced in section 4.3.1. Nevertheless, the extremely high computational cost associated with performing such a simulation prevents the possibility of carrying out extensive grid independence studies. In [80], the grid independence of the result is shown only for the case in which the presence of surface roughness is modelled through the parametric forcing approach of Forooghi et al. [22]. In this case, two solutions on the mesh of figure A.7 with polynomial degrees $N = 3$ and $N = 5$ are compared. The result is reported in figure A.8, where several mean radial velocity profiles at different radial stations are compared between the two solutions.

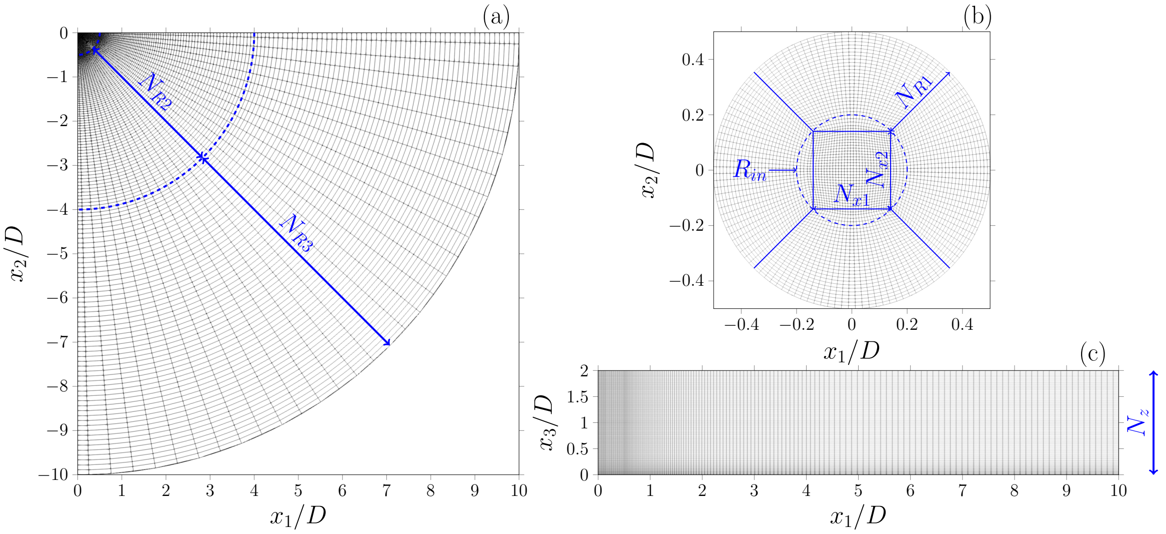

Figure A.7: Computational mesh of the jet flow domain. Values of the parameters depicted in the figure are reported in table A.2. (a) Top view, $x_1 - x_2$ plate; (b) Top view, inset of the jet inflow section, $x_1 - x_2$ plane; (c) Lateral view, $x_1 - x_3$ plane.

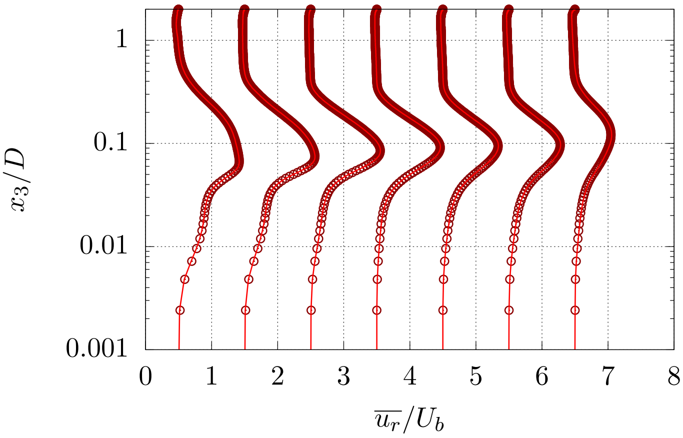

Figure A.8: Comparison between two different order solutions for a representative PFA-resolved case. The figure depicts mean radial velocity profiles at $r/D = 0.6,\ 0.8,\ 1.0,\ 1.2,\ 1.4,\ 1.5,\ 2.0$. Profiles are shifted to the right from each other by 1.0 units for better visualization. ○ ○ ○, 3^{rd} order solution; ——, 5^{th} order solution.

It is further remarked that the high computational cost associated with the IBM-resolved roughness cases prevented the possibility of acquiring flow statistics over large time spans. In this respect, [80] report flow statistics computed by sampling over a time window of $\approx 40D/\overline{U}_b$. Hence, some dependence on the interval of statistics acquisition is likely to still affect the data and might justify the discrepancies observed in figure 5.34 between the DNS data and the experimental measurements at large radial distances.

The smooth and rough wall impinging jets simulations presented in [82] and [83], which are reported in section 5.4 as cases $J06 - J07$, target a smaller Reynolds number using the same computational mesh as the smooth wall case, $J05$, shown in figure A.2. The grid independence study was carried out on the smooth wall case, $J05$, only and thus it is described in section A.2 of this appendix. Unfortunately no experimental measurements exist for the configurations investigated by the cases $J06$ and $J07$. Hence, the validation of the numerical framework relied on the smooth wall case, $J05$ (shown in figure **??**). Furthermore, unlike cases $J01 - J04$, surface roughness is resolved in the simulations using a body-fitted mesh obtained by deforming the elements of the mesh according to the strategy presented in section 4.3.2. In comparison to the IBM method used for cases $J01 - J04$ (the IBM is presented in section 4.3.1), this approach has the advantages of not compromising the accuracy of the solver and of enabling the accurate computation of the momentum and scalar fluxes at the wall.

It is further remarked that the cases $J05 - J07$, unlike cases $J00 - J04$, consider also the scalar transfer problem. The reason behind the fact that only three low-Reynolds number cases consider the scalar transfer problem is the computational cost required to run these simulations for a long period of time. In fact, the transient necessary for the scalar field to reach statistically stationary conditions greatly exceeds that of the velocity field. At $Re = 5\,300$ and $Pr = 1$, the volume-averaged scalar value reached a statistically stationary condition after $\mathcal{O}(1000)D/\overline{U}b$ starting from a uniform initial scalar field at equilibrium with the scalar at the nozzle exit section; conversely, for the velocity field the transient is in the order of $\mathcal{O}(100)D/\overline{U}_b$.